UNIVERSITEIT
ANTWERPEN

Faculteit Wetenschappen
Departement Natuurkunde

On the wavefront aberrations of the human eye and the search for their origins

Proefschrift voorgelegd tot het behalen van de graad van
Doctor in Wetenschappen aan de Universiteit Antwerpen
te verdedigen door

JOS ROZEMA

Promotor: **Prof. Dr. Dirk van Dyck** **Antwerpen, 2004**
Copromotor: **Prof. Dr. Marie-José Tassignon**

"As when a man, about to sally forth,
Prepares a light and kindles him a blaze
Of flaming fire against the wintry night,
In horny lantern shielding from all winds;
Though it protect from breath of blowing winds,
Its beam darts outward, as more fine and thin,
And with untiring rays lights up the sky:
Just so the Fire primeval once lay hid
In the round pupil of the eye, enclosed
In films and gauzy veils, which through and through
Were pierced with pores divinely fashioned,
And thus kept off the watery deeps around,
Whilst Fire burst outward, as more fine and thin.

The gentle flame of eye did chance to get,
Only a little of the earthen part.

From which by Aphrodite, the divine,
The untiring eyes were formed.

Thus Aphrodite wrought with bolts of love

One vision of two eyes is born."

Empedocles[1] (5th centure BC)

"Nun ist es nicht zuviel gesagt, dass ich einem Optiker gegenüber, der mir ein Instrument verkaufen wollte, welches die letztgenannten Fehler hätte, mich vollkommen berechtigt glauben würde, die härtesten Ausdrücke über die Nachlässigkeit seiner Arbeit zu gebrauchen und ihm sein Instrument mit Protest zurückzugeben. In Bezug auf meine Augen werde ich freilich letzteres nicht thun, sondern im Gegentheil froh sein, sie mit ihren Fehlern möglichst lange behalten zu dürfen."

Hermann von Helmholtz[2] (1821-1894)

Table of Contents

TABLE OF CONTENTS ..... *- 5 -*

LIST OF COMMONLY USED ABBREVIATIONS AND VARIABLES ..... *- 9 -*

ACKNOWLEDGEMENTS ..... *- 11 -*

PROLOGUE: AIM OF THIS WORK ..... *- 13 -*

CHAPTER I INTRODUCTION TO OCULAR WAVEFRONT ABERRATIONS ..... *- 15 -*

I.1 HISTORICAL INTRODUCTION TO ABERROMETRY ..... - 15 -
I.1.1 PHYSIOLOGICAL OPTICS - 15 -
I.1.2 HISTORY OF WAVEFRONT ABERRATIONS - 17 -
I.2 THE EYE'S OPTICAL SYSTEM ..... - 17 -
I.2.1 PHYSIOLOGY OF THE EYE - 17 -
I.2.2 MATHEMATICAL EYE MODELS - 18 -
I.3 WHAT ARE WAVEFRONT ABERRATIONS? ..... - 22 -
I.4 WAVEFRONT SENSING AND RECONSTRUCTION ..... - 22 -
I.4.1 FOCAL SHIFT - 22 -
I.4.2 WAVEFRONT RECONSTRUCTION - 24 -
I.4.3 REFERENCE AXES - 26 -
I.4.4 POLYNOMIALS USED FOR WAVEFRONT RECONSTRUCTION - 27 -
I.4.5 WAVEFRONT CHARACTERIZATION PARAMETERS - 32 -
I.5 ABERROMETER TECHNIQUES ..... - 34 -
I.5.1 SUBJECTIVE SERIAL TECHNIQUES - 35 -
I.5.2 OBJECTIVE SERIAL TECHNIQUES - 37 -
I.5.3 SUBJECTIVE PARALLEL TECHNIQUES - 37 -
I.5.4 OBJECTIVE PARALLEL TECHNIQUES - 38 -
I.5.5 OTHER TECHNIQUES - 41 -

PART I: CLINICAL COMPARISON OF 6 ABERROMETERS

CHAPTER II CLINICAL COMPARISON OF 6 ABERROMETERS: TECHNICAL SPECIFICATIONS ..... *- 49 -*

II.1 ABSTRACT ..... - 49 -
II.2 INTRODUCTION ..... - 49 -
II.2 MATERIALS AND METHODS ..... - 50 -
II.2.1 PRINCIPLES USED TO MEASURE THE ABERRATIONS - 50 -
II.2.2 MEASUREMENT DETAILS - 54 -
II.2.3 ALIGNMENT - 54 -
II.2.4 CALCULATION DETAILS - 56 -
II.2.5 DATA ANALYSIS - 57 -
II.2.6 MISCELLANEOUS - 58 -
II.3 RESULTS ..... - 58 -
II.3.1 PRINCIPLES USED TO MEASURE THE ABERRATIONS - 58 -

II.3.2 MEASUREMENT DETAILS - 58 -
II.3.3 ALIGNMENT - 59 -
II.3.4 CALCULATION DETAILS - 61 -
II.3.5 DATA ANALYSIS - 61 -
II.3.6 MISCELLANEOUS - 62 -
II.3.7 USER AND PATIENT PARAMETERS - 62 -
II.4 DISCUSSION - 63 -
II.4.1 VFA - 63 -
II.4.2 OPD-SCAN - 63 -
II.4.3 ZYWAVE - 63 -
II.4.4 WASCA - 64 -
II.4.5 MULTISPOT - 64 -
II.4.6 ALLEGRETTO - 64 -
II.5 CONCLUSION - 65 -
ACKNOWLEDGEMENTS - 65 -

CHAPTER III CLINICAL COMPARISON OF 6 ABERROMETERS II: STATISTICAL COMPARISON ON A TEST GROUP - 67 -

III.1 ABSTRACT - 67 -
III.2 INTRODUCTION - 67 -
III.3 PATIENTS AND METHODS - 68 -
III.3.1 PATIENTS - 68 -
III.3.2 ABERROMETERS - 68 -
III.3.3 TEST PERIOD - 69 -
III.3.4 MEASUREMENTS AND CALCULATIONS - 69 -
III.3.5 STATISTICAL COMPARISON - 72 -
III.4 RESULTS - 73 -
III.4.1 REFRACTION - 76 -
III.4.2 ZERNIKE POLYNOMIALS - 76 -
III.4.3 RMS - 76 -
III.4.4 INTERACTION ANALYSIS BETWEEN THE EYE AND THE ABERROMETERS - 77 -
III.4.5 INDIRECT COMPARISON USING LINEAR MODELS - 79 -
III.5 DISCUSSION AND CONCLUSION - 81 -
ACKNOWLEDGEMENTS - 82 -

PART II: LAMINOGRAPHIC PHASE RECONSTRUCTION OF THE OCULAR ANTERIOR SEGMENT

CHAPTER IV THREE-DIMENSIONAL RECONSTRUCTION OF OBJECTS USING LAMINOGRAPHY - 85 -

IV.1 HISTORICAL INTRODUCTION TO LAMINOGRAPHY - 85 -
IV.2 MATHEMATICAL INTRODUCTION - 86 -
IV.2.1 DEFINITIONS - 86 -
IV.2.2 RECONSTRUCTION METHODS - 86 -
IV.2.3 RESOLUTION - 90 -
IV.3 LAMINOGRAPHIC RECONSTRUCTION - 91 -
IV.3.1 RECONSTRUCTION OF A GENERAL OBJECT - 92 -
IV.3.2 DEPENDENCY ON THE ANGLE OF INCIDENCE - 94 -
IV.3.3 RECONSTRUCTION OF LAYERS OTHER THAN THE FOCAL LAYER - 94 -
IV.3.4 CONTRAST SENSITIVITY - 95 -

IV.3.5 SMEARING (WASH-OUT) - 95 -
IV.4 CONCLUSION ..... - 97 -

CHAPTER V LAMINOGRAPHY APPLIED TO THE HUMAN EYE ..... - 99 -

V.1 ABERRATION LAMINOGRAPHY ..... - 99 -
V.2 REFRACTIVE CORRECTION ..... - 100 -
V.2.1 TWO-DIMENSIONAL RAY TRACING - 100 -
V.2.2 THREE-DIMENSIONAL RAY TRACING - 102 -
V.3 PERIPHERAL WAVEFRONT MEASUREMENTS ..... - 106 -
V.3.1 PERIPHERAL ABERRATION DATA - 107 -
V.3.2 DISCUSSION - 109 -
V.4 RECONSTRUCTIONS ..... - 109 -
V.4.1 VALIDATION OF THE RECONSTRUCTION TECHNIQUES - 109 -
V.4.2 NAVARRO DATA - 112 -
V.4.3 ATCHISON DATA - 113 -
V.4.4 FULL-FIELD MEASUREMENTS - 114 -
V.5 CONCLUSIONS ..... - 115 -

PART III: DESIGN AND FIRST RESULTS OF A CURVATURE SENSING ABERROMETER

CHAPTER VI PRINCIPLES OF CURVATURE SENSING ..... - 119 -

VI.1 INTRODUCTION ..... - 119 -
VI.2 MATHEMATICAL PRINCIPLES ..... - 119 -
VI.2.1 DERIVATION OF THE TECHNIQUE - 119 -
VI.2.2 RECONSTRUCTION TECHNIQUES - 121 -
VI.2.3 DETERMINATION OF $\partial I/\partial z$ - 126 -
VI.2.4 INFLUENCE OF NOISE - 127 -
VI.2.5 MEASURING DEFOCUS IMAGES - 129 -
VI.3 USED MATERIALS ..... - 131 -
VI.4 RESULTS ..... - 131 -
VI.4.1 COMPARISON OF RECONSTRUCTION TECHNIQUES - 131 -
VI.4.2 COMPARISON WITH ZERNIKE PHASE CONTRAST - 132 -
VI.4.3 DEPENDENCY OF PHASE RESOLUTION WITH dz - 134 -
VI.4.4 DEPENDENCY ON PUPIL SHAPE - 134 -
VI.5 CONCLUSIONS ..... - 135 -

CHAPTER VII DESIGN AND FIRST RESULTS OF A CURVATURE SENSING ABERROMETER ..... - 137 -

VII.1 CSA DESIGN ..... - 137 -
VII.1.1 PROOF OF PRINCIPLE USING THE SERIAL LENS METHOD - 137 -
VII.1.2 DESIGN OF A PARALLEL CSA USING THE GRATING METHOD - 138 -
VII.2 FIRST RESULTS ..... - 138 -
VII.2.1 VERIFICATION OF THE METHOD - 138 -
VII.2.2 TEST EYES AND HUMAN EYES - 140 -
VII.3 CONCLUSIONS ..... - 140 -

EPILOGUE: CONCLUSIONS AND THOUGHTS ON THE FUTURE EXPANSION OF THIS WORK ..... *- 141 -*

SAMENVATTING EN CONCLUSIES ..... *- 143 -*

LIST OF PUBLICATIONS ..... *- 145 -*

BIBLIOGRAPHY ..... *- 147 -*

List of commonly used abbreviations and variables

Abbreviations

Wavefront analysis

FFT = Fast Fourier Transform
MTF = Modulation Transfer Function
OTF = Optical Transfer Function
PSF = Point Spread Function
PTF = Phase Transfer Function
RMS = Root-Mean-Square
RMS_{tot} = Total RMS
RMS_{HO} = Higher Order RMS
ZRMS = Zonal RMS

Names of devices

CSA = Curvature Sensing Aberrometer
(c)SLO = (confocal) Scanning Laser Ophthalmoscope
COAS = Complete Ophthalmic Analysis System
HS = Hartmann-Shack
LRT = Laser Ray Tracing
OPD = Optical Path Difference
SH = Shack-Hartmann
VFA = Visual Function Analyzer

Ophthalmic terms

ASE = Aberrometer Spherical equivalent
CSE = Clinical Spherical Equivalent
LoS = Line of Sight
OD = Oculus Dexter; right eye
OS = Oculus Sinister; left eye

Terms used in Figures

N = Nasal (i.e. side of the nose)
T = Temporal (i.e. side of the temple)
S = Superior (i.e. upper side)
I = Inferior (i.e. lower side)

Optical terms

APD = Avalanche Photo Diode
CCD = Charge Coupled Device
LED = Light Emitting Diode
NA = Numeric Aperture

Names of methods, equations, points

ART = Algebraic Reconstruction Technique
COC = Center of Curvature
ROC = Radius of Curvature
GS = Gerchberg-Saxton
POI = Point of Incidence
TIE = Transfer of Intensity Equation
TWE = Transfer of Wavefront Equation

Organizations

OSA = Optical Society of America
ESCRS = European Society for Cataract and Refractive Surgery
FRO = (Belgian) Fund for Research in Ophthalmology

Variables

Coefficients and indices

$n, m, j, \ldots$: index names
N, M : maximum index/ number
$a_k, b_k, \ldots$: polynomial coefficient
W_{ijk} : Seidel coefficient

Coordinates

o : origin
$\vec{r} = (x,y,z)$: Carthesian coordinates in real space (pupil plane)
(u,v,w) : Carthesian coordinates in Fourier space (retinal plane)
(ρ,θ) : polar coordinates
$(\delta u, \delta v)$: focal shift

General optical variables

λ : wavelength
k : wavenumber
n : refractive index
r : radius of curvature
c_n : curvature ($= 1/r$)
K : conic constant
d : thickness of optical medium
f : focal distance
I : intensity
A : amplitude
φ : phase/ wavefront aberration

Polynomials

u_j : general polynomial
Z_n : Zernike polynomial (single index)
Z_n^m : Zernike polynomial (double index)
R_n^m : radial component of Zernike polynomial
Θ_m : angular component of Zernike polynomial
N_n^m : Noll normalization factor for Zernike polynomial
P_k : Legendre polynomial

General laminography (Chapter IV)

P, Q : point
M : magnification
S_k : source position
ψ : angle of incidence
h : distance from source to focal plane
d : distance from focal plane to image plane
δm : horizontal resolution
δn : vertical resolution
μ : attenuation
α : attenuation factor

Refractive laminography (Chapter V)

ψ : angle of incidence
θ : angular direction
γ, γ' : Snell's angles
α_m : skew ray angle (2D raytracing)
α_m : angle in (y,z) plane (3D raytracing)
β_m : angle in (x,z) plane (3D raytracing)
Δz_m : difference along optical axis between point of incidence and surface apex
R_m : local radius of curvature
χ_m : angle between optical axis and local radius of curvature in COC

Curvature sensing (Chapter VI)

Γ : area in which TIE is defined
Ω : edge of Γ
$G(x,y;x',y')$: Green's function

Acknowledgements

Over the years that it took to complete this research many people have passed by and given a contribution to my work by giving advice, comments or friendship and support. Without their help this thesis would be a lot thinner…

First I want to thank my promoter, Prof Dirk van Dyck, for giving me the opportunity to do this work and keeping me focused, as well as my co-promoter Prof Marie-José Tassignon for giving me many new opportunities and a large number of interesting discussions. I'm also grateful to Dr. Frans van de Velde who helped me take my first steps in the field of aberrometry.

Lots of thanks to Andrey Larichev and Nikita Irochnikov for providing their MultiSpot aberrometer and performing a number of curvature sensing measurements. Also thanks to Michael Mrochen and the different companies that lend us their aberrometers and helped us with figuring out their technical details.

A special acknowledgement to the technical people in the University of Antwerp that helped me in many different ways: Flor Peeters, Luc Sanspoux, Freddy Schallenberg and the late Jan Decroo.

Not to forget all the people that were part of the Vision Lab for a longer or shorter period of time: my room mates Erik Claes, Edwin Bogo and Greg Tisson for many laughs. Steve De Backer, Jan Sijbers, Erik Raman, Paul Scheunders, Gert Van de Wouwer and Barbara Weyn for help on various subjects. And Eva Bettens, Etienne Cornelis, Bart De Boeck, Arjan den Dekker, Wim D'Haes, Jef Driesen, Toon Huysmans, Jaber Juntu, Alexander Leemans, Dirk Meersman, Andrei Postnov, Yu Shixin, Alain Smolders, Inton and Inden Tsang, Elke Van de Casteele, Ann Van Den Bogaert, Wouter Van den Broek and Gert Van Gompel for the good atmosphere, making the Vision Lab a fun place to work.

And of course the people of the Department of Ophthalmology in the University Hospital: Nezahat Bostan, Laure Gobin and Rudi(c) Leysen for their friendship. Kris Baelemans, Sophie Ceuterick, Jeroen Claeys, Tanja Coeckelbergh, Veva de Groot, Prof. Robert de Keizer, Katrien de Keyzer, Chris de Smedt, Ilse de Veuster, Pascale Evens, Claudia Ferdinandus, Daisy Godts, Stefan Kiekens, Maaike Klinkenberg, Carina Koppen, Inge Leysen, Danny Mathysen, Kynza Mgaieth, Bruno Reyntjens, Patrick Schraepen, Leen Smet, Erica Smets, Chris Snoeckx, Brigitte Swenters, Rene Trau, Jan van Looveren, Greet Vandeweyer, Kristien Verbruggen, Dominik Verhelst and Sofie Wynants for being such great people to work with.

Greg, Andrei and Liubov for the aperiodical pool nights and subsequent long discussions over a pita and a Martini.

Last, but definitely not least, to my dear wife Silvia that has made me so happy over the last couple of years, as well as my family and in-laws for all their support and interest.

Jos Rozema
Antwerp, 8 December 2004

Prologue: aim of this work

Most eyes are far from perfect. Every eye presents a unique set of optical aberrations that influence the incident light, ranging from slightly blurred vision to distorted and double sight. Till recently the only way to compensate for these ocular aberrations was by adding a new optical element. This could be done by either spectacles or contact lenses, both of which require only general information about the ocular refraction. The results obtained are satisfactory for most patients, but not optimal as small, uncorrected aberrations remain.
With the introduction of refractive surgery other methods became popular that modified the cornea in such a way that aberrations would be minimized, using corneal incisions or laser ablations. The first generation of laser systems could only make similar corrections as could be achieved using spectacles, but they quickly evolved into flexible platforms theoretically capable of sculpting the inverse of the ocular wavefront aberrations on the anterior ocular surface. However in order to achieve the best possible result with these systems very detailed knowledge of the ocular aberrations is imperative.

One way to obtain this knowledge is by studying the aberrations' origins, as is presented in this work. Here a number of different aspects influencing aberration measurement and the localization of the aberration sources within the eye will be highlighted:

The **first chapter** will introduce many of the concepts commonly used in this field of optics, such as the definitions of wavefront aberrations, wavefront measurements, a number of derived quantities (RMS, PSF, MTF,…) and a basic description of the different aberrometer types.

Part I focuses on the similarities and the differences between 6 aberrometers that are on the market today. How reliable are the measurements provided by these machines? And will each of them give you the same result if you apply them to the same eye under clinical circumstances? The accent lies not on which device is 'the best', but rather on the minimal technical requirements any good aberrometer should have (in our opinion) in order to provide reliable and reproducible measurements. (**Chapter II**)
In an effort to determine the aberrometer's clinical reliability, we have performed a series of measurements on a fixed group of subjects and compared the results statistically. These results are presented in **Chapter III**.

After establishing the quality of the wavefront measurements, we can start the search for the aberrations' origins in **Part II**. This search will lead past known reconstruction techniques in tomography and their properties (**Chapter IV**). Next these methods are redefined to take the ocular refraction into account, which allows making a 3D phase reconstruction of the anterior eye segment from a number of off-axis wavefront measurements. The description of this refraction corrected laminography technique and the obtaining of the off-axis measurements are given in **Chapter V**.

In **Part III**, curvature sensing is introduced as a new high-resolution wavefront sensing method. These high resolutions can be used to study wavefronts in greater detail, but also obtain better off-axis measurements for the laminographic reconstructions described above. **Chapter VI** describes curvature sensing, a large number of the reconstruction techniques in the literature and the properties and verifications of these techniques for general

microscopical applications. This is elaborated in **Chapter VII** to a proof of principle setup for the measurement of lenticular aberrations.

Finally a number of conclusions are given in the **Epilogue**, as well as a number of future research lines.

Chapter I Introduction to ocular wavefront aberrations

I.1 *Historical introduction to aberrometry*

The eye has always fascinated both layman and scientist, either for its romantic nature or in an effort to understand the deeper principles of vision. It has inspired vast numbers of theories, some of which still hold today, but also many that have been forgotten in time or were reduced to historical footnotes. This paragraph provides a far from complete overview of what aspects of vision have been studied before by past generations of scientists and attempts to place them in a historical context.

I.1.1 **Physiological optics**[3]

Already in the Antiquity a theory circulated among the ancient Greeks that eye sight was the result of fire particles that were emitted by the eye to meet similar particles coming from an object[1]. When these particles meet, vision is achieved. This theory by Empedocles of Acragas (5th century BC) is often referred to as the "Fire of the Eye" or the "tentacle theory" and was accepted by great philosophers and scientists such as Plato, Euclid and Ptolemy. This widespread belief lasted until well in the Middle Ages, despite the notion of Aristotle that

> *"If the visual organ proper really were fire, which is the doctrine of Empedocles, […], and if vision were the result of light issuing from the eye as from a lantern, why should the eye not have had the power of seeing even in the dark?*[4]*"*

Aristotle had the more modern conception that things are seen by influences resulting from their presence rather than from rays emerging from the eye. Aristotle was also the first to report myopia and hyperopia, and discovered the change in ability to focus with age. Only in the 16th century a first scientific explanation was given when Francis Maurolycus incorrectly suggested that the curvature of the crystalline lens[5] was its main cause.
Meanwhile in the 10th century Cairo Alhazen spent much of his time conducting experiments involving a dark room with a hole in it. In one experiment he hung five lanterns in front of the hole and noticed that there were five images on the opposite wall in the dark room. The placement of an obstruction between one of the lanterns and the hole resulted in the disappearance of the opposite image on the wall. As the lantern, the obstruction and the hole were in a straight line this demonstrated that light traveled in straight lines and that, even though the light from the five lanterns all traveled through the same hole at the same time, it did not get mixed up. Alhazen proposed that this is how the eye worked. This was the first scientific description of the 'camera obscura'.
In the 15th century Leonardo da Vinci supposed that vision was achieved by an image on the retina, which he identified as the sensitive receptor of the eye. But he struggled with the question how this image was optically inverted to be upright before being sent to the brain:

> *"Necessity has provided that all the images of objects in front of the eye shall intersect in two places. One of these intersections is in the pupil, the other in the crystalline lens; and if this were not the case the eye could not see as great a number of objects as it does. […] No image, even of the smallest object, enters the eye without being turned upside down; but as it penetrates into the crystalline lens it is once more reversed and*

thus the image is restored to the same position within the eye as that of the object outside the eye.[6]"

When Johannes Kepler studied the eye 100 years later he proposed a ray tracing model of the eye. In order to do this he assumed that every point on a light source emits rays of light in all directions, but only those rays that pass through the pupil can enter the eye. This way a cone of light rays can be defined with the top in the point source and the circular base in the pupil. In a normal eye all of the rays in this cone are then refracted to meet again at a single point on the retina. If the eye is not normal, the second short interior cone comes to a point not on the retina but in front of it or behind it, causing blurred vision. With this simple model he managed to explain not only ametropia, but also the effects of eyeglasses that were already in use for more than three centuries. Before Kepler nobody had been able to explain this. On the subject of the nature of the retinal image he wrote:

"Thus vision is brought about by a picture of the thing seen being formed on the concave surface of the retina. That which is to the right outside is depicted on the left on the retina, that to the left on the right, that above below, and that below above.[7]"

with which he disproved Leonardo's assumption. Kepler was also the first to define important concepts, such as the far point of the eye and identified the macula, the central zone of the retina, as the location of sharpest sight.
At the same time the Jesuit priest Christoph Scheiner experimentally verified Keplers theory on the retinal image by mounting an ox eye with the sclera removed in a diaphragm and observing the inverted image. Scheiner was also the first to investigate the accommodation of the eye on objects at different distances and to observe that no accommodation is possible in the absence of the crystalline lens. Further he measured the refractive indices of the different optical media in the eye and made the first anatomically correct representation of the eye (Figure I-1). But his most important invention for the purposes of this thesis was the Scheiner disc, the first aberrometer.
In the late 18th century Scheiner's observations were refined by the English physician Thomas Young, who found that accommodation occurs due to curvature change of the crystalline lens. This was published in an 1801 paper in which he sums up a large deal of the physiological optics known at the time[8]. At the same time physiologist Johannes Purkinje found the reason for these curvature changes: a contraction of the ciliary muscle around lens. Purkinje also studied the reflections of light of the corneal and lenticular surfaces in an attempt to estimate their refractive powers. These reflections are now named in his honor.

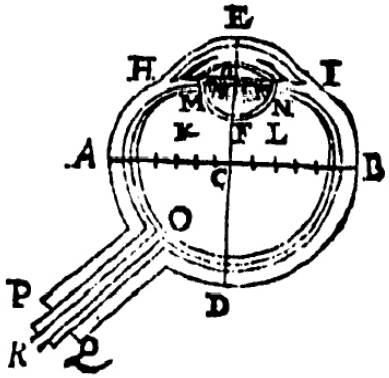

Figure I-1: Scheiner's schematic eye (1619)[9].

In 1867 Hermann von Helmholtz laid the foundations of the modern physiological optics by his book '*Handbuch der Physiologischen Optik*'[10]. Here he gave a very complete oversight of the state of the art at his time and added studies on accommodation, color perception and the way both eyes work together to form a single image. Another one of his accomplishments is the invention of the ophthalmoscope, a device that allows studying a patient's retina directly.

I.1.2 History of wavefront aberrations

In the previous section the early work on ametropia has been discussed, which was mostly done by Kepler and Scheiner. It was shown to be the result of a mismatch of the corneal curvature with the length of the eye, combined with the dioptric power of the lens. When the eye is too short (or the cornea too flat), the image of an object at infinity is formed behind the retina; this condition is known as hyperopia or farsightedness. On the other hand when the eye is too long (or the cornea too curved) the image is formed in front of the retina. This is called myopia or nearsightedness. Both conditions can easily be corrected by putting either a positive or negative spherical lens in front of the eye in order to move the image to the retina.
Apart from being too flat or too curved a cornea can have more irregular shapes that influence the optical quality of the eye as was first mentioned in Young's 1801 paper. This was developed further in the mid 19th century when Seidel developed his theory of geometric aberrations[11], which would later serve as a theoretical base for the aberration theories at the time. In this formalism ocular aberrations were divided into defocus, astigmatism, coma, spherical aberration, distortion and field curvature[12].
But after the first detailed aberrations measurements in the experiments of Ivanoff[13] and Smirnov[14] it quickly became clear that a more general idea of aberrations was needed to explain ocular aberrations. In stead of a system of geometric aberrations, as proposed by Seidel, they suggested that a wave description of aberrations might be more accurate to describe the irregular patterns seen in aberration maps.
When Howland introduced the first aberrometer[15] that was practical to use in 1977, polynomial coefficients were used for the representation of wavefronts. To date, this is still the most commonly used data representation for this purpose. This will be discussed in further detail in I.4.4b).

I.2 *The eye's optical system*

I.2.1 Physiology of the eye

The optics of the human eye is composed of the following optical components (Figure I-2):

- *Cornea*: a strongly curved fully transparent structure of approximately *500μm* thick. It is the first and strongest refracting surface of the eye.
- *Anterior chamber*: a volume of transparent watery liquid (*aqueous humor*) between the cornea and the crystalline lens.
- *Pupil*: circular opening in the *iris*, a colorful membrane located in front of the crystalline lens, that can be adjusted in diameter. Serves mainly to regulate the light influx and to reduce the effects of aberrations.

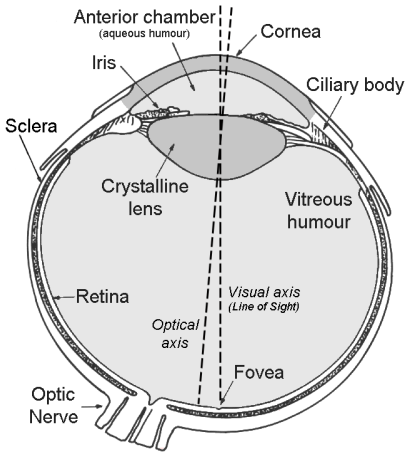

Figure I-2: anatomy of a human eye. All optical media have grey shades, where darker shades indicate higher refractive indices.

- *Crystalline lens*: biconvex body consisting of a large number of transparent fiber-shaped cells. The optical density of these fibers increases towards the core of the lens. Together with the pupil it is the only adjustable part of the eye.
- *Vitreous humor*: transparent watery liquid that fills the largest part of the eye ball.
- *Retina*: light sensitive tissue, basically an extension of nerve fiber endings leading directly to the brain. The different structures will absorb and scatter most of the incident light, causing the light to loose most of its coherence. About 4% of the light is reflected back in the direction of the pupil.

Of these media the cornea and the lens are the refractive elements that project an image on the retina. The central part, the fovea, has a very high density of photoreceptor cells making it the region that provides the sharpest possible vision. Photoreceptors are divided into two classes:

- *Rods*: cells highly sensitive to light of any wavelength in the visual range; incapable of color sight. Located mainly in the peripheral retina.
- *Cones*: cells capable of color sight, but less sensitive to low intensities then rod cells; can be split up in three kinds with each a specific spectral sensitivity: R-, G, and B-cones (with peak sensitivity in respectively red, green and blue). Located mainly in the fovea.

I.2.2 **Mathematical eye models**

In order to calculate the optical properties of the eye a mathematical eye model is indispensable. That is why in the last 100 years a lot of them have been defined for all kinds of different purposes. But for brevity we restrict ourselves to highlighting the following four models as they are the most famous ones at this moment. Although these models serve as an approximation of the real dioptric system of the eye, it is imperative to keep in mind that individual eyes of patients can strongly deviate from these models[16].
Specific parameters are needed for the definition of refractive surfaces in these models, which can be chosen spherical or aspherical. The most general form for such a surface is[17]:

$$z = \frac{\left(x^2 + y^2\right)}{r + \sqrt{r^2 - (K-1)\left(x^2 + y^2\right)}} + \sum_{k=2}^{\infty} A_{k-1}\left(x^2 + y^2\right)^{2k} \qquad \text{(I-1)}$$

with (x,y) coordinates in a plane perpendicular to the optical axis and z the coordinate along the optical axis. The most important parameter in formula I-1 is the radius of curvature r that describes how convex (concave) or flat a spherical surface is. This spherical surface is then corrected by means of conic constant K that serves, together with the higher order aspherical constants A_i, to give the spherical surface an aspherical deformation. The shape of this deformation depends on the K-value:

- $K < -1$: Hyperboloid
- $K = -1$: Paraboloid
- $-1 < K < 0$: Ellipse rotated about its major axis
- $K = 0$: Sphere
- $K > 0$: Ellipse rotated about its minor axis

Other parameters needed for the definition of these eye models are the thicknesses d of the optical media and the refractive indices n (for a specific wavelength λ). For our purposes the constants A_i will be disregarded.

a) Gullstrand exact eye model[18]

This model was devised by Allvar Gullstrand (1862-1930) in order to better understand the image formation in the eye. This model is very complete, separating the core and the outer layers of the lens into two different media (see Table I-1, Figure I-3)*. The accommodation is also taken into account, with different sets of parameters for the 'rest' situation and accommodated situation. For the work associated with this eye model Gullstrand was awarded the Nobel Prize in Medicine in 1911. Some of Gullstrand's other achievements include his PhD thesis on astigmatism[19], which refined Young's theory on this subject, the invention of the slit lamp and of an improved ophthalmoscope.

b) Navarro wide angle schematic eye model[20,21]

This model (1999) is very interesting because it was designed to include the possibility of simulating the image formation away from the optical axis for a number of wavelengths. It is composed of four aspherical surfaces and one aperture stop (pupil). The optical properties (Seidel aberrations, chromatic aberrations, MTF) of this model were found to be in reasonably good agreement with experimental values for eccentricities up to *60°*. This was later also verified for the off-axis wavefront aberrations of the model[22].
Like the Gullstrand model, this model also contains both parameters for the accommodated and the non-accommodated eye (see Table I-1, Figure I-3).

* Actually the Gullstrand model contains a gradually changing refractive index ('gradient index') from the shell towards the core of the crystalline lens by means of formula:

$$n(r,z) = 1.406 - 0.0062685\,(z-z_0)^2 + 0.0003834\,(z-z_0)^3 - (0.00052375 + 0.00005735\,(z-z_0) + 0.00027875\,(z-z_0)^2)\,r^2 - 0.000066716\,r^4$$

with r is the distance in a plane perpendicular to the optical axis and z the distance along the optical axis. z_0 is chosen in the middle of the crystalline lens (so $z_0 = 1.7$ *mm*). This function gives a central index of 1.406 and a surface or edge index of 1.386, the values given in Table I-2.

Table I-1: definition of the different eye models

Name	Gullstrand model without accommodation[23]				Navarro wide angle model without accommodation				Reduced Indiana eye			
Parameter (in *mm*)	***r***	***d***	***n***	***K***	***r***	***d***	***n* *(589.3nm)***	***K***	***r***	***d***	***n***	***K***
Air			1				1				1	
Anterior cornea	7.7	0.5	1.376	0	7.72	0.55	1.376	-0.26	5.55	1.57	1.333	0.6
Posterior cornea	6.8	3.1	1.336	0	6.50	3.05	1.3374	0				
Pupil	+∞	0	1.336	0	+∞	0	1.3374	0	+∞	20.65	1.333	0
Anterior lens	10	0.54	1.386	0	10.20	4	1.42	-3.1616				
Anterior lens nucleus	7.91	2.42	1.406	0								
Posterior lens nucleus	-5.76	0.64	1.386	0								
Posterior lens	-6	17.2	1.336	0	-6	16.32	1.336	-1				
Retina					-12							

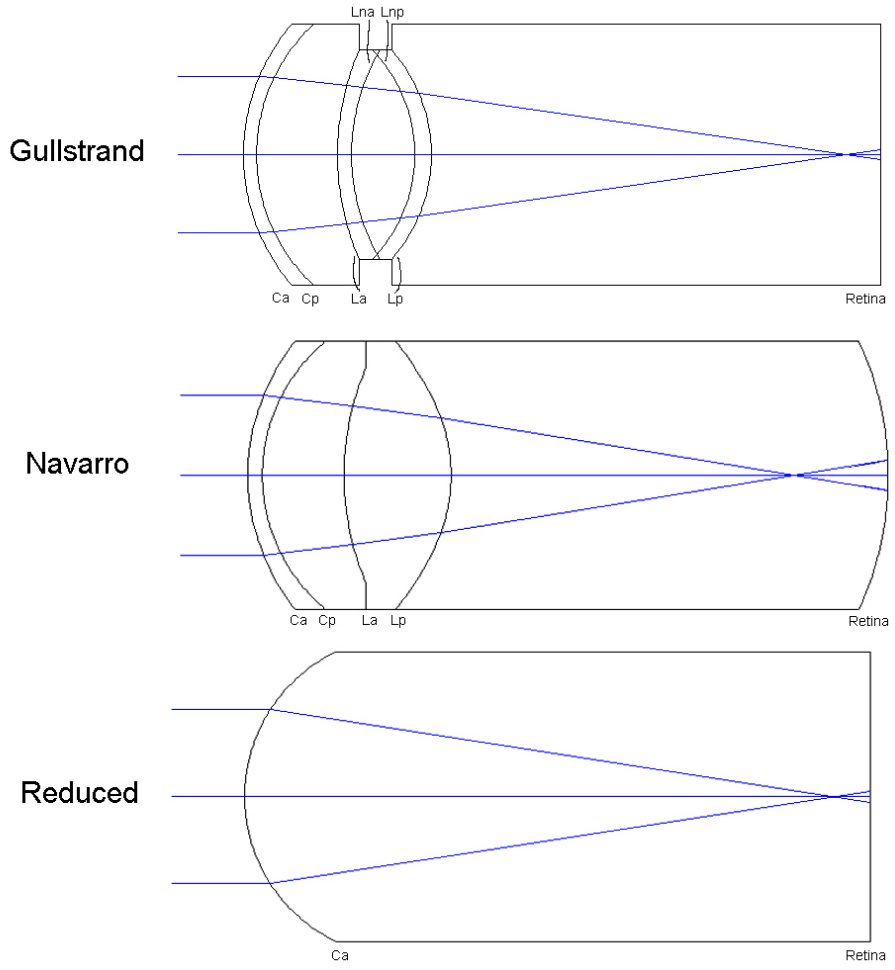

Figure I-3: definition of the three eye models. (Ca: anterior cornea; Cp: posterior cornea; La: anterior lens; Lna: anterior lens nucleus; Lnp: posterior lens nucleus; Lp: posterior lens)

c) Reduced eye model

The easiest model possible is a model with only one single refracting surface. At first this was modeled by a spherical interface between air and water. But as these interfaces have the problem that they introduce large quantities of spherical aberrations, this was replaced by means of the 'Reduced Indiana Eye'[24] (see Table I-1, Figure I-3), an evolved version of the 'Chromatic eye'[25]. This model contains only one elliptical surface (instead of spherical). The refractive index within the eye model depends on the wavelength and is defined by:

$$n(\lambda) = 1.31848 + \frac{0.006662}{\lambda(\mu m) - 0.1292} \qquad \text{(I-2)}$$

Even though this model is very simple, it has been found to match the ocular chromatic aberrations and spherical aberration rather closely.

d) Optical properties of these eye models

According to geometrical optics any optical system composed of several optical elements can, when considered along the model's optical axis (i.e. the paraxial approximation) be characterized by means of 6 cardinal points. These points are:

- *Focal points f_1, f_2*: point to which a parallel beam entering the system will converge. f_1, called 'front focal point', is the convergence point for a parallel beam entering the system from behind; analogous for the back focal point f_2.
- *Principal points P_1, P_2*: cross-section points of the two principal planes with the optical axis. These principal planes are defined as the collection of points in which the extensions of an incident beam parallel to the optical axis and the exiting beam on the other side of the optical system intersect.
- *Nodal points N_1, N_2*: two points on the optical axis with the distinct property that when a beam is directed at one of these points it seems to emerge from the other point on the other of the optical system.

Table I-2: optical properties of the different eye models

Cardinal point	Gullstrand	Navarro	Reduced Indiana Eye*
λ	unknown	589.3 nm	589.3 nm
P_1	1.35 mm	1.58 mm	0 mm
P_2	1.60 mm	1.89 mm	
N_1	7.08 mm	7.14 mm	5.55 mm
N_2	7.33 mm	7.45 mm	
f_1	-17.05 mm	-16.55 mm	-16.67 mm
f_2	24.4 mm	22.35 mm	22.22 mm
P	58.64D	60.42D	60 D

* Since the Reduced Indiana Eye only contains one refractive surface, both principal points will coincide, as well as the nodal points.

Table I-2 gives an oversight of the cardinal points for the different eye models. The values for the focal points seem to correspond well with each other, as well as the total refractive power *P* of the system. However the cardinal points seem to vary more between the different models.

I.3 *What are wavefront aberrations?*

Light can be considered as a series of waves emanating from a source. If the light source is an infinitely small point source the resulting waves will be spherical, which will at large distances approximate plane waves. Using a lens these waves can be manipulated to converge towards or diverge from a specific point in space, called the focal point. This point is located at a focal distance *f* from the lens (see I.2.2d).
If a point source is placed in the focal point of an ideal lens, this lens will transform the incoming spherical waves into perfectly plane waves (see the dashed lines in Figure I-4). An imperfect lens however, such as a lens with local variations in curvature or refractive index, will superimpose the plane waves with a distortion (solid lines in Figure I-4). The difference between the distorted waves and the undistorted waves is called the *wavefront aberration* φ of this lens. It can easily be seen that the amplitude of wavefront aberrations directly depends on the quantity and the size of the optical imperfections causing them.
In geometrical optics rays are used in stead of waves, but it suffices to know that these aberrated rays are perpendicular to the wavefront aberrations as described above.
A *wavefront sensor*, or *aberrometer*, is a device designed to measure the amount of aberrations present in an optical system.

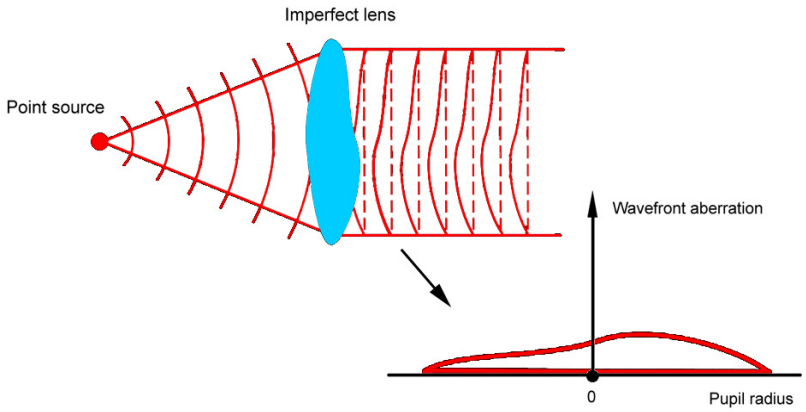

Figure I-4: definition of wavefront aberrations.

I.4 *Wavefront sensing and reconstruction*

I.4.1 **Focal shift**

Every wavefront sensor on the market today is in one way or another based on focal shift. This is a basic property of a perfect lens that, regardless of the point of incidence, an incident beam parallel to the lens' optical axis is always refracted through the focal point (see dashed

beam in Figure I-5). However when the lens has some aberrations this is no longer true and each incident beam is refracted through a different point of the focal plane (solid beam in Figure I-5). The distance within the focal plane between the cross-section point of the refracted beam and the focal point is called the focal shift and is directly proportional to the local gradient of the lens' wavefront aberration. As rays are perpendicular to the local wavefront, each local wavefront tilt gives rise to an equal tilt added to the refracted beam*.

In the human eye the spot pattern can be measured either on the retina, or in a plane that is optically conjugated with the retina. In both cases it must be kept in mind that the image of the spot pattern has passed through the aberrated eye optics twice. There where the subject can observe the Point Spread Function (since from his point of view the light only went through the optics just once), a fundus camera registers the autocorrelation[27] (rather than the autoconvolution) of the Point Spread Function image. All information regarding odd aberrations is lost this way.

Every objective wavefront sensing technique is confronted with this 'double-pass' problem, but in most cases it can be reduced considerably by turning it into a 'one-and-a-half- pass' method. Here a narrow sample beam is used, making sure that the spot on the retina is only aberrated by the usually very mild local aberrations. The reflection of this narrow spot now serves as a diffuse secondary source that homogeneously illuminates the pupil opening from behind. When the light passes through the lens and cornea it is distorted by the ocular wavefront aberrations.

In practice it can be difficult to determine an accurate value for the focal shift, since due to the local aberrations of the lens the point size can be rather large. This is remedied by calculating either the centroid (the geometric center of the spot) or the 'center of mass', which is given by[28]:

$$\rho_u = \frac{\iint u \cdot I(u,v)dudv}{\iint I(u,v)dudv}, \rho_v = \frac{\iint v \cdot I(u,v)dudv}{\iint I(u,v)dudv} \qquad \text{(I-3)}$$

with (u,v) the coordinates in the focal plane and (ρ_u, ρ_v) the coordinates of the center of mass. Usually the center of mass is preferred as the centroid can sometimes be hard to determine.

A more mathematical description can also be given. Suppose (x,y) are the coordinates of the incident beam in the lens plane and $\varphi(x,y)$ the wavefront aberration of the lens in that location. If the horizontal and the vertical vector components of the focal shift are given by $\delta u(x,y)$ and $\delta v(x,y)$, then we find that:

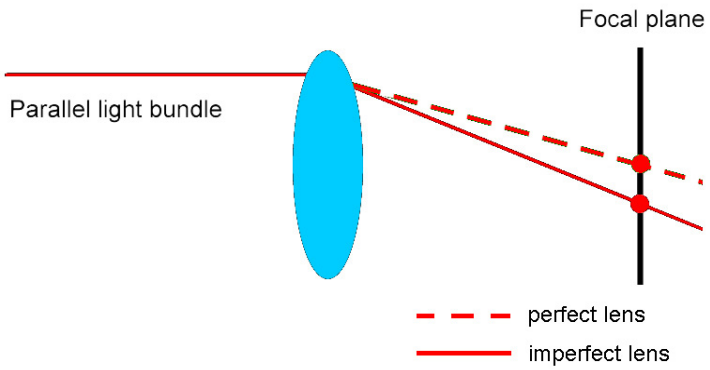

Figure I-5: focal shift

* A more elaborate explanation on this subject can be found in reference [27].

$$\begin{cases} \delta u(x,y) = f\,\dfrac{\partial \varphi(x,y)}{\partial x} \\ \delta v(x,y) = f\,\dfrac{\partial \varphi(x,y)}{\partial y} \end{cases} \tag{I-4}$$

with f the local length of the lens causing the focal shift. By mapping ($\delta u(x,y)$, $\delta v(x,y)$) for a grid of beam entry locations on the lens, one can directly map the gradient of the wavefront aberration. From this gradient data the wavefront aberration $\varphi(x,y)$ can be reconstructed through integration.

I.4.2 **Wavefront reconstruction**

a) Integration by polynomial fit[29, 30]

In this method it is assumed that the wavefront aberration $\varphi(x,y)$ can be represented as a linear combination of orthogonal polynomials $Z_k(x,y)$ defined on the unit circle (such as e.g. Taylor[31, 32], Legendre[33], Zernike[34, 35, 36], Didon[37] or Karhunen-Loève[38, 39] polynomials). So in other words:

$$\varphi(x,y) = \sum_{n=0}^{N} a_n Z_n(x,y) \tag{I-5}$$

with a_n the polynomial coefficients.
Suppose now a set of K experimentally determined focus shifts in points (x_k,y_k) ($k = 1{:}K$) in the pupil plane. Then the aim is to solve a system:

$$\begin{bmatrix} \varphi(x_1,y_1) \\ \varphi(x_2,y_2) \\ \vdots \\ \varphi(x_K,y_K) \end{bmatrix} = \begin{bmatrix} Z_1(x_1,y_1) & Z_2(x_1,y_1) & \cdots & Z_N(x_1,y_1) \\ Z_1(x_2,y_2) & Z_2(x_2,y_2) & & Z_N(x_2,y_2) \\ \vdots & & \ddots & \vdots \\ Z_1(x_K,y_K) & Z_N(x_K,y_K) & \cdots & Z_N(x_K,y_K) \end{bmatrix} \cdot \begin{bmatrix} a_1 \\ a_2 \\ \vdots \\ a_N \end{bmatrix} \tag{I-6}$$

to determine the coefficients a_n. However, the local wavefront values $\varphi(x_k,y_k)$ remain unknown in this problem, rendering a direct polynomials fit impossible. Instead the K focal shifts ($\delta u(x_k,y_k)$, $\delta v(x_k,y_k)$) have been determined, to which the partial derivatives of $\varphi(x,y)$ can be fit:

$$\begin{aligned} \frac{\partial \varphi(x,y)}{\partial x} &= \sum_{n=1}^{N} a_n \frac{\partial Z_n(x,y)}{\partial x} \\ \frac{\partial \varphi(x,y)}{\partial y} &= \sum_{n=1}^{N} a_n \frac{\partial Z_n(x,y)}{\partial y} \end{aligned} \tag{I-7}$$

Here the $n = 0$ term is disregarded since for each polynomial series this is a constant. The focal shift vector R can now be defined as:

$$R = \left[\delta u(x_1,y_1),\ldots,\delta u(x_K,y_K),\delta v(x_1,y_1),\ldots,\delta v(x_K,y_K)\right]^T \tag{I-8}$$

The most straightforward way to determine estimators $\hat{a}_n$ for coefficients a_n is by using a least-squares polynomial fit. The function to be minimized is then[29]:

$$\sum_{k=1}^{K}\left(\left(\delta u(x_k,y_k)-\sum_{n=1}^{N}\hat{a}_n\frac{\partial Z_n(x_k,y_k)}{\partial x}\right)^2+\left(\delta v(x_k,y_k)-\sum_{n=1}^{N}\hat{a}_n\frac{\partial Z_n(x_k,y_k)}{\partial y}\right)^2\right) \tag{I-9}$$

After minimization with respect to $\hat{a}_m$ ($m = 1,...,N$) and some simplification the following set of N equations is found:

$$\begin{aligned}&\sum_{k=1}^{K}\left(\delta u(x_k,y_k)\frac{\partial Z_m(x_k,y_k)}{\partial x}+\delta v(x_k,y_k)\frac{\partial Z_m(x_k,y_k)}{\partial y}\right)\\&=\sum_{n=1}^{N}\hat{a}_n\sum_{k=1}^{K}\left(\frac{\partial Z_m(x_k,y_k)}{\partial x}\frac{\partial Z_n(x_k,y_k)}{\partial x}+\frac{\partial Z_m(x_k,y_k)}{\partial y}\frac{\partial Z_n(x_k,y_k)}{\partial y}\right)\end{aligned} \tag{I-10}$$

or written in matrix form:

$$DR = DD^T\hat{A} \tag{I-11}$$

with $\hat{A} = [\hat{a}_1, ..., \hat{a}_N]$ and

$$D=\begin{bmatrix}\frac{\partial Z_1(x_1,y_1)}{\partial x} & \frac{\partial Z_1(x_2,y_2)}{\partial x} & \cdots & \frac{\partial Z_1(x_K,y_K)}{\partial x} & \frac{\partial Z_1(x_1,y_1)}{\partial y} & \frac{\partial Z_1(x_2,y_2)}{\partial y} & \cdots & \frac{\partial Z_1(x_K,y_K)}{\partial y}\\ \frac{\partial Z_2(x_1,y_1)}{\partial x} & \frac{\partial Z_2(x_2,y_2)}{\partial x} & \cdots & \frac{\partial Z_2(x_K,y_K)}{\partial x} & \frac{\partial Z_2(x_1,y_1)}{\partial y} & \frac{\partial Z_2(x_2,y_2)}{\partial y} & \cdots & \frac{\partial Z_2(x_K,y_K)}{\partial y}\\ \vdots & \vdots & \ddots & \vdots & \vdots & \vdots & \ddots & \vdots\\ \frac{\partial Z_N(x_1,y_1)}{\partial x} & \frac{\partial Z_N(x_2,y_2)}{\partial x} & \cdots & \frac{\partial Z_N(x_K,y_K)}{\partial x} & \frac{\partial Z_N(x_1,y_1)}{\partial y} & \frac{\partial Z_N(x_2,y_2)}{\partial y} & \cdots & \frac{\partial Z_N(x_K,y_K)}{\partial y}\end{bmatrix} \tag{I-12}$$

so finally the result is given by:

$$\hat{A} = (DD^T)^{-1}\,DR \tag{I-13}$$

which can be filled in in formula (I-5) to obtain the estimated wavefront.

b) Integration by direct integration

As before, this method starts from K experimental focus shifts in points (x_k, y_k) ($k = 1:K$), which form a rectangular grid in the pupil plane. It assumes that if the phase value in one central point (x_0,y_0) is known, the phase in the rest of the pupil area can be reconstructed. Choose e.g. $\varphi(x_0,y_0) = 0$, then the phase value in a nearby point $(x_0 + \delta x,y_0)$ is given by[40]:

$$\varphi(x_0+\delta x,y_0)=\varphi(x_0,y_0)+\delta u(x_0,x_0+\delta x)/f \tag{I-14}$$

with $\delta u(x_0,x_0+\delta x)$ the focal shift component in the u-direction. A similar formula can be used for points at a distance Δy in the y-direction, or general points. The problem with this method is that it is very sensitive to noise on the $(\delta u(x_k,y_k), \delta v(x_k,y_k))$ data. Also it is hard to make this procedure numerically stable.

Recently Hamam[41] described a variation of direct integration, which starts from the observation that the diameter s of the focal spot depends on the wavelength λ of the used light, the focal length f and the diameter D of the lens used:

$$s = \lambda f / D \tag{I-15}$$

and an approximation of the focal shift formula (I-4):

$$\begin{cases} \delta u(x,y) = (f/D)\delta W_x \\ \delta v(x,y) = (f/D)\delta W_y \end{cases} \tag{I-16}$$

with δW_x the maximum change in wavefront over the aperture of the lens in the x-direction (i.e. the component causing the largest focal shift), and δW_y the maximum change in the y-direction. When the focal shift is increased by one spot diameter s, this becomes:

$$\begin{cases} \delta u(x,y) + s = (f/D)\delta W_x + s = (f/D)(\delta W_x + \lambda) \\ \delta v(x,y) + s = (f/D)\delta W_y + s = (f/D)(\delta W_y + \lambda) \end{cases} \tag{I-17}$$

This provides a direct way to determine the change in wavefront: if the wavefront increases by one wavelength λ over the lens diameter, the focal shift increases by one spot size s relative to the unaberrated position. So simply measuring the focal shift in spot size units s provides ($\delta W_u(x,y)$, $\delta W_v(x,y)$). Using a direct integration algorithm as discussed above the wavefront can be reconstructed.
In the commercial COAS device (WaveFront Sciences) the direct integration technique is implemented in a stable way, however the exact algorithm has not been published to our knowledge.

I.4.3 **Reference axes**

When measuring wavefront aberrations is it important to know in which reference axis system these aberrations are defined. In optics usually the convention of the optical axis is used. However in case of the human eye no clear definition of the optical axis exists since the crystalline lens and the corneal apex are slightly tilted and decentered with respect to each other. In order to remedy this two different reference axes were defined for the measurement and calculation of ocular aberrations (definitions taken from [42]):

- *Visual axis* (Figure I-6a):
  The (broken) line connecting the fixation point to the eye's first nodal point on the one side and the second nodal point to the center of the fovea.
- *Line of Sight* (Figure I-6b):
  The (broken) line passing through the center of the eye's entrance and exit pupils connecting the fixation point to the fovea (or in other words: the path of the chief ray going from the fixation point to the retinal fovea).

As a convention ocular aberrations are measured with respect to the Line of Sight, and the pupil center is considered as the origin of a Cartesian reference frame.

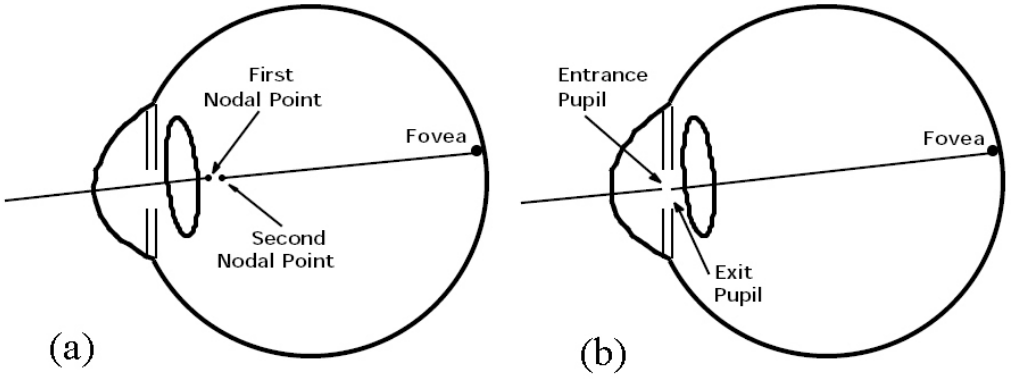

Figure I-6: definition of the visual axis (*a*) *and the line of light* (*b*) (*taken from* [42]).

I.4.4 **Polynomials used for wavefront reconstruction**

Since the pupil of a human eye is approximately circular, polynomials defined on the unit circle are needed for the polynomial wavefront reconstruction described in (I.4.2a). In the following a short list is given of the polynomials used for this application

a) Seidel primary aberrations

The Seidel aberrations are a number of non-orthogonal functions that naturally follow from the geometrical theory of aberrations in the paraxial approximation (i.e. near the optical axis of the system). Until Seidel's paper[11] the description of the reflection and refraction of a paraxial beam on a surface was limited to the first order terms of the necessary trigonometric functions. Seidel extended this to the third order and obtained five functions to describe the basic optical errors. These aberrations are given by (see also Figure I-7):

- *Spherical aberration*: $\frac{1}{4}\rho^4$; a difference in focal length depending on the radial distance ρ due to an incorrect change in the radius of curvature over the lens.
- *Coma*: $x_0\rho^3\cos\theta$; third order tilt, gives rise to a 'comet tail' distortion of the focal point.
- *Astigmatism*: $x_0^2\rho^2\cos^2\theta$; the radius of curvature changes in different angular directions θ, resulting in two line shaped focal points.
- *Field curvature*: $\frac{1}{2}x_0^2\rho^2$; describes a curvature of the focal plane (related to the astigmatism).
- *Distortion*: $x_0^3\rho\cos\theta$; a difference in magnification of the image depending on the object size, resulting in a distorted picture.

with (ρ,θ) polar coordinates in the pupil area and x_0 the object height. Besides these aberrations there were also the lower order aberrations:

- *Piston*: 1; constant term.

- *Tilt*: $\rho\cos\theta$; flat slope that displaces the image.
- *Focus shift*: ρ^2; a longitudinal misalignment of the optical system and the image screen.

Usually these polynomials are multiplied by a coefficient W_{ijk}, where the *ijk* indices indicate the powers of x_0, ρ and *cos* θ respectively. A wavefront description using Seidel aberrations is then given by:

$$\varphi(\rho,\theta,x_0) = W_{000} + W_{011}\rho\cos\theta + W_{020}\rho^2 + W_{040}\frac{1}{4}\rho^4 + W_{031}\rho^3\cos\theta + W_{222}x_0^2\rho^2\cos^2\theta + W_{220}x_0^2\rho^2 + W_{311}x_0^2\rho\cos\theta \quad \text{(I-18)}$$

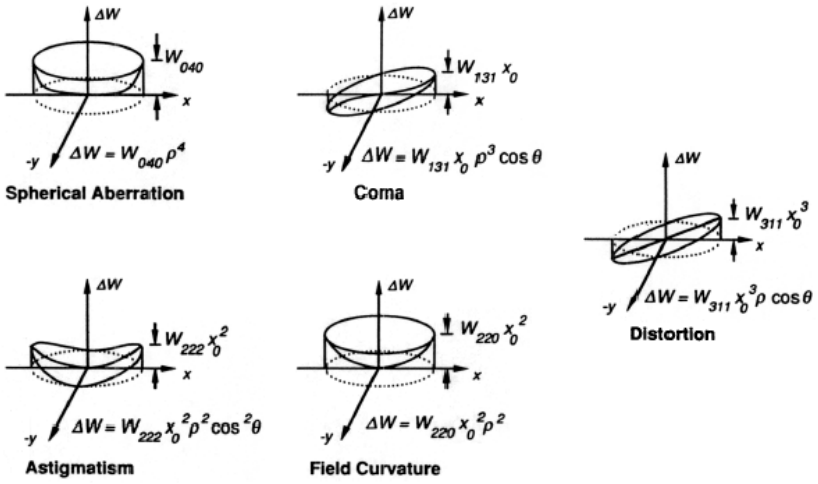

Figure I-7: Seidels' primary aberrations (taken from [43]*)*

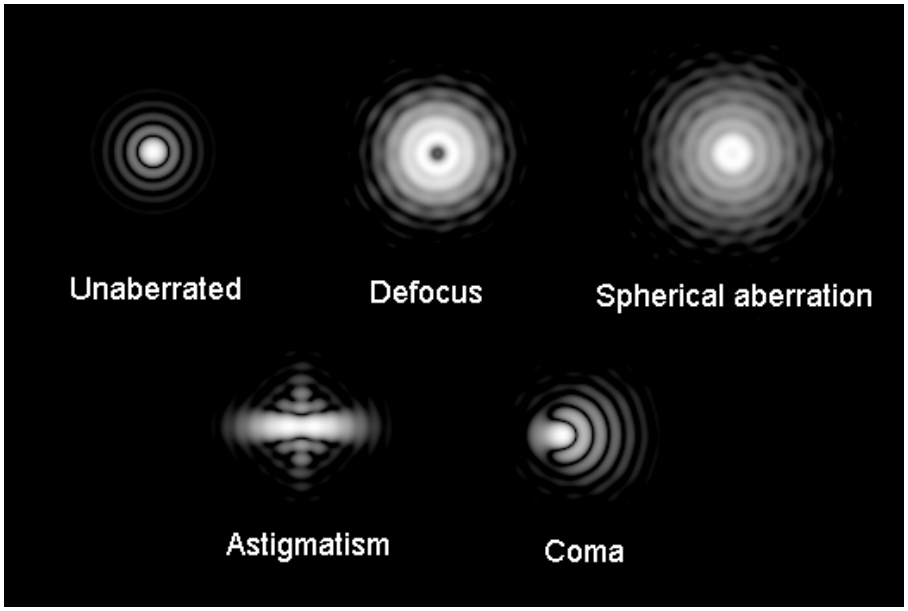

Figure I-8: the effect of primary aberrations on a Point Spread Function (taken from [43]*)*

Later Seidels' work was extended by other authors to include 5th and higher order aberrations. The profound effect individual aberrations can have on image formation is shown in Figure I-8. As these aberrations are not linearly independent, they are not so useful for wavefront reconstruction purposes.

b) Zernike series

In the 1930's Zernike was looking for an improved description of optical aberrations by means of polynomials, which he needed for the mathematical description of his 'phase contrast' technique[44, 45]. This technique allowed seeing a direct combination of the amplitude and phase of an image and meant a revolution in microscopy. For this innovation he was given the 1953 Nobel Prize in Physics.
For a mathematical description of phase contrast in a microscope, detailed knowledge of the PSF of both the microscope and the aberrations introduced by the sample is necessary. For this purpose he proposed his 'circle polynomials' that are composed of a radial part $R_n^m(\rho)$ and an angular part $\Theta_m(\theta)$ defined by:

$$Z_n^m(\rho,\theta) = R_n^m(\rho)\Theta_m(\theta) \tag{I-19}$$

with n and m integers, $n > |m|$ and n - m even, where index n is called the *order* of the polynomial, m the meridional frequency. In reference [35] it is derived that the radial part is given by:

$$R_n^{|m|}(\rho) = \sum_{s=0}^{(n-|m|)/2} (-1)^s \frac{(n-s)!}{s!\left(\frac{n+|m|}{s}-s\right)!\left(\frac{n-|m|}{s}-s\right)!}\rho^{n-2s} \tag{I-20}$$

and the angular part by:

$$\Theta_m(\theta) = \begin{cases} \sin(m\theta) & for\ \ m < 0 \\ \cos(m\theta) & for\ \ m \geq 0 \end{cases} \tag{I-21}$$

Usually a normalization factor N_n^m is multiplied with the polynomials. This Noll normalization has the value[46]:

$$N_n^m = \sqrt{\frac{2(n+1)}{1+\delta_{m0}}} \tag{I-22}$$

Here δ_{m0} is the Kronecker delta, with a value *1* if $m = 0$ and a value *0* otherwise.

The main advantages of Zernike polynomials are that they are closely related to the Seidel aberrations (see Table I-3) and that they are orthogonal over the unit circle, so that[47]:

$$\int_0^1 \int_0^{2\pi} Z_n^m(\rho,\theta) Z_{n'}^{m'}(\rho,\theta)\rho d\rho d\theta = \frac{\pi}{n+1}\delta_{nn'}\delta_{mm'} \tag{I-23}$$

Table I-3: oversight of the Zernike polynomials up till the 5th order according to the OSA standards

No.	n	l=n-2m	m	Norm	Polar coordinates	Carthesian coordiantes	Name
0	*0*	*0*	*0*	*1*	*1*	*1*	Piston
1	*1*	*-1*	*1*	*2*	$\rho sin(\theta)$	x	Tilt 0°
2	*1*	*+1*	*0*	*2*	$\rho cos(\theta)$	y	Tilt 90°
3	*2*	*-2*	*2*	$\sqrt{6}$	$\rho^2 sin(2\theta)$	$2xy$	Astigmatism 0°
4	*2*	*0*	*1*	$\sqrt{3}$	$2\rho^2-1$	$2x^2+2y^2+1$	Defocus
5	*2*	*+2*	*0*	$\sqrt{6}$	$\rho^2 cos(2\theta)$	y^2-x^2	Astigmatism 45°
6	*3*	*-3*	*3*	$\sqrt{8}$	$\rho^3 sin(3\theta)$	$3xy^2-x^3$	Trefoil 0°
7	*3*	*-1*	*2*	$\sqrt{8}$	$(3\rho^3-2\rho)sin(\theta)$	$3xy^{2+}3x^3-2x$	Coma 0°
8	*3*	*+1*	*1*	$\sqrt{8}$	$(3\rho^3-2\rho)cos(\theta)$	$3yx^{2+}3y^3-2y$	Coma 90°
9	*3*	*+3*	*0*	$\sqrt{8}$	$\rho^3 cos(3\theta)$	y^3-3x^2y	Trefoil 30°
10	*4*	*-4*	*4*	$\sqrt{10}$	$\rho^4 sin(4\theta)$	$4xy^3-4x^3y$	Tetrafoil (Quadrufoil) 0°
11	*4*	*-2*	*3*	$\sqrt{10}$	$(4\rho^4-3\rho^2)sin(2\theta)$	$8xy^3+8x^3y-6xy$	2nd order astigmatism 0°
12	*4*	*0*	*2*	$\sqrt{5}$	$6\rho^4-6\rho^2)+1$	$6x^4+12x^2y^2+6y^4-6x^2-6y^2+1$	Spherical aberration
13	*4*	*+2*	*1*	$\sqrt{10}$	$(4\rho^4-3\rho^2)cos(2\theta)$	$4y^4-4x^4-3y^2+3x^2$	2nd order astigmatism 45°
14	*4*	*+4*	*0*	$\sqrt{10}$	$\rho^4 cos(4\theta)$	$x^4-6x^2y^2+y^4$	Tetrafoil (Quadrufoil) 22.5°
15	*5*	*-5*	*5*	$\sqrt{12}$	$\rho^5 sin(5\theta)$	$5xy^4-10x^3y^2+x^5$	Pentafoil 0°
16	*5*	*-3*	*4*	$\sqrt{12}$	$(5\rho^5-4\rho^3)sin(3\theta)$	$15xy^4+10x^3y^2-5x^5-12xy^2+4x^3$	2nd order trefoil 0°
17	*5*	*-1*	*3*	$\sqrt{12}$	$(10\rho^5-12\rho^3+3\rho)sin(\theta)$	$10xy^4+20x^3y^2+10x^5-12xy^2-12x^3+3x$	2nd order coma 0°
18	*5*	*+1*	*2*	$\sqrt{12}$	$(10\rho^5-12\rho^3+3\rho)cos(\theta)$	$10yx^4+20y^3x^2+10x^5-12yx^2-12y^3+3y$	2nd order coma 90°
19	*5*	*+3*	*1*	$\sqrt{12}$	$(5\rho^5-4\rho^3)cos(3\theta)$	$5y^5-10x^2y^3-15x^4y-4y^3+12x^2y$	2nd order trefoil 30°
20	*5*	*+5*	*0*	$\sqrt{12}$	$\rho^5 cos(5\theta)$	$y^5-10x^2y^3+5x^4y$	Pentafoil 18°

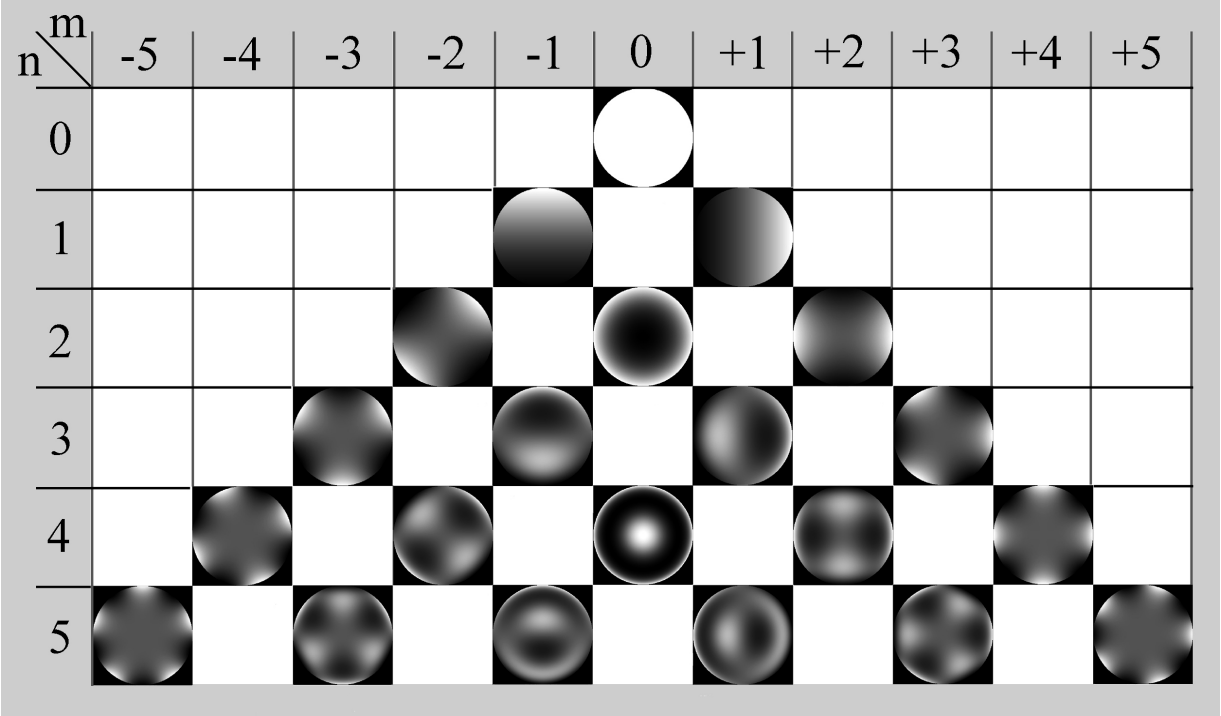

Figure I-9: The first five orders of Zernike polynomials.

and their mathematical form is preserved when a random rotation α is applied to the optical system.
In order to regulate the many different indexing schemes for Zernike polynomials used in the literature (such as the Born & Wolf notation[47], the Malacara notation[48] and several other ones) an OSA taskforce has set a number of standards[42]. Not only does it state the correct forms for the Zernike indexes and normalizations, it also sets the convention to measure aberrations along the Line of Sight. The Zernike polynomials according to these standards are shown in Figure I-9.

The Zernike theory for the calculation of point spread functions was later extended to obtain higher accuracies in the focal plane[49, 50] and the regions near the focal plane[51].

c) Taylor series

These polynomials are widely used for all kinds of applications. Their general form is:

$$\begin{aligned}\varphi(x,y) &= \sum_{k=0}^{N}\sum_{l=0}^{k} a_{kl}x^{l}y^{k-l} \\ &= a_{00} + a_{10}x + a_{01}y + a_{20}x^{2} + a_{02}y^{2} + a_{21}xy + \cdots\end{aligned} \tag{I-24}$$

In order to use these polynomials on a sampling grid within a circular pupil a Gramm-Schmidt orthogonalization is needed. The resulting polynomials are reported in [15] and [52] and will not be discussed further here.

d) Legendre series

Products of Legendre polynomials $P_l(x)$ can also be used. These are given by:

$$\begin{aligned} P_{kl}(x,y) &= P_k(x)\cdot P_l(y) \\ &= \left(\sum_{m=0}^{\lfloor k/2\rfloor}(-1)^k\binom{m}{k}\binom{2m-2k}{m}x^{m-2k}\right)\cdot\left(\sum_{n=0}^{\lfloor l/2\rfloor}(-1)^l\binom{n}{l}\binom{2n-2l}{n}x^{n-2l}\right) \end{aligned} \qquad \text{(I-25)}$$

with $\lfloor r \rfloor$ the floor function (rounds off the numerical argument downwards). Again these functions need to be orthogonalized by means of a Gramm-Schmidt procedure. A description of the use of these polynomials for wavefront sensing is given in [53].

I.4.5 **Wavefront characterization parameters**

Besides the polynomial coefficients described above there are a number of other parameters that can be used for wavefront characterization. Here the most commonly used data representations are given, however currently a number of researchers are looking for other methods of data representation[54, 55] which are not included.

a) Root-Mean-Square (RMS)

This is the square root of the averaged squared distance between the points on the aberrations surface and the average value of the aberration, or mathematically:

$$RMS = \sqrt{\frac{\sum_{x,y}(\varphi(x,y)-\overline{\varphi})^2}{N}} \qquad \text{(I-26)}$$

with $\overline{\varphi}$ the average wavefront error and N the number of points (x,y) used in the calculation. In case an orthonormal polynomial series (e.g. Zernike) is used for the wavefront representation, formula (I-26) can be simplified to:

$$RMS = \sqrt{\sum_k a_a^2} \qquad \text{(I-27)}$$

where a_k are the polynomial coefficients. This opens the possibility to calculate the RMS associated with specific types of aberrations. For Zernike polynomials with the single indexing scheme one can e.g. distinguish:

$$\begin{aligned} RMS_{total} &= \sqrt{\sum_{k=0}^{N} a_k^2} \\ RMS_{higher\ order} &= \sqrt{\sum_{k=6}^{N} a_k^2} \\ RMS_{2nd\ order} &= \sqrt{\sum_{k=3}^{5} a_k^2} \\ RMS_{3rd\ order} &= \sqrt{\sum_{k=6}^{9} a_k^2} \\ &\vdots \end{aligned}$$

The advantage of using the RMS is that the flatness of a whole surface is characterized by one single number. A flat wavefront has an *RMS = 0*, an aberrated wavefront has an *RMS > 0*. However convenient, one must be careful using this parameter since it can be treacherous for specific types and combinations of aberrations[56].
One way to make the RMS slightly more sensitive to local aberrations is calculating it in specific zones, as is described further in this thesis (see III.3.4).

b) Point Spread Function (PSF)

The PSF can be considered as the image of a distant point source as seen through the system's aberrated optics, which can be calculated using a Fourier transform:

$$PSF(x', y') = \left| \Im\left\{ A(x, y) e^{2\pi i \varphi(x,y)} \right\} \right|^2 \tag{I-28}$$

with $A(x,y)$ and $\varphi(x,y)$ the amplitude and the phase in the pupil plane and $PSF(u,v)$ defined in the focal plane. Ideally the PSF is a single point, but usually it is smeared out according to the aberrations present. Convolving the image of an object with the PSF gives the aberrated image (see Figure I-10).02.

c) Strehl ratio

This is the normalized intensity of an aberrated PSF calculated by dividing the on-axis intensity of the PSF of the aberrated optical system by that of the same optical system without aberrations:

$$Strehl = \frac{PSF_{aberrated}(x', y')}{PSF_{ideql}(x', y')} = \frac{\left| \Im\left\{ A(x, y) e^{2\pi i \varphi(x,y)} \right\} \right|^2 (0,0)}{\left| \Im\{ A(x, y) \} \right|^2 (0,0)} \tag{I-30}$$

This concept, introduced by Strehl[57], again characterizes the optical quality into one single number smaller than or equal to one.

d) Optical Transfer Function (OTF) (see Figure I-10)

This complex function, which describes the change in image contrast due to aberrations, is calculated by:

$$OTF(u, v) = \Im\{ PSF(x', y') \} = A(x, y) e^{2\pi i \varphi(x,y)} \star A(x, y) e^{2\pi i \varphi(x,y)} \tag{I-29}$$

with $\star$ denoting the cross-correlation. Since formula (I-29) is complex two other quantities Modulation Transfer Function (MTF) and Phase Transfer Function (PTF) are defined:

$$\begin{cases} MTF(u, v) = |OTF(u, v)| \\ PTF(u, v) = ArcTan\left(\dfrac{imag(OTF(u, v))}{real(OTF(u, v))} \right) \end{cases} \tag{I-30}$$

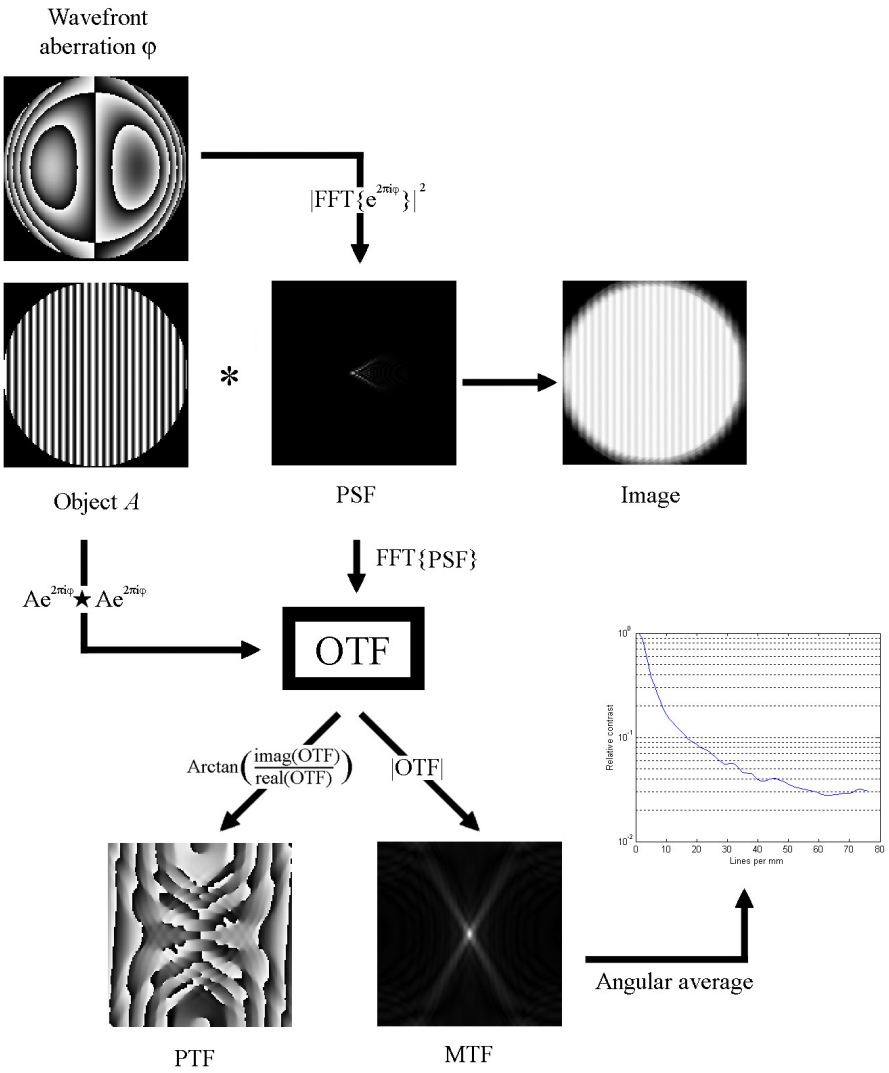

Figure I-10: oversight of Fourier optics modalities used for wavefront characterization.

The MTF describes the contrast with which a series of lines with sinusoidal intensity variation can be seen through the aberrated optics at various spatial frequencies. Usually it is represented as a logarithmic plot in function of the spatial frequency of a grid. The plotline is then the angular average.
The PTF on the other hand is related to shifts and contrast reversals in the image.

I.5 *Aberrometer techniques*

This section is dedicated to giving an oversight of the large variety of aberrometers reported in the literature. Please note that in the following the laser light used has been rendered incoherent by optical means (neutral density filter, retinal reflection (see I.2.1),…) in order to avoid any influence by laser speckle. The beam splitters mentioned are highly transmissive in order not to loose too much of the faint light coming back from the eye.
For other technical details on aberrometers we refer to Chapter II.

I.5.1 **Subjective serial techniques**

This group contains the methods that measure each coordinate one by one and require that the subject gives active feedback in some way. These are also called 'psychophysical methods'.

a) Scheiner disc

This was the first aberroscope known in literature, described in Scheiner's book[58] as follows:

> *"Make a number of perforations with a small needle in a piece of pasteboard, not more distant from one another than the diameter of the pupil of the eye... if it is held close to one eye, while the other is shut, as many images of a distant object will be seen as there are holes in the pasteboard... at a certain distance, objects do not appear multiplied when they are viewed in this manner."*[*]

This method, known as the Scheiner disc, is a very simple way to determine whether the eye is ametropic or not. Suppose a disc with two holes and a point source located at infinity on the optical axis of the eye (as shown in Figure I-11), then the incident light on the disc will be divided into two separate beams parallel to the optical axis. When these two beams enter the eye they will be individually refracted, resulting in two separate images on the retina. Only when the eye has no ametropia both beams will coincide to form one single image.
In his famous paper[8] Young used this method to measure the aberrations over various regions of the eye. But instead of holes he used slits in a dark plate and behind which he placed trial lenses to compensate for ocular ametropia until only one slit was seen by the subject. He did this for various separation distances between the slits.
The Scheiner method is still used by amateur astronomers to estimate the optical quality of their telescope.

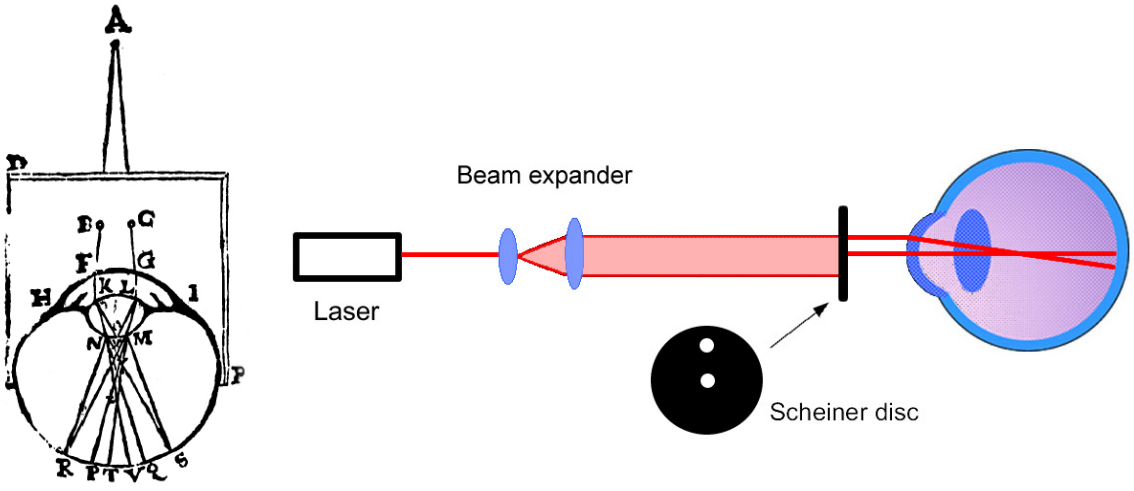

Figure I-11: Scheiner disc, original design[58] (1619) on the left and modern version on the right.

[*] Translation courtesy of David Williams ('History of Ophthalmic Wavefront Sensing', lecture at 4th Int. Congress on Wavefront Sensing and Aberration Free Refractive Correction, San Francisco, Feb 14-16, 2003)

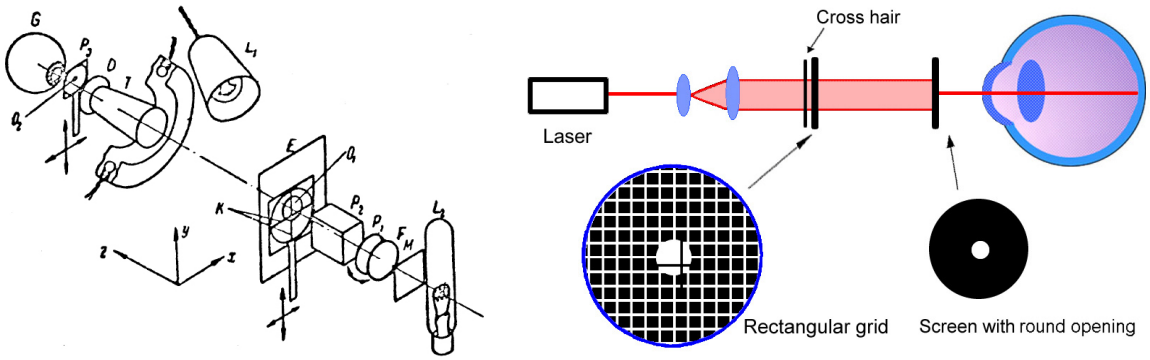

Figure I-12: Smirnov aberrometer: original version[14] (1961) on the left and modern version on the right.

b) Smirnov aberrometer

This idea was proposed by Ivanoff[13] and later by Smirnov[14]. A subject is asked to look through a small hole towards a reference screen with a rectangular grid. This screen has a central hole with a movable crosshair that is put in alignment with the grid. Due to local aberrations in his eye the subject will see a misalignment between the crosshair and the reference grid. The measurement consists of moving the crosshair until the subject perceives it to be aligned again with the pattern on the screen. Next the entire device is moved to a new pupil position and the whole procedure was repeated.
At the time the measurement took about 1-2 hours and the data processing could last up till 20 hours. This caused Smirnov to remark that "the practicing ophthalmologist will find little use for such detailed measurement", even though his device gave him valuable insights into the nature of optical aberrations. He was also the first to suggest that it should be possible to make customized contact lenses to compensate for the individual aberrations of the eye.

c) Spatially resolved refractometer

This aberrometer, developed by Webb and Penney[59], resembles that of the ray tracing method.

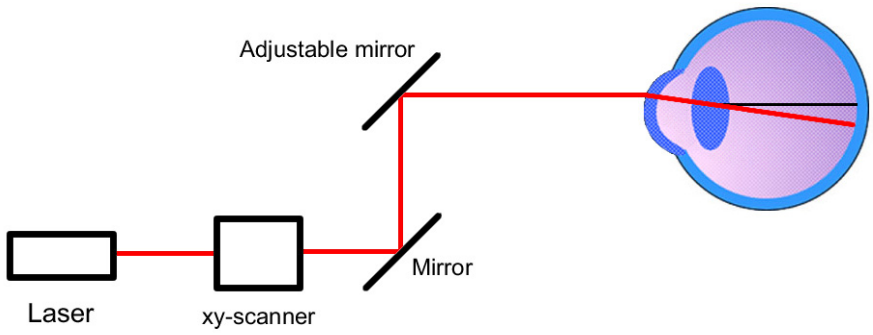

Figure I-13: Spatially resolved refractometer

During the measurement the subject is asked to look at a target image, while a light beam is projected into the eye at a specific sample position. Due to local aberrations the beam is deflected away from the focal point. By means of a joystick linked to an adjustable mirror the subject now has to realign the incident beam with the target image and from this correction the local wavefront tilt can be derived. The measurement takes a couple of minutes due to its serial and psychophysical character.

I.5.2 **Objective serial techniques**

This is the group of methods in which the aberrations in each pupil coordinate are measured one by one in an objective way. Only the Laser Ray Tracing technique can be classified in this group.

Ray tracing is the closest to the basic Scheiner principle as it sends individual beams to various locations of the eye. This method, simultaneously developed by both the groups of Molebny[60] and Navarro[61], only requires a scanning system capable of delivering a narrow laser beam to specific pupil plane coordinates (Figure I-14). The retinal image of each incident beam is then determined by taking a picture using a linear array of photodetectors that are optically conjugated with the retina. Comparing the center of mass of the retinal spot with a predetermined reference position the focal shift can easily be determined.
As the scanning system can be reprogrammed to scan the laser beam in different sampling patterns this method is very flexible[62]. In a recent study it was found that changing the sampling geometry can cause systematic errors in identifying specific combinations of Zernike modes[63]. Another advantage is that spot cross-over (which will be explained later) cannot occur. However, as this is a serial method, its measurement speed greatly depends on the speed of the scanner and the camera.
Ray tracing has recently been incorporated into the Tracey Visual Function Analyzer, an aberrometer commercialized by Tracey technologies[64].

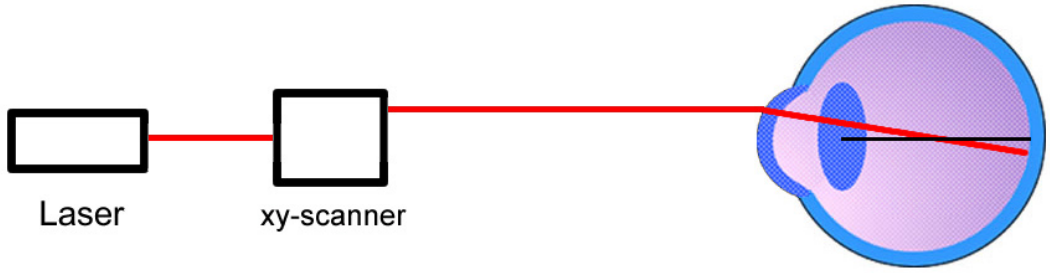

Figure I-14: scheme of the ray tracing method.

I.5.3 **Subjective parallel techniques**

This is the group of aberrometers that perform one parallel measurement over the entire pupil area at once, but that require active feedback from the patient.

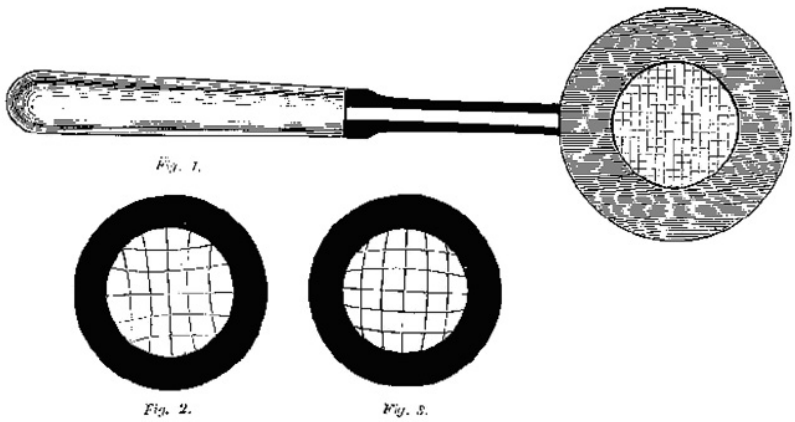

Figure I-15: Tscherning original method (1894) using engraved lines on a magnifying glass.

a) Subjective Tscherning method

This method was proposed by Marius Tscherning at the end of the 19th century, he tried to map the aberrations other than defocus, cylinder and spherical aberration using a device he called 'aberroskop' (see Figure I-15). He described it as follows:

> "*This* [*device*] *consists of a planoconvex lens of 4 Diopter, with a square micrometer grid engraved on the plane side. If an emmetropic eye, or an eye made emmetropic by means of trial lenses, looks trough this lens towards a distant light source it will see the shadow of the micrometer grid in the scattered light. But only eyes whose refraction is even throughout the whole pupil surface will perceive the grid as untwisted. To all eyes that do no answer this requirement the lines will appear bent,…*"[65]

The idea behind this aberroscope is that the planoconvex lens projects an image of the grid onto the retina, which while passing through the eye optics is twisted by the ocular aberrations (see Figure I-15, bottom). By studying these distortions it is possible to get a rough idea of the shape of the aberrations, mainly of the three 'regular' aberration patterns (defocus, astigmatism and spherical aberration).
One practical problem of this method is that the grid image on the retina is very blurred, making it hard to estimate its shape. It is also a subjective method, since it requires the subject to observe the grid pattern himself and draw it afterwards on a paper.

The first objection was remedied in 1977 by Howard and Bradford Howland[15], who proposed to replace the planoconvex lens in Tscherning's device by a cylindrical lens. This had the advantage that the grid lines were better focused on the retina, resulting sharper image patterns.

I.5.4 **Objective parallel techniques**

These aberrometers perform a large number of measurements over the whole pupil area at once by parallel sampling, without any feedback from the patient.

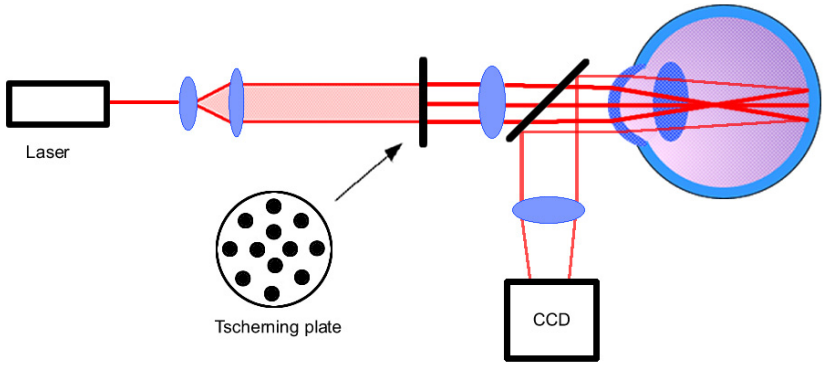

Figure I-16: modern objective Tscherning device using a plate with a number of apertures.

a) Objective Tscherning method

The problems resulting from the subjective nature of the original Tscherning method were also solved by Howland[66], who introduced a fundus camera in his setup which could directly photograph the distorted grid pattern found on the retina.
Recently another version of the technique has been proposed by Mierdel et al.[67, 68], where the Tscherning grid was replaced by a plate with multiple perforations (see Figure I-16). The apertures in this screen serve to split the incoming collimated beam into a number of narrow beams. A spherical defocus lens placed right behind the screen projects the image of the screen onto the retina, which is recorded by a fundus camera. The distorted image can then be analyzed automatically to extract the focal shifts. This version of the objective Tscherning aberrometer is commercialized by WaveLight.

b) Hartmann-Shack aberrometer*

In the beginning of the 20th century Joseph Hartmann used Young's version of the Scheiner disc for the quality testing of the optics in a spectrometer[69]. As his interests shifted towards the testing of telescope objectives, he proposed an improved version of this method, which consisted of a screen with a large number of openings[70]. He explained the method as follows:

> *"In short the purpose of objective testing is to fully determine the dependency of the optical path on three parameters r, φ and λ. For this purpose a single beam (r,φ,λ) incident on the objective must be isolated and fixated in image space. The isolation of*

* Ever since the principle of lenticular Hartmann screens was introduced for the measurement of ocular aberrations there has been a controversy about the politically correct name of this method. Short after its invention in 1971 by Shack and Platt for military and astronomical purposes it was dubbed 'Shack's modified Hartmann screen', or 'Shack - Hartmann' for short (J. Ref Surg. **17**, Sept/ Oct 2001, pp. S573-577). Later, in 1994, when this technique was first used for the measurement of ocular aberrations by Liang and Bille, it was named 'the Hartmann-Shack method'. This has given rise to lengthy discussions on this subject, but, as observed by Thibos ('Principles of Hartmann-Shack aberrometry', lecture at Wavefront Sensing Congress, Santa Fe, 2000), this argument is rather futile since the basic idea was already long before introduced by Scheiner.

the beam is done by placing a screen with a small opening in location (r,φ) *in front of the objective and sending monochromatic light with wavelength* λ *parallel to the optical axis through this opening. In order to locate the refracted beam in image space, one needs to determine its cross-section with two randomly chosen planes perpendicular to the optical axis;…*"[70]

Basically this means that a collimated beam coming from the objective under study is divided in a large number of beams by means of the apertures in the Hartmann screen (see Figure I-17, left). The beams passing through the holes will again have a certain tilt, which on a distant image screen is translated into a displacement of the image spots relative to the spots of a non aberrated wavefront. By correlating the displacement of each spot with its associated aperture in the Hartmann screen, one can estimate the gradient of the wavefront as explained before in I.4.2a).
This modification of Scheiner's method had the advantage that all measurements could be done at once for the whole entry pupil of the optical setup. But its main disadvantage is that the sizes of the individual Hartmann spots are quite large, making it difficult to accurately locate the spot centers.

Roughly 70 years later Roland Shack and Ben Platt proposed to replace the Hartmann screen with an array of lenses[71]. In this setup each lens serves the same purpose as the individual holes from the Hartmann screen, but with the distinct advantage that the light passing through each subaperture is focused on the image screen. This results in much smaller spots compared to the original Hartmann screens, which benefits the resolution of the $(\delta u(x,y), \delta v(x,y))$ measurements. Another advantage is that the entire pupil area can be used for measurement, there where the apertures in the original Hartmann screens had to have certain spacing between them for proper working.
The Hartmann-Shack technique also has a limitation in the form of the 'cross-over' effect, which occurs in regions with steep wavefronts. If a local wavefront slope is steeper than a certain threshold value, its associated spot in the lenslet focal plane will be displaced into an area associated with the spot of a neighboring lenslet. This makes it impossible to correlate the spot with the aperture projecting it, rendering the measurement useless for automatic processing.

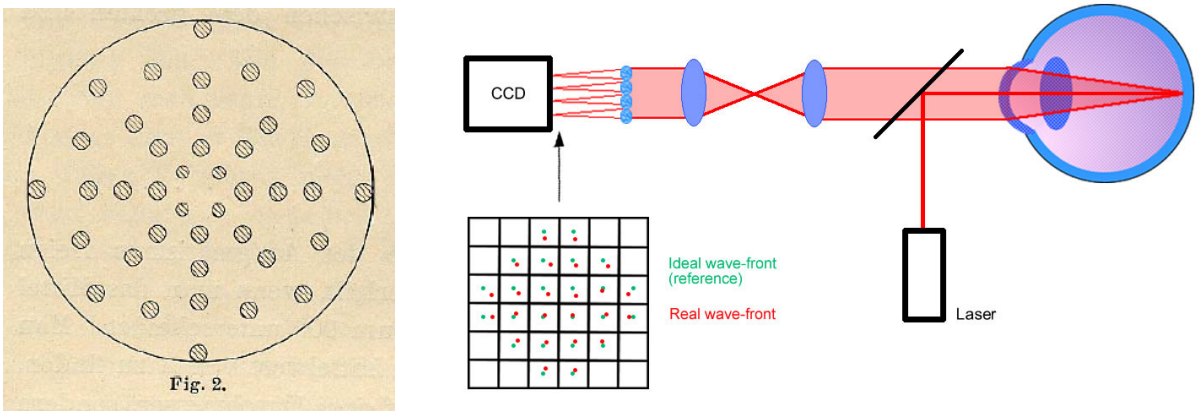

Figure I-17: the Hartmann-Shack method: original version[70] *(1904) of the Hartmann screen on the left and modern lenticular version as proposed by Liang et al. on the right.*

The cross-over effect depends both on the size of the individual lenslets and the amplitude of the wavefront being measured, both of which can be optimized. For the lenslet size an equilibrium must be found between a large aperture size on the one hand (desirable since it receives more light and gives smaller focal spots) and a smaller aperture on the other hand (provides higher sampling resolutions). The wavefront amplitude is optimized by partial compensation using trial lenses or spatial light modulators[72, 73, 74]. Usually the remainder of the aberrations is well within the active range of the Hartmann-Shack sensor.

The first application of this technique on human eyes was in 1992 by Liang and Bille[75]. Since then it has become the most popular wavefront sensing technique to date, used in over 15 different commercial sensors (for an incomplete oversight see Table I-4). The classic Hartmann screens are still in use today, mainly for the testing of telescope mirrors.

Table I-4: (incomplete) list of commercially available Hartmann-Shack aberrometers

Company	Commercial name aberrometer
Alcon (Summit/ Autonomous)	LadarVision
Bausch & Lomb	Zywave
Brookfield Optical Systems	ABRA 2010
Schwind*	ORK
Topcon	KR 9000 PW
VISX / 20/10 Perfect Vision	WaveScan
WaveFront Sciences	COAS
Zeiss/ Meditec*	WASCA

I.5.5 **Other techniques**

Several other methods have been reported whose principles do not fit the above categories. These will be listed here.

a) Direct calculation using PSF

This method calculates the wavefront aberrations from the PSF taken over the entire pupil area. However, as said before in I.4.1, this is hard to measure directly since any external image taken from the PSF passes through the aberrated optics again and results in the autocorrelation of the PSF.
The technique was first proposed for the use in eyes by Artal *et al.*[76,77], who at first assumed that the retinal image was the autoconvolution of the PSF. Using a Gerchberg-Saxton (GS) algorithm[78] he derived the wavefront aberrations with knowledge of the ocular PSF and the pupil (see Figure I-18). In order to make sure that the iterative process in the GS-algorithm would converge he had to make an initial estimation of the wavefront first.
When Artal later reported[27] that his assumption about the retinal PSF was incorrect (the image on the camera was the autocorrelation of the PSF instead of autoconvolution), the technique was modified[79, 80]. In the new version the PSF was calculated from two retinal images, each recorded at a different pupil size. Once a reliable estimate for the PSF was available, it could be used for the calculation of the wavefront aberrations.
The biggest disadvantage of this method is the large calculation times required.

* Licensed by WaveFront Sciences

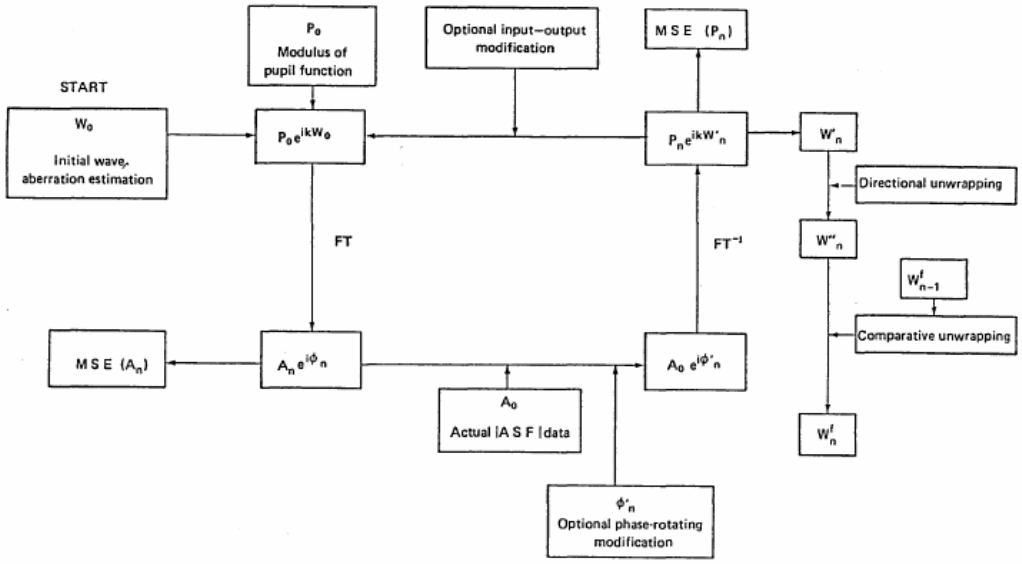

Figure I-18: the Gerchberg-Saxton algorithm used by Artal (figure taken from [77]*).*

b) Foucault knife-edge aberrometer

The knife-edge principle was presented by Leon Foucault[81, 82] in 1857 and was first used in an aberrometer in 1969 by Berny and Slansky[83]. In this aberrometer monochromatic light is sent through a slit shaped opening, which is projected on the retina as a secondary source (Figure I-19). The analysis of the outgoing wavefront is done by means of a lens and a flat metal plate ('knife-edge') that blocks part of the light near the lens' focal plane. Next a second lens projects the resulting image of the pupil plane on the CCD camera. Due to the knife-edge a number of shadows appear that can be directly attributed to ocular wavefronts aberrations.
In the knife-edge plane the image of the retinal source is distorted by focal shifts (u, v) of individual rays passing through pupil plane points (x,y). The size of these shifts can be determined by dividing the image I containing the Foucault shadows by an image I_0 recorded without the knife-edge. This way the u-component, perpendicular to the knife-edge, can be estimated by:

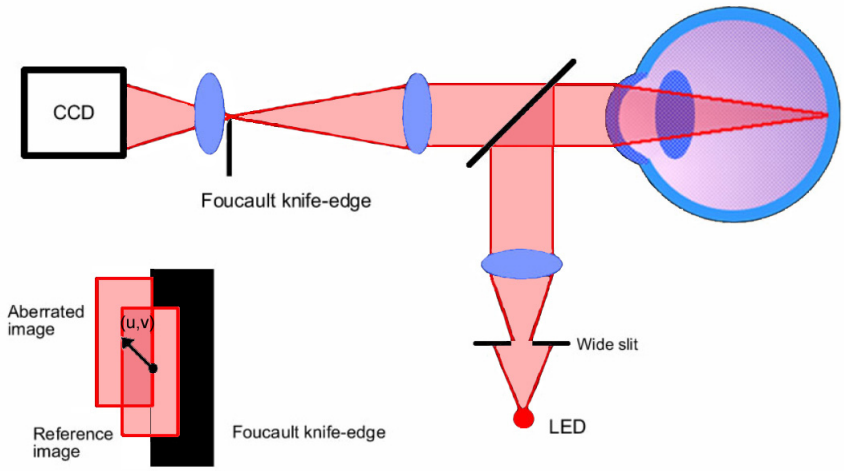

Figure I-19: Foucault knife-edge test, applied to the human eye (1969).

$$\frac{I}{I_0} = \frac{a \pm (u - u_0)}{2a} \qquad \text{(I-31)}$$

with u_0 an off-set value for the normalization of the non-aberrated case and $2a$ the geometrical width of the slit behind the source. The v-component is obtained by rotating the knife-edge over 90º and repeating the measurement. This gives us a pupil image and wavefront gradient values in both the u- and the v-direction for each pixel of the image, which can be integrated by a method described in I.4.2.
Formula (I-31) is an approximation that is only valid if the slit image is not completely covered or uncovered by the edge. Although this is clearly a double-pass method, one may assume that only about 2% of the variance in the final wavefront calculation can be attributed to the first pass[84].
To our knowledge this method has not been developed any further for wavefront sensing.

c) Automatic retinoscope

The automatic retinoscope is an automated version of the hand-held retinoscope that ophthalmologists use in everyday clinical practice.

The hand-held device uses a slit of white light that is scanned over the pupil area, part of which goes through the pupil opening and reflects on the retina. This reflection can behave in three ways:

- The reflection is shaped like a slit and moves in the *same direction* as the incident scanning slit of light, indicating an ocular ametropia higher then -1.5D along the scanned line (i.e. low myopic or hyperopic).
- The reflection is shaped like a slit and moves in the *opposite direction* of the incident light, indicating an ametropia of lower then -1.5D along the scanned line (i.e. myopic).
- The reflection fills the entire pupil opening, a situation called the *neutral point*.

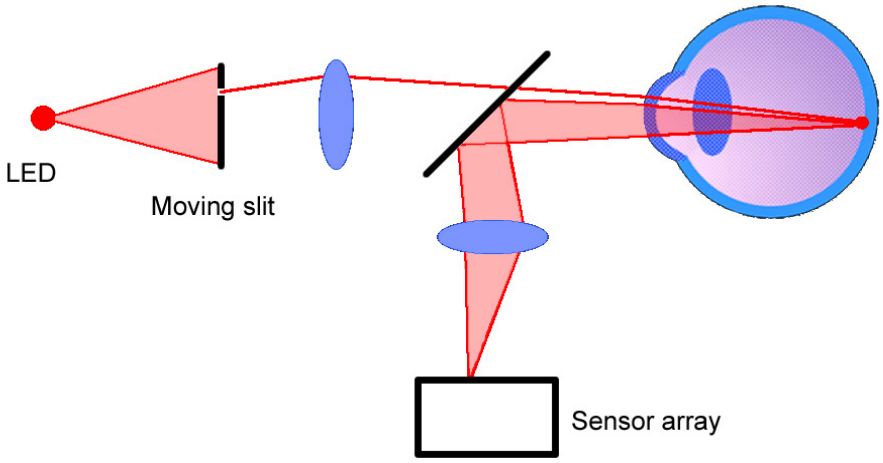

Figure I-20: Automatic retinoscope

The difference in relative scanning speed between the incident and the reflected light is directly proportional to the difference between the refraction along the scanned meridian and -1.5D. In a clinical examination a number of meridians in the pupil area are tested this way, where for each meridian trial lenses are placed in front of the eye until the neutral point is found. By mapping the refraction along a number of these meridians it is possible to get a general idea of the ocular refraction.

In the automated retinoscope[85,86] (see Figure I-20) a slit of monochromatic light is scanned along a large number of meridians. The direction and speed of the reflected light are measured by a sensor array. Using these parameters a refractive map of the entire eye can be calculated[*], which can be translated to a wavefront map and Zernike polynomials coefficients.

d) Confocal method

The confocal Scanning Laser Ophthalmoscope (SLO) can also be used to get an idea of the local refractive zones of an eye using a principle similar to Laser Ray Tracing (see I.5.2).
This device is originally intended to produce live video images from the posterior segment of the eye. For this purpose it uses a scanning system to sweep a laser beam over the retina (Figure I-21). After reflection on the retina the light goes back through the scanning unit to compensate for the sweeping movement, after which a lens focuses this light through a pinhole diaphragm on an avalanche photo diode (APD). Only when the retinal reflection is within the virtual image of the pinhole, the reflected light can reach the APD and contribute to the imaging process. If this is not the case a dark 'shadow' emerges on that location. A more detailed description of the working principles of the SLO can be found in [87].

Comparing the basic setup of the SLO in Figure I-21 and the LRT in Figure I-14, two big differences can be found:

- *Location and function of the scanning unit*:
  In the LRT this is usually an opto-acoustic device or a mirror system used to move the laser beam parallel to the optical axis and send the laser beam through a well-known location of the eye optics. The scanning unit inside the SLO on the other hand contains a polygon and a galvanometer mirror to sweep the laser beam over the retina and obtain a live retinal video sequence (Figure I-21). To compensate for the continuous sweeping movement of the reflection it needs to be descanned before it can be sent to the pinhole.
- *Presence of the confocal pinhole in the SLO, optically conjugated to the retina*: This reduces the depth of focus and specular reflections from the eye optics, which consequently increases the contrast of the images. In addition it is useful for estimating height differences within the retinal image. For the LRT the use of a confocal pinhole would only limit the maximum size of focal shifts that can be registered.

Usually very clear retinal images can be obtained using the SLO. However in some patients with irregular local wavefront aberrations these overlaying shadowlike patterns are found, roughly located in the areas with the strongest aberrations. This is due to focal shift on the

[*] In order to work properly the sensor array not only measures along the meridians, but also in several points above and below the meridian. Otherwise only radially and point symmetric aberrations (with respect to the pupil center) can be determined with this method. Further information can be found in reference [85].

retina, where the laser spot leaves the virtual image of the confocal pinhole. Since only light that reflects within this virtual image can be detected by the APD the local intensity in the retinal image is reduced. This intensity reduction, called vignetting, is usually a nuisance that frustrates the realization of clear retinal images.

In recent technical reports[88, 89] it was stated that, even though their full nature has not yet been determined, SLO vignetting patterns could be used as an indication of the local wave-front aberrations of heavily aberrated eyes. It was also noted that shadow patterns were dependent on the amount of prefocus introduced by the SLO, confirming the refractive origin of these shadows.
In practice a good overview of the shadow patterns in the pupil area can be obtained by placing the focal point of the SLO just in front of the corneal apex. This situation is called the 'Maxwellian view'[90], in which for non-aberrated eyes the scanning beams inside the eye remain parallel to the optical axis. Hence the magnifications of the retina image and the observed shadow patterns are the same, so the relative size of the vignetting shadows can easily be estimated.

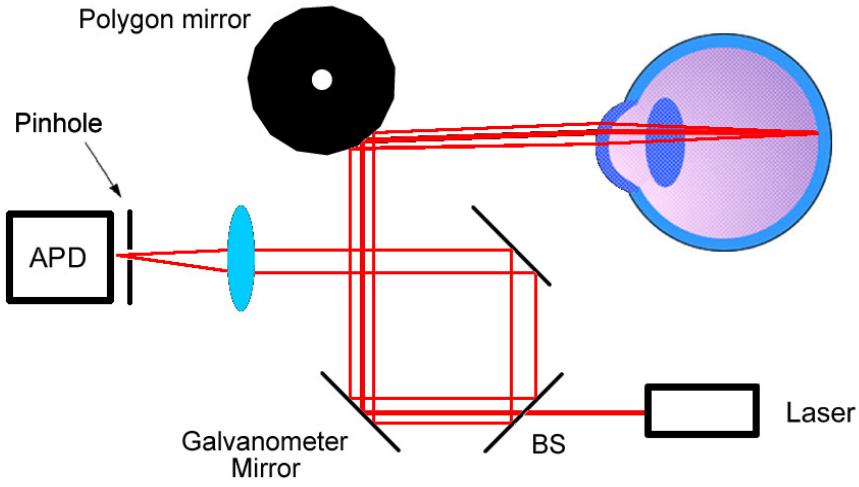

Figure I-21: scanning laser ophthalmoscope

PART I

Clinical comparison of 6 aberrometers

Recent years have seen a boom in the number of commercial wavefront sensing devices on the market. Each of these aberrometers is based on a different technique with different methods for analyzing the raw data and with different ways of interpreting the results. One can ask whether all these embodiments will provide the same results when tested on a fixed group of test eyes… The first part of this thesis tries to answer this important question.

Chapter II Clinical comparison of 6 aberrometers: technical specifications

Jos J. Rozema, MSc[*,**], Dirk E. M. Van Dyck, PhD[*], Marie-José Tassignon, MD PhD[**]

* Vision Lab, University of Antwerp, Antwerp, Belgium
** Department of Ophthalmology, University of Antwerp, Belgium

None of the authors have any financial interests in the products mentioned in this article.

This research is sponsored by an ESCRS grant (2002) and a 2002 grant of the Belgian Fund for Research in Ophthalmology (2002)

Reprint request to: J. Rozema, University Hospital Antwerp, Wilrijkstraat 10, 2650 Edegem, Belgium

II.1 *Abstract*

Purpose: To provide a detailed assessment of the techniques, technical features and practical use of 6 aberrometers made available to our institution in the period of September 2002 to January 2004.

Setting: Department of Ophthalmology, University Hospital Antwerp, Antwerp, Belgium

Materials: A number of technical and practical parameters will be listed for the Visual Function Analyzer (Tracey), the OPD-scan (ARK 10000), the Zywave, the WASCA, the MultiSpot Hartmann-Shack device and the Allegretto Wave Analyzer. These parameters include details on the working principles, the data acquisition, the aberrometer alignment, the wavefront calculation and the data analysis. Also operator and patient comfort as well as practical advantages and disadvantages are discussed.

Conclusion: Because measuring aberrations in clinical practice is relatively new, most devices are still in progress and will implement new applications and improvements according to the clinicians' needs. However, all devices meet at least half of the following parameters: alignment, correction for source wavelength, data averaging, measurement quality check and inhibition of accommodation.

II.2 Introduction

Since aberrometry presents larger applications than enhancing the quality of the ablation zone in an excimer laser treatment, the choice of the most appropriate machine will mainly depend on the ophthalmologists' practice style. Making a practical comparison between the different devices available on the market is not an easy task because of the variety in principles used, e.g. ray tracing[60,61], Hartmann-Shack[75,91], Tscherning[68] and automatic retinoscopy[85,86].
To our knowledge only two publications attempted to make a comparative list[92,93] of characteristics, but both of them relied on unedited information directly provided by the manufacturers and the tables presented were far from complete. Additionally each of the manufacturers used his own terminology which might be confusing to non-specialists.
The purpose of this paper is to provide a number of technical and practical parameters that can be useful in choosing an aberrometer for daily clinical practice. The main focus will be on

the wavefront measurements themselves, rather than on their possible application in refractive surgery.
The aberrometers under study are:

- *Visual Function Analyzer* (*VFA; Tracey*): based on ray tracing; can be combined with EyeSys Vista corneal topographer.
- *OPD-scan* (*ARK 10000; Nidek*): based on automatic retinoscopy. Provides integrated corneal topography and wavefront measurement in one device.
- *Zywave* (*Baush & Lomb*): a Hartmann-Shack system that can be combined with the Orbscan corneal topography system.
- *WASCA* (*Zeiss/ Meditec*): a high resolution Hartmann-Shack system.
- *MultiSpot 250-AD Hartmann-Shack sensor*[94]: a custom made Hartmann-Shack system, engineered by the Laboratory of Adaptive Optics at the Moscow State University, that includes an adaptive mirror to compensate for accommodation.
- *Allegretto Wave Analyzer* (*WaveLight*): an objective Tscherning device.

This study was conducted in the period between October 2002 and January 2004. Within this period the companies of the above aberrometers were kind enough to make their devices available to our institution.
We would like to highlight that the following results represent only the devices as they were made available to our department in the study period mentioned above. Since the devices are subjected to constant changes and improvements we advise potential users to carefully verify all parameters for each model and each device.

II.2 *Materials and methods*

The different technical and practical parameters of the devices studied in this comparison are shown in Table II-1. The importance of each of these parameters will now be discussed.

II.2.1 **Principles used to measure the aberrations**

The aberrometers listed above comprise four different techniques which are all based on the principle of focal shift. This principle states that a perfect lens always refracts any incident light beam parallel to the lens' optical axis through its focal point (see Figure II-1, top). However in case the lens is aberrated this is no longer true for each parallel incident beam. Instead some of the beams are focused in front of or behind the focal point, so the cross-section point of the refracted beam with the focal plane appears to have shifted from the focal point. This is called 'focal shift' and can be used as a definition of what is measured by an aberrometer.
When the incident beam is moved to another spot on the lens surface the focal shift will vary in accordance with the lens' local aberrations in that spot. Mapping the relation between the different points of incidence and the corresponding focal shifts then provides a general idea of the wavefront slopes in those positions. Using a statistical least-squares fit procedure and (the mathematical derivatives of) Zernike polynomials an estimate to the ocular wavefront can be found.

Starting from this common basic principle aberrometers can further be categorized according to their respective technical properties. One possible classification can be based on subjective

(psychophysical) and objective devices. The first category requires the patient to give some feedback during the measurement process; objective devices perform the entire measurement autonomously. In general objective devices perform measurements faster than subjective devices. Subjective devices also rely completely on the patient's ability to communicate with the examiner, making these methods less interesting for the testing of children or disabled patients.
Another subdivision can be based on the serial or parallel principles used in the different machines, respectively referring to a one-by-one measurement of the data points or an instantaneous collective measurement of all points. Parallel methods can be very fast, whereas serial methods require a longer measurement time. Serial methods on the other hand cannot suffer from the cross-over effect (see further) which might hamper parallel measurements.
A third classification can be based on the single or double-pass principles, indicating the number of times the measurement beam has to pass the aberrated eye optics. Since the light is aberrated at each passage it is important to keep the number of passages as low as possible, preferably to one. However objective measurements cannot be performed in a single-pass way, creating the necessity to reduce the negative effects of double-pass using a number of optical tricks. Subjective methods on the other hand can easily be made single-pass.
Finally a last classification can be based on forward projection of the measurements (i.e. the focal shifts are projected on the retina) or backward projection (i.e. the focal shifts are projected directly on the camera). A backward projection requires a source on the retina, such as a reflection of a narrow laser beam. As this narrow laser beam remains relatively unaffected by the first pass, this can be considered a good approximation of single-pass.

In this work we have chosen to use the serial-parallel classification: two serial and two parallel methods will further be discussed in this order. Only the most important aberrometer components will be discussed to illustrate the working principles. Components such as the computer for data processing or prefocus lenses for refraction compensation are not included, even though they are required for proper functioning of the devices.

a) The ray tracing principle (Figure II-1, center left)

This is a serial, double-pass method using forward projection, which can be implemented in both an objective[60,61] and subjective way[65]. This technique is the best possible approximation of the basic focal shift principle described above.
Ray tracing uses a narrow laser beam that is directed into the eye parallel to the eye's line of sight by means of a *xy*-scanner. Once in the eye the local aberrations in the beam's entry position cause a focal shift of the retinal image with respect to a certain reference position. Using a beam splitter and lens L_2 the retinal image is captured on a linear array of photodetectors and is available for further processing. The *xy*-scanner, comprising two separate scanners for the *x*- and *y*-directions, moves the beam repeatedly to a new entry position until homogeneously spread measurements are available for the whole pupil area.
Ray tracing is a rather simple, highly flexible technique. In principle the *xy*-scanner could be programmed to include other scan geometries than the standard rectilinear or polar scan grids. Its uncomplicated nature also makes it very robust for extreme aberrations.

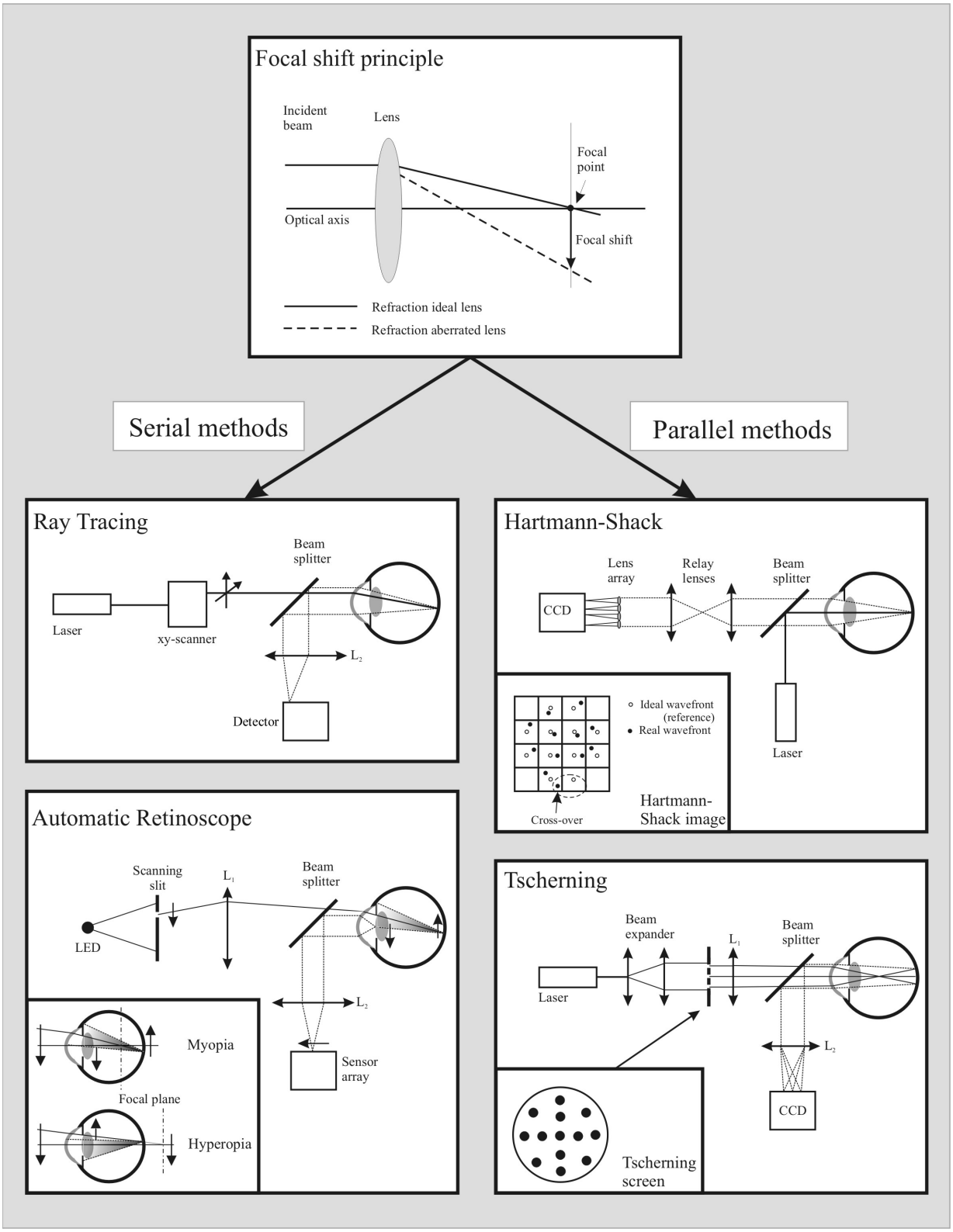

Figure II-1: The principles of the wavefront sensors. (Top) focal shift principle; (Center left) ray tracing; (Center right) Hartmann-Shack; (Bottom left) Automatic retinoscope; (Bottom right) Tscherning. Single sided arrows indicate direction of movement for beams.

b) The principle of the automatic retinoscope[85, 86] (Figure II-1, bottom left)

This is an automated version of the handheld retinoscope, implemented in an objective, serial, and double-pass way. It uses focal shift in a different way (see inset), starting from the observation that the retinal image of a light beam coming from a superior direction is located below the optical axis in a myopic eye and above the optical axis in a hyperopic eye. Since the retina can be considered as a spherically concave mirror (reflecting about 4% of the incident light), the beam is reflected back in more or less the original direction in a myopic eye. In a hyperopic eye however the reflection is directed to the opposite side of the pupil. Moving the incident beam along a certain pupilairy meridian (indicated by arrows in figure) will result in a reflected beam that goes respectively in the same or the opposite direction as the incident beam. The difference in direction and the ratio between the speed of the incident beam and that of its reflection can now be used to estimate the ocular refraction along this meridian.
The automatic retinoscope uses a LED source that is placed behind a screen with a fast moving slit. Using lens L_1 the image of the slit is projected on the pupil plane, where a portion of the light will pass the pupil opening. Depending on the ocular refraction along the scanned meridian the reflected beam moves with a specific speed and direction. This is registered by projecting the pupil plane on an array of photosensitive diodes using a beam splitter and lens L_2. When the orientation of both the scanning slit and the diode array are changed to measure another meridian, an ametropia map (in dioptres) is obtained that can be transposed into a wavefront map (in μm).

c) The Hartmann-Shack principle[75, 91] (Figure II-1, center right)

This is an objective, parallel, double-pass method using backward projection. A Hartmann-Shack device uses a narrow laser beam that is sent along the ocular line of sight into the eye where it reflects on the retina. This reflection serves as secondary source that illuminates the pupil area from behind. The outgoing light is then guided through a set of relay lenses that projects the pupil plane onto an array of tiny lenses that splits up the wavefront into a number of individually focused spots on a CCD camera. Due to focal shift the resulting spot pattern (see inset) shows spot displacements compared to the reference positions. This way the wavefront slopes are determined for the entire pupil at once.
However fast and uncomplicated (as no moving parts are required), the performance of this parallel method is limited to aberrations that are not too complicated. In order to determine the focal shift directly, each reference position is allocated a neighborhood in which the shifted spots are directly associated with a specific reference position (square grid in figure inset). For rapidly varying wavefronts with steep slopes this can sometimes result in focal shifts becoming so large that spots cross over to neighborhoods belonging to another reference positions (see bottom of inset). This makes it impossible to determine the focal shift in those areas. Cross-over can be partially prevented by using prefocus lenses that correct the ocular refraction.

d) The Tscherning principle (Figure II-1, bottom right)

This is a parallel, double-pass method using forward projection, which can be implemented in both an objective[68] and subjective way[65]. Contrary to the Hartmann-Shack the Tscherning aberrometer uses not one, but a group of laser beams that enter the eye. These beams are

generated using a wide laser beam passing through a screen with a large number of round holes. Lens L_1 projects an image of the Tscherning screen onto the retina, resulting in a spot pattern resembling a Hartmann-Shack pattern, where again spots are displaced due to focal shift. The retinal image is then retrieved using a beam splitter and lens L_2. The distortions in the retinal spot pattern are then used to obtain the wavefront as before.
The Tscherning method may also suffer from the cross-over effect, as is the case with the Hartmann-Shack method. Similar countermeasures are implemented to prevent cross-over.

II.2.2 **Measurement details**

- *Wavelength*: color of the light used for measurements.
- *Compensation of chromatic aberrations*: calculated compensation of the chromatic defocus using a numeric model.
- *Maximum number of samples*: in general it can be said that the more samples taken within the pupil area, the more accurate the measurement will be. However, since the data processing following the measurement plays an equally important role, a large number of samples does not necessarily mean a more reliable measurement.
- *Sample grid geometry*: geometry of the sample grid in the pupil plane.
- *User defined grid size*: the possibility of grid size modification by the user.
- *Measurement speed*: time required for one measurement
- *Maximum measurable pupil size*: largest pupil size that can be measured.
- *Dioptric range of prefocus*: range within which the patients' refractive error can be compensated by the internal lenses of the aberrometer.
- *Check for quality of measurement*: in order to estimate the reliability of a measurement, either automatically by the computer or afterwards by the user.
- *Automatic averaging of measurements*: preprocessing of the data by averaging.
- *Possibility of automatic measurement*: indicates whether the aberrometer can perform a measurement by itself after optimal alignment has been achieved.
- *Inhibition of accommodation*: wavefronts change drastically with accommodation of the crystalline lens. Therefore it is necessary to eliminate accommodation using optical tricks. One commonly used method is putting the target at optical infinity. Another method, called "fogging", is to make the target out of focus so that accommodation will not help to get a sharp image. Another approach is the use of adaptive optics.
- *Speckle reduction*: coherent laser light often forms granular dots in the images due to small local interferences that complicate the determination of the spot centers. This can be avoided by breaking the light's coherence, by averaging or by using special filters (either in the hardware or software of the device).

II.2.3 **Alignment**

- *Measurement axis*: the axis along which a measurement is taken. This can be done along the Line of Sight (LoS), which is the line connecting the fovea, the pupil center and the fixation target or along the visual axis (connecting the fovea, the eye's nodal points and the fixation target). Even though both axes differ only slightly from each other, the difference in wavefront can be considerable. The OSA standard[95] advises to use the LoS as it is physiologically the most important axis. Conversions between both axes are possible, but not advisable as it would introduce a number of errors into the calculations.

Table II-1: Technical comparison of the aberrometers under study[*, **, *]**

	VFA	OPD-scan	Zywave	WASCA	MultiSpot	Allegretto
Device details						
Device type or serial number	2066-1	ARK 10000	Zywave II (2.0.1)	Not available	I-a	1071
Software version	1.00	1.11a	4.45 SP1	1.41.6	1.5	4.10
Method	Ray Tracing	Automatic retinoscope	Hartmann-Shack	Hartmann-Shack	Hartmann-Shack	Objective Tscherning
Measurement details						
Wavelength (nm) [a]	650	808	785	850	780	660
Chromatic correction [b]	No	Yes	Yes	Yes (555 nm)	No	Yes (546 nm)
Maximum number of samples [a]	256	1440	80	1452	180	168
Sample grid geometry [a, c]	polar	by meridian	rectilinear	rectilinear	rectilinear	rectilinear
User defined grid size [a, c]	Yes	No	No	No	No	No
Measurement speed [a]	< 50 ms	< 0.4 s	< 1s	13 ms	< 30ms	40 ms
Max. measurable pupil size [b, c]	8 mm	6 mm	8.5 mm	9 mm	8 mm	8 mm
Dioptric range prefocus [a, c]	Sph: -15→ +15D	Sph: -20 → 22D Cyl: 0 →± 12D	Sph: -14 → 8D Cyl: 0 → ±5D	Sph: -15 → 7D Cyl: 0 → ±5D	Sph: -15 → 10D Cyl: 0 →± 6D	Sph: -12 → 6D Cyl: 0 → ±4D
Automatic check of measurement quality [a, c]	Number of rejected spots	Yes	"Repeatability criteria"	No	Comparison tilts with HS spots	Comparison tilts with spots
Automatic averaging of measurements [a, b]	No	3 measurements	Best 3 out of 5	No	User defined	User defined
Inhibition of accommodation [b]	Fogging	Fogging	Fogging	Object at infinity	Object at infinity / adaptive mirror	Fogging (user defined)
Possibility of automatic measurement [a, c]	Yes	No	No	No	No	Yes
Speckle reduction [b]	low-pass filter	Does not apply	Averaging	Pinhole	"wobbling mirror"	averaging/ low-pass filter
Alignment						
Measurement axis [b]	Line of Sight	Visual axis	Line of sight	Line of sight	Line of sight	Line of sight
Patient target [a, c]	Red cross	Balloon on horizon	Mountain and road	Spider web	Small circle	Star in yellow circle
Alignment procedure for operator [a, c]	Variable line pointing to pupil center	Dots parallel to pupil	Circle parallel to pupil	Pupil inside crosshair / offset values	2 circles and half cross / calculated pupil	Purkinje reflexes and pupil centre
Calculation details						
Number of Zernike polynomials used [a, c]	27 (6th order)	27 (6th order)	20 (5th order)	Up till 65 (10th order)	Up till 27 (6th order)	Up till 27 (6th order)
Pupil size for Zernike polynomials [a, c]	Automatic/ User defined	6 mm	Pupil size	Automatic/ User defined	Automatic/ User defined	Automatic/ User defined
Report axis [a, b]	Line of sight	Line of sight	Line of sight	Line of sight	Line of sight	Line of sight
Consistent with OSA Zernike notation? [c]	Yes	No (not normalized)	Not yet (Born & Wolf notation)	No (inverted sign)	Yes	Yes (+ own notation)
Possibility of aberration film sequence [a, c]	No	No	No	2 frame/ sec	Video rate	No

[*] This data is subjected to constant change and represents only the devices made available by the companies to our institution in the period September 2002 – January 2004.
[**] Some of the data in this table was previously published[92, 93].
[***] Sources: [a] Aberrometer manual; [b] Company delegate; [c] Observation by the authors

Table II-1(continued): Technical comparison of the aberrometers under study*, **, ***

	VFA	OPD-scan	Zywave	WASCA	MultiSpot	Allegretto
Data Analysis						
Raw data [a, c]	Yes	No	Yes (mesh)	Yes	Yes	Yes
Refraction [a, c]	Yes	Yes	Yes	Yes	Yes	Yes
Wavefront [a, c]	Yes	Yes	Yes	Yes	Yes	Yes
Higher order wavefront [a, c]	Yes	Yes	Yes	Yes	Yes	Yes
RMS [a, c]	Yes	Yes	Yes	Yes	Yes	Yes
3D wavefront [a, c]	No	No	Yes	Yes	Yes	Yes
Total refraction map [a, c]	Yes	Yes	No	No	Yes	Yes
PSF [a, c]	Yes	No	Yes	Yes (real data)	Yes	Yes
MTF [a, c]	No	No	No	No	No	No
Visual acuity [a, c]	Yes	No	No	Yes	Yes	No
Error estimate map [a, c]	Yes	No	No	No	Yes	Yes
Irradiance map [a, c]	No	No	No	Yes	No	No
Zernike coefficient values (on screen) [a, c]	Yes	Yes	Yes	Yes	Yes	Yes
Change of refraction with pupil size [a, c]	Yes (3, 4.5, 6 mm zones)	Yes (3, 5, 7 mm zones)	Yes (3mm – Pupil size)	Yes (user defined)	No	Yes (user defined)
Miscellaneous						
Data export of Zernike coefficients [a, c]	Yes	Yes	Yes	Yes	Yes	Yes
Data export of wavefront maps [a, c]	Yes	Yes	No	No	Yes	Yes
Customized printout [a, c]	Yes	Yes	Yes	Yes	Yes	Yes
Calibration check [a, c]	Test eye	Test eye	2 test eyes	Test eye	Test eye	Test eye
Requirement for dilation [a, b]	Small pupils	Small pupils	Small pupils	Small pupils	Small pupils	Small pupils

* This data is subjected to constant change and represents only the devices made available by the companies to our institution in the period September 2002 – January 2004.
** Some of the data in this table was previously published[92, 93].
***Sources: [a] Aberrometer manual; [b] Company delegate; [c] Observation by the authors

- *Patient target*: depiction of the fixation target to minimize patient's eye movement.
- *Alignment procedure for operator*: in order to make sure the aberrometer optics are well aligned with the LoS it is imperative that a good alignment procedure is in place. This can be done by using the landmarks of the patient's physiology or by creating reflections that can serve as artificial landmarks.

II.2.4 Calculation details

The time needed to complete the data processing is a very important parameter. However, since this parameter varies strongly with the type of computer used, it was not included in this study.
Most of the following calculation parameters have little clinical interest and are only useful when reporting numerical Zernike data.

- *Number of Zernike polynomials used*: this parameter indicates the spatial resolution of the wavefront image. The more Zernike polynomials used the higher the spatial resolution.

- *Pupil size for Zernike polynomials*: Zernike polynomials are mathematical functions defined on a unit circle. When expressing wavefront aberrations in terms of Zernike coefficients it is imperative that this goes accompanied by the pupil diameter over which the aberrations were determined. These coefficients will change when the measurement is repeated for another pupil size, and may cause problems if data from different pupil sizes is compared. However calculations have been described[96] allowing to derive the Zernike coefficients of a smaller pupil size starting from a larger one.
- *Report axis*: the axis used to report the Zernike polynomials. According to the OSA standards for reference axes[95] this should be the LoS.
- *Consistent with OSA Zernike notation*: the sign and normalization convention used to report the Zernike coefficients were determined by the OSA standards[42], although a number of other conventions are currently still in use.
- *Possibility of making aberration film sequence*: some devices offer the possibility to perform a series of measurements allowing an animated reconstruction of the data.

II.2.5 **Data Analysis**

A list of all the data displays available:

- *Raw data*: provides an image of the original spot diagram.
- *Refraction*: sphere, cylinder and axis
- *Wavefront*: total wavefront aberrations.
- *Higher order wavefront*: the remaining wavefront aberrations after correction of the sphere and cylinder.
- *RMS*: Root-Mean-Square, a parameter defined by RMS = $\sqrt{\sum_i Z_i^2}$ (sum is taken over all Zernike coefficients Z_i), providing a measure for wavefront flatness. As this formula can be easily modified by only including selected Zernike coefficients many different types of RMS can be defined, such as: total RMS (all coefficients, except the tilts), higher order RMS (all coefficients from radial orders higher than 2) and nth order RMS (all coefficients belonging to the n^{th} radial order).
- *3D wavefront*: a 3D display of the wavefront. This can be a useful tool for estimating the shape of the measured wavefront.
- *Total refraction map*: refraction map of the whole eye optics calculated from the wavefront.
- *PSF*: the Point Spread Function, the image of a point source as seen by the patient calculated from the wavefront.
- *MTF*: the Modulation Transfer Function indicates the contrast with which lines of specific spatial frequencies can be perceived by the patient.
- *Visual acuity*: a simulation of the Snell "E" as seen by the patient calculated from the measured wavefront.
- *Error estimate map*: a regional map of the difference between the measured data and the data simulated using the Zernike polynomial fit. This may be useful as a quality control.
- *Irradiance map*: image of the pupil area in which the amount of light passing through each section of the pupil is indicated. This can be used for mapping opacities in the eye optics.
- *Zernike coefficient values* (*on screen*): the numeric values of the Zernike polynomial coefficients shown on screen.
- *Change of refraction with pupil size*: a graph or table where the refraction is set in function of the pupil size.

II.2.6 **Miscellaneous**

A number of properties that could not be included under the previous categories:

- *Data export of Zernike coefficients*: the possibility to export the numeric values of the Zernike coefficients in a file.
- *Data export of wavefront maps*: the possibility to export the wavefront image (or another illustration) in a file.
- *Customized printout*: the possibility to modify the printout according to the examiner's needs.
- *Calibration check*: method for calibration
- *Requirement for dilation*: to precise whether dilation of the pupil in recommended before measuring.

II.3 *Results*

The values of the above parameters for each aberrometer are shown in table 1. Note that this data is subjected to constant change and represents only the devices made available by the companies or their Belgian delegates to our institution in the period of September 2002 to January 2004.

II.3.1 **Principles used to measure the aberrations**

The VFA uses ray tracing, while the OPD-scan uses automatic retinoscopy. Three devices use the Hartmann-Shack principle (Zywave, WASCA and MultiSpot) and the Tscherning principle is used by the Allegretto.

II.3.2 **Measurement details**

- *Wavelength*: in each device a monochromatic LED or laser source is used that emits red or infrared light (ranging from 650 nm for the VFA till 850 nm for the WASCA). At these wavelengths the measured aberrations will be slightly different from the most relevant aberrations in the middle of the visual spectrum[97]. Especially the sphere can differ up till 0.7D between infrared and green wavelengths[98].
- *Compensation chromatic aberrations*: all aberrometers have this feature, except the MultiSpot and the VFA. However both devices will include this feature in the next software release.
- *Maximum number of samples*: this parameter ranges from 80 (Zywave) up till 1452 (WASCA).
- *Sample grid geometry*: all devices use a rectilinear sample grid. The VFA on the other hand scans over a polar (concentric) grid and the OPD-scan measures over a series of meridians.
- *User defined grid size*: only the VFA has this feature, which can generate grid sizes going from 2mm up till 8mm.

- *Measurement speed*: the WASCA does its measurements in 0.013s. The other devices need about 0.03 to 0.5s.
- *Maximum measurable pupil size*: the parameter ranged from 6mm (OPD-scan) up till 9mm (WASCA).
- *Dioptric range of prefocus*: the dioptric ranges of the devices are comparable (on average: -15D → 7D Cyl: 0 → ±5D), with an exception for the OPD-scan that offers the range of -20D → +22D (cylinder 0 → ±12D).
- *Automatic check for quality of measurement*: 5 out of the 6 devices provide such estimation. The VFA estimates the reliability of the data points by rejecting points having an intensity below a certain threshold. Measurements with up till three rejected points are still acceptable. Alternatively the user can reject data points by himself. In the OPD-scan this is done automatically. Faulty measurements can immediately be redone. The Zywave calculates the "repeatability criteria" which should stay below a certain threshold given by the manufacturer. The MultiSpot device provides an error map in which the calculated wavefront is used to recalculate the corresponding spot pattern. This calculated spot pattern is then compared with the experimentally determined one and the deviations are shown in the map. The Allegretto uses a similar principle. The WASCA has no quality check.
- *Automatic averaging of measurements*: in 4 out of the 6 machines some preprocessing of the data occurs by averaging. The OPD-scan averages 3 separate measurements and checks for their quality. Any wrong measurement is rejected and repeated. The Zywave does 5 measurements and uses the "repeatability criteria" to determine the best 3 of them for averaging. The MultiSpot device records the wavefronts during a number of seconds. The operator can later select a period over which the averaged wavefront is calculated. In the Allegretto 4 measurements are taken that can be manually selected to be used for averaging. Both the WASCA and the VFA do not use averaging.
- *Inhibition of accommodation*: the VFA, OPD-scan, Zywave and Allegretto use fogging, while the WASCA and the MultiSpot place the object at optical infinity. In the Allegretto the fogging can be switched off if necessary. The MultiSpot also has the possibility to compensate the accommodation in real-time using an adaptive mirror that is controlled using a feedback loop that minimizes the total aberrations.
- *Possibility of automatic measurement*: only the Allegretto and the VFA have this option. In both cases an autonomous measurement is taken as soon as the best possible alignment is achieved.
- *Speckle reduction*: this is achieved by the use of numerical filters (VFA, Allegretto) or by averaging multiple measurements (Zywave, Allegretto). The MultiSpot and the WASCA respectively use a "wobbling mirror" and a pinhole. Since the OPD-scan uses a low-coherence LED source speckle reduction is not required for this device.

II.3.3 **Alignment**

- *Measurement axis*: all devices measure along the Line of Sight (LoS). Only the OPD-scan uses the visual axis and converts the results to the LoS standard.
- *Patient target* (Figure II-2): most targets point towards the center enhancing the fixation of the patient. Only the Zywave has an off-centered target (Figure II-2c), making the patient more inclined to look around. This may result in off-axis readings.
- *Alignment procedure for operator* (Figure II-3): in 3 out of 6 devices this procedure consists of the alignment of a fixed circle (Figure II-3a: OPD-scan and Zywave; no image available for the OPD-scan) or cross overlay (Figure II-3b: WASCA) and the pupil itself.

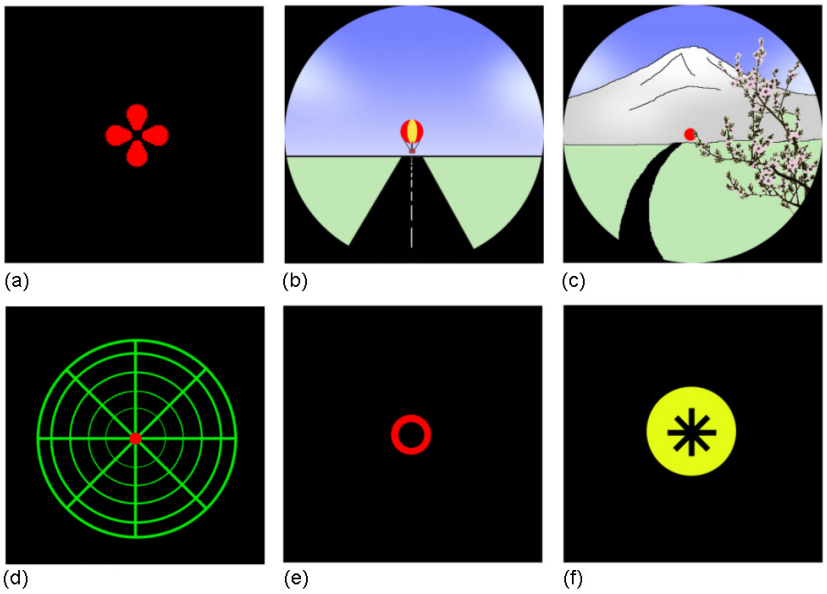

Figure II-2: Reproductions of the fixation targets for the patient. (a) VFA, (b) OPD-scan, (c) Zywave, (d) WASCA, (e) MultiSpot and (f) Allegretto.

This method solely depends on the operator's skill to perform this task and is therefore sensitive to errors both along the optical axis as in the horizontal and vertical direction. On the other hand the WASCA gives offset values that, in the "free running mode" can also be used as an alignment tool.

The VFA determines the pupil edge, from which the pupil center can be found (Figure II-3c). The misalignment of the device's optical axis with respect to the pupil center is indicated by a green line. Using this line the alignment can be corrected.

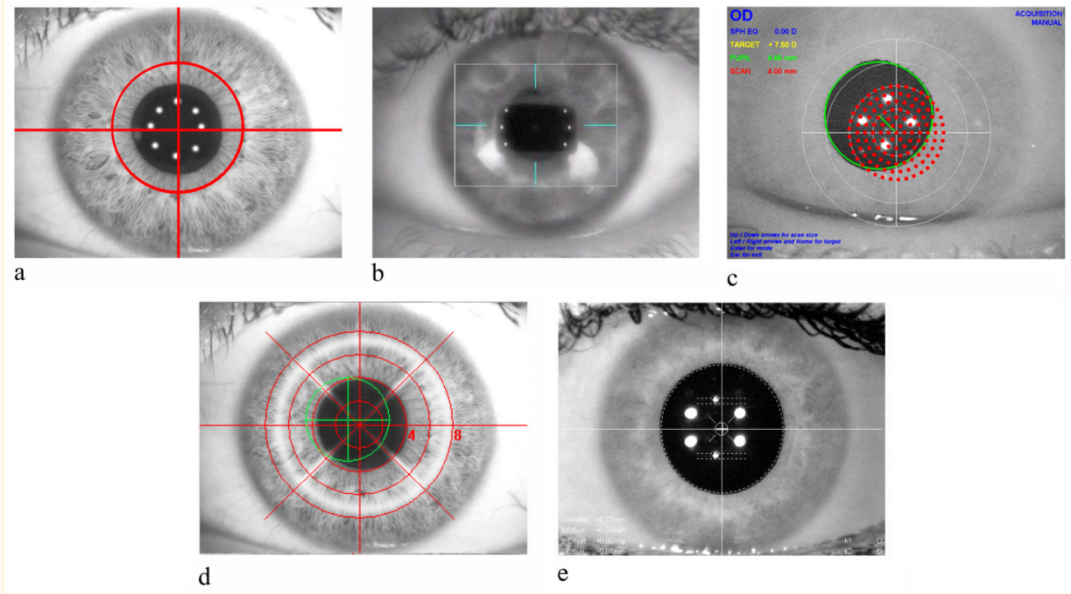

Figure II-3: Reproductions of the live pupil images used for alignment of the aberrometer in increasing degree of complexity. (a) Zywave, (b) WASCA, (c) VFA, (d) MultiSpot and (e) Allegretto. An image of the OPD-scan alignment screen could not be obtained.

The MultiSpot device (Figure II-3d) uses two circles, each with a half cross, for the positioning along the visual axis. The horizontal positioning is done both visually by aligning a series of concentric circles with the physiological pupil as well as by aligning a calculated pupil. The calculated pupil is optically conjugated in size and location with the spot image on the CCD camera.
The Allegretto uses an elaborated alignment procedure (Figure II-3e). First the edge of the pupil is determined automatically in order to find its center, which is marked by a small cross. Next the device is moved along the optical axis until two reflections on the cornea ("Purkinje reflections") coincide with an overlay line. Finally the cross in the pupil center has to coincide with an overlay cross for a horizontal and vertical alignment. Because this procedure is quite demanding for the operator, as well as the very low alignment tolerance (100μm), an automatic measurement procedure has been included.

II.3.4 **Calculation details**

- *Number of Zernike polynomials used*: this parameter varies from 20 (5th order) for the Zywave up till 65 (10th order) for the WASCA. The MultiSpot, the Allegretto and the WASCA are able to determine how many polynomials should be used by estimating the data quality and pupil size. However this selection can also made by the user. The OPD-scan, Zywave and VFA use a fixed number of Zernike polynomials.
  In the latest software edition of the WASCA the "zonal reconstruction" technique has been introduced for wavefront reconstruction. This does not rely on Zernike polynomials or the pupil shape anymore. If desired, the Zernike coefficients can still be calculated as an option.
- *Pupil size for Zernike polynomials*: the devices studied use either a fixed pupil size of 6mm (OPD-scan), the physiological size (Zywave) or a user defined size (WASCA, MultiSpot, Allegretto and VFA).
- *Consistent with OSA Zernike notation*: only the MultiSpot and the VFA comply with this standard. The OPD-scan and the WASCA make an approximation, but without normalization or inverted signs. The Zywave and Allegretto use different notations, but will include the OSA Zernike standard in their new software.
- *Possibility of aberration film sequence*: the WASCA has the possibility to make short 10 frame movies of a wavefront change. The MultiSpot can record wavefronts up till 20s (600 frames) and store them as a list of Zernike coefficients.

II.3.5 **Data Analysis**

- *Raw data*: is provided by most aberrometers in one way or another. Because of the different working principles of the OPD-scan raw data is not available for this device.
- *Refraction*: all aberrometers provide this feature.
- *Wavefront*: all aberrometers provide this feature.
- *Higher order wavefront*: all aberrometers provide this feature.
- *RMS*: all aberrometers provide various types of RMS, including total RMS, higher order RMS and the RMS for a number of radial or angular orders.
- *3D wavefront*: most aberrometers provide this feature, except the OPD-scan and the VFA who will include in their next software release.

- *Total refraction map*: this feature is available in the OPD-scan, the MultiSpot, the Allegretto and the VFA.
- *PSF*: all aberrometers provide this feature, except the OPD-scan that will include it in the next software release. The WASCA gives the "retinal spot image" which is an image of the PSF on the retina; the other aberrometers calculated the PSF from the wavefront.
- *MTF*: none of the aberrometers provide this feature.
- *Visual acuity*: this feature is only present in the WASCA, MultiSpot and VFA devices.
- *Error estimate map*: available in the MultiSpot and the Allegretto. The former shows a color map, while the latter superimposes the calculated spot over the original spot pattern.
- *Irradiance map*: this feature is only present in the WASCA.
- *Zernike coefficient values* (*on screen*): all aberrometers provide this feature.
- *Change of refraction with pupil size*: available in the Zywave as a graph. The other devices show either the refraction for a fixed set of pupil sizes (OPD-scan, VFA) or allow the user to change the pupil size (WASCA, Allegretto). The MultiSpot does not have this feature.

II.3.6 **Miscellaneous**

- *Data export of Zernike coefficients*: all aberrometers provide this feature. The OPD-scan, Zywave and MultiSpot provide the coefficients for the entire measured pupil, while the VFA gives the coefficients for four different pupil sizes. In the WASCA and Allegretto the user can determine the size.
- *Data export of wavefront maps*: most aberrometers have this feature except the Zywave and the WASCA which only export Zernike coefficients.
- *Customized printout*: all aberrometers provide this feature.
- *Calibration check*: all aberrometers use one or two test eyes as a calibration check.
- *Requirement for dilation*: in all cases the manufacturers recommend to dilate the pupil to enlarge the measurement area.

II.3.7 **User and patient parameters**

These subjective parameters are not included in Table II-1. They represent our own experiences and the patient's impressions about the devices as they were available to us in the period of September 2002 to January 2004.

Patient comfort: how does the patient experiences the measurement?

- *VFA*: no problems.
- *OPD-scan*: no problems.
- *Zywave*: no problems.
- *WASCA*: the spider web target was tiring to some patients after a short while.
- *MultiSpot*: no problems
- *Allegretto*: the measurement flash is sometimes experienced as uncomfortable. The constantly changing sound of the step motors is distracting for some.

Operator Comfort: how does the operator experiences the measurement? (Evaluation between: very easy – easy – short learning curve – long learning curve)

- *VFA*: requires a short learning curve to operate.
- *OPD-scan*: easy to use with comprehensive software.
- *Zywave*: very easy to use.
- *WASCA*: easy to use.
- *MultiSpot*: requires a long learning curve to operate.
- *Allegretto*: requires a short learning curve to operate; comprehensive software. The recalibration of the step motors every 5 measurements is time consuming.

II.4 *Discussion*

II.4.1 **VFA**

It is the only device that uses ray tracing, making it very flexible and robust to extreme aberrations. Measurements were obtained in pathological conditions, such as cataract or corneal diseases. The VFA also allows a large amount of freedom to the operator during and after the measurements.
If the optical target is removed the patient is able to see straight through the device to a distant target. This way the patient's accommodation can be tested directly by varying the distance between the target and the eye.
The VFA can be integrated with EyeSys Vista corneal topographer, so the anterior corneal aberrations can be subtracted from the total aberrations.

II.4.2 **OPD-scan**

This device uses automatic retinoscopy and also has an integrated corneal topographer. The OPS-scan provides a large list of different corneal and refractive maps that can be interesting for a closer study of the eye's refraction. The compact design with the integrated computer and corneal topographer is ideal for small practices.
When using this device it is very important to make sure the pupil is fully dilated (no size variations during the measurement) in order to avoid irregular shapes of the calculated pupil. If one wishes to export Zernike polynomial data from the OPD-scan one has to make sure the minimal pupil diameter is 6mm as the polynomials are by default calculated for this diameter. This means that for smaller pupil sizes measurements are shown for areas outside the physiological pupil, introducing erroneous Zernike coefficients.
During the measurement there is an automatic check for its quality. However, sometimes this automatic check fails to reject a bad measurement. Because the user cannot reject bad measurements, the whole procedure has to be redone.
The alignment procedure is not very elaborated and needs a steady hand of the operator. Using such a system it is easy to introduce slight misalignments in the wavefront measurement, resulting in erroneous values of the tilt and the coma aberrations.
In the next software release the corneal topography and the wavefront map can be linked to each other, which creates the possibility of subtracting the corneal aberrations from the total aberrations. This can be interesting e.g. for studying the wavefront effects of cataract or IOLs.

II.4.3 **Zywave**

Every step of the measurement process is done by consecutively clicking the button on the joystick. In one measurement 5 spot patterns are recorded and the best 3 are automatically selected using the "repeatability criteria".

During our evaluation period there was one healthy patient for whom 4 out of 5 samples showed a cylinder of 0.5D and one showed a clearly false value of -4D. The system failed to recognize this extreme value and gave the final astigmatism value of -3.75D, a correction that did not correspond with the patients' objective refraction. Repeated measurements on this patient showed similar results.
Optionally this device the refraction as a function of the pupil diameter is plotted in a graph. However, it should be kept in mind that not all calculated points are equally accurate due to higher order aberrations. Adding error bars to this graph would benefit to the clinical value.
The alignment system relies on the alignment of a circle and a crosshair with the pupil edge. This simple alignment may introduce errors into the measurements, as well as the fixation target which may be confusing to the patient. One alternative is to ask the patient to look slightly above the red dot of the laser source for fixation.
Coupling the Zywave with the Orbscan II corneal topographer would be complementary. However this option is not yet available.

II.4.4 **WASCA**

This Hartmann-Shack based device measures the highest number of samples. It also shows the wavefront in case of missing data points, which are represented by blanks on the wavefront map. However in order to avoid errors no holes can be allowed inside the Zernike pupil when the polynomials are calculated.
The "Free-running mode" is interesting as it shows a moving image of the wavefront. This way accommodative changes can be studied and saved into short wavefront movies.
The alignment procedure is rather limited, although this can be remedied using the "free-running mode" and the offset values offered to the operator.
In the latest software release WASCA offers a new reconstruction algorithm based on zonal reconstruction, resulting in an improved resolution of the wavefront images.

II.4.5 **MultiSpot**

This is the only aberrometer in our study that contains a bimorph mirror for the purpose of compensating the patient's accommodation in real time. The MultiSpot can also be used to simulate the ideal vision by compensating the patient's aberrations.
Other interesting features of this device are the possibility of recording short wavefront movies and the error map that shows the difference between the measured and the calculated spot pattern.
One disadvantage of the MultiSpot is that it might take the operator some time to learn how to use the device properly.

II.4.6 **Allegretto**

The Allegretto has an exceptionally elaborated alignment procedure, resulting in a highly accurate location of the pupil centre. However, in case of elliptical pupil shapes this estimation is sometimes displaced from the true centre and the alignment needs to be done manually. Also the source intensity is sometimes hard to adjust, depending on the installed camera.
This aberrometer is characterized by a long list of available options for the fine-tuning of the measurements and data representation that are interesting for wavefront research. But because of this large number of options some training is required to operate the Allegretto to its full potential.

II.5 *Conclusion*

When choosing an aberrometer it is important to keep in mind the purpose it will serve in daily clinical practice. If the aim is to use it as an extended corneal topographer, many of the options in the more elaborate systems are useless. These same options however could be very helpful for clinical studies. Either way, in our opinion there are a number of minimal requirements the aberrometer should meet in performing the measurements, such as:

- A highly accurate alignment procedure
- A source wavelength in the middle of the visual range, or a numerical compensation of the chromatic aberrations.
- An averaging over several measurements
- An automatic test of the measurement quality
- An inhibition procedure for accommodation

These parameters should at least be considered as equally important as the data assessment, such as the number of samples, the number of Zernike polynomials and the dioptric range of the prefocus. However, most studied aberrometers do not provide all of these features.
Besides the common parameters already offered by each aberrometer, such as the refraction values, the total and higher order wavefronts, the total and higher order RMS values and the Zernike coefficient values the minimal data representations should be:

- An error estimate map
- A refraction map
- The PSF
- The MTF
- A graph of refraction vs. pupil size (including an error estimate on the refraction)

Furthermore a depiction of the raw data can be useful in some cases, as well as the simulated visual acuity map. The Zernike notation details and the data export functions are only interesting when the numerical data is used for comparative studies using data from different wavefront devices.
The consistency of the measurements by these aberrometers in terms of refraction and wavefront aberrations has not been determined in this paper. This will be discussed in a second paper.

Acknowledgements

We would like to thank the companies Nidek, Bausch & Lomb, Zeiss, WaveLight and Tracey and their Belgian representatives for temporarily providing their aberrometer for our study. Also Michael Mrochen is kindly thanked for the lending of the MultiSpot aberrometer as well as Andrei Larichev and Nikita Irochnikov for providing the necessary technical assistance. This project was supported by an ESCRS research grant (2002) and a grant (2002) of the FRO (Belgian Fund for Research in Ophthalmology).

Chapter III Clinical comparison of 6 aberrometers II: Statistical comparison on a test group

Jos J. Rozema[*,**], MSc, Dirk E. M. Van Dyck[*], PhD, Marie-José Tassignon, MD PhD[**]

[*] Vision Lab, University of Antwerp, Antwerp, Belgium
[**] Department of Ophthalmology, University of Antwerp, Belgium

None of the authors have any financial interests in the products mentioned in this article.

This research is sponsored by an ESCRS grant (2002) and a 2002 grant of the Belgian Fund for Research in Ophthalmology (2002)

Reprint request to: J. Rozema, University Hospital Antwerp, Wilrijkstraat 10, 2650 Edegem, Belgium

III.1 *Abstract*

Purpose: To compare and mutually validate the measurements of 6 aberrometers: the Visual Function Analyzer (Tracey), the OPD-scan (ARK 10000), the Zywave, the WASCA, the MultiSpot Hartmann-Shack device and the Allegretto Wave Analyzer.

Setting: University Hospital Antwerp, Antwerp, Belgium

Methods: This prospective study was conducted on a group of 44 healthy eyes having a refraction ranging from -5.25D to +5.25D (cyl. 0D to -2D). For each aberrometer and each eye the refractive and the averaged Zernike data was used to calculate a number of parameters, such as various kinds of RMS, the Strehl ratio and the MTF ratio. A repeated measures ANOVA test, followed by a Newman-Keuls test in case of a significant difference, was used to compare these parameters. This was complemented by paired T-tests. A similar analysis is done for the comparison of the variances of these parameters.

Results: The aberrometers give comparable values for all Zernike polynomials and derived parameters, with the following exceptions: the OPD-scan underestimated the polynomials describing 4- and 5-fold symmetries and the VFA slightly overestimated the astigmatism terms. The 3rd order radial RMS value was different for each device, as well as the RMS in the central 2mm zone. The WASCA presented the lowest variance.

Conclusion: These results suggest that for healthy eyes all aberrometers produce globally similar results but punctual variations did occur.

III.2 *Introduction*

When comparing aberrometers, two aspects that should be kept in mind: the technical aspect, comprising the working principles, the practical realization of the aberrometers and the extra features offered, and the statistical analysis of the measurements when applied on a test group. This second aspect will be the focus of this paper.
Recently several papers have been published in which some of the basic techniques used in modern aberrometers are compared. The most important of these studies are:

- A comparison[99] of the Smirnov and the Hartmann-Shack method

- A comparison[100] of Hartmann-Shack and the laser ray tracing
- A comparison[101] of Hartmann-Shack and the laser ray tracing and the spatially resolved refractometer.
- A comparison[102] of Hartmann-Shack and a crossed-cylinder aberroscope.

In each of these papers the comparisons were developed extensively. However, since each of these tests were done on experimental aberrometer setups, located in laboratories and under perfectly controlled circumstances, these studies only verify the principles used in each aberrometer rather than the devices themselves. This is the reason why these papers do not necessarily validate the practical realizations of the aberrometers as they are on the market today.
In one abstract[103] it has been attempted to compare two clinical aberrometers, the Zeiss/ Meditec WASCA Hartmann-Shack aberrometer and the Schwind ORK Tscherning aberrometer. It was noted in this study that the RMS values of the total wavefront for both devices were comparable, but that the RMS values of the higher order polynomials were significantly different. Another study[104] compared 6 aberrometers: Alcon LADARwave, B&L Zywave, Nidek OPD-scan, Topcon Wave-Front Analyzer, Tracey Visual Function Analyzer and the Wavefront Sciences COAS (Zeiss WASCA), and it was concluded that measurements by different devices could not be used interchangeably. Also the suggestion was given that wavefront devices with less than 70 data points in a 6mm pupil might have a larger variance in their measurements. However no significant relationship to this effect could be found. Finally a last paper[105] describes a comparison between the VISX WaveScan system (Hartmann-Shack) and the Tracey Visual Function Analyzer. The authors concluded that the measurements of both devices were reliable and reproducible, compared to each other and to the manifest refraction. The VFA was found to be more robust to large refractive errors.
In this paper the comparisons will be expanded to a larger number of parameters for 5 commercially available clinical aberrometers and one custom-made device, comprising 4 different wavefront sensing techniques. This will be done on a series of healthy eyes.

III.3 *Patients and Methods*

III.3.1 **Patients**

The test group consisted of 44 eyes (22 subjects) with an average age of 31 ± 7 years. Only subjects with mild refractive errors were allowed, ranging from -5.25D to +5.25D (cyl. 0D to -2D). For each aberrometer a number of 7 to 15 subjects from this group were measured, determined by their availability at the time a device was at our disposal. The subjects were dilated with 0.5% Tropicamide in case of a pupil diameter below 6mm. Once dilated for the first aberrometer, a subject was consistently dilated further throughout the test. At the end of all tests 7 eyes were measured with each aberrometer and could be included in the overall comparison. The other measurements were used for the indirect comparison by means of a model described further on.

III.3.2 **Aberrometers**

The aberrometers in this study are:

- *Visual Function Analyzer* (*VFA; Tracey*)[60, 61]: based on ray-tracing of individual beams.

- *OPD-scan* (*ARK 10000; Nidek*)[85, 86]: based on automatic retinoscopy.
- *Zywave* (*Baush & Lomb*): a Hartmann-Shack[52] system.
- *WASCA* (*Zeiss/ Meditec*): a high resolution Hartmann-Shack system
- *MultiSpot 250-AD*[94] *Hartmann-Shack sensor*: a custom made Hartmann-Shack system with an adaptive mirror for accommodation correction, engineered by the Laboratory of Adaptive Optics at the Moscow State University.
- *Allegretto Wave Analyzer* (*WaveLight*): an objective Tscherning device[68].

Further details on the working principles of these machines can be found in [13].

III.3.3 **Test period**

Since it was logistically impossible to have all the aberrometers at our disposal at once the tests were spread over two periods: the OPD-scan, Zywave Allegretto and MultiSpot were tested from October 2002 until February 2003, the WASCA and the VFA were tested from November 2003 until January 2004. Even though the higher order aberrations might vary over these time spans, it is reported[106] that these variations are an order of magnitude smaller than the higher order aberrations themselves. Nevertheless the subject's refraction was used as a means to verify this assumption.

III.3.4 **Measurements and Calculations**

With each aberrometer five measurements were preformed on a number of eyes from the test group. For each eye the average and the variance of the different parameters were calculated and used for further study. The clinical refraction was determined by means of a Nidek ARK-700 autorefractometer.
As the wavefronts are often expressed in terms of Zernike polynomials a selection of these polynomials can easily be used for comparison purposes. However at the time this study was performed the Zernike polynomials provided by most aberrometers could not be used in a direct manner for several reasons:

- The pupil size used for calculating the Zernike polynomials varies per aberrometer. The OPD-scan uses a fixed pupil size of 6mm, while the WASCA, MultiSpot, VFA and the Allegretto allow the user to define the size. The Zywave on the other hand used the physiological pupil size.
- Each device used a different convention in the order, sign and normalization of their Zernike polynomials.
- The number of Zernike polynomials used varied with each aberrometer, ranging from the 5th (Zywave) up till the 10th order (WASCA).

The first and second points can easily be compensated by respectively resizing and a renormalization for the polynomials. The third point was solved by truncating the Zernike series at the 5th order (see Figure III-1). This was either done automatically by the aberrometer itself or manually in the Zernike series. A comparison of the total RMS value before and after truncating served as quality measure for the wavefront fit by the truncated series. All Zernike polynomials used in this study are defined on a 6mm pupil and renormalized to meet the OSA standards[42].

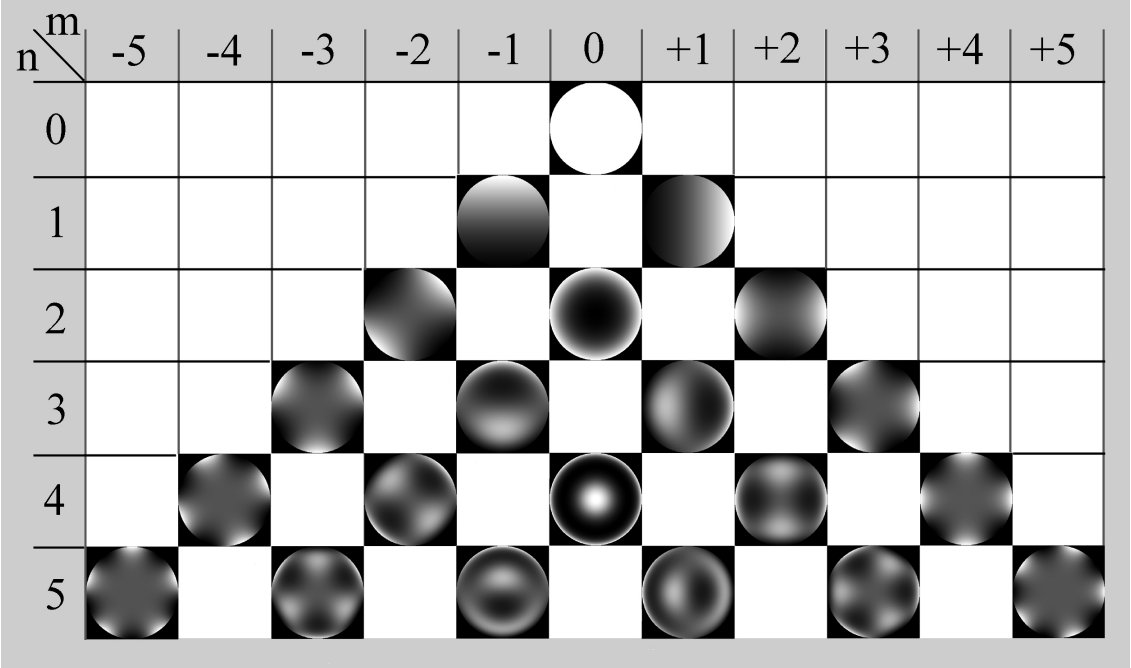

Figure III-1: Pyramidal oversight of the first 21 Zernike polynomials. The radial orders (characterized by index n) are found in the rows, the angular orders (characterized by index m) are listed in the columns.

By means of the refraction and the Zernike data the following parameters were derived that can be used for comparison:

- *Refraction* (sphere, cylinder and axis): the refraction parameters as given by the aberrometer.
- *Zernike polynomials from the 2nd up till the 5th radial order*: resized to a 6mm pupil and renormalized if necessary to meet the OSA standards.
- *Total and higher order RMS*: calculated from the Zernike polynomial data. This is an indication of the flatness of the wavefront and is calculated using:

$$RMS_{tot} = \sqrt{\frac{\sum_{x,y=1}^{N}\left(W(x,y)-\overline{W}\right)^2}{N^2}} \qquad \text{(III-1)}$$

with $W(x,y)$ a point on the wavefront, $\overline{W}$ the average of the whole wavefront and N the number of wavefront pixels. In case the Zernike polynomial coefficients a_i are known, this can be simplified to:

$$RMS_{tot} = \sqrt{\sum_{i=3}^{N} a_i^2} \qquad \text{(III-2)}$$

Formula (III-2) is easy to calculate and can be modified to find the RMS associated with a specific set of N Zernike terms. Usually the total RMS (all terms of radial order higher than 1) and the higher order RMS (all terms of radial orders higher than 2) are used.

- *RMS_{rad} of the 2nd up till the 5th radial order*: RMS-values calculated separately for each radial order (rows of the Zernike pyramid; Figure III-1). These parameters are

automatically given by most aberrometers and are often used in studies; however their exact clinical meaning is not always clear.

- *RMS_{ang} of the 0^{th} up till the 5^{th} angular order* (*or meridional frequency*): RMS-values calculated separately for each angular order (columns of the Zernike pyramid; Figure III-1). The angular order RMS has the advantage that it is sensitive to specific wavefront symmetries (e.g. all orders of astigmatism or trefoil) rather than to a sum of all kinds of symmetries available in one radial order as in the previous set of parameters (e.g. in the third order radial RMS the contributions of the primary trefoils and the primary comas are added).

However in a recent report[107] it was stressed that RMS is not a reliable measure for the estimation of the visual quality of a patient since the contribution of each Zernike mode to the visual quality is not equal. Terms at the side of the Zernike pyramid (i.e. angular order $m = \pm$ radial order n) have less influence on the image quality than those at its center ($m = \pm 1, 0$). In order to counter this effect we also used a number of Zonal RMS (*ZRMS*) parameters that are not influenced by this problem, which are RMS values calculated by means of formula (III-1) in the zones defined in Figure III-2. In this approach the surface of the wavefront is considered, rather than its Zernike decomposition, giving a measure of flatness within the zones instead of over the whole pupil area. While a region with an unusual aberration shape will go unnoticed using the global values given by RMS_{tot} or RMS_{HO} they might be found using *ZRMS*.

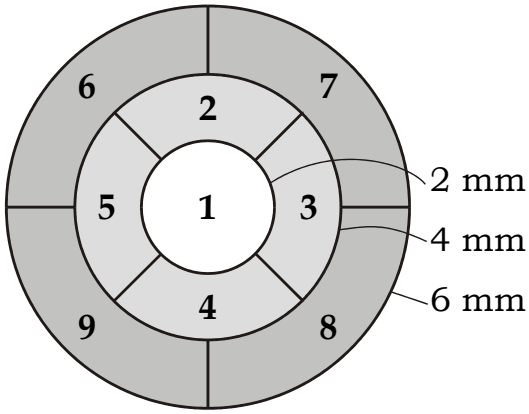

Figure III-2: Definition of the 9 zones used for zonal reconstruction.

Besides a direct comparison of the above parameters for each aberrometer, it is also possible to do an indirect comparison with a model. This indirect comparison can serve as a benchmark that every aberrometer should meet. The advantage of this approach is that there is no longer a need to use a fixed standard group of subjects. A number of parameters can be mapped in function of the refraction by means of measurements on a large group of subjects. This data can be further analyzed with e.g. linear regression. However it is important to note that by its nature the indirect method is less accurate than the direct statistical comparison, making it more interesting for the purpose of calibration rather than for comparison.
In this study we will use this method for:

- *Sphere*: the value of the sphere given by the aberrometer in function of the clinical sphere. This is modeled by:

$$Sphere_A = a_S \cdot Sphere_C + b_S \qquad \text{(III-3)}$$

The fit parameters in (III-3) ideally have values $a_S = 1$ and $b_S = 0D$, with a tolerance of $\pm 5\%$ for a_S and $\pm 0.25D$ for b_S (which is the smallest possible variation on the autorefractometer measurements).

- *Cylinder*: the value of the cylinder given by the aberrometer in function of the clinical cylinder. Here model (III-3) applies again, with the same tolerances.
- *Axis*: value of the axis given by the aberrometer in function of the clinical axis. Again model (III-3) applies, but here the ideal fit parameters have the values $a_A = 1.00 \pm 0.05$ and $b_A = (0 \pm 10)°$.
- *Spherical equivalent*: value of the spherical equivalent (calculated by: *Sphere* + *Cylinder/2*) given by the aberrometer (*ASE*) in function of the clinical spherical equivalent (*CSE*). Again model (III-3) can be used with the same tolerances as for the sphere.
- RMS_{tot}: the evolution of the total RMS in function of the clinical spherical equivalent (CSE). This function has a V-shape and can be described by:

$$RMS_{tot} = a_{tot} \cdot \left| CSE \right| + b_{tot} \tag{III-4}$$

with $\left| \cdot \right|$ the absolute value. Multiplying both RMS_{tot} and a_{tot} in (III-4) by $sign(CSE)$ results in a linear curve that can be fitted by linear regression.
A theoretical value for a_{tot} can be estimated by assuming that *CSE* depends on the normalized defocus coefficient C_2^0 as follows:

$$CSE = \frac{-4C_2^0}{R^2 + \left(-2C_2^0\right)^2} \approx \frac{-4C_2^0}{R^2} \tag{III-5}$$

with *CSE* in dioptres and R the pupil radius. The approximation in (III-5) can be made since $C_2^0 << R$. Next it follows that:

$$C_2^0 \approx \frac{-R^2}{4} \cdot CSE = \left(-2.25 \frac{\mu m}{D}\right) \cdot CSE \tag{III-6}$$

for $R = 3mm$. If we assume that no large quantities of astigmatism or higher order aberrations are present the Zernike defocus coefficient C_2^0 can be used as a rough approximation of the wavefront. This results in:

$$RMS_{tot} = \left|C_2^0\right| = 2.25 \frac{\mu m}{D} \cdot \left|CSE\right| \tag{III-7}$$

So the ideal parameter values in (III-4) for $a_{tot} = 2.25\mu m/D$ with a tolerance of 5% and for $b_{tot} = 0 \pm 0.56\mu m$ (corresponding to a clinical refraction of $\pm 0.25D$ by means of formula (III-7).

III.3.5 **Statistical comparison**

The direct statistical comparison of the parameters is done using repeated measures ANOVA with a significance level of 95% over the 7 healthy eyes that have been consistently tested with each aberrometer. In case the initial assumption of equal parameter values for each aberrometer is rejected, a Newman-Keuls test is performed to determine the deviating aberrometer(s).

Next a student T-test is performed on each pair of aberrometers using a number of eyes tested by both devices. Since the T-test studies pairs of aberrometers, more details on the correspondences between devices can be found. However this also increases the possibility of false rejections. The ANOVA on the other hand studies the whole group and is as such less sensitive. Note that since the premises of both statistical methods are different it is possible that some of the results might seem contradictory.
Finally the variances on the measurements for a selection of parameters were analyzed in the same way. As a reference the minimum and maximum values of the variance sizes are given for each parameter.
In order to reduce the chance of false negatives in the following, we say that the parameter value for one aberrometer differs significantly from that of other aberrometers if the ANOVA or at least two T-tests are found to be significant. One single significant T-test will be disregarded.
The statistical power of the T-tests have also been calculated for an effect size d = 0.8 (in standard deviation units) using the method defined in [108].

III.4 *Results*

Direct comparison of the wavefront images of the same eye recorded by each device is the most direct way to compare, as it is done in Figure III-3. It can be seen that the general shape of the wavefront is maintained, although some differences exist between the locations of the central minimum. This can be explained by slight errors in the alignment. Also the magnitude of the wavefronts seems to vary, more specifically with the Zywave, where the amplitude seems to be lower than those of the other measurements. Similar differences were found in all of the other 6 eyes studied.

An extensive oversight of the statistical comparison for the parameters is given in Table III-1, and that of their variances in Table III-2. Both tables consist of two parts: on the left side the ANOVA and the Newman-Keuls results are shown, the right side shows the results of the paired T-tests. Table III-2 also shows the minimum and maximum variances for each parameter. In both tables significant differences are indicated by a gray shade, statistical powers of the tests were included in caption.

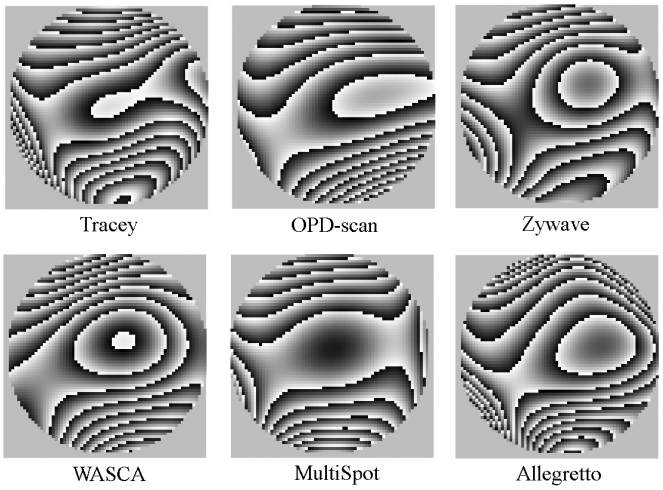

Figure III-3: Wavefront aberrations of eye ES OS (ref: -1.25; -1.00 @12°) measured with each aberrometer. The steps correspond with 2µm increments.

Table III-1: results ANOVA and T-test on the values of the given parameters

Significant differences (p < 0.05) are indicated by gray shade.

	ANOVA **	Newman-Keuls **	T - test														
			VFA					OPD-scan				Zywave			WASCA		MultiSpot
			O**	Z**	W***	M**	A**	Z*	W**	M*	A*	W**	M*	A*	M**	A**	A*
Sphere	.001	WAO//OZV//ZVM	.01	.91	.43	.86	.01	.27	.64	.58	.21	.07	.52	<.01	.06	.48	.05
Cyl	<.001	OZAW//ZAWM//V	.01	.01	<.01	.02	<.01	.04	.02	.15	.29	.24	.61	.53	.35	.39	.24
Axis	.151		.15	.30	.48	.22	.51	.23	.15	.50	.09	.12	.32	.04	.15	.24	.09
$Z_3 = Z_2^{-2}$	.305		.02	.01	.47	.36	.04	.09	.01	.50	.03	.13	.93	.08	.55	.27	.65
$Z_4 = Z_2^{0}$	.050		.60	.65	.06	.76	.04	.02	.33	.74	.05	.07	.17	<.01	.02	.76	.09
$Z_5 = Z_2^{+2}$	<.012	ZOAWM//V	.01	.01	.26	.05	.01	<.01	.12	.95	.77	.22	.13	.02	.08	.11	.84
$Z_6 = Z_3^{-3}$	.425		.46	.09	.91	.15	.19	.51	.46	.34	.70	.97	.53	.98	.78	.86	.54
$Z_7 = Z_3^{-1}$	.143		.08	.75	.01	.08	.18	.05	.92	.08	.02	.22	.33	.82	.69	.40	.16
$Z_8 = Z_3^{+1}$	.447		.64	.13	.40	.87	.36	.54	.19	.99	.85	.36	.64	.55	.07	.49	.90
$Z_9 = Z_3^{+3}$	.690		.90	.53	.60	.12	.70	.80	.89	.25	.98	.88	.08	.56	.36	.99	.05
$Z_{10} = Z_4^{-4}$	.391		.34	.50	.18	.70	.43	.06	.33	.28	.78	.31	.42	.15	.02	.26	.62
$Z_{11} = Z_4^{-2}$	.706		.97	.18	.87	.68	.56	.86	.96	.27	.63	.18	.36	.73	.58	.40	.32
$Z_{12} = Z_4^{0}$	.667		.67	.45	.46	.49	.43	.45	.48	.33	.41	.83	.17	.30	.59	.67	.68
$Z_{13} = Z_4^{+2}$	.141		.06	.25	.86	.37	.18	.09	.03	.05	.02	.32	.26	.39	.46	.44	.93
$Z_{14} = Z_4^{+4}$	.009	MOWZA//WZAV	.04	.39	.05	.01	.21	.11	.06	.29	.11	.50	.09	.71	.12	.44	.02
$Z_{15} = Z_5^{-5}$	.378		.30	.60	.03	.33	.41	.20	.30	.36	.55	.18	.05	.15	.98	.75	.96
$Z_{16} = Z_5^{-3}$	.002	V//MWOZA	.01	.01	.49	.11	.05	.28	.49	.06	.97	.27	.26	.23	.28	.34	.07
$Z_{17} = Z_5^{-1}$	.062		.03	.51	.02	.01	.07	.66	.41	.01	.39	.15	.09	.37	.30	.78	.29
$Z_{18} = Z_5^{+1}$	.877		.79	.84	.90	.21	.84	.69	.40	.17	.55	.79	.67	.28	.80	.40	.06
$Z_{19} = Z_5^{+3}$	.715		.80	.67	.96	.28	.99	.43	.61	.55	.84	.46	.05	.34	.03	.82	.19
$Z_{20} = Z_5^{+5}$	.168		.17	.16	.06	.05	.84	.01	.59	.04	.50	.03	.01	.48	.35	.39	.14
RMS_{tot}	<.001	MZO// OA// WA//AV	.01	<.01	<.01	<.01	.07	.99	.02	.58	.19	<.01	.54	.35	<.01	.99	.18
RMS_{HO}	.001	MO//OZWAV	.05	.09	<.01	.01	.16	.54	.67	<.01	.75	.93	.01	.72	.02	.92	.01
RMS_{rad} 2	<.001	ZMO//AW//V	.01	<.01	.02	<.01	.07	.95	.01	.88	.19	<.01	.83	.38	<.01	.90	.27
RMS_{rad} 3	.002	AMOZW// OZWV	.02	.17	<.01	<.01	.01	<.01	.02	<.01	<.01	.71	<.01	<.01	<.01	<.01	.43
RMS_{rad} 4	.012	WAOMZ//ZV	.07	.19	<.01	.02	.01	.06	.88	.58	.73	.18	.02	.05	.62	.95	.64
RMS_{rad} 5	.122		.84	.54	.09	.03	.76	.07	.12	.05	.60	.06	.01	.39	.46	.11	.11
RMS_{ang} 0	.005	MZOAW// OAWV	.09	.05	.34	.02	.58	.79	.03	.87	.23	.03	.69	.48	.01	.87	.31
RMS_{ang} 1	.018	MOWA// OWAZV	.05	.34	<.01	.01	.24	.04	.40	.02	.18	.36	.01	.17	.03	.69	.02
RMS_{ang} 2	.001	MZOAW//V	.01	.01	<.01	<.01	.01	.87	.13	.23	.79	.21	.30	.78	.15	.35	.20
RMS_{ang} 3	.050		.93	.06	.01	.08	.39	<.01	.18	<.01	.03	.25	.36	.45	.41	.91	.13
RMS_{ang} 4	<.001	O//WMZA//V	<.01	.02	<.01	.03	<.01	<.01	.01	<.01	<.01	.39	.24	.63	.69	.20	.41
RMS_{ang} 5	.029	O//WVMZA	<.01	.11	.59	.33	.12	<.01	.01	<.01	.04	<.01	.69	.19	.12	.04	.22
ZRMS 1	<.001	OMA//AZW// ZWV	<.01	.26	<.01	<.01	.01	.02	.03	.47	.02	.89	.01	.24	<.01	.09	.04
ZRMS 2	.010	MOZAW// OZAWV	.13	.14	.02	.01	.18	.17	.25	.61	.14	.28	.07	.98	.01	.65	.08
ZRMS 3	<.001	MZOWA//V	.01	<.01	<.01	<.01	.01	.31	.79	.19	.47	.61	.07	.65	.20	.74	.07
ZRMS 4	.038	MOZAW// OZAWV	.03	.06	.12	.01	.08	.90	.36	.72	.20	.49	.68	.52	.10	.70	.28
ZRMS 5	.012	MOZAW//AWV	.03	.05	.04	.01	.03	.70	.10	.97	.35	.25	.79	.59	.09	.89	.18
ZRMS 6	.050		.03	.06	.17	.03	.06	.63	.17	.54	.17	.11	.43	.72	.03	.46	.34
ZRMS 7	.001	MZOWA//AV	.01	<.01	<.01	.01	.21	.77	.34	.57	.10	.21	.49	.19	.30	.35	.09
ZRMS 8	.035	ZWMOA//AOV	.05	.01	.02	.10	.07	.32	.28	.83	.66	.89	.71	.58	.61	.35	.98
ZRMS 9	.029	MZOAW//AWV	.02	.04	<.01	.05	.07	.77	.44	.29	.73	.18	.51	.96	.32	.82	.50

* Standard group, 10 eyes, CSE -4.5D -> +4.25D; Confidence level: 95% ($p < 0.05$); statistical power $\beta = 0.72$

** Standard group, 7 eyes, CSE -2.50D -> +4.25D; Confidence level: 95% ($p < 0.05$); $\beta = 0.57$

*** Standard group, 12 eyes, CSE -2.50D -> +4.25D; Confidence level: 95% ($p < 0.05$); $\beta = 0.79$

Table III-2: results ANOVA and T-test on the variances of the given parameters
Significant differences ($p < 0.05$) are indicated by gray shade.

				T - test														
				VFA					OPD-scan				Zywave			WASCA		MultiSpot
	min → max	ANOVA **	Newman-Keuls **	O*	Z*	W**	M*	A*	Z*	W*	M*	A*	W*	M*	A*	M*	A*	A*
Sphere	.119→.227D	.345		.84	.22	.10	.65	.20	.15	.12	.58	.15	.98	.22	.54	.48	.79	.32
Cyl	.035→.142D	.007	WZVA// ZVAMO	.24	.31	.01	.09	.91	.06	.03	.93	.20	.01	.06	.33	.03	.11	.03
Axis	2.11→20.2°	.103		.10	.31	.04	.07	.39	.16	.07	.15	.11	.14	.57	.60	.02	.09	.24
$Z_3 = Z_2^{-2}$	.076→.213 µm	.028	WZAMV// ZAMVO	.60	.04	<.01	.77	.55	.11	.06	.53	.30	.54	<.01	.18	<.01	.14	.58
$Z_4 = Z_2^{0}$	.202→.447 µm	.287		.39	.36	.02	.57	.18	.74	.10	.71	.53	.26	.25	.78	.17	.31	.14
$Z_5 = Z_2^{+2}$	.076→.229 µm	.068		.44	.10	.01	.88	.64	.05	.01	.81	.49	.01	.37	.50	.13	.15	.53
$Z_6 = Z_3^{-3}$	.046→.232 µm	<.001	WZV//ZVA//O	<.01	.96	<.01	.20	.11	<.01	<.01	.03	.02	.04	.24	.17	.01	.02	.74
$Z_7 = Z_3^{-1}$	.053→.208 µm	.367		.69	.49	<.01	.24	.36	.54	.21	.45	.55	.01	.79	.96	.03	.02	.55
$Z_8 = Z_3^{+1}$	.075→.241 µm	.054		.17	.94	.01	.72	.76	.13	.03	.02	.11	.19	.66	.81	.10	.09	.51
$Z_9 = Z_3^{+3}$	.050→.262 µm	.002	WZMVA//O	.01	.29	.02	.35	.78	.01	<.01	.01	.18	.17	.88	.34	.04	.23	.43
$Z_{10} = Z_4^{-4}$	.002→.104 µm	<.001	OWZ//WVM//VMA	<.01	.48	<.01	.58	.08	.01	<.01	<.01	.01	.29	.37	.16	.08	.04	.18
$Z_{11} = Z_4^{-2}$	.045→.119 µm	.266		.11	.37	.04	.49	.45	.21	.15	.21	.59	.18	.61	.77	.27	.24	.56
$Z_{12} = Z_4^{0}$	.040→.139 µm	.353		.39	.60	.01	.75	.25	.67	.19	.42	.20	.22	.81	.34	.07	.58	.14
$Z_{13} = Z_4^{+2}$	.045→.168 µm	.002	WVMZA//O	.02	.66	.03	.81	.67	.04	.01	.08	.09	.04	.98	.79	.04	.01	.74
$Z_{14} = Z_4^{+4}$	.002→.135 µm	.038	OWVMZ// WVMZA	<.01	.63	.02	.78	.36	<.01	.01	.03	.07	.02	.98	.43	.14	.18	.46
$Z_{15} = Z_5^{-5}$	.002→.107 µm	.209		.03	.12	.38	.44	.28	<.01	.01	.01	.13	.66	.10	.49	.51	.48	.27
$Z_{16} = Z_5^{-3}$	.036→.087 µm	.050		.02	.14	.52	.42	.04	.28	.08	.05	.52	.82	.62	.41	.75	.07	.11
$Z_{17} = Z_5^{-1}$	.042→.108 µm	.528		.59	.28	.88	.12	.70	.97	.75	.38	.56	.29	.10	.18	.21	.44	.08
$Z_{18} = Z_5^{+1}$	.042→.137 µm	.186		.10	.19	.17	.52	.87	.61	.21	.04	.13	.43	.21	.36	.21	.58	.39
$Z_{19} = Z_5^{+3}$	.033→.155 µm	<.001	VMWZA//O	<.01	.03	.07	.47	.20	.01	.02	<.01	.09	.53	.09	.63	.19	.54	.34
$Z_{20} = Z_5^{+5}$	.002→.098 µm	<.001	O//VMZW// WA	.01	.30	.18	.17	.01	.01	.01	.01	<.01	.50	.83	.07	.37	.23	.01
RMS_{tot}	.138→.294 µm	.223		.35	.33	.01	.54	.28	.66	.07	.71	.89	.19	.33	.45	.10	.03	.69
RMS_{HO}	.072→.304 µm	.085		.09	.16	.01	.38	.70	.15	.05	.18	.10	.03	.69	.57	.01	.04	.64
RMS_{rad} 2	.146→.404 µm	.180		.25	.34	.01	.51	.23	.95	.11	.57	.95	.10	.45	.84	.08	.04	.45
RMS_{rad} 3	.081→.233 µm	.015	AWMZV// ZVO	.22	.77	.01	.29	.15	.15	.08	.09	.06	.05	.30	.02	.61	.82	.56
RMS_{rad} 4	.045→.150 µm	.417		.25	.40	.17	.20	.14	.53	.23	.48	.43	.25	.91	.86	.07	.03	.88
RMS_{rad} 5	.045→.163 µm	.068		.14	.10	.19	.83	.22	.62	.15	.08	.14	.28	.14	.27	.11	.73	.05
RMS_{ang} 0	.186→.441 µm	.245		.22	.35	.02	.49	.17	.83	.32	.49	.96	.16	.45	.72	.21	.23	.28
RMS_{ang} 1	.068→.195 µm	.163		.41	.87	.01	.63	.91	.41	.12	.34	.33	<.01	.44	.52	.07	.01	.53
RMS_{ang} 2	.078→.237 µm	.003	WZA//ZAV//AVOM	.36	.04	.01	.51	.48	<.01	.01	.90	.22	.03	.07	.20	.05	.12	.07
RMS_{ang} 3	.054→.211 µm	<.001	WZVAM//O	<.01	.43	.03	.44	.65	.01	<.01	.12	.02	.43	.18	.10	.08	.08	.67
RMS_{ang} 4	.002→.088 µm	.002	O//WZVMA	<.01	.39	.02	.89	.27	.02	<.01	.03	.01	.51	.60	.21	.31	.09	.26
RMS_{ang} 5	.001→.080 µm	.001	OV//VWMZ//MZA	.01	.24	.42	.19	.13	<.01	<.01	<.01	.02	.50	.84	.28	.41	.18	.19

* Standard group, 6 eyes, CSE -2.50D -> +4.25D; Confidence level: 95% ($p < 0.05$); statistical power $\beta = 0.49$
** Standard group, 11 eyes, CSE -2.50D -> +4.25D; Confidence level: 95% ($p < 0.05$); $\beta = 0.75$

The values in the ANOVA column represent the significance that can be attributed to the initial supposition that the values for that particular parameter measured by each aberrometer can be considered equal. If the supposition is rejected ($p < 0.05$), the Newman-Keuls analysis shows which aberrometer deviates from the others. This is presented in the following format: each aberrometer is represented by the first letter of its name and adjacent letters indicate a confirmation of the initial supposition between these devices. If however letters are separated by the double dash symbol ('//'), no significant relationship exists between them. E.g. O // VMZW // WA means that the measurements of the OPD-scan are significantly different from those of the other devices and that there is a full mutual confirmation between the VFA, the MultiSpot, the Zywave and the WASCA. The WASCA measurements also correspond with those of the Allegretto, but the latter does not correspond with any of the other five devices.

The large sets of paired T-tests are organized per aberrometer. In the first 5 columns the VFA is compared with the other devices. Next the results for the OPD-scan and respectively the Zywave, the WASCA, the MultiSpot and the Allegretto are shown in an analogue order. Again the supposition of equality is rejected at probabilities lower than 5%.
In the following an interpretation for the significant differences is given per parameter group.

III.4.1 **Refraction**

The ANOVA results in Table III-1 indicate that significant differences exist for the values of the sphere and cylinder given by each device. Newman-Keuls and the paired T-test show that the VFA gives slightly higher sphere values than the WASCA and the Allegretto (a difference of about 0.5D). For the cylinder the VFA is significantly higher than its fellow aberrometers (about 0.2D). For the axis values no significant differences are found.
Studying the refraction variances by ANOVA (Table III-2) it is seen that these are different for the cylinder, where the WASCA is shown to be significantly lower than the MultiSpot and the OPD-scan. This is confirmed by the T-tests.

III.4.2 **Zernike polynomials**

No significant differences were found between the aberrometers for nearly all of the Zernike coefficient values. The only exceptions are the primary astigmatism Z_2^{+2}, the primary tetrafoil Z_4^{+4}, the secondary trefoil Z_5^{-3} and the secondary coma Z_5^{-1}:

- Z_2^{+2}: the T-test gives significantly higher values for the VFA compared to OPD-scan, Zywave and the Allegretto, which corresponds with the slightly higher values of the astigmatism found in the previous paragraph. This is confirmed by ANOVA.
- Z_4^{+4}: the VFA is significantly higher than the MultiSpot and the OPD-scan (confirmed by both ANOVA and T-tests).
- Z_5^{-3}: the VFA gives lower values than the other aberrometers (confirmed by the T-test for OPD-scan and the Zywave).
- Z_5^{-1}: the VFA values are significantly lower than those of the OPD-scan, MultiSpot and WASCA (not confirmed by ANOVA).

A look at Table III-2 immediately shows that the correspondences found for the Zernike coefficients are no longer true for their variances. This is especially found in coefficients located at the side of the Zernike pyramid (Figure III-1), mainly due to two reasons. The first reason is that the variance of the OPD-scan is sometimes significantly higher than those of the other aberrometers (such as for Z_3^{-3}, Z_3^{+3}, Z_4^{+2} and Z_5^{+3}) and sometimes significantly lower (for Z_4^{-4}, Z_4^{+4} and Z_5^{+5}). This will be clarified further in the next paragraph when the RMS values are discussed. The second reason is that the variances of the WASCA are found to be relatively low. This is confirmed by ANOVA and the T-tests for Z_2^{+2}, Z_2^{-3}, Z_3^{+3}, Z_4^{-4} and Z_4^{+2}.

III.4.3 **RMS**

Using the Newman-Keuls test it is found that the RMS_{tot} values of both the VFA and the WASCA differ significantly from those of all the other devices except the Allegretto (confirmed by T-tests). For the higher order RMS_{HO} the MultiSpot gives significantly lower

values and the VFA tends to give slightly higher values. The variance of RMS_{HO} on the other hand has a lower value for the WASCA (T-tests, unconfirmed by ANOVA).
In the RMS of the radial Zernike orders more differences are found:

- $RMS_{rad\ 2}$: T-tests show exactly the same differences as RMS_{tot}. Since these Zernike terms usually have the largest values, this is not surprising.
- $RMS_{rad\ 3}$: nearly no significances at all using both statistical methods.
- $RMS_{rad\ 4}$: the VFA has significantly higher values than the Allegretto, MultiSpot and the WASCA, which is confirmed by ANOVA.
- $RMS_{rad\ 5}$: the MultiSpot has significantly lower values than the Zywave and the VFA, however this is not confirmed by ANOVA.

No significant differences were found in the variances of the radial orders, with the exception of $RMS_{rad\ 3}$ (significantly higher values for the OPD-scan according to ANOVA, but unconfirmed by T-tests). The RMS of the angular Zernike orders shows the following:

- $RMS_{ang\ 0}$: significant differences are found between the WASCA on the one side and the OPD-scan and Zywave on the other side. ANOVA however shows a significant difference between the VFA and the MultiSpot (confirmed by T-test).
- $RMS_{ang\ 1}$: lower values of the MultiSpot compared to all devices, which is confirmed by ANOVA for Zywave and VFA.
- $RMS_{ang\ 2}$: higher values for the VFA compared to all other aberrometers, confirmed by ANOVA.
- $RMS_{ang\ 3}$: higher values for the OPD-scan (T-tests), but unconfirmed by ANOVA.
- $RMS_{ang\ 4}$: the OPD-scan gives lower values than the other devices, while the VFA gives higher values. Both are confirmed by ANOVA.
- $RMS_{ang\ 5}$: the OPD-scan gives lower values than the other devices, which is confirmed by ANOVA. The WASCA also shows lower values.

The low values of both $RMS_{ang\ 4}$ and $RMS_{ang\ 5}$ for the OPD-scan indicate that the associated Zernike coefficients (Z_4^{-4}, Z_4^{+4}, Z_5^{-5} and Z_5^{+5}) may be underestimated, which is confirmed by the raw Zernike coefficient data. However as these coefficients may have positive and negative values (with an average of 0) this was not seen in the statistical comparison above. RMS on the other hand does not depend on the coefficient sign, making this kind of deviations detectable. Another confirmation is given by the significantly low variance values of the OPD-scan for $RMS_{ang\ 4}$ and $RMS_{ang\ 5}$ (using both methods). The variances of $RMS_{ang\ 3}$ do not correspond either, but here the value of the OPD-scan is higher than that of the others (ANOVA), while for the $RMS_{ang\ 2}$ variances the WASCA has significantly lower values (ANOVA and T-tests).
The comparison of the RMS in the 9 zones as defined in Figure III-2 shows that a distinction should be made between the results in the central 2mm zone and those in the other 8 zones: in the central zone a large number of significant differences are found, while in the rest only the VFA deviates from the other aberrometers. These results are confirmed by ANOVA.

III.4.4 **Interaction analysis between the eye and the aberrometers**

With the previous results in mind one may ask in how far they depend on our choice of subjects. To answer this question we calculated for each aberrometer and for each parameter the interquartile range and determined the number of parameters for which each eye was an

outlier*. These results were put in a table upon which a two-dimensional χ^2 test was performed to determine what interaction between an eye and an aberrometer was relevant. This way it was found that no interaction exists between the 7 eyes and the 6 aberrometers for the results in Table III-1 ($\chi^2(30) = 28{,}8$; $p = 0.52$).
For the parameter's variances from Table III-2 however two eyes showed a relevant interaction ($\chi^2(25) = 63{,}9$; $p < 0.001$):

- *Eye #4*: showed 15 outliers for the Allegretto, most of which in the higher quartile.
- *Eye #7*: showed 10 outliers for the OPD-scan, most of which in the higher quartile.

This could be an indication that some of the relevant differences or equalities in parameter variances found earlier for these two aberrometers are less reliable.

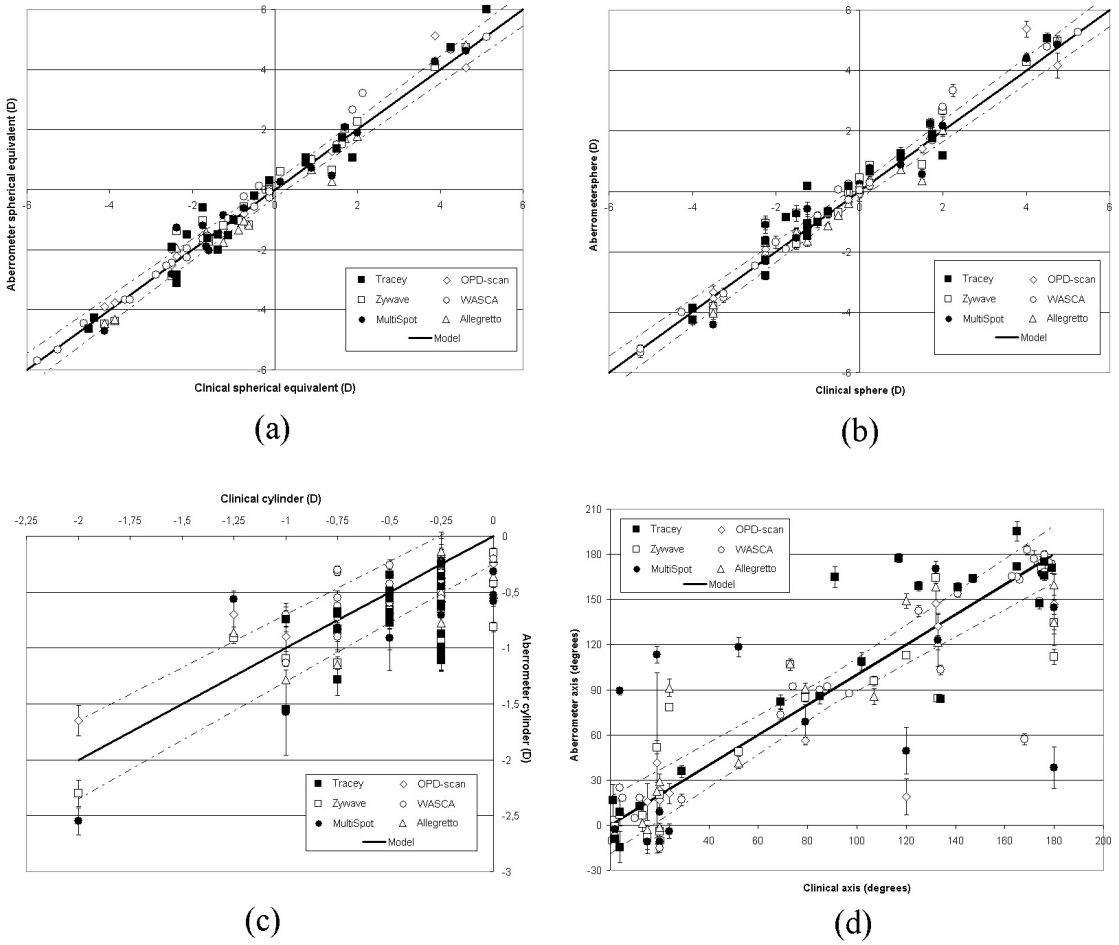

Figure III-4: change in aberrometer refraction in function of the clinical refraction measured by an autorefractometer. This can be compared with the model (bold line) and the given tolerances (dashed lines). (a) Aberrometer spherical equivalent versus clinical spherical equivalent; (b) aberrometer sphere versus clinical sphere; (c) aberrometer cylinder versus clinical cylinder; (d) aberrometer axis versus clinical axis.

* Calculated using SPSS and defined as: values in boxplots that have a distance of at least 1,5 times the box length from either the upper or lower box edge. For most cases this box length can be set equal to the interquartile range.

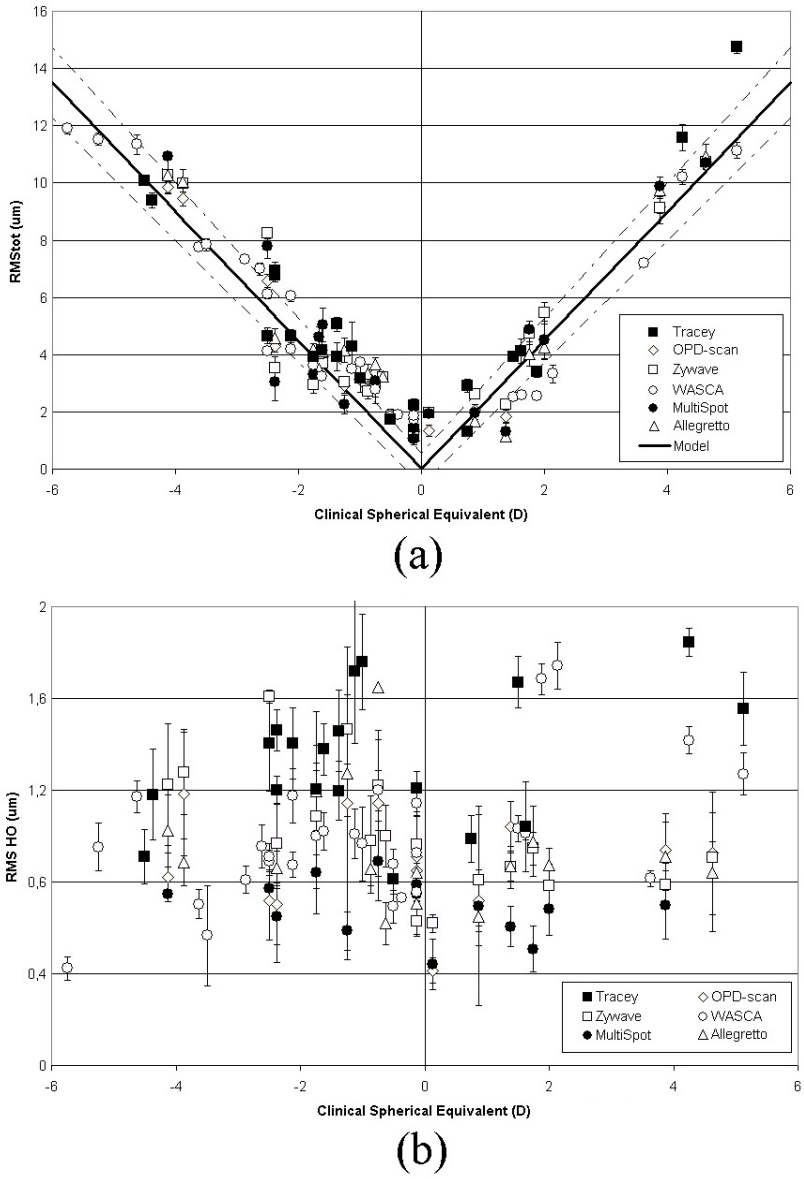

Figure III-5: Change in RMS values given by the aberrometers in function of the clinical spherical equivalent measured by an autorefractometer. This can be compared with the model (bold line) and the given tolerances (dashed lines). (a) Total RMS versus clinical spherical equivalent; (b) Higher order RMS versus clinical spherical equivalent.

III.4.5 **Indirect comparison using linear models**

The refractive calibration of the aberrometers can be checked by means of the curves given in Figure III-4. Here the refractive values given by the aberrometers are compared with those given by the autorefractometer.
For each of these parameters one would expect a straight line, as described by model (III-3). Figure III-4a shows the aberrometer spherical equivalent (ASE) versus the clinical spherical equivalent (CSE), together with a model of the ideal case and two dashed lines indicating the tolerances defined earlier. All aberrometers follow the model and most of their data points lay

Table III-3a: Slope of the curves in Figure III-4a (ASE vs. CSE)

Aberrometer	# eyes	a_{ref}	b_{ref}	R^2
VFA	21	1.0473	0.1026	0.9632
OPD-Scan	14	1.0099	0.1038	0.9783
Zywave	20	1.0337	0.0794	0.9688
WASCA	29	1.0365	0.0193	0.9892
MultiSpot	17	1.0076	0.0231	0.9605
Allegretto	18	1.0314	-0.1517	0.9763

Table III-3b: Slope of the curves in Figure III-4b
Aberrometer sphere vs. clinical sphere

Aberrometer	# eyes	a_{ref}	b_{ref}	R^2
VFA	21	1.0477	0.2203	0.9621
Zywave	20	1.0368	0.2051	0.9616
OPD-Scan	14	1.0253	0.1035	0.9718
WASCA	29	1.0362	0.1776	0.9879
MultiSpot	17	0.9939	0.2065	0.9400
Allegretto	18	0.9939	-0.1050	0.9733

Table III-3c: Slope of the curves in Figure III-4c
Aberrometer cylinder vs. clinical cylinder

Aberrometer	# eyes	a_{ref}	b_{ref}	R^2
VFA	21	**0.4366**	**-0.5405**	0.1220
OPD-Scan	14	**0.6644**	-0.1795	0.8417
Zywave	20	**0.8341**	**-0.3263**	0.7669
WASCA	29	**0.6392**	-0.1826	0.5409
MultiSpot	17	**0.9171**	**-0.3069**	0.6677
Allegretto	18	**0.7205**	**-0.2759**	0.5742

Table III-3d: Slope of the curves in Figure III-4d
Aberrometer axis vs. clinical axis

Aberrometer	# eyes	a_{ref}	b_{ref}	R^2
VFA	21	0.9993	7.6887	0.8568
OPD-Scan	14	**0.8475**	0.7841	0.8051
Zywave	20	**0.7841**	**11.499**	0.7734
WASCA	29	**0.9330**	2.4917	0.8611
MultiSpot	17	**0.5820**	**25.919**	0.3679
Allegretto	18	**0.9016**	7.9266	0.8070

Table III-4: Slopes of the curves describing RMS_{tot} vs. CSE

Aberrometer	# eyes	a_{tot} *(µm/D)*	b_{tot} *(µm/D)*	R^2
VFA	21	**2.5306**	-0.0269	0.9679
OPD-Scan	14	2.2884	**-2.241**	0.9671
Zywave	18	**2.4321**	-0.1647	0.9624
WASCA	29	2.1341	**-0.6848**	0.9793
MultiSpot	17	**2.4233**	-0.2016	0.9529
Allegretto	16	**2.3996**	**-0.6060**	0.9773

within the tolerated area (dashed lines). If a linear fit is applied to this data the parameters in Table III-3a are obtained. Both the a_{ref} and the b_{ref} parameters for each device remain within the given tolerances.
A similar graph can be made of the aberrometer sphere versus the clinical sphere (Figure III-4b) and again a linear fit is given (Table III-3). Both the graph and the fit parameters are similar to those of the spherical equivalent and follow the proposed model.
However when the aberrometer cylinder and the clinical cylinder are compared, larger differences are seen (Figure III-4c, Table III-3c). A rough linear relationship can still be distinguished, but the associated R^2 values, that give a measure of the correspondence between both data sets, are rather low. This is due to the fact that the values for this parameter are closely packed around the origin with only a limited number of higher values, so no conclusion can be drawn from this data.

In the aberrometer axis data a large spreading is found (Figure III-4d, Table III-3d), although the linear relationship is clearly present for each device except for the MultiSpot. In order to obtain a good linear fit 180° was added to some of the data points near the end of the graph with a maximum of 210°. Analogously 180° was subtracted from some of the data points near the beginning of the graph with a minimum of -30°.

The total RMS in function of the clinical spherical equivalent is shown in Figure III-5a. Again each aberrometer seems to follow the model quite well. The majority of the data points remain within the tolerance range, except in the central region. This deviation is mainly due to higher order aberrations that were not included in the model. Most of the linear fit parameters (Table III-4) however do not seem to remain within the tolerance range, probably due to the same reason.
As could be expected, the graph of the higher order RMS in function of the clinical spherical equivalent only shows random fluctuations (figure 5b). As a result no model can be defined.

III.5 *Discussion and conclusion*

From this extensive list of results several trends can be derived:

- The underestimation of the Zernike terms Z_4^{-4}, Z_4^{+4} and Z_5^{+5} by the OPD-scan and the corresponding overestimation of Z_3^{-3}, Z_3^{+3}, Z_4^{+2} and Z_5^{+3}. This can perhaps be due to the nature of the retinoscopy technique which measures the refraction along meridians in the pupil area, rather than on a fixed grid, as is the case for the other devices. Even though these underestimated Zernike terms have relatively little influence on the visual performance, the detection of four- and fivefold symmetries in the wavefront may be problematic for the OPD-scan.
- The VFA showed differences in a number of radial and angular RMS values and many of the ZRMS, where higher values were measured. This corresponds to the slightly higher astigmatism values found in Table III-1.
- The WASCA device is found to have relatively low variances on many of the studied parameters, an indication that measurements done with this device are highly repeatable.
- Both the astigmatism and the astigmatism axis values (Figure III-4c and d) for each device did not correspond very well with the clinical values, which shows that both values may change drastically with a minor alteration in wavefront.
- The underestimation of RMS_{HO} by the MultiSpot, which is probably due to a pupil resizing procedure included in its software and the presence of a bimorph mirror in its setup.

- The strong differences in the 3rd order radial RMS (corresponding to the primary coma and trefoil terms) for nearly all machines are striking and need to be looked at in more detail.
- The considerable differences found in the central 2mm zone of Figure III-2, which is the zone where usually the Purkinje reflections of the source occur. Although most aberrometers have probably incorporated means to avoid any negative influence by these reflections, it might be just these countermeasures, which are different for each device, that cause the differences in this area.

These results can also be compared with some technical features of the aberrometers, as discussed in the first part of the study:

- *Number of samples*: In reference [104] a relationship was suggested between the amplitude of the variance and the number of samples taken by the aberrometer. This could not be confirmed in this study as the variance amplitudes for each aberrometer seemed to vary strongly for each parameter. Although this could be an explanation for the relatively low variances of the WASCA (1452 samples).
- *Alignment procedure*: no significant relationship was seen between the aberrometers' alignment procedure and the variance. The Allegretto and the MultiSpot, which had highly elaborate alignment procedures, did not have significantly lower variances. However this should not lead to the conclusion that a good aberrometer alignment is of lesser importance.
- *Automatic averaging*: there does not seem to be any relationship between variance amplitudes and the automatic averaging over a number of measurements. The three devices that include some form of automatic averaging (OPD-scan, Zywave and Allegretto) did not have significantly lower variances compared to the other machines. Most companies will advise it is better to do several measurements and compare these in some way. We agree with this advice, especially when applied to customized refractive surgery where the treatments relies on the measurements obtained.

When considering the results of this paper it is important to realize that since human eyes are not standardized, as would be the case e.g. in an optical eye model, a measurement by one aberrometer deviating from its fellow aberrometers is not necessarily 'wrong'. Further comparisons need to be done at a later stage using more objective models to determine the true deviations. Whether these deviations are clinically significant remains to be studied.

The results in this study only represent the outcomes as provided by the aberrometers as they were made available to us during the test period. These are under constant technological evolution in order to reach more accurate and reproducible results.

Acknowledgements

We would like to thank the companies Nidek, Bausch & Lomb, Zeiss, Tracey and WaveLight and their Belgian delegates for temporarily providing their aberrometers for testing. Also Mr. Michael Mrochen is kindly thanked for the lending of the MultiSpot aberrometer as well as Andrey Larichev and Nikita Irochnikov for providing the necessary technical assistance.
This project was supported by an ESCRS research grant (2002) and a grant (2002) of the FRO (Belgian Fund for Research in Ophthalmology).

PART II

Laminographic phase reconstruction of the ocular anterior segment

The search for the source of ocular wavefront aberrations is usually limited to the curvatures and thicknesses of the individual refractive media and the irregularities of the anterior corneal surface. Even though it is important from the geometric optics point of view, this approach is not sensitive enough to understand the origins of higher order aberrations. In the following a laminographic method is proposed as a first step to investigate these origins. Also a number of suggestions are given for further improvement of the method.

Chapter IV Three-dimensional reconstruction of objects using laminography

IV.1 *Historical introduction to laminography*

Short after Röntgen first reported his discovery of X-rays[109], a large number of imaging applications were found for the newfound radiation. Especially the medical sciences benefited from its strongly penetrating power. However due to the way X-ray images were recorded only areal attenuation images could be obtained, with darker patches where the radiation was absorbed and lighter patches where the radiation could pass through the object unharmed. All spatial information about the exact 3D location inside the object of a specific part of the image was lost.
A first solution to this problem was given by Pohl who invented the 'Omniskop' (see Figure IV-1), a device in which a patient could be positioned in many directions, allowing the capture of X-ray images under different angles. This gave the doctor a better understanding of the internal structures of the patients' body.
Later Pohl[110], and simultaneously with him Ziedses des Plantes[111], described a method to reconstruct one single plane (the 'focal layer') inside an object with a minimization of the influence of other layers above and below this specific layer. This method, later dubbed 'Laminography', consists of a photo plate mechanically linked with a moveable source. By moving the combination of source and photo plate into different directions (see Figure IV-2), in such a way that parts of the focal layer are always projected on the same spot of the photo plate with the same orientation and magnification, a clear image of the focal layer can be obtained. Parts of other layers, above and below the focal layer, will move during the motion of the source and their influence is spread out over a larger area, resulting in background intensity.
This technique is based on the parallax of the different source positions and will be mathematically explained in the following. Please note that in this chapter only the application of laminography for attenuations with X-ray images is used. Phase laminography, which requires refractieve corrections, will be explained in Chapter V.

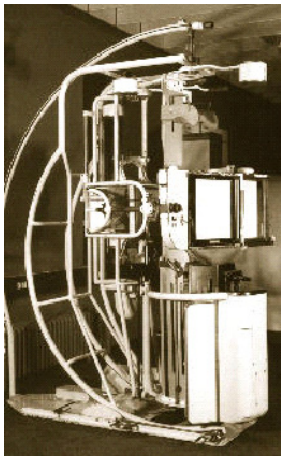

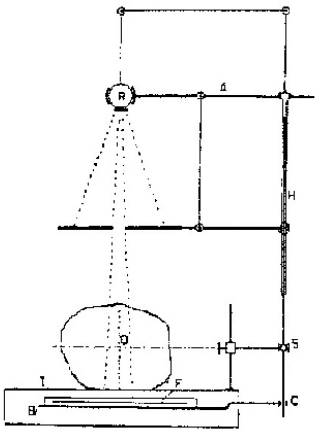

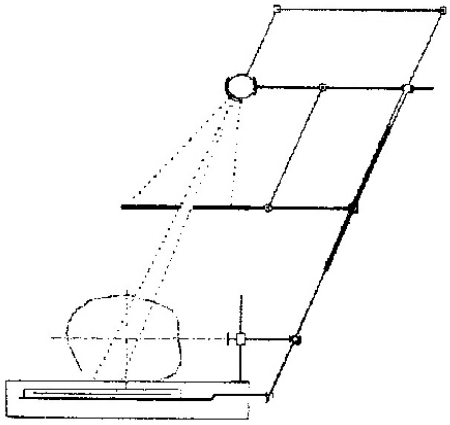

Figure IV-1(left): "Omniskop" by Ernst Pohl (1922) (*image taken from* [112])
Figure IV-2(right): "Planigraph" by Bernhard Ziedses des Plantes (1932)[111]

IV.2 *Mathematical introduction*

IV.2.1 Definitions

First a number of definitions need to be given for the proper mathematical description of laminography. Suppose we have a focal plane, located within a three-dimensional object and a point source located at a height h from this focal plane, which in turn is at a distance d from the projection plane (Figure IV-3). We name the perpendicular projection of the source in the focal plane origin o, with Cartesian axes (x,y). In the projection of the focal plane a similar system of axes (X,Y) can be defined in source projection O. Any point $p(x,y)$ in the focal plane at a distance r from origin o will be projected on a point $P(X,Y)$ in the projection plane at a distance R from the origin O. The relationship between R and r is given by:

$$R = (h+d)\tan\alpha = \frac{h+d}{h} r := M \cdot r \qquad \text{(IV- 1)}$$

Here $M = (h+d)/h$ is the magnification factor of the projection which depends on the relative distances between the source, the focal plane and the projection plane. In the same way follows that:

$$\begin{cases} X = M \cdot x \\ Y = M \cdot y \end{cases} \qquad \text{(IV- 2)}$$

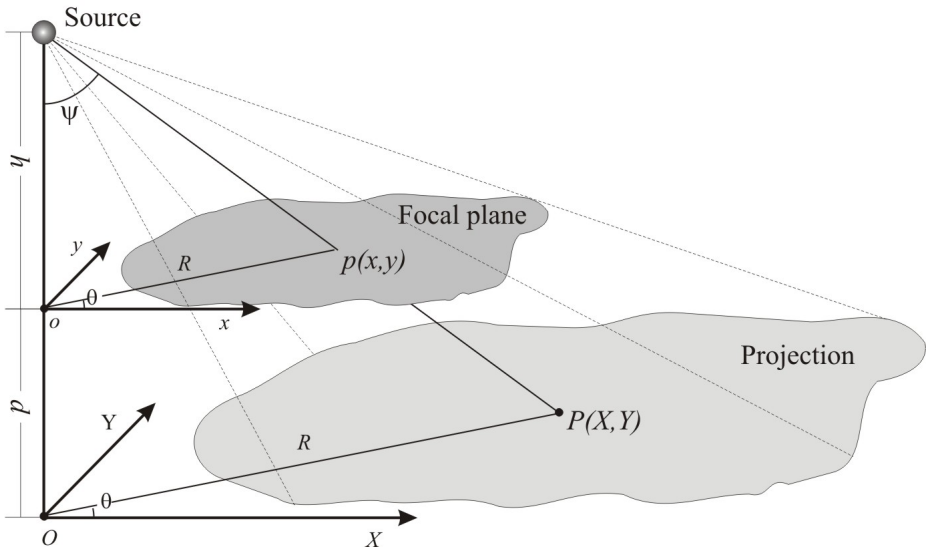

Figure IV-3: definitions of the different axes in the projections

IV.2.2 Reconstruction methods

Suppose a series of N source positions S_i ($i = 1:N$) along a circle with an angular step $\Delta\theta = 2\pi/N$ relative to the rotation axis (Figure IV-4). An angle of incidence ψ can be defined between the rotation axis and the line connecting a source position S_i and the cross- section point of the rotation axis and the focal plane.

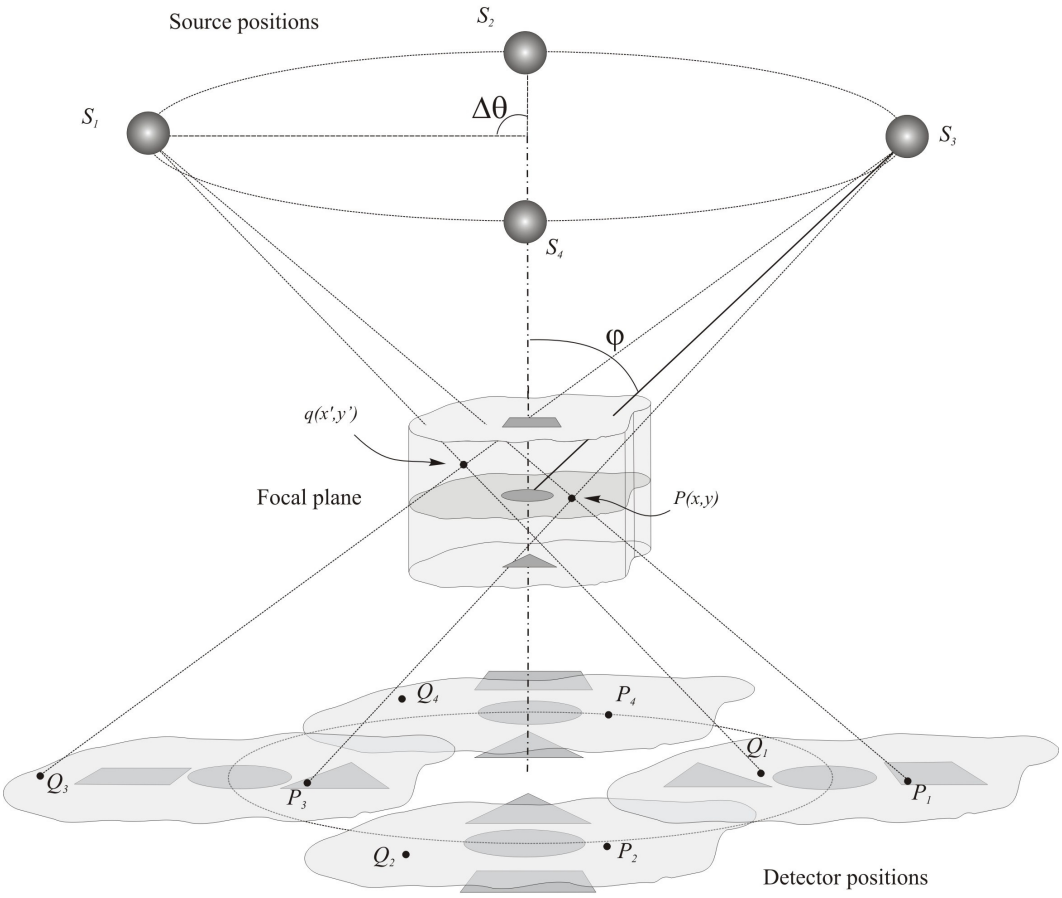

Figure IV-4: Projections of the object at several source positions

For each pixel $P(X_i,Y_i)$ of each projection in Figure IV-4 an imaginary line can be drawn back to the source S_i, representing the optical path that the ray ending up in (X_i,Y_i) has followed. Each of these rays crosses a number of voxels (volume elements) of the object that attenuate its intensity. When these rays end up on the detector, only the total sum of these attenuations is measured; all data regarding the attenuation of the individual voxels along the ray's path is lost.
In the following we will discuss three different methods that can be used to reconstruct the attenuations of the focal plane or even the whole object:

- Tomosynthesis
- Spiral scan
- Reversed ray tracing
- Other techniques

Each of these methods will be discussed in the following.

a) Tomosynthesis

In tomosynthesis the reconstruction occurs by superimposing all N projections. If this is done in such a way that the points (X_i,Y_i) of each projection coincide, with (X_i,Y_i) the corresponding projection points of (x,y) in the focal plane, the image of the focal plane is

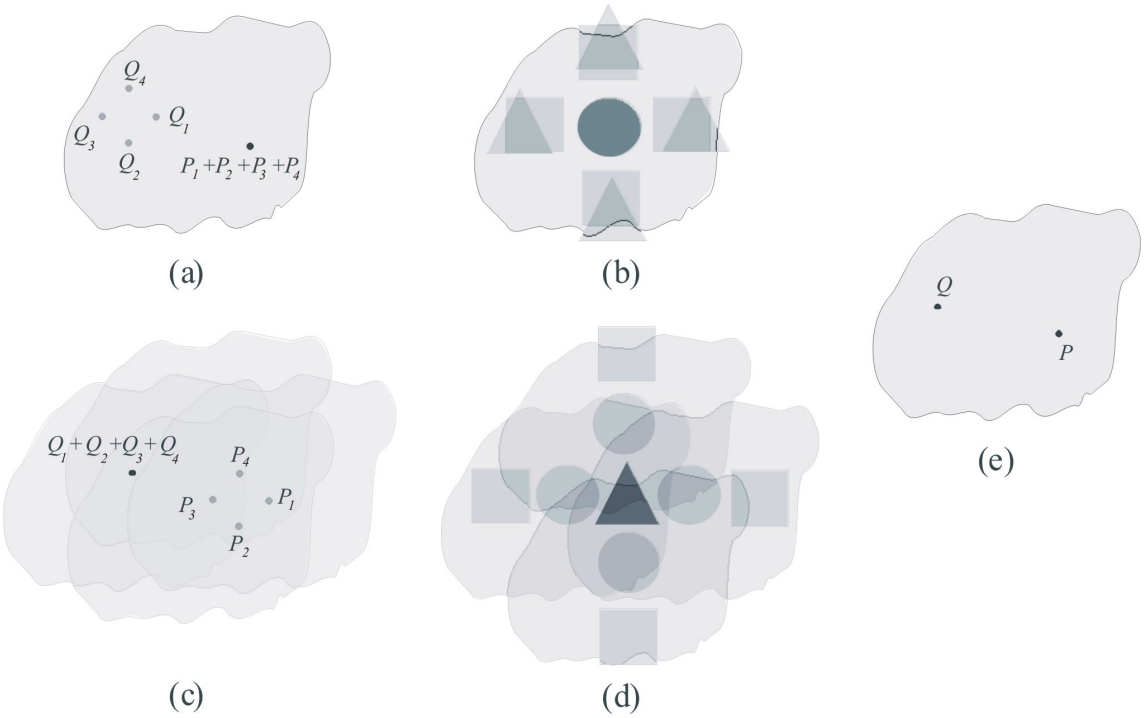

Figure IV-5: reconstruction of the focal plane of Figure IV-4 by tomosynthesis. (a) Reconstruction of point p(x,y) in the focal plane, (b) Reconstruction of the circle located in the focal plane, (c) Reconstruction of point q(x',y') above the focal plane, (d) Reconstruction of the triangle located below the focal plane. These reconstructions can be compared with a standard radiogram recorded along the rotation axis (e).

reinforced, while information from other layers above and below the focal layer will be averaged away into background intensity. This is shown in Figure IV-5(a) in which the point $p(x,y)$ in the focal plane is reconstructed by the superposition of four projections. In this reconstruction the information of point $q(x',y')$, which is located above the focal layer, is spread over four separate points. Each of these four points $Q_i(X'_i,Y'_i)$ will have a significantly lower contrast than the reconstruction $P(X,Y)=\sum_{k=1}^{N} P_k(X_k,Y_k)$ of $p(x,y)$.

This difference is better visible in Figure IV-5(b) where the circle in the focal plane has been clearly reconstructed and the other two shapes are randomly superimposed. Increasing the number of projections will considerably improve this difference.

The main advantage of tomosynthesis is that it requires little calculations, resulting in short calculation times. Moreover, it is easy to expand this technique to reconstruct planes near the focal plane by shifting the projections until points $Q_i(X'_i,Y'_i)$ coincide. This is shown in Figure IV-5(c) and (d) for point $Q(X',Y')=\sum_{k=1}^{N} Q_k(X'_k,Y'_k)$ and the triangle. However the distance between the reconstructed and the focal plane can not be too large as the reconstruction quality severely decreases for larger distances.

The size of the shift required for the reconstruction of the plane containing $q(x',y')$ can be found by a similar formula as that of the vertical resolution δn (see IV.2.3b).

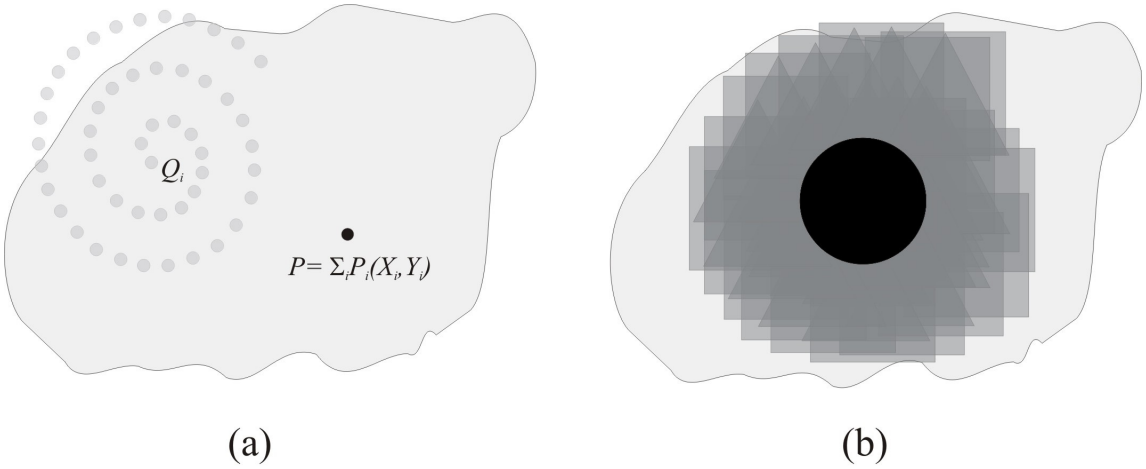

Figure IV-6: Reconstruction of the focal plane of Figure IV-4 using spiral scan: (a) reconstruction of point p(x,y) in the focal plane, (b) reconstruction of the circle in the focal plane.

b) Spiral scan

This reconstruction method is closely related to tomosynthesis and refers to a modified way of recording the N projections. Here the track of the source positions describes a spiral or a series of concentric circles, varying both the rotation angle $\Delta\theta$ and the angle of incidence ψ. This results in a better spread of the information coming from layers different than the focal plane, improving the results of the averaging (see Figure IV-6).
The advantages and limitations of this technique are similar to those of tomosynthesis.

c) Reversed ray tracing

In this method the imaginary rays going from the source S_i to pixels (X_i, Y_i) of each projection are used. Each voxel that comes into contact with a ray is added the intensity value of the associated pixel (X_i, Y_i) of this ray. If this is done for all rays, a reconstruction of a whole segment of the object can be made, rather than of a single plane. A segment is said to be well reconstructed if rays from all projections pass through it.
This technique can be used both for sources moving on a circle (as in Figure IV-3) or on a spiral as discussed above. It is also possible to apply a numerical band-pass filter on the projections prior to the reconstruction, which in some cases improves the quality of the reconstruction. The main disadvantage of this method is the high number of calculations required for the reconstruction, resulting in long calculation times.
Usually this method is called 'backprojection', but in order not to confused this technique with 'filtered backprojection', a non-related reconstruction method, we dubbed it here 'reversed ray tracing'.

d) Other techniques

Several other techniques known from tomography can also be used for this kind of reconstructions. The most practical method for this situation is filtered backprojection adapted with a fan beam algorithm[113], which requires a very large number of projections perpendicular to the line connecting the source and the center of the focal plane at various angles of incidence. These projections are different from the horizontal projections used earlier.

This technique is not capable of giving the focal plane directly as tomosynthesis did, but instead a whole segment of the object can be reconstructed at once after a lengthy calculation. Since filtered backprojection cannot be used in the case of a refractive object[114] (such as the eye), this method will not be elaborated further in this work.

Another reconstruction technique is algebraic reconstruction (ART)[115], which supposes that each voxel of the object is an unknown in a system of equations set out by the each pixel of the projections. This system of equations is extremely large and requires some algebraic ingenuity to make it more manageable. Even in this manageable form, the necessary calculations are still extensive.
Although this technique might be interesting for our application (better contrast sensitivity, less smearing), we lacked the time to implement it.

IV.2.3 **Resolution**

For the calculation of the ideal horizontal and vertical resolution we need the angles and distances defined in Figure IV-7. In the following no scattering or refraction is included, which will both reduce the actual resolution to a certain extend.

a) Horizontal resolution

Suppose δm is the distance between neighboring points p and q_1 located in the focal plane n and call Δ the distance between the projections of these points on a plane at a vertical distance d_n from the focal plane. As follows from equation (IV -1) the relationship between δm and Δ is given by:

$$\Delta = \frac{h_n + d_n}{h_n}\delta m \Rightarrow \delta m = \frac{h_n}{h_n + d_n}\Delta \qquad \text{(IV-3)}$$

The values for δm can be found by choosing Δ equal to the pixel size of the camera capturing the projection, which is the highest possible resolution in case the size of the system's PSF equals one pixel. Decreasing the pixel size Δ and increasing the distance d_n will result in higher horizontal resolutions (i.e. smaller values for δm).

b) Vertical resolution

Here the distance δn between two neighboring points p and q_2 located in different planes n and $n+1$ is calculated. In Figure IV-7 it can be seen that:

$$\begin{cases} r_n = d_n tg\psi_n = d_n r / h_n \\ r_{n+1} = d_{n+1} tg\psi_{n+1} = d_{n+1} r / h_{n+1} \end{cases} \qquad \text{(IV-4)}$$

We also know that:

$$\Delta = r_n - r_{n+1} = r\left(\frac{d_n}{h_n} - \frac{d_{n+1}}{h_{n+1}}\right) = r\frac{d_n h_{n+1} - d_{n+1} h_n}{h_n h_{n+1}} \qquad \text{(IV-5)}$$

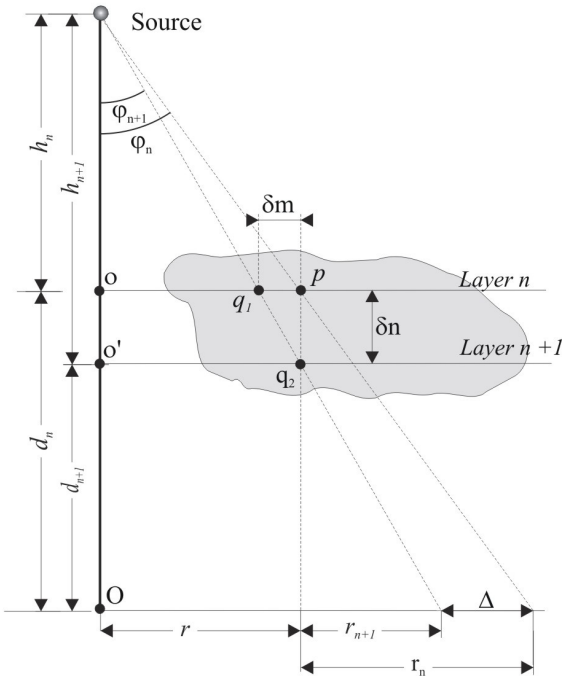

Figure IV-7: Definition of the distances needed to calculate the horizontal resolution δm and the vertical resolution δn.

Since $d_{n+1} = d_n - \delta n$ and $h_{n+1} = h_n + \delta n$, this can be rewritten as:

$$\Delta = r\frac{d_n(h_n+\delta n)-(d_n-\delta n)h_n}{h_n(h_n+\delta n)} \tag{IV-6}$$

So that δn can be calculated:

$$\delta n = \frac{h_n^2\Delta}{rd_n+(r-\Delta)h_n} = \frac{h_n\Delta}{tg\psi_n(d_n+h_n)-\Delta} \tag{IV-7}$$

Again Δ is chosen to be the pixel size of the camera. Formula (IV-7) shows that the vertical resolution increases (i.e. δn decreases) when the pixel size Δ decreases or when the angle of incidence ψ_n increases. The ideal case would be $\psi_n = \pi/2$, where the tangent becomes maximal.

Formula (IV-6) can also be used to calculate the shift Δ needed for the superposition of the projections in tomosynthesis if a plane other than the focal plane is being reconstructed. Here δn is the distance between the focal plane and the reconstructed plane.

IV.3 *Laminographic reconstruction*

Based on the theory given above the properties of these techniques will be studied by means of a number of reconstruction of virtual objects.

IV.3.1 **Reconstruction of a general object**

Suppose an object as shown in Figure IV-8, composed out of a cross with an open center that has been rotated 90° over 64 planes. Suppose also that the object has an attenuation μ that is uniformly distributed over the object and that it is suspended in a vacuum (so there is no attenuation from the medium around the object). From the top view (top center) only the central hole can be clearly seen, together with a blurred cross shape. This is the view one would obtain with a standard radiogram along the rotation axis[*].
For the laminographic reconstructions we choose plane 30, near the center of the object, to be the focal plane of the projections. We take the angle of incidence $\psi = 40^o$ and the number of projections at 36.
When both tomosynthesis and reversed ray tracing are applied to this setup, the reconstructed cross-sections shown in the bottom of Figure IV-8 are obtained. The reconstructions are similar in quality and clearly show the inner part of the cross. Note the circular artifact in the center of the cross.
In Figure IV-9 a hollow cylinder is added to the object and reconstructed with the same parameters as before. The top view now only shows the cylinder clearly. The reconstructions of this object are similar to the ones in Figure IV-8, but the central artifact has almost disappeared.

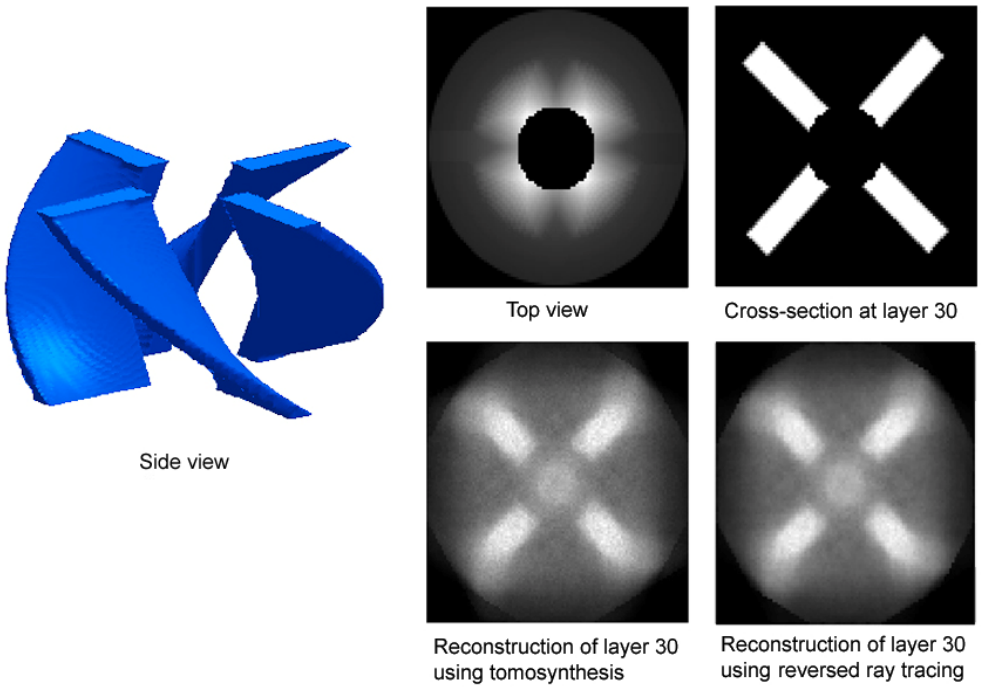

Figure IV-8: reconstruction of a virtual object composed of a twisted cross. A cross-section of the object at half height (layer 30) can be made by tomosynthesis and reversed ray tracing with N = 36 and ψ = 40° (bottom center and right).

[*] For better viewing these images were inverted, meaning that bright areas represent high attenuations. This will be done further throughout the rest of this chapter.

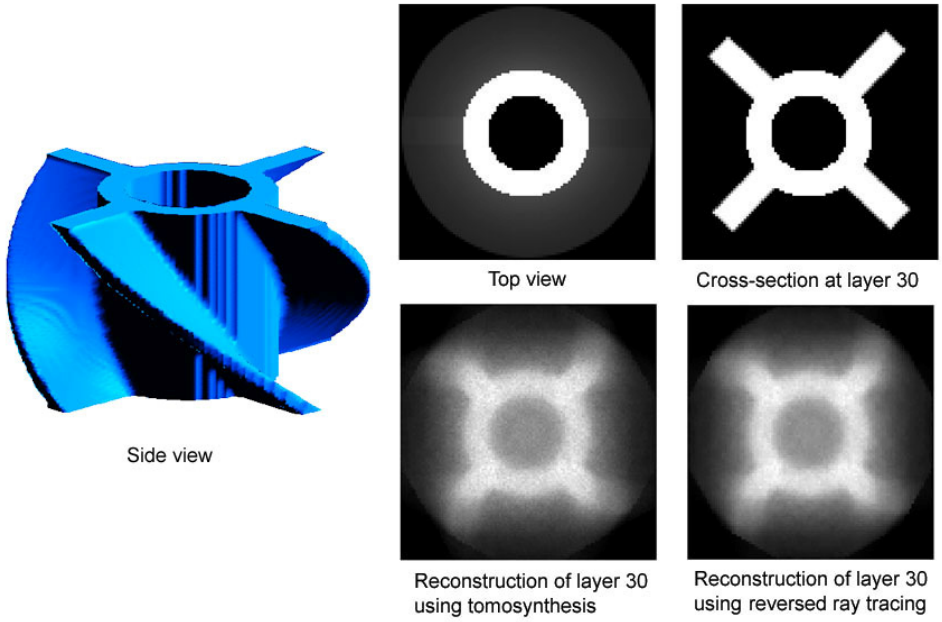

Figure IV-9: reconstruction of a virtual object composed of a twisted cross and a hollow cylinder. A cross-section of the object at half height (layer 30) can be made by tomosynthesis and reversed ray tracing with N = 36 and ψ = 40° (bottom center and right).

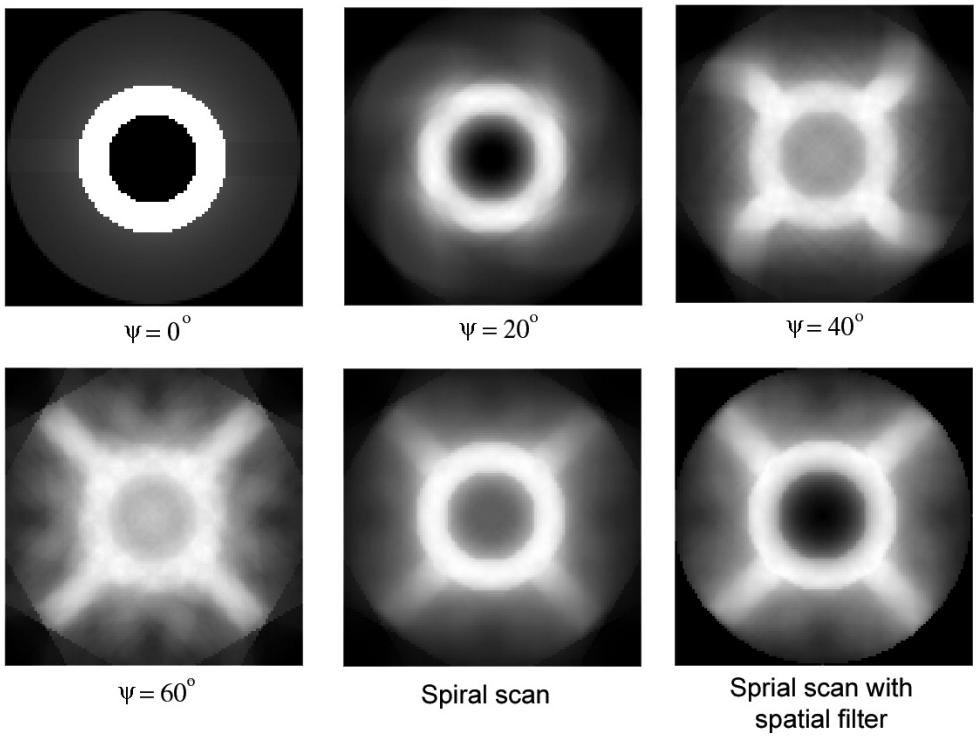

Figure IV-10: the contrast change in the reconstructions of the Figure IV-9 object at different angles of incidence ψ (tomosynthesis, N = 12 projections).

IV.3.2 **Dependency on the angle of incidence**

In formula (IV-7) it was found that there is a direct dependency of the vertical resolution δn and the angle of incidence ψ. This will be illustrated in the following paragraph using the object shown in Figure IV-9.

At lower ψ -values (e.g. 20^o), only the central part of the reconstruction corresponds with the cross-section of the object (shown for tomosynthesis in Figure IV-10). The outer part is severely blurred due to the larger displacements between layers for this part of the object. But with an increasing ψ a clear improvement of the reconstruction quality is seen here, resulting from the increasing vertical resolution. At $\psi = 90^o$ (as is the case in tomography) the best possible resolution is achieved, although in practice this is not always possible for each application.
The reconstructions of $\psi = 0^o, 20^o, 40^o$ and 60^o can also be used to calculate the spiral scan reconstruction of the object, which shows less artifacts then the $\psi = 60^o$ case. The contrast of this image can slightly be enhanced by means of a spatial ramp filter that amplifies the outer parts:

$$I'(\rho) = \rho \cdot I(\rho) \tag{IV-8}$$

where ρ is the radial distance to the rotation axis.

IV.3.3 **Reconstruction of layers other than the focal layer**

Although laminography is intended for the reconstruction of the focal layer alone, it is also possible to reconstruct other layers. In tomosynthesis, as shown before, this is done by shifting the projections before the superposition. However it can easily be understood that in the projections parts of the object close to the source will be enlarged more than parts further away from the source (but closer to the camera). Therefore simply shifting the projections will only work well for a limited region above and below the focal layer with more or less the same magnification. It is possible to compensate for this effect by enlarging or shrinking specific parts of the projections using a model of the object, but this is a troublesome process.

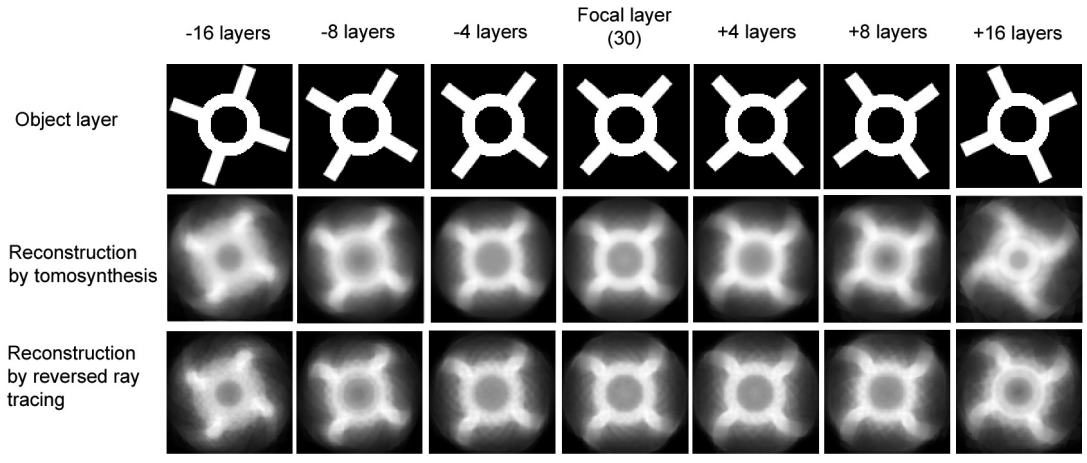

Figure IV-11: reconstruction of layers near the focal layer using tomosynthesis and reversed ray tracing ($\psi = 40°$, $N = 18$).

Reversed ray tracing on the other hand reconstructs the whole object by its nature and is therefore more suitable for the reconstruction of other planes.
This is demonstrated in Figure IV-11 where the reconstructions by both techniques are shown for a range of layers. The focal layer is well reconstructed in both cases, as well as a region of ±4 layers around the focal layer. But at larger distances (±8 layers and further) the images clearly starts to blur, especially the central cylinder. Also a difference is visible between the two techniques for layers close to the projection plane (+16 layers): while reversed ray tracing still provides a decent reconstruction, tomosynthesis shows a severely distorted picture and the central cylinder has decreased in diameter. However in all images for both techniques the orientation of the twisted cross is still correctly represented.

IV.3.4 **Contrast sensitivity**

One other parameter that can be investigated is the contrast sensitivity of the reconstruction, which is a measure for the smallest contrast differences within the object's attenuation distribution that can still be reconstructed by means of reversed ray tracing.
Again we use the object of Figure IV-9, but this time the object, with an uniformly distributed attenuation μ, is immersed in a medium with an attenuation of $\alpha \cdot \mu$ ($0 \leq \alpha \leq 1$). Up till now α was always assumed to be equal to 0.
In the following α is given values ranging from 0.9 up till 0.995, resulting in the reconstructions shown in Figure IV-12. It is seen that for lower values of α (i.e. values up till $\alpha = 0.95$) the reconstruction still strongly resembles the previous ones as in Figure IV-9. However with decreasing attenuation contrast, the object becomes more and more unrecognizable. At an α -value of 0.99 the reconstruction of the cross' arms and the cylinder seem to form a square; however the round central hole is still clearly visible. Finally for $\alpha = 0.995$ this feature also fades, resulting in a solid square.
It is important to note that contrast sensitivity depends on the sensitivity of the camera used to register the projections. The results shown in Figure IV-12 are calculated using 8-bit projections. If this number were increased to 10 or 16 bits the contrast for the given α -values would be much better and the fading of the object would take place at α-values much closer to 1.

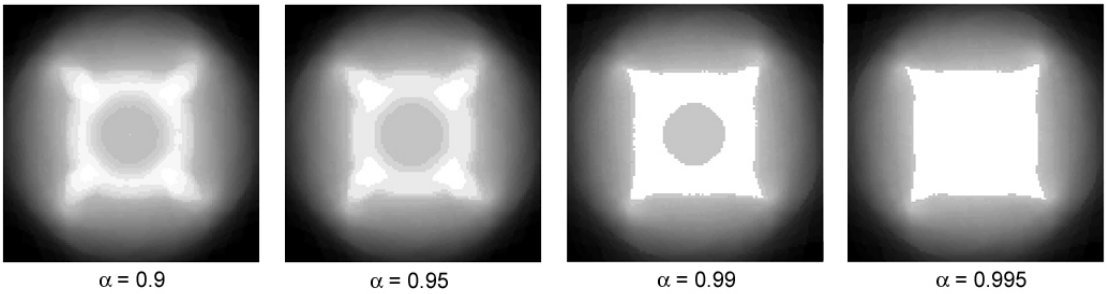

Figure IV-12: reversed ray tracing reconstruction of the object in Figure IV-9 in case of objects with limited contrast ($\psi = 40°$, $N = 18$).

IV.3.5**Smearing (wash-out)**

By far the biggest problem in laminographic reconstruction is smearing or wash-out. This is the effect that object regions with large attenuations not only affect the corresponding parts of

the reconstruction, but also other regions in the path of the rays connecting the attenuating region and its projection. A similar effect results from a region with a low attenuation.
Smearing can also be understood using Figure IV-4. Suppose point $p(x,y)$ has a strong attenuation, then the corresponding projection point $P(X,Y) = \Sigma_i\ p_i$ (with p_i all the object points on the ray connecting the source and P, which by consequence goes through p) will have a higher total attenuation value as well. When the reconstruction of the object is made by either reversed ray tracing or tomosynthesis using projection $P(X,Y)$, not only point $p(x,y)$ in the reconstruction will have a high attenuation, but also all the points p_i. This results in a 'shadow' of the strongly attenuating region in each source direction θ. If several of the shadows coincide, they add up to a clearly visible area in the reconstruction.
Figure IV-13 illustrates this using a disc shaped object floating in empty space. Even though in reality the regions above and below the disc have no attenuation, the reconstruction gives them a strong signal (bottom right). A vertical slice through the reconstructed object (bottom left) shows a more dramatic picture in which the disc has been distorted to a diamond shape. Note that the bottom side of the diamond is longer then the top side as a result of the spreading of the beam coming from the source.
To illustrate the smearing of regions with low attenuations we inverted the above object and reconstructed it as well (Figure IV-14). Here the same remarks apply as in Figure IV-13. In this case two new artifacts appear: a dark region at the edge of the object and two white outward fans at the side of the diamond.

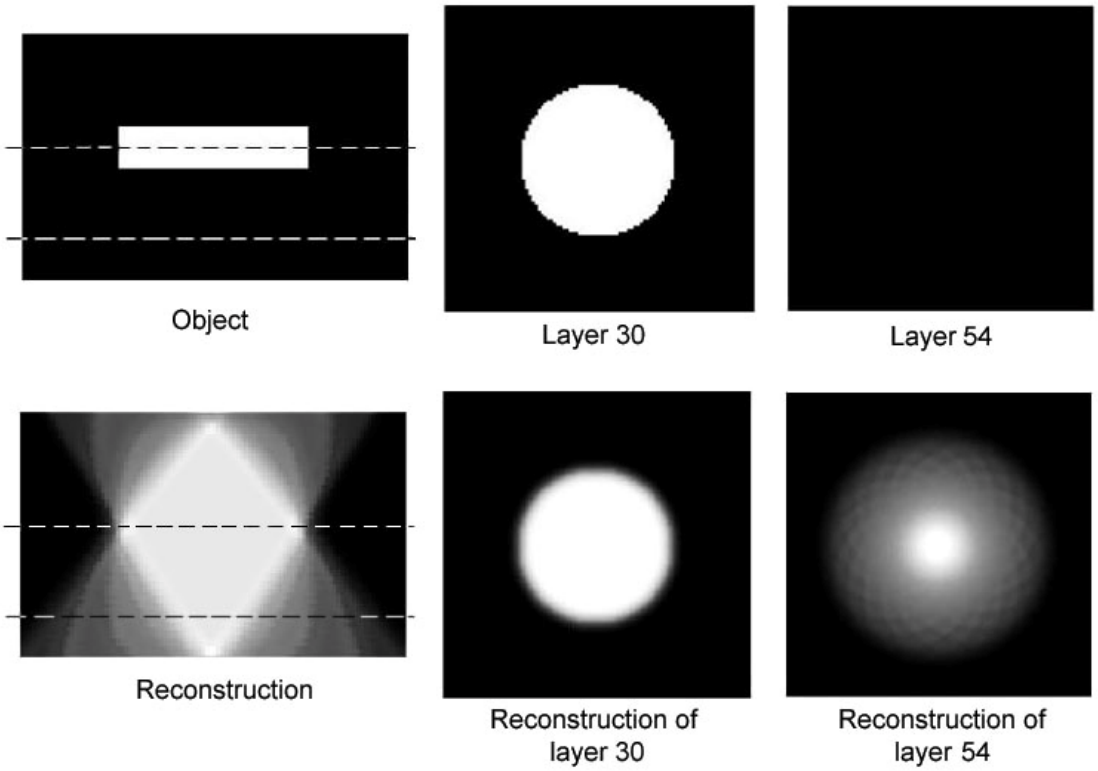

Figure IV-13: reconstructions of an object with high contrast, in the form of a disc in an empty space. Layers with a strong signal (center) are usually well reconstructed. Layers with little or no signal (right) can in the reconstruction show a strong signal due to wash-out. (Reversed ray tracing, focal layer: 30, $\psi = 40°$, $N = 18$).

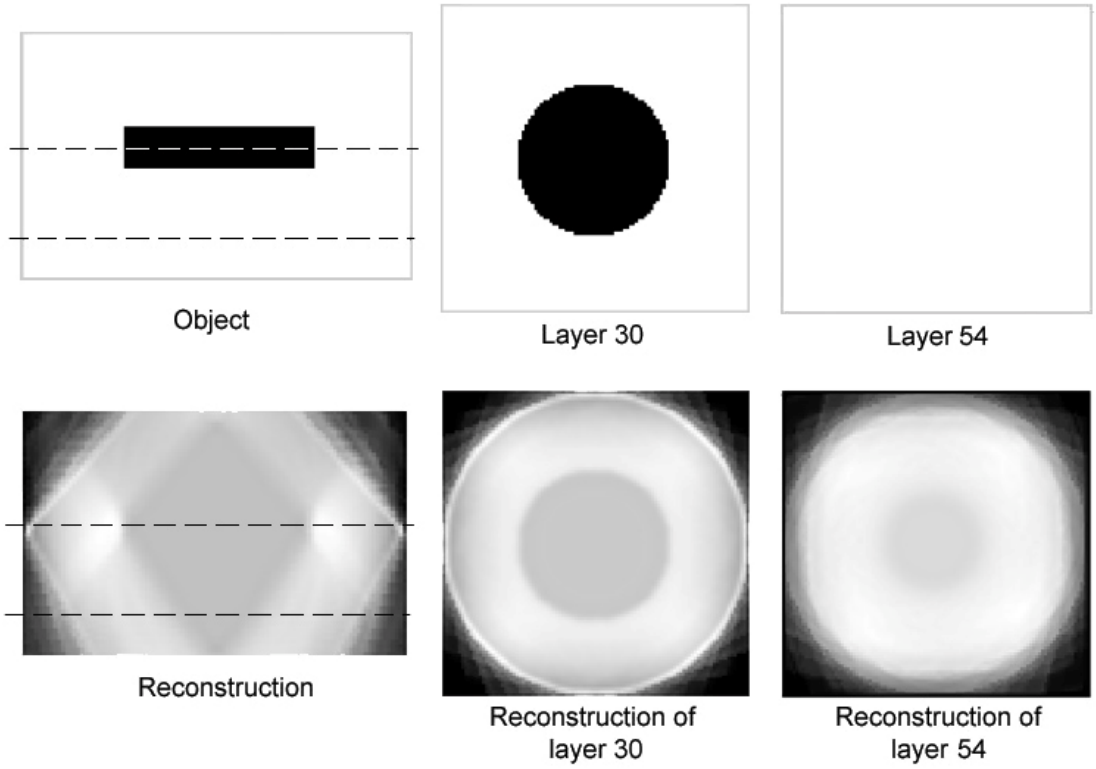

Figure IV-14: inverted version of the object shown in Figure IV-13 (same parameters).

From both figures it can be seen that smearing decreases with increasing angles of incidence ψ, and is therefore a direct result of the limited angle problem[113]. At the ideal value of $\psi = 90°$ the smearing is reduced to minimum and the reconstruction will closely resemble the object[*].

IV.4 *Conclusion*

The previous results lead to the conclusion that laminography can provide a decent reconstruction of a single focal layer inside an object, either by tomosynthesis or by reversed ray tracing, under specific circumstances:

- The attenuation should not have rapid changes along the rotation axis in the vicinity of the focal plane to avoid the blurring shown in Figure IV-10.
- Strong contrasts, either near of far away from the focal plane, should be avoided as shown in Figure IV-13 and Figure IV-14.

However both of these effects can be reduced by increasing the angle of incidence ψ.

[*] The projections at $\psi = 90°$ will look like the vertical cross-section given in the top right of Figure IV-13. The horizontal reconstruction will be a polygon with $2N$ sides. Increasing the number of projection will give a better approximation of the round disc. Note that in this specific case it is also possible to reconstruct the object perfectly with only two projections: the top view and one side view.

Chapter V Laminography applied to the human eye

In the previous we discussed attenuation laminography for X-rays. Hereby we ignored any refraction that the beams passing through the object might undergo. This approximation works well for highly energetic radiation, which for most applications is hardly influenced by this effect. But for light near the visual spectrum (wavelengths of 390-780 *nm*) it becomes very prominent and needs to be taken into account. A number of procedures needed to correct for the refraction are described in this chapter.
When applied to the eye laminography can provide information on the sources of aberration, such as their location and relative influence, and provide insight into the distribution of refractive index within the eye. This could lead to an in-vivo method to determine the gradual changes in refractive index distribution within the crystalline lens, which has been studied extensively in vitro [116, 117, 118, 119, 120] but is to date still not well understood.
In this chapter a proof of principle approach is given to use laminography in a refractive system, more specifically in the human eye. Note that only phase projections are considered in the following.

V.1 *Aberration laminography*

A light ray entering the eye is refracted four times before it reaches the retina. As each refraction changes the direction of the ray (see Figure V-1) the ray tracing going from the projection towards the secondary point source on the retina no longer encloses a 'tilted cone' as was the case in the non-refractive case (Figure IV-4). Instead it forms a more complex volume which may be estimated by means of ray tracing and an eye model. The reversed ray tracing technique can easily be modified to include these refractive corrections.
The tomosynthesis technique on the other hand does not require any changes, since by default an aberrometry recording is focused on the pupil. Because of this, and because all light coming from the retina has to pass through the pupil opening, the pupil can be considered as the focal plane of reconstruction. As before, a simple superposition of the projections can provide a reconstruction of the pupil plane.

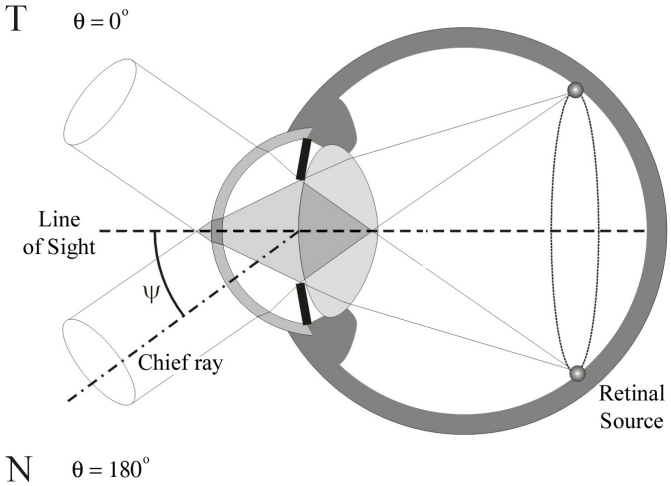

Figure V-1: refraction of the projections in the right eye.

For both techniques the angle of incidence ψ is defined between the optical axis and the chief ray, the line connecting the center of the projection and the pupil center. Angle θ indicates the orientation of the projection, with $\theta = 0^o$ the horizontal hemi-meridian in the nasal direction and progressing in the counter-clockwise direction.

V.2 *Refractive correction*

In the following paragraph the two-dimensional case is discussed first, in which the rays remain within a plane containing the optical axis ('skew rays'). Later this is expanded to the three-dimensional case ('meridional rays'). In both cases the refractive corrections in the reversed ray tracing technique are done by means of the Navarro wide angle schematic eye (see I.2.2b).

V.2.1 **Two-dimensional ray tracing**

Suppose a two-dimensional optical system as shown in Figure V-2 consisting of two optical interfaces *m* and *m+1*. A light ray originating from the source *S*, located on interface *m* and with an angle α_m with the optical axis can now be traced through the system. The aim is to determine the Point of Incidence (POI) on the $(m+1)^{th}$ interface and the refracted angle α_{m+1} so the full path of the ray is known.
First define the coordinates (see Figure V-2):

$$\begin{cases} S & = (x_m, \Delta z_m) \\ POI & = (x_{m+1}, z_m + \Delta z_{m+1}) \\ COC & = (0, z_m + r_{m+1}) \end{cases} \tag{V-1}$$

with Δz_{m+1} the aspherical curvature of the $(m+1)^{th}$ optical interface and r_{m+1} its radius of curvature originating from the Center of Curvature (COC). A ray leaving source *S* under an angle α_m will then intersect the $(m+1)^{th}$ interface in POI, which is found by solving the following system:

$$\begin{cases} x_{m+1} = x_m + (z_m + \Delta z_{m+1} - \Delta z_m)\tan\alpha_m \\ \Delta z_{m+1} = \dfrac{c_{m+1}x_{m+1}^2}{1 + \sqrt{1 - (K_{m+1}+1)c_{m+1}^2 x_{m+1}^2}} \end{cases} \tag{V-2}$$

The solution of (V-2) for Δz_{m+1} is:

$$\Delta z_{m+1} = \frac{A - \sqrt{A^2 - c_{m+1}B(x_m + (z_m - \Delta z_m)\tan\alpha_m)}}{B} \tag{V-3}$$

with:

$$\begin{cases} A = 1 - c_m(x_m \tan\alpha_m + (z_m - \Delta z_m)\tan\alpha_m) \\ B = c_{m+1}(1 + K_{m+1} + \tan^2\alpha_m) \end{cases} \tag{V-4}$$

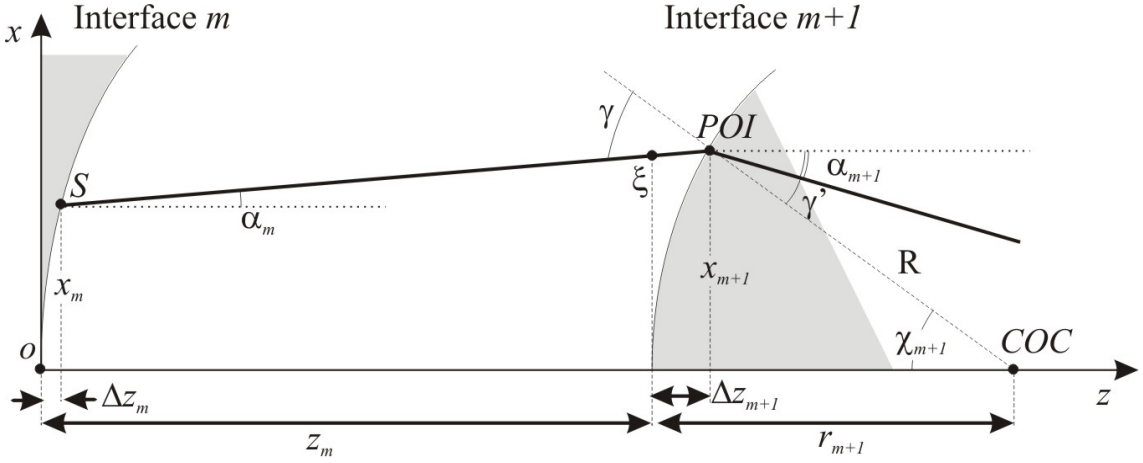

Figure V-2: Diagram of the two-dimensional ray tracing through an optical system.

Once POI is determined by means of (V-2) and (V-3) the refraction of the ray on the $(m+1)^{th}$ refractive surface can be calculated using Snell's Law:

$$n_{m+1} \sin \gamma' = n_m \sin \gamma \tag{V-5}$$

where the angles γ and γ' are determined with respect to the normal vector on the refractive interface in POI. In this point the local radius of curvature R_{m+1} is:

$$R_{m+1} = \sqrt{x_{m+1}^2 + \left(r_{m+1} - \Delta z_{m+1}\right)^2} \tag{V-6}$$

The angle χ_{m+1} between the optical axis and the normal vector in POI is given by:

$$\chi_{m+1} = \arcsin\left(\frac{x_{m+1}}{R}\right) \tag{V-7}$$

From Snell's Law (V-5) and the identities $\chi_{m+1} = \gamma' + \alpha_{m+1} = \gamma - \alpha_m$ (convex surface, $r_{m+1} > 0$) and $\chi_{m+1} = \gamma' - \alpha_{m+1} = \gamma + \alpha_m$ (concave surface, $r_{m+1} < 0$) follows:

$$\begin{cases} r_{m+1} > 0 : \alpha_{m+1} = \chi_{m+1} - \arcsin\left(\dfrac{n_m}{n_{m+1}} \sin\left(\alpha_m + \chi_{m+1}\right)\right) \\ r_{m+1} < 0 : \alpha_{m+1} = -\chi_{m+1} + \arcsin\left(\dfrac{n_m}{n_{m+1}} \sin\left(\alpha_m - \chi_{m+1}\right)\right) \end{cases} \tag{V-8}$$

This should be repeated for each optical interface in the system until a screen is reached. Figure V-3 shows this for a Navarro eye model and a source at infinity. Note the outer rays that focus slightly in front of the retina due to the model's spherical aberrations.
The two-dimensional ray tracing calculation described here can only be used in situations in which both the rays and the optical axis remain within one single plane. This is for example the case for on-axis sources in the absence of non-rotationally symmetric wavefront aberrations.

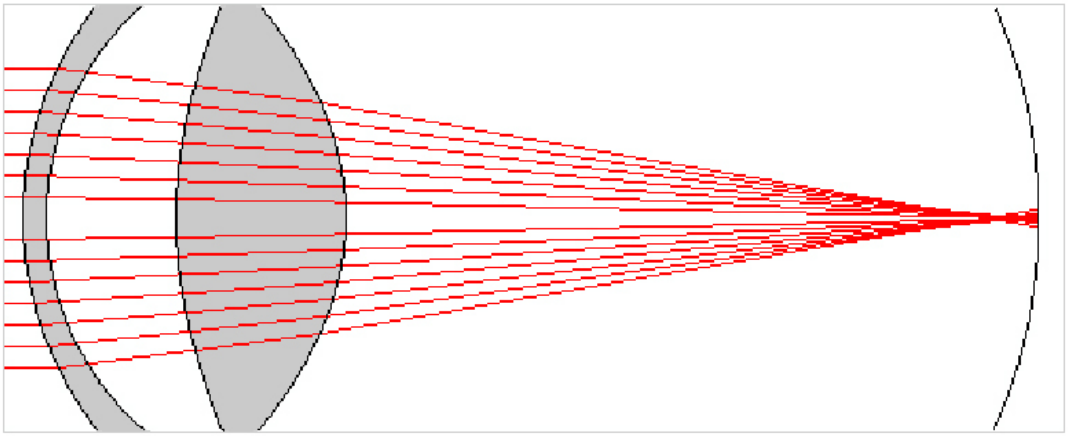

Figure V-3: results of the two-dimensional ray tracing applied to a Navarro model.

V.2.2 **Three-dimensional ray tracing**

When the rays do not remain within one single plane throughout the optical system, which is the case in most applications, the incident ray is determined by the source point S and two angles α_m and β_m shown in Figure V-4. Again the objective is to find the POI at interface $m+1$ and the angles α_{m+1} and β_{m+1} in order to define the refracted ray.

As before the following points need to be defined:

$$\begin{cases} S & = (x_m, y_m, \Delta z_m) \\ POI & = (x_{m+1}, y_{m+1}, z_m + \Delta z_{m+1}) \\ COC & = (0,0, z_m + r_{m+1}) \end{cases} \tag{V-9}$$

Here the system to solve is given by:

$$\begin{cases} x_{m+1} = x_m + (z_m + \Delta z_{m+1} - \Delta z_m)\tan\alpha_m \\ y_{m+1} = y_m + (z_m + \Delta z_{m+1} - \Delta z_m)\cos^{-1}\alpha_m \tan\beta_m \\ \rho = \sqrt{x_{m+1}^2 + y_{m+1}^2} \\ \Delta z_{m+1} = \dfrac{c_{m+1}\rho_{m+1}^2}{1 + \sqrt{1 - (K_{m+1}+1)c_{m+1}^2\rho_{m+1}^2}} \end{cases} \tag{V-10}$$

and the solution is:

$$\Delta z_{m+1} = \frac{C - \sqrt{C^2 - c_{m+1}D\left(\left(x_m + (z_m - \Delta z_m)\tan\alpha_m\right)^2 + \left(y_m + (z_m - \Delta z_m)\cos^{-1}\alpha_m \tan\beta_m\right)^2\right)}}{D} \tag{V-11}$$

with:

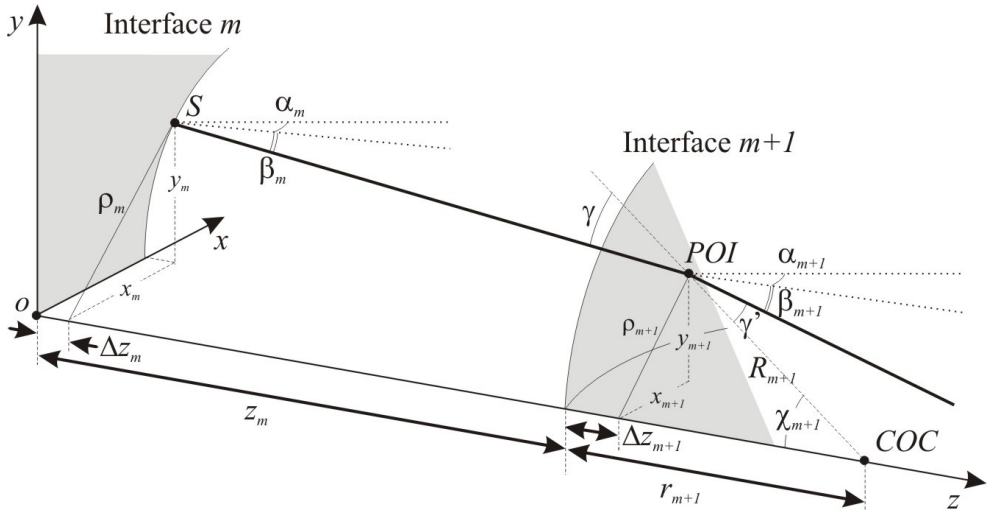

Figure V-4: Diagram of the three-dimensional ray tracing through an optical system.

$$\begin{cases} C = 1 - c_m\left(x_m \tan\alpha_m + y_m \cos^{-1}\alpha_m \tan\beta_m + \left(z_m - \Delta z_m\right)\left(\tan^2\alpha_m + \cos^{-2}\alpha_m \tan^2\beta_m\right)\right) \\ D = c_{m+1}\left(1 + K_{m+1} + \tan^2\alpha_m + \cos^{-2}\alpha_m \tan^2\beta_m\right) \end{cases} \tag{V-12}$$

Note that taking $\beta_m = 0$ results in the two-dimensional case given in formulas (V-3) and (V-4). Following the same reasoning as in the two-dimensional case we find for the local radius of curvature in the POI:

$$R_{m+1} = \sqrt{\rho_{m+1}^2 + \left(r_{m+1} - \Delta z_{m+1}\right)^2} \tag{V-13}$$

and again (V-7) is used to find χ_{m+1}.

Next we need to make the assumption that *COC* is located on the optical axis (i.e. only rotationally symmetric aberrations are considered). In this case we can define a number of lines:

$$\begin{cases} D_1 = \overline{S - POI} = \sqrt{\left(x_{m+1} - x_m\right)^2 + \left(y_{m+1} - y_m\right)^2 + \left(z_m + \Delta z_{m+1} - \Delta z_m\right)^2} \\ D_2 = \overline{S - COC} = \sqrt{x_m^2 + y_m^2 + \left(z_m + r_{m+1} - \Delta z_m\right)^2} \\ R_{m+1} = \overline{COC - POI} = \sqrt{x_{m+1}^2 + y_{m+1}^2 + \left(r_{m+1} - \Delta z_{m+1}\right)^2} = \sqrt{\rho_{m+1}^2 + \left(r_{m+1} - \Delta z_{m+1}\right)^2} \end{cases} \tag{V-14}$$

These lines form the sides of a triangle with top angle π-γ (convex surface) or γ (concave surface), so by means of the cosine rule we find:

$$\begin{cases} \mathrm{r}_{m+1} > 0: \quad D_2^2 = D_1^2 + R_{m+1}^2 - 2D_1R_{m+1}\cos\left(\pi - \gamma\right) \Rightarrow \gamma = \arccos\left(-\dfrac{D_2^2 - D_1^2 - R_{m+1}^2}{2D_1R_{m+1}}\right) \\ \mathrm{r}_{m+1} < 0: \quad D_2^2 = D_1^2 + R_{m+1}^2 - 2D_1R_{m+1}\cos\gamma \qquad \Rightarrow \gamma = \arccos\left(\dfrac{D_2^2 - D_1^2 - R_{m+1}^2}{2D_1R_{m+1}}\right) \end{cases} \tag{V-15}$$

Then from Snell's Law (V-5) we find:

$$\gamma' = \arcsin\left(\frac{n_m}{n_{m+1}}\sin\gamma\right) \tag{V-16}$$

which is valid for refraction at both convex and concave surfaces. However for the calculation of the angles α_{m+1} and β_{m+1} a distinction needs to be made between these two cases.

a) Convex surfaces ($r_{m+1} > 0$)

The description of refraction at a convex interface (Figure V-5a) can be considerably simplified by defining a new base (ξ,η) within the plane containing the points *S*, *POI* and *COC*. Suppose a new base (*x', y', z'*) in *POI*, parallel to the axes (*x,y,z*), then we find in this base:

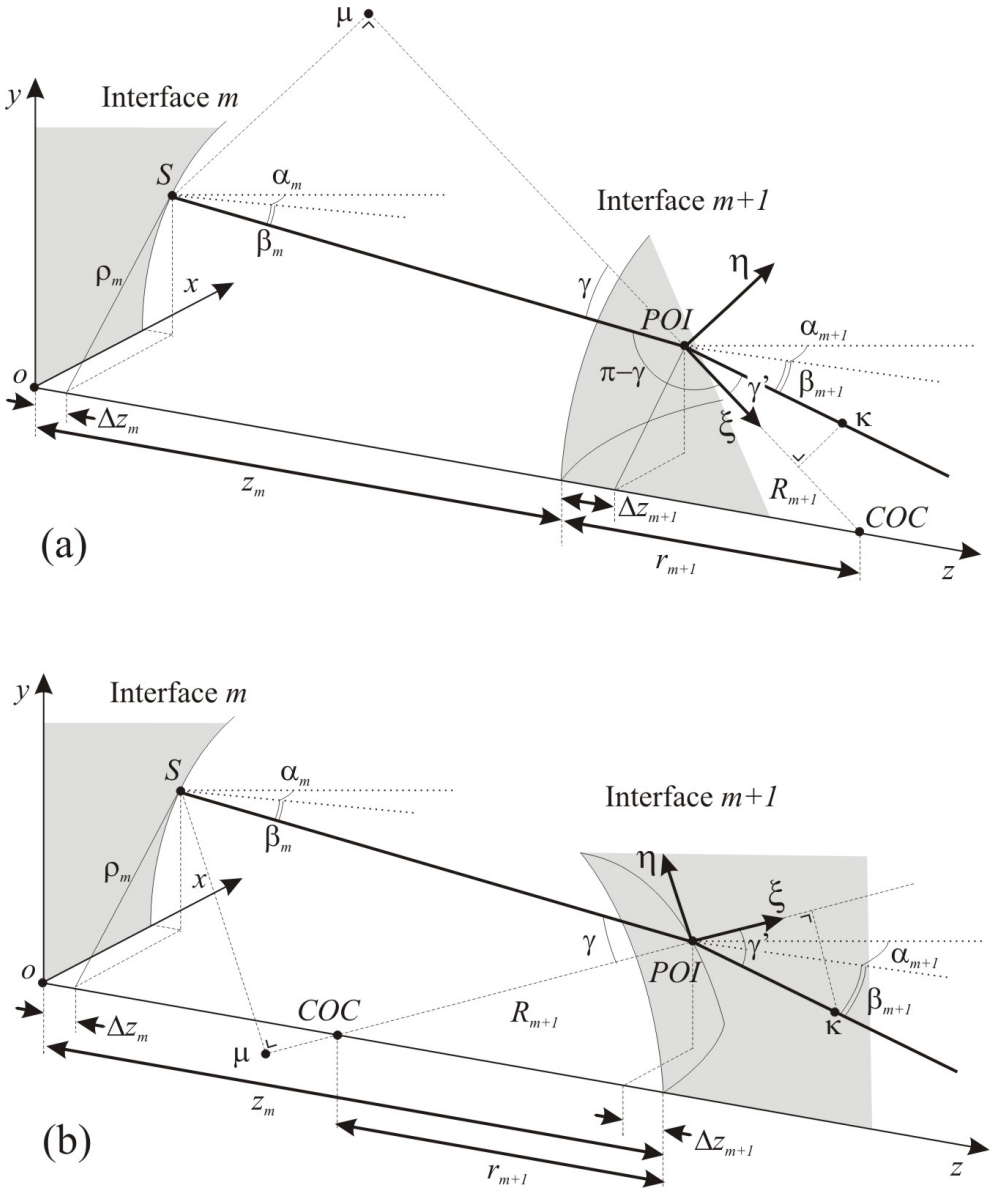

Figure V-5: Refraction of the incident ray on a convex (*a*) *and a concave* (*b*) *surface.*

$$\begin{cases} S & = \left(x_{m+1} - x_m, y_{m+1} - y_m, \Delta z_{m+1} - z_m - \Delta z_m\right)_{(x',y',z')} \\ POI & = \left(0,0,0\right)_{(x',y',z')} \\ COC & = \left(-x_{m+1}, -y_{m+1}, r_{m+1} - \Delta z_{m+1}\right)_{(x',y',z')} \end{cases} \quad \text{(V-17)}$$

where $(\ )_{(x',y',z')}$ indicates the axes system in which the coordinates are given.
The ξ-axis is chosen on the normal line of *POI* and directed towards *COC*. The unit vector $\vec{\xi}$ is then defined by:

$$\vec{\xi} = \frac{1}{R_{m+1}}\left(-x_{m+1}, -y_{m+1}, r_{m+1} - \Delta z_{m+1}\right)_{(x',y',z')} \quad \text{(V-18)}$$

For the definition of unit vector $\vec{\eta}$ a point μ is needed, which is the perpendicular projection of the source *S* on the extension of the normal line through *POI*:

$$\mu = -\left(D_1 \cos\gamma\right)\vec{\xi} = \frac{D_1 \cos\gamma}{R_{m+1}}\left(-x_{m+1}, -y_{m+1}, r_{m+1} - \Delta z_{m+1}\right)_{(x',y',z')} \quad \text{(V-19)}$$

The components of $\vec{\eta}$ are then given by subtracting the coordinates of points μ and *S* and shifting it back to *POI:*

$$\left(\vec{\eta}\right)_{i'} = \frac{\left(\mu\right)_{i'} - \left(S\right)_{i'}}{c} + \left(S\right)_{i'} \quad \text{(V-20)}$$

with $(\ )_{i'}$ ($i' = x', y', z'$) the three coordinates of vector $\vec{\eta}$ and *c* a normalization constant:

$$c = \left|\overline{\mu S}\right| = D_1 \sin\gamma \quad \text{(V-21)}$$

Using an arbitrary point $\vec{\kappa} = \left|\kappa\right|\left(\cos\gamma', \sin\gamma'\right)_{(\xi,\eta)}$ on the refracted beam the refraction angles α_{m+1} and β_{m+1} can be derived. When $\left|\kappa\right|$ is chosen to be equal to *1*, we find:

$$\begin{cases} \alpha_{m+1} = \arctan\left(\dfrac{\kappa_{x'}}{\kappa_{z'}}\right) \\ \beta_{m+1} = \arctan\left(\kappa_{y'}\right) \end{cases} \quad \text{(V-22)}$$

with:

$$\left(\kappa\right)_{i'} = \cos\gamma'\left(\vec{\xi}\right)_{i'} + \sin\gamma'\left(\vec{\eta}\right)_{i'} \quad \text{(V-23)}$$

b) Concave surfaces ($r_{m+1} < 0$)

This situation is shown in Figure V-5b and differs from the convex case in a number of minor details. The definition of the three points *S*, *POI* and *COC* remain the same, as well as those

of the unit vector $\vec{\xi}$ and auxiliary point μ. Only the second unit vector $\vec{\eta}$ has a reversed sign since in this case μ is located below S instead of above:

$$(\vec{\eta})_{i'} = -\frac{(\mu)_{i'} - (S)_{i'}}{C} + (S)_{i'} \qquad \text{(V-24)}$$

Normalization constant C is still given by (V-21). Arbitrary point $\vec{\kappa} = |\kappa|(\cos\gamma', -\sin\gamma')_{(\xi,\eta)}$ on the refracted beam is now given by:

$$(\kappa)_{i'} = \cos\gamma'(\vec{\xi})_{i'} - \sin\gamma'(\vec{\eta})_{i'} \qquad \text{(V-25)}$$

and the angles α_{m+1} and β_{m+1} follow from (V-22).

This model has been tested for off-axis sources using the anterior segment of the Navarro eye model, with incident light at an angle of 20º and 40º (Figure V-6 a and c). When these results are compared with results obtained with commercial ray tracing software (OSLO LT 6.1) it can be seen that the results roughly correspond with each other (Figure V-6 b and d).

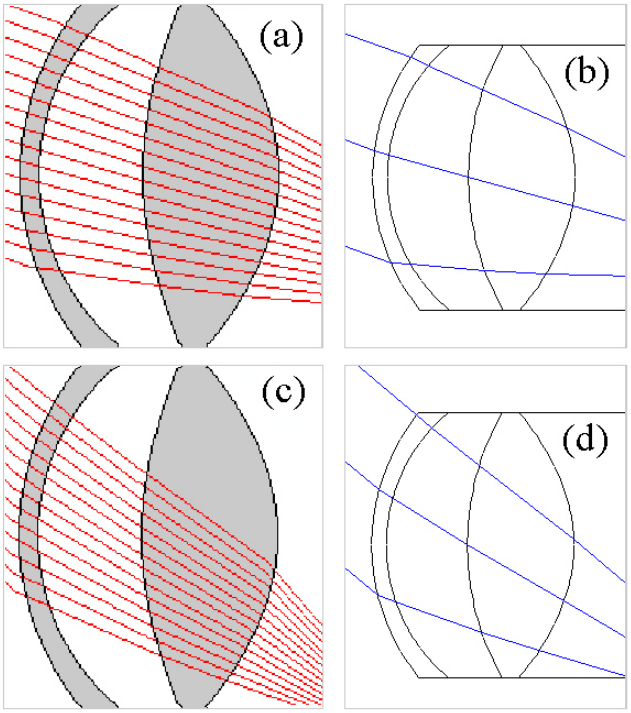

Figure V-6: results of the three-dimensional ray tracing algorithm described above applied to the Navarro model with rays incident at angles of 20º (a) and 40º (c). This is compared with the results provided by OSLO LT 6.1 (b) and (d).

V.3 *Peripheral wavefront measurements*

Applying these reconstruction procedures described earlier on the Navarro eye model, a low-resolution estimate of the aberration distribution in the anterior eye segment can be obtained

within a biconical volume of ±80 mm^3. This is the region where the ray tracing of each of the measured peripheral wavefronts have overlapped. The volume, shaded gray in Figure V-1, is the widest at the pupil aperture and comprises parts of the cornea, the anterior chamber and the crystalline lens. It ranges from ±1mm in front of the anterior surface of the cornea to ±0.1mm in front of the posterior surface of the crystalline lens.

V.3.1 Peripheral aberration data

The above calculations will first be applied to single Zernike polynomials: defocus Z_2^0, astigmatism Z_2^2 and coma Z_3^1, corresponding to the most common terms in peripheral aberrometry. The amplitudes of these terms were assumed the same for each of the 36 projections and were rotated in each position to maintain the orientation of the aberrations with respect to the eye.

Next we use two models for peripheral aberrations: one defined by adding *2 μm* of defocus Z_2^0, astigmatism Z_2^2 and coma Z_3^{-1} and the Navarro eye model. Again these aberrations were assumed the same in all directions (see Figure V-7, first two lines).

The peripheral aberrations measured and published by Navarro[121] were also used (subject EM, right eye). Since these aberrations were only measured in the temporal field (nasal retina) it was assumed that the wavefront aberrations would be uniform along each hemi-meridian. The wavefront data was scaled down from a 6.7mm pupil to 6mm to facilitate the comparison with the other data. Again the wavefronts were rotated for each position (Figure V-7).

Atchison measured the right eye of 5 subjects (Spherical equivalent ranging from +1.5D till -2D) along the full horizontal meridian, of which the RMS[122] and refractive values[123] were published. This author showed that the assumption that aberrations are uniform in each direction is not correct since there is a clear difference between the wavefront amplitudes of the nasal and the temporal field (as was also demonstrated for the refraction in references [124], [125] and [126]). For subjects DS, DA and LS this dataset provided Zernike coefficient values for the directions $\theta = 0^o$ and $\theta = 180^o$; in other directions we used interpolations of

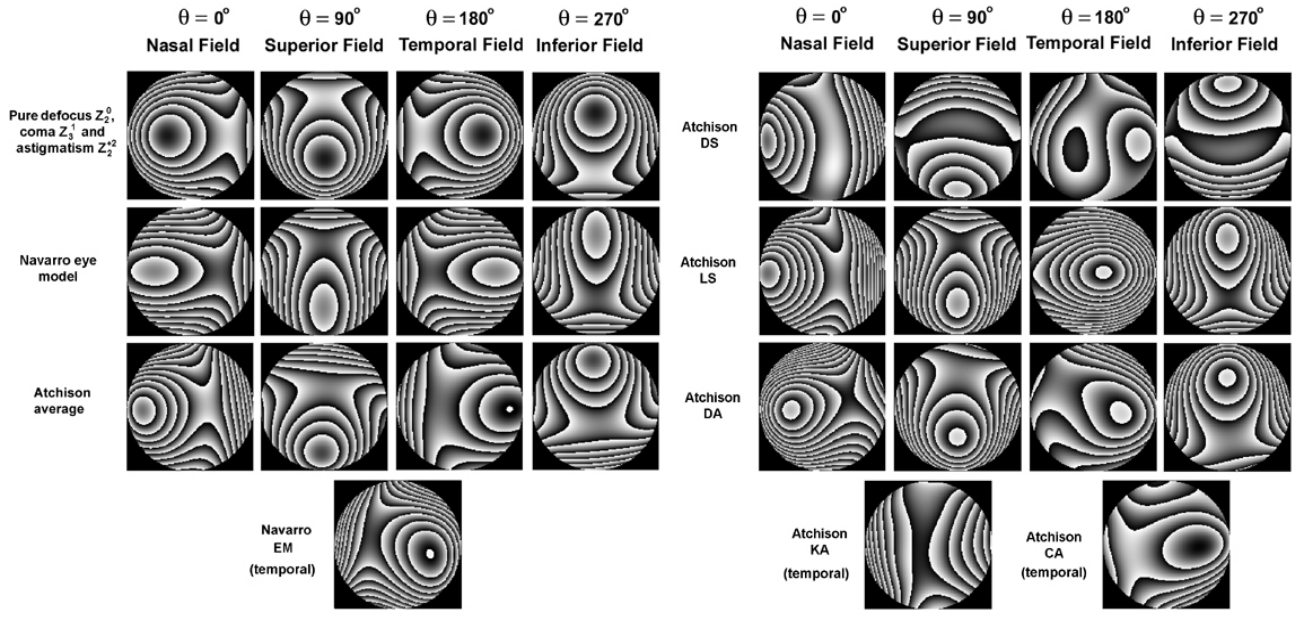

Figure V-7: peripheral wavefront measurements of the different data sets at an angle of incidence ψ = 40°. Steps correspond to increments of 1μm.

these values for our reconstructions (see Figure V-7, second and fourth column). The data from the other two subjects was treated in the same manner as the Navarro data.
Both the Navarro and the Atchison subjects were measured at a wavelength of 543nm and under full dilation and cycloplegia by means of a 1% solution of cyclopentolate.
Finally we performed a number of peripheral wavefront measurements ourselves using a Zeiss/ Meditec WASCA aberrometer (Figure V-8). The technical details of this device were discussed in Chapter II and will not be repeated here. This device was chosen because of its high resolution and the 'zonal reconstruction', which makes it possible to measure non-circular pupil areas. This was necessary since the pupil shape will flatten by a factor *cos* ψ under an angle of incidence ψ (see appendix B in [123]). A clock shaped grid attached to the measurement head was used as a fixation target.
The wavefront data of one right eye (Spherical equivalent +4.5D) was measured along twelve hemi-meridians (30º increments) and at four angles of incidence ψ (0º, 20º, 30º and 40º). Each measurement was repeated three times and averaged. The subject was dilated using one drop of 0.5% Tropicamide. During the measurements another drop was administered after each hour passed.

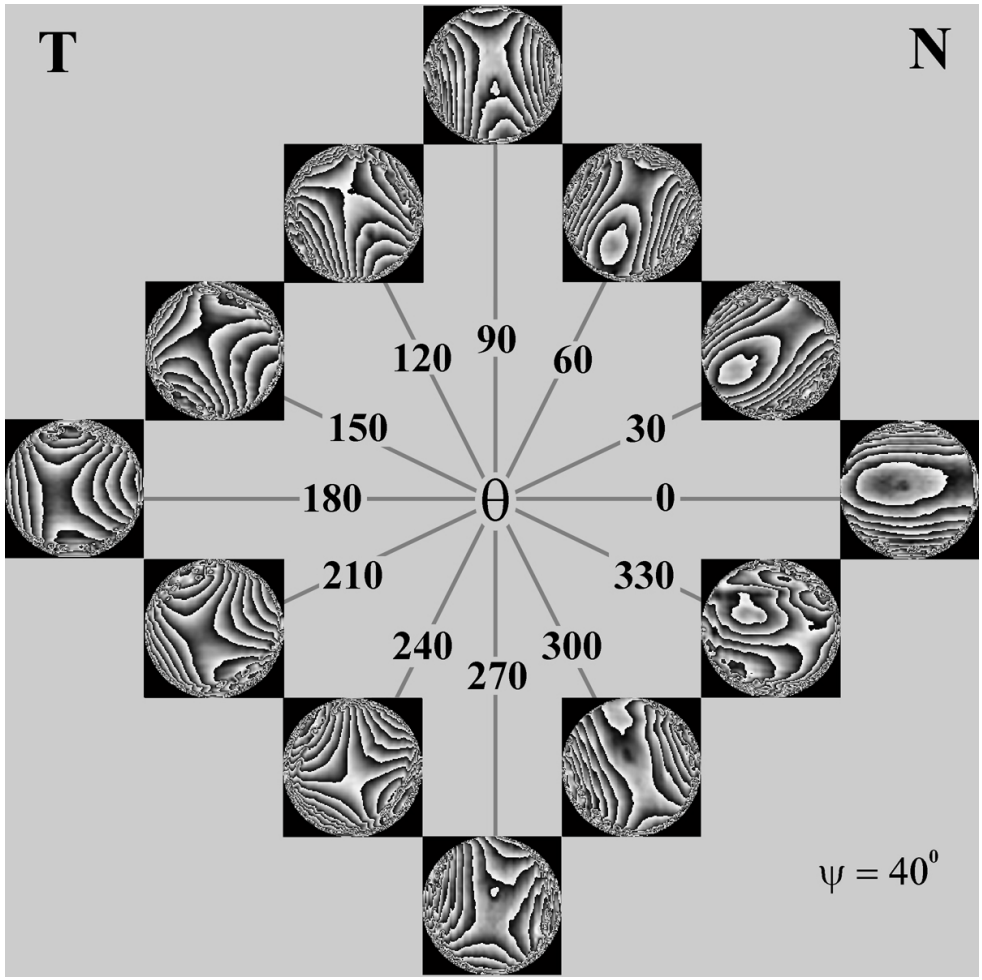

Figure V-8: twelve peripheral wavefront measurements after subtraction of on-axis defocus term and multiplication with a circular pupil for subject LG at angle of incidence ψ *= 40º. Each step corresponds with 2μm.*

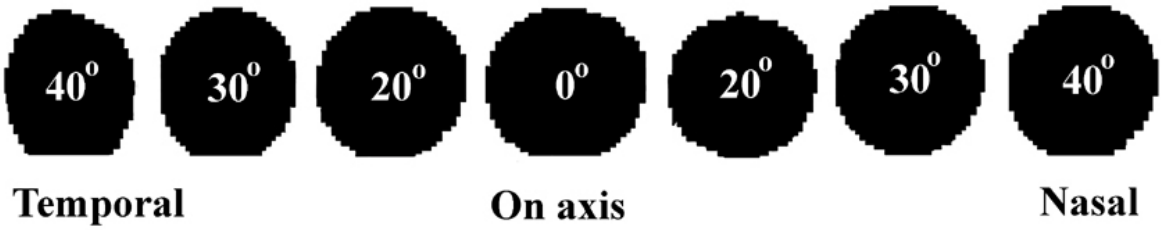

Figure V-9: change in pupil shape over the horizontal visual field for subject LG.

V.3.2 **Discussion**

From the higher order aberration data presented both in Figure V-7 and Figure V-8 it can be seen that astigmatism and coma-like aberrations are the most influential. Both types of aberrations increase rapidly with increasing ψ[121, 122], resulting in images similar to the defocus-astigmatism-coma model. At the same time the defocus seems to vary in a more irregular way (see [121] and the Atchison data).
Comparing the aberrations of real eyes with those of the two model eyes, it can be seen that overall they have similar shapes. However the aberrations of the individual real eyes are less symmetrical with respect to the horizontal axis than the models. This asymmetry may be attributed to, among others, irregular deformations of the refractive surfaces and minor differences in direction of optical axes between the cornea and the crystalline lens[15, 127]. Note that the averaged Atchison data, containing data from all his series, is much more symmetrical.
The Atchison data (right hand in Figure V-7) also shows that the shapes and amplitudes in the temporal and the nasal fields differ both in shape and in amplitude. This is possibly due to a slightly tilted lens and/ or pupil. In general the aberrations are found to be larger in the nasal field, which is confirmed by our own data (Figure V-8). One possible reason for this difference is that the nasal field is more used for vision nearby.
When the change in pupil shape is studied (Figure V-9), it is found that it does not follow the theoretical model[123], even though it accurately describes the pupil coordinates. In the case of subject LG the pupil flattens when the angle of incidence is increased on the temporal side. On the nasal side however this does not occur and the pupil remains more or less round. This could be an indication that the pupil plane of this eye is not perpendicular to the line of sight, but rather tilted by *10-20°* in the nasal direction. Since LG has a rather severe hyperopia it is possible that in the course of her life her crystalline lens and pupil have slightly tilted to obtain a better near vision. Similar variances in pupil shape across the visual field have been reported as well by Atchison[128].

V.4 *Reconstructions*

V.4.1 **Validation of the reconstruction techniques**

a) Validation of pupil plane reconstructions

In order to test the validity of both the reversed ray tracing and the tomosynthesis methods, we did a number of numerical simulations using a Navarro eye model. Since in this simulation we no longer depend on previously measured data, all recording and reconstruction parameters could be chosen by ourselves. Apart from the angle of incidence ψ,

which was increased to 48˚, all parameters were taken the same as before. This is the angle under which the smearing effect found in backprojection reconstructions is minimal, but where the peripheral aberrations are still measurable for real eyes.
First the off-axis aberrations for $\psi = 48^{\circ}$ were calculated and the rotation symmetrical Zernike terms (defocus Z_2^0 and spherical aberration Z_4^0) were neglected to avoid their distorting influence (seeV.4.1b). The reconstruction is made for three different objects: one unaltered model (Figure V-10, first column), one with a centered radial sine distortion (refractive index: $n \pm 0.5$) in the pupil plane (Figure V-10, second column) and one with a decentered radial sine distortion (Figure V-10, third column). The pupil planes of each of the original objects are shown in the first line. These objects are reconstructed using tomosynthesis (second line) and reversed ray tracing (third line).
The tomosynthesis reconstruction (see IV.2.2a) shows for the unaltered eye model a slightly dark central region that was not originally there. For the other two objects it can be seen that the sinusoidal patterns are superimposed on the intensity distribution of the unaltered model. The patterns themselves are reconstructed well.
The refraction corrected reversed ray tracing reconstruction (see V.2.2) of the pupil plane shows similar properties. In this case the unaltered model shows dark faint circles which are artifacts inherent to the method and can be reduced by increasing the number of data points in the projections. The reconstruction of the altered models again show sine patterns superimposed on the artifacts, resulting in a certain distortion of the pattern. This is mainly seen in the off-axis object.

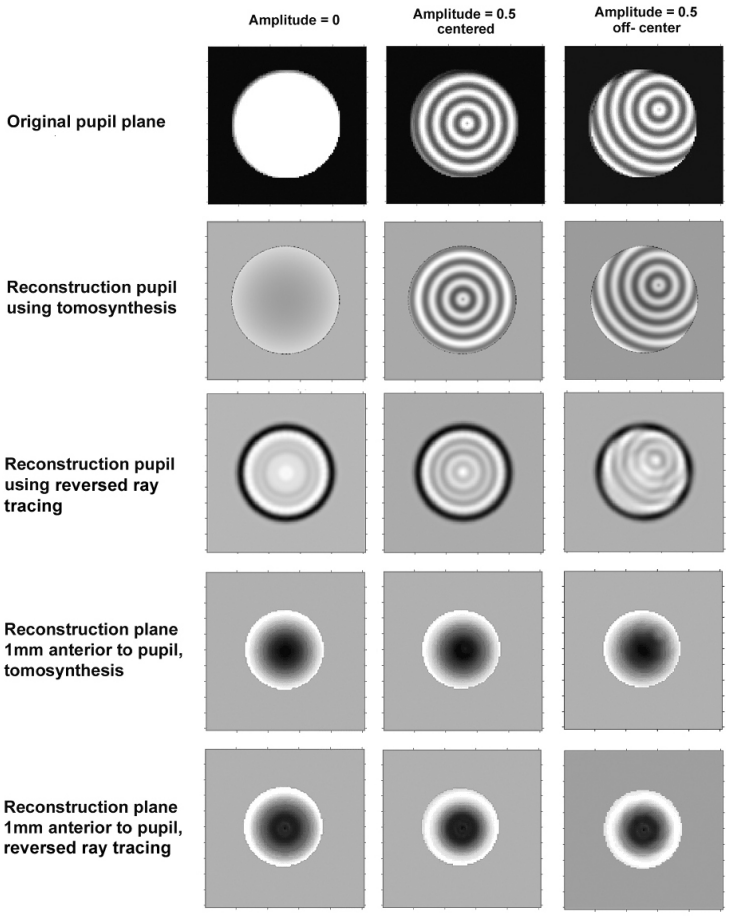

Figure V-10: pupil plane reconstruction ($\psi = 40°$, $N = 36$) of the Navarro model using tomosynthesis and reversed ray tracing.

The previous results have been recalculated for sine patterns with amplitudes down to $n \pm 0.005$. Using tomosynthesis and under full correction of the defocus and the spherical aberration the pattern can still be distinguished. Reversed ray tracing on the other hand has trouble reconstructing these small differences, partially due to the annular artifacts.
One other reconstruction property that can be tested is the resolution along the optical axis δn. In order to do this a plane 1mm anterior to the pupil plane is reconstructed using both methods. In all six reconstructions a bright edge can be seen due to the smearing of the lenticular aberrations. In the center however no patterns can be distinguished, with the exception of the off-centre tomosynthesis reconstruction. This is an indication that the resolution δn along the optical axis is higher for reversed ray tracing than for tomosynthesis.

b) Contribution of single Zernike polynomials

When the Zernike decomposition is made of a peripheral wavefront, it can be seen that these are mainly composed of the defocus Z_2^0, astigmatism Z_2^2 and coma Z_3^1 terms. In this section the individual contribution of each of these three terms is studied using reversed ray tracing. The amplitudes of the projections are chosen to be $-3\mu m$ for the defocus Z_2^0 and $3\mu m$ for the astigmatism Z_2^2 and coma Z_3^1. The peripheral aberrations are assumed to be uniform in all directions.
In Figure V-11a the reconstruction of a single defocus term is shown. Comparing the reconstruction with the model overlay it can be seen that no distinction can be made between the different eye segments. Only at the anterior and posterior tips and the superior and inferior edges of the central volume slightly darker areas are present, due to the overlap of the negative values from the defocus edges in those areas. Similar effects are found for other rotation symmetric aberrations, such as the various orders of spherical aberration, which reconstruct into checked patterns.
.

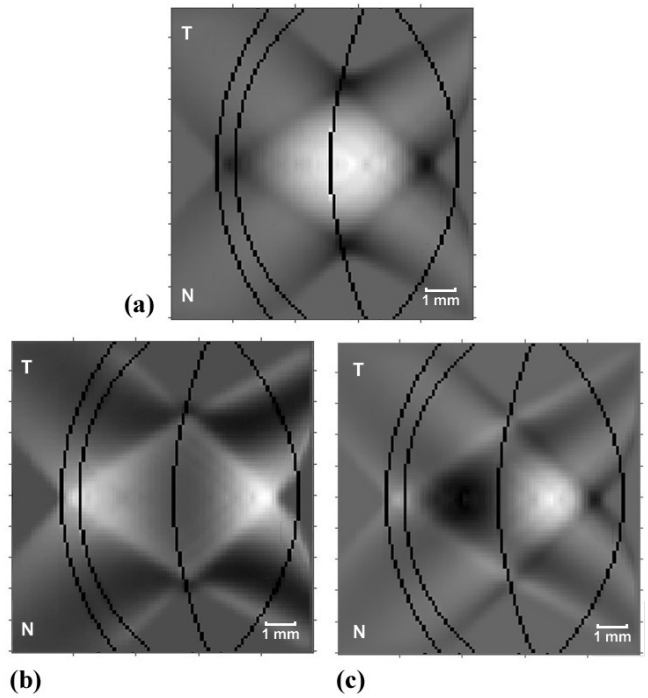

Figure V-11: laminographic reconstruction ($\psi = 48°$, $N = 36$) for (a) $-3\mu m$ pure defocus Z_2^0, (b) $3\mu m$ pure astigmatism Z_2^2 and (c) $3\mu m$ pure coma Z_3^1.

In the reconstruction of the astigmatism (Figure V-11b) two maxima can be distinguished in the cornea and the lens. This roughly, but inaccurately, represents the aberration distribution in the cornea and the lenticular nucleus.
The result from the single coma term (Figure V-11c) seems to be in closer accordance with the expected refractive index distribution of a true eye. This gives an indication of the origin of the large presence of coma-like aberrations found in higher order Zernike decompositions of peripheral wavefront data. There is a clear difference between a dark area, located at the anterior chamber, and a bright area in the crystalline lens. In the front tip is another bright area, corresponding to the cornea. The gray values in the top and bottom part of the anterior chamber and lens seem to be smeared out.
A simulation using OSLO LT shows that the manifestation of the defocus term, and part of the astigmatism term, is mainly due to a combination of the cornea and the ocular length. As most of the cornea is not located in the reconstructable volume in Figure V-1 the defocus term in the wavefront projections can be disregarded. In some cases, where it is beneficial to the quality and the contrast of the reconstruction, this is also done for the astigmatism terms. This operation, corresponding to correction of the spherical and cylindrical errors of the eye in that direction, will reduce the blurring of the reconstruction

V.4.2 **Navarro data**

If reversed ray tracing is applied to the data of Navarro's subject EM we find the result in Figure V-12. For this reconstruction 36 identical projections are used under an angle $\psi = 40°$. This is done for two situations: Z_1^1, Z_1^{-1} and $Z_2^0 = 0$ (Figure V-12a) and for the higher order aberrations only: Z_1^{-1}, Z_1^1, Z_2^{-2}, Z_2^0 and $Z_2^2 = 0$ (Figure V-12b).
It is found that for the higher order reconstruction the cross-section has more contrast, giving a clear image comparable to that of the coma term alone (Figure V-11c). The different ocular structures are well visible near the optical axis of the Navarro model. Away from the optical axis smearing effects take their toll. Note that due to smearing the reconstructed cornea appears to be in front of the model cornea.
The pupil plane reconstruction is rotation symmetric for both situations due to the repeated use of the same projection. Therefore the information content of this plane is rather low and will not be shown here.

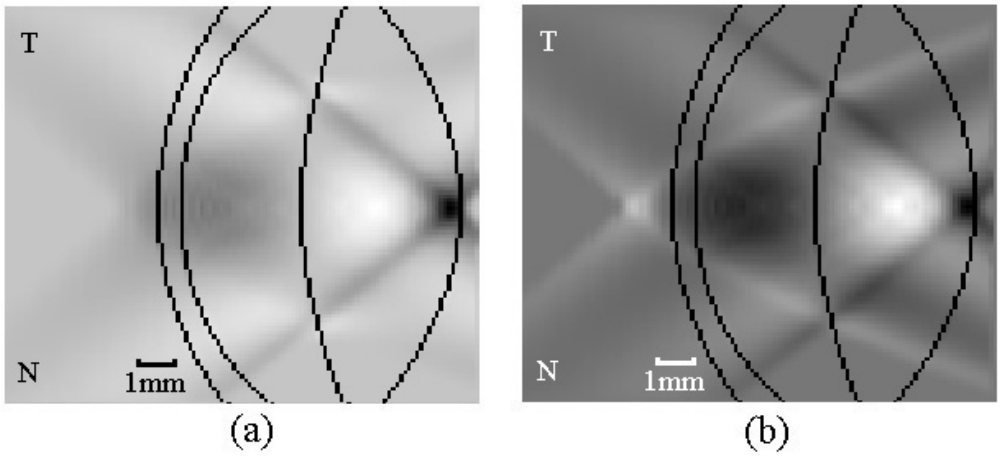

Figure V-12: anterior segment reconstruction ($\psi = 40°$, $N = 36$) for Navarro's subject EM. (a) Tilt and defocus disregarded; (b) higher order aberrations only.

V.4.3 **Atchison data**

a) Reversed ray tracing

Reconstruction of the interpolated Atchison data reconstructed under 40° gives the result shown in Figure V-13. It can be seen that despite the asymmetrical distribution of peripheral aberrations in the data set (see Figure V-7) neither the reconstruction of the horizontal (*x,z*) cross-section plane, nor the vertical (*y,z*) cross-section plane shows any large scale asymmetry for each of the three subjects. In the pupil plane however a shadow is seen on the temporal side for all subjects, which might be an indication for a tilted lens. Such lens tilts have already been found using MRI imaging[129, 130].

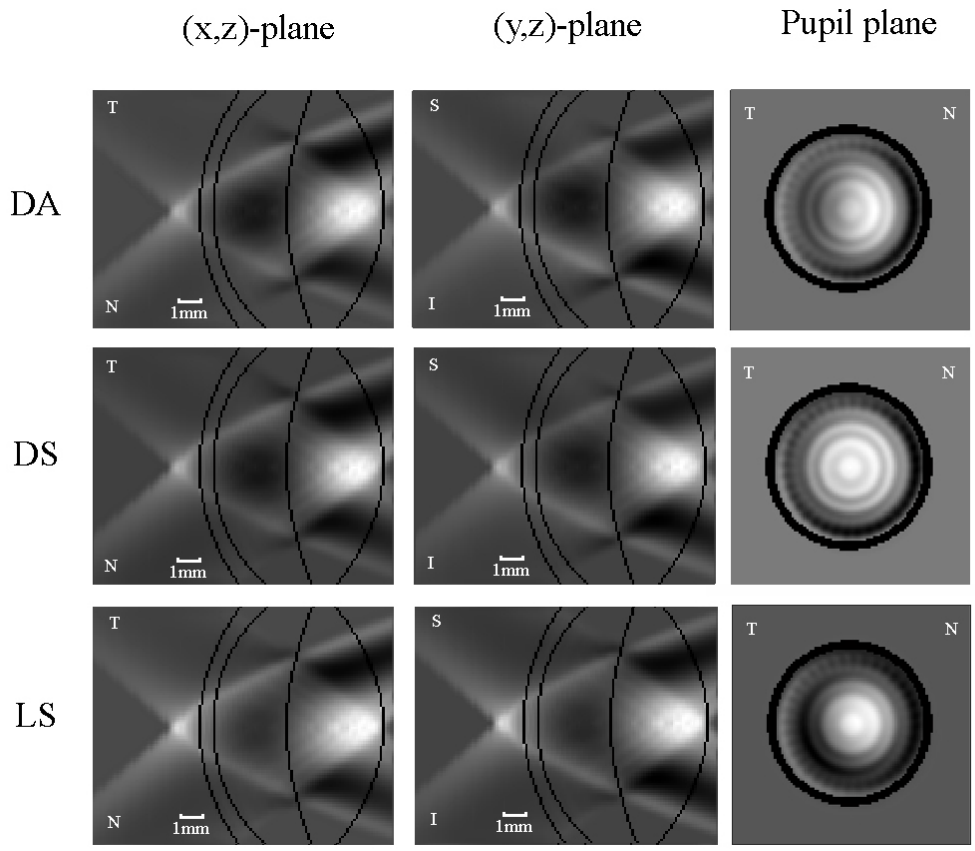

Figure V-13: reversed ray tracing reconstructions ($\psi = 40°$, $N = 36$) *for three subjects of the Atchison data set. Tilt and defocus terms are disregarded in each projection and the pupil diameter is 6mm.*

b) Pupil reconstruction by tomosynthesis and spiral scan

Tomosynthesis and Spiral Scan applied to the Atchison data for several angles of incidence ψ gives the pupil reconstructions in Figure V-14, where the asymmetrical aberration distributions seen in Figure V-13 are also found. For $\psi = 10°$ first a distribution resembling a spherical aberration is found, but with increasing ψ values the central peak shifts in the nasal direction. At $\psi = 40°$ the distribution closely resembles a coma aberration.

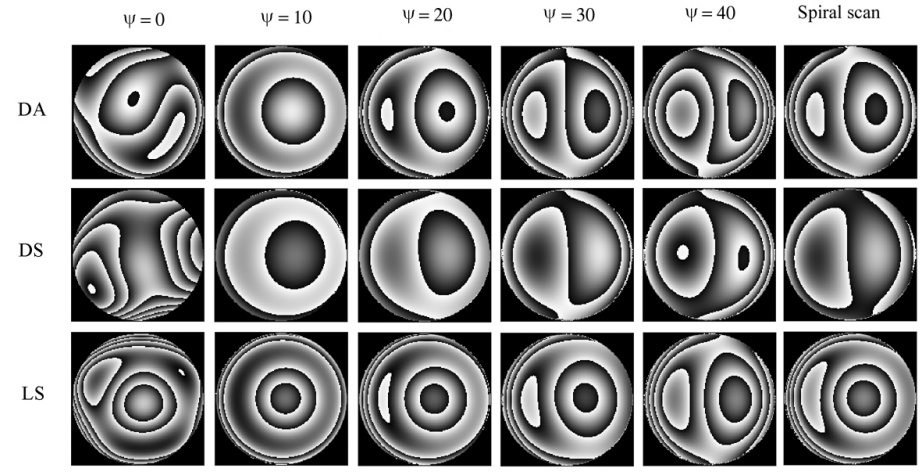

Figure V-14: tomosynthesis and spiral scan reconstructions (N = 36) for three subjects of the Atchison data set. In each projection the tilt and defocus terms are disregarded. Steps correspond to increments of 1 μm and the pupil diameter is 6mm (Left = T, right =N).

The Spiral Scan reconstruction in Figure V-14 and the pupil plane in Figure V-13 show a close correspondence with each other, both in aberration shape and amplitude. This reinforces the previous assumption of a slightly tilted lens for all three subjects.

V.4.4 Full-field measurements

The reconstruction of the full-field data of subject LG is shown in Figure V-15. Since this is the only dataset we have measured ourselves, it was possible to determine a number of biometric parameters of this eye. These parameters (see Table V-1) can aide to customize the Navarro eye model to the individual characteristics of LG's eye.
Due to large amounts of smearing the quality of the 3D reconstructions is not very high, both for the case with the tilt and defocus subtracted from the peripheral aberrations and for the higher order peripheral aberrations alone. The pupil plane reconstructions by reversed ray tracing are remarkably uniform, with only a slight shadowy region in the upper nasal part. The tomosynthesis reconstruction shows less uniformity, with a minimum in upper nasal section.

Table V-1: biometrical data of LG's right eye

Ocular refraction	*4.50D, -0.50D @ 125°* *
Anterior corneal radius	*8.13mm***
Posterior corneal radius	*6.50mm***
Central corneal thickness	*0.692mm***
Anterior chamber depth	*3.17mm*†
Ocular length	*22.52mm*†
Lens thickness	*4.17mm*‡

* Nidek ARK-700 autorefractometer
** Bausch & Lomb Orbscan II
† Zeiss IOL master (based on OCT)
‡ Alcon Ophthascan ultrasound biometer

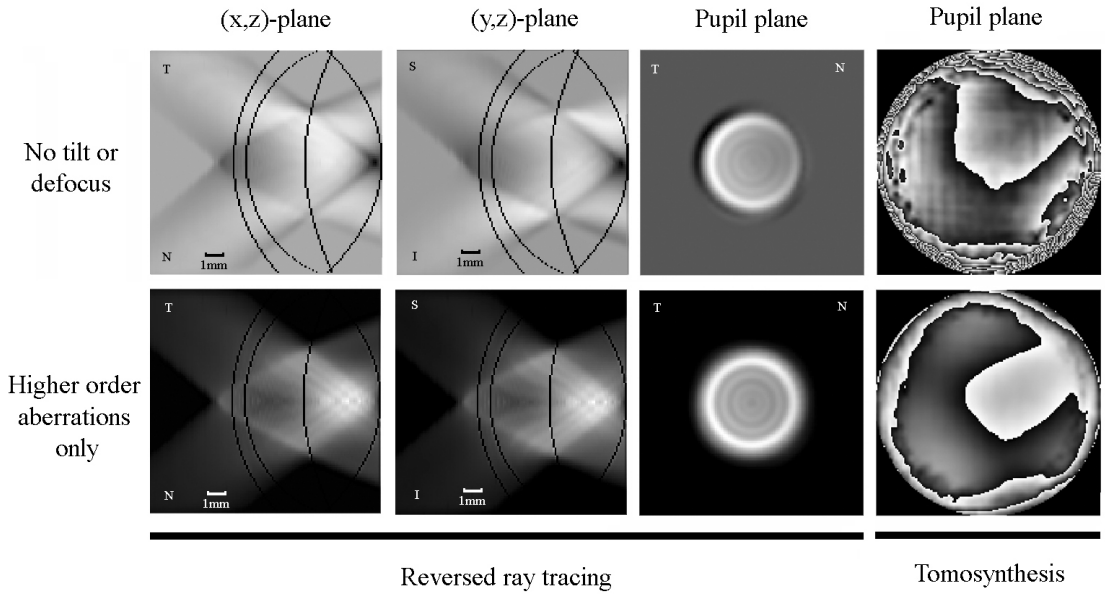

Figure V-15: full-field reconstruction of subject LG's right eye (ψ = 40°, N = 36). Steps correspond to increments of 1 µm and the pupil diameter is 6mm.

V.5 *Conclusions*

From the previous result we can conclude the following:

- Neither reversed ray-tracing, nor tomosynthesis are very reliable techniques for the 3D reconstruction of the aberration sources due to the many smearing artifacts that influence the quality of the reconstruction.
- Both techniques give a reasonable reconstruction of the pupil plane, where asymmetries can be found. These asymmetries are related to a tilt in the pupil or the crystalline lens. The results of both techniques confirm each other.
- Tomosynthesis takes considerably less time to reconstruct the pupil plane, but reversed ray tracing is capable of reconstructing the whole eye at once. Given the low quality of the 3D reconstructions, the short calculation times of tomosynthesis make this the preferred technique for pupil plane reconstructions.

An example of how to make a practical realization of a tomographic scanner capable of automatically measuring the peripheral aberrations of the eye is described in [169].

PART III

Design and first results of a Curvature Sensing Aberrometer

Up till now each of the discussed aberrometers used a rather coarse subsampling of the pupil plane by means of a number of skewed rays to determine aberrations. Therefore these aberrometers only have a limited resolution compared to e.g. interferometry. In this part a new kind of aberrometer will be presented, based on curvature sensing. This device is capable of achieving the highest possible resolution, the camera pixel size, without the need of lengthy calculations.

Chapter VI Principles of curvature sensing

VI.1 *Introduction*

Curvature sensing was invented for adaptive optics applications in astronomy. Here real-time compensation of continuous changing atmospheric wavefront aberrations is important to improve stellar image quality. Up till now curvature sensing has been incorporated in a number of large telescopes, the most famous of which is ESO's Very Large Telescope in Chile.
Recently new applications were found in many different fields of imaging, going from astronomy and optical microscopy, to transmission electron microscopy[131,132], neutron radiography[133], X-ray imaging[134], and many other domains. An application in ocular aberrometry was recently suggested[135], but to our knowledge it has not been implemented yet.
In this chapter the properties of curvature sensing are discussed for general purposes. This will be narrowed down to wavefront sensing in Chapter VII

VI.2 *Mathematical principles*

VI.2.1 **Derivation of the technique**

This method is based on the observation that wavefront aberrations can have a minute influence on the intensity distributions in planes near the best focus. This is shown in Figure VI-1 for the case of a pupil under uniform illumination. Here the bold line represents the wavefront, the dashed line is the ideal plane wave and individual rays, perpendicular to the wavefront, are indicated by the arrows.
For plane waves the rays are parallel, which results in a uniform intensity distribution on a screen placed slightly behind the pupil opening. An aberrated wavefront however will show locally converging and diverging rays, which gives rise to brighter (convergent) and darker (divergent) areas. In every-day life this effect can be observed in the scintillating patterns on the bottom of a swimming pool.
From these intensity patterns the aberration of wave in the pupil plane can be derived using the paraxial approximation[136, 137] of the Fresnel diffraction theory[138]:

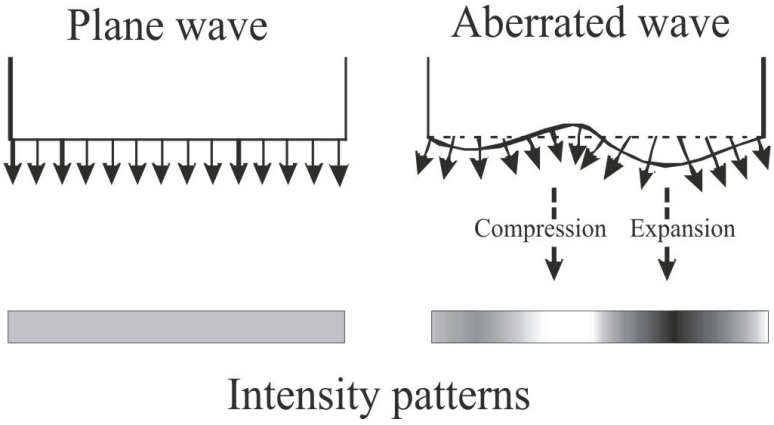

Figure VI-1: 2D illustration of curvature sensing of a uniformly illuminated pupil.

$$\left(i\frac{\partial}{\partial z} + \frac{\nabla_{\perp}^2}{2k} + k \right) u(x,y) = 0 \tag{VI-1}$$

with z taken in the direction of the optical axis and $\nabla_{\perp}^2 = \Delta_{\perp}$ the Laplacian calculated in the (x,y) plane. This can be solved by a wave equation:

$$u(x,y) = \sqrt{I(x,y)} e^{i\varphi(x,y)} \tag{VI-2}$$

where $I(x,y)$ is the intensity of the light in the image plane and $\varphi(x,y)$ the wavefront aberration. When (VI-2) is filled in into (VI-1) and multiplied by $u^*(x,y)$, the complex conjugate of (VI-2), and $u^*(x,y)$ is filled in separately into (VI-1) and multiplied by $u(x,y)$. Adding these two results gives:

$$2k\frac{\partial\varphi(x,y)}{\partial z} = 1 - \left(\nabla_{\perp}\varphi(x,y)\right)^2 + \frac{1}{2I(x,y)}\nabla_{\perp}^2 I(x,y) - \frac{1}{4I^2(x,y)}\left(\nabla_{\perp} I(x,y)\right)^2 \tag{VI-3}$$

and if they are subtracted we find:

$$\begin{aligned} -k\frac{\partial I(x,y)}{\partial z} &= \nabla_{\perp}\cdot\left(I(x,y)\nabla_{\perp}\varphi(x,y)\right) \\ &= I(x,y)\nabla_{\perp}^2\varphi(x,y) + \nabla_{\perp} I(x,y)\cdot\nabla_{\perp}\varphi(x,y) \end{aligned} \tag{VI-4}$$

with $\nabla_{\perp} = \left(\partial/\partial x, \partial/\partial y\right)$ is the gradient operator in the (x,y) plane and $\nabla_{\perp}\cdot$ the divergence. Equation (VI-3) is called the Transport of Wavefront Equation (TWE) and describes the change in wavefront along the optical axis. Solving this for $\varphi(x,y)$ is not an easy task since $\partial\varphi(x,y)/\partial z$ cannot be measured. The second equation on the other hand contains $\partial I(x,y)/\partial z$, which is found by taking the difference between the intensities measured in two closely spaced planes near the image plane. Formula (VI-4) is known as the Transport of Intensity Equation (TIE), as it describes how a change in intensity along the z-axis is related to the curvature (first term, right hand side) and the slope (second term) of the wavefront aberration in the image plane.

The problem can be simplified considerably by assuming the image consists of a bright region Γ of constant intensity I_0 within a region of zero intensity:

$$I(x,y) = \begin{cases} I_0 & if\ (x,y) \in \Gamma \\ 0 & if\ (x,y) \notin \Gamma \end{cases} \tag{VI-5}$$

This restricts the effect of the curvature term to Γ as the intensity is zero elsewhere. The gradient term has now only influence on the edge Ω of Γ, since only there $\nabla_{\perp} I(x,y) \neq 0$. Applied to telescopes and adaptive optics (VI-5) is accepted as a reasonable assumption[139, 140]. In the absence of a large Stiles-Crawford effect[141, 142], this is also valid for human eyes. In both cases Γ is considered a circular opening.

In order to solve the TIE analytically boundary conditions need to be defined. These are found by filling (VI-5) in into (VI-4):

$$-\frac{k}{I_0}\frac{\partial I(x,y)}{\partial z} = H(\Gamma)\nabla_{\perp}^2\varphi(x,y) + \delta_{\Omega}\cdot\nabla_{\perp}\varphi(x,y) \tag{VI-6}$$

with $H(\Gamma)$ the step function defined in Γ (1 inside Γ and 0 outside) and δ_{Ω} the Kronecker delta defined on contour Ω of Γ. Equation (VI-6) shows that the change in intensity along the z-axis depends on two separate components that both need to be determined:

$$\begin{cases} \nabla_{\perp}^2\varphi(x,y) = -\frac{k}{I_0}H(\Gamma)\frac{\partial I(x,y)}{\partial z} := f(x,y) \\ \nabla_{\perp}\varphi(x,y) = -\frac{k}{I_0}\delta_{\Omega}\frac{\partial I(x,y)}{\partial z} := g(x,y) \end{cases} \tag{VI-7}$$

which is the Poisson equation with Neumann boundary conditions. Here functions $f(x,y)$ and $g(x,y)$ are assumed to be continuous and smooth respectively over Γ and Ω.
It has been demonstrated[143] that for these boundary conditions and in the absence of points where $I(x,y) = 0$ the TIE has a unique solution. Points of zero intensity will serve as singularities, causing the loss of the solution's uniqueness[144].

In practice there are several different methods to solve the TIE. The most important ones mentioned in the literature will be described in the following.

VI.2.2 **Reconstruction techniques**

a) Optical solution of the Poisson equation

This method[139, 145] uses the fact that the dynamic equation of a bimorph or a membrane mirror in function of the control voltage distribution is very similar to the Poisson equation. By solving equations (VI-7) in terms of the voltage and applying the result in a closed loop to the adaptive mirror the wavefront is immediately compensated.

b) Green's function solution

This solution was proposed by Teague[138] and later by Woods and Greenaway[146]. It uses Green's second theorem and Green's functions $\nabla_{\perp}^2 G(x,y;x',y') = \delta(x-x')\delta(y-y')$ to find:

$$\varphi(x,y) = -\frac{k}{I_0}\int_{\Gamma}\frac{\partial I(x,y)}{\partial z}G(x,y;x',y')dx'dy' \tag{VI-8}$$

This can be solved with a polynomials series approximation $u_i(x,y)$:

$$a_i = -\frac{k}{I_0}\iint_{\Gamma}\frac{\partial I(x,y)}{\partial z}G(x,y;x',y')u_i(x,y)dx'dy' \tag{VI-9}$$

Suppose now that $u_i(x,y) = \delta(x-x_i)\delta(y-y_i)$, which is an orthonormal base, and $\partial I/\partial z$ is split up in it's pixel components:

$$\frac{\partial I(x,y)}{\partial z} = \sum_j d_j \left(\delta(x - x_j)\delta(y - y_j)\right) \tag{VI-10}$$

with $j = 1,\ldots, N^2$ a the number of pixels in the image and d_j the intensity of the individual pixels. This is filled in in (VI-9):

$$a_i = -\frac{k}{I_0}\sum_j d_j G(x_i, y_i; x_j, y_j) \tag{VI-11}$$

Using the Green's function solution of a 2D Poisson equation:

$$G(x_i, y_i; x_j, y_j) = \frac{-1}{4\pi}\ln\left((x_i - x_j)^2 + (y_i - y_j)^2\right) \tag{VI-12}$$

we find:

$$a_i = \frac{k}{4\pi I_0}\sum_j d_j \ln\left((x_i - x_j)^2 + (y_i - y_j)^2\right) \tag{VI-13}$$

which can be calculated as a system of equations. However, since the size of this of this system is $[N^2 x N^2]$ the calculations can become lengthy for large images, making it less suitable for real-time applications.

c) Reconstruction using polynomial series

The TIE can also be solved using the least squares fitting of orthonormal polynomials in a way similar to I.4.2a). This has been done for Zernike polynomials (in uniform[147] and non-uniform[148] lighting conditions), Legendre polynomials[149], Karhunen-Loève polynomials[150] and Appell-Kampé de Fériet polynomials[150]. Another paper[151] proposes a direct integral solution for the determination of the best fit.
The polynomial solution of the TIE starts from the assumption that the phase $\varphi(x,y)$ can be approximated by a orthonormal series of polynomials $u_n(x,y)$ defined over an area Γ:

$$\varphi(x,y) = \sum_{n=0}^{\infty} a_n u_n(x,y) \tag{VI-14}$$

If (VI-4) is multiplied on both sides by $u_n(x,y)$ and integrated over Γ we find:

$$-k\int_\Gamma \frac{\partial I(x,y)}{\partial z} u_n(x,y)dxdy = \int_\Gamma \nabla_\perp \cdot \left(I\nabla_\perp \varphi(x,y)\right)u_n(x,y)dxdy \tag{VI-15}$$

The expression on the left-hand side is the n^{th} polynomial coefficient of $-k\partial I/\partial z$ and will from now on be called F_n. Filling (VI-14) in into the right-hand side of (VI-15) gives after simplification[148]:

$$F_n = \sum_{m=0}^{\infty} a_m \int_\Gamma I(x,y)\nabla_\perp u_m(x,y)\cdot\nabla_\perp u_n(x,y)dxdy \tag{VI-16}$$

Defining a polynomial mode matrix *M*:

$$M_{nm} = \int_{\Gamma} I(x,y)\nabla_{\perp} u_m(x,y) \cdot \nabla_{\perp} u_n(x,y) dxdy \tag{VI-17}$$

which leads to:

$$a = M^{-1} F \tag{VI-18}$$

A proof for the invertibility of *M* is given in [148]. In order to solve the TIE system (VI-18) needs to be solved, which can be done in a straight forward manner. However generating matrix *M* can take a long calculation time, depending on after how many terms the polynomial series is truncated.
The use of polynomial series has the advantage that the whole phase can be characterized by a limited number of coefficients. More coefficients yield better results, but also longer calculation times for *M*.

d) Algebraic solution of the Fourier series

Van Dyck[152] proposed a method in which the amplitude $A(x,y) = \sqrt{I(x,y)}$ and the phase $\varphi(x,y)$ of the aberrated light are decomposed into Fourier series:

$$\begin{cases} A(\vec{r}) = \sum_{\vec{\rho}} A_{\vec{\rho}}(z) e^{2\pi i \vec{\rho}\cdot\vec{r}} \\ \dfrac{\partial A(\vec{r})}{\partial z} = \sum_{\vec{\rho}} \dfrac{\partial A_{\vec{\rho}}(z)}{\partial z} e^{2\pi i \vec{\rho}\cdot\vec{r}} \\ \varphi(\vec{r}) = \sum_{\vec{\rho}} \varphi_{\vec{\rho}}(z) e^{2\pi i \vec{\rho}\cdot\vec{r}} \end{cases} \tag{VI-19}$$

with $\vec{r} = (x,y)$ the coordinates in the image plane and $\vec{\rho} = (u,v)$ those in the Fourier plane. Substituting (VI-19) into the TIE written in terms of the amplitude (see [152]) and rearranging the corresponding terms we find:

$$\sum_{\vec{\rho}'} \left(\vec{\rho}^{\,2} - (\vec{\rho} - \vec{\rho}')^2\right) A_{\vec{\rho}-\vec{\rho}'}(z) \varphi_{\vec{\rho}'}(z) = \frac{k}{\pi} \frac{\partial A(z)}{\partial z} \tag{VI-20}$$

This is a large system of *N* equations and *N* unknowns $\varphi_{\vec{\rho}'}(\vec{r})$ with *N* the number of pixels in the image. $A_{\vec{\rho}-\vec{\rho}'}(z)$ is a convolution factor, where $\vec{\rho} - \vec{\rho}'$ indicates the vector centered in the origin with the same length and direction as $\vec{\rho} - \vec{\rho}'$. Solving system (VI-20) directly gives the exact solution for $\varphi(x,y)$.
As in the previous method this method is time consuming due to the large dimensions of the matrix [$N^2 x N^2$].

e) Direct iterative solution[153]

This solution uses the substitutions:

$$\nabla_{\perp}\varphi(x,y)=\left.\frac{\partial\varphi}{\partial x}\right|_{(x,y)}\vec{e}_x+\left.\frac{\partial\varphi}{\partial y}\right|_{(x,y)}\vec{e}_y=\frac{\varphi(x+1,y)-\varphi(x-1,y)}{2dx}\vec{e}_x+\frac{\varphi(x,y+1)-\varphi(x,y-1)}{2dy}\vec{e}_y$$

$$\nabla_{\perp}^2\varphi(x,y)=\left.\frac{\partial^2\varphi}{\partial x^2}\right|_{(x,y)}+\left.\frac{\partial^2\varphi}{\partial y^2}\right|_{(x,y)}$$

$$=\frac{\varphi(x+1,y)-2\varphi(x,y)+\varphi(x-1,y)}{(dx)^2}+\frac{\varphi(x,y+1)-2\varphi(x,y)+\varphi(x,y-1)}{(dy)^2} \tag{VI-21}$$

so (VI-4) becomes:

$$\begin{aligned}-k\frac{\partial I(x,y)}{\partial z}=&I(x,y)\big(\varphi(x+1,y)+\varphi(x-1,y)+\varphi(x,y+1)+\varphi(x,y-1)-4\varphi(x,y)\big)\\&+0.25\Big(\big(\varphi(x+1,y)-\varphi(x-1,y)\big)\vec{e}_x+\big(\varphi(x,y+1)-\varphi(x,y-1)\big)\vec{e}_y\Big)\cdot\\&\Big(\big(I(x+1,y)-I(x-1,y)\big)\vec{e}_x+\big(I(x,y+1)-I(x,y-1)\big)\vec{e}_y\Big)\end{aligned} \tag{VI-22}$$

where *dx* and *dy* were assumed to be 1 pixel. Formula (VI-22) can now be rewritten to a system of equations in $\varphi(x,y)$:

$$\begin{aligned}\varphi(x,y)=&\frac{1}{4}\big(\varphi(x+1,y)+\varphi(x-1,y)+\varphi(x,y+1)+\varphi(x,y-1)\big)\\&+\frac{1}{4}\big(\varphi(x+1,y)-\varphi(x-1,y)\big)\cdot\big(I(x+1,y)-I(x-1,y)\big)\\&+\frac{1}{4}\big(\varphi(x,y+1)-\varphi(x,y-1)\big)\cdot\big(I(x,y+1)-I(x,y-1)\big)+\frac{k}{4I(x,y)}\frac{\partial I(x,y)}{\partial z}\end{aligned} \tag{VI-23}$$

This system can easily be solved in an iterative way by estimating an initial solution, such as the zero matrix or a Gaussian, and filling this in into (VI-23). After a number of iterations this should give an approximation of the phase $\varphi(x,y)$.
For this method the periodic boundary conditions were used:

$$\begin{aligned}I(1,y)&:=I(N,y)\\I(x,1)&:=I(x,N)\end{aligned} \tag{VI-24}$$

which means that the image is numerically wrapped around a sphere.

In principle these calculations can approximate the solution pretty well, but it usually takes a while due to the large number of iterations.

f) Reweighing of Fourier terms

Here (VI-4) is again solved using Fourier series of the wavefront aberration $\varphi(x,y)$ and of the *z*-derivative of the intensity:

$$\begin{cases} F(x,y) = k\dfrac{\partial I(x,y)}{\partial z} = \sum_{u,v} F_{uv} e^{2\pi i(ux+vy)} \\ \varphi(x,y) = \sum_{u,v} \varphi_{u,v} e^{2\pi i(ux+vy)} \end{cases} \tag{VI-25}$$

Filling this in into the TIE (see [154]) gives a system of equations that for a homogeneous intensity I_0 can be simplified to:

$$\varphi_{u,v} = \frac{(ab)^2}{(2\pi)^2\left(u^2b^2 + v^2a^2\right)I_0} F_{u,v} \tag{VI-26}$$

with (a,b) the dimensions of the image. This provides a very fast method to obtain the Fourier transformation of the phase directly. An inverted Fourier transformation then provides the phase $\varphi(x,y)$ itself.
For non-homogeneous illuminations however the system of equations cannot be simplified, resulting again in lengthy calculations.

g) Fourier solution of inverted Laplacian[155, 156]

This is actually an extension of the reweighed Fourier terms method. Following the description given in [156] it starts from the TIE and the definition of a function $C(x,y)$:

$$\nabla_\perp C(x,y) = I(x,y)\nabla_\perp \varphi(x,y) \tag{VI-27}$$

So (VI-4) becomes the Poisson equation:

$$-k\frac{\partial I(x,y)}{\partial z} = \nabla_\perp \cdot \left(\nabla_\perp C(x,y)\right) = \nabla_\perp^2 C(x,y) \tag{VI-28}$$

Taking the inverse Laplacian of both sides, followed by a gradient gives:

$$-k\nabla_\perp \nabla_\perp^{-2}\left(\frac{\partial I(x,y)}{\partial z}\right) = \nabla_\perp C(x,y) \tag{VI-29}$$

which, using (VI-27), becomes:

$$\nabla_\perp \varphi(x,y) = \frac{-k}{I(x,y)}\nabla_\perp \nabla_\perp^{-2}\left(\frac{\partial I(x,y)}{\partial z}\right) \tag{VI-30}$$

Applying the divergence operator $\nabla_\perp \cdot$ and another inverse Laplacian to (VI-30), we find the solution:

$$\varphi(x,y) = -k\nabla_\perp^{-2}\left(\nabla_\perp \cdot \left[\frac{1}{I(x,y)}\nabla_\perp \nabla_\perp^{-2}\left(\frac{\partial I(x,y)}{\partial z}\right)\right]\right) \tag{VI-31}$$

It is very difficult to solve this equation directly. Instead a Fourier approach is used to arrive at[156]:

$$\varphi(x,y) = B\left(\varphi_x(x,y) + \varphi_y(x,y)\right) \tag{VI-32}$$

$$\begin{cases} \varphi_x(x,y) = \Im^{-1}\left\{\dfrac{u}{u^2+v^2}\Im\left\{\dfrac{1}{I(x,y)}\Im^{-1}\left\{\dfrac{u}{u^2+v^2}\Im\left\{\dfrac{\partial I(x,y)}{\partial z}\right\}\right\}\right\}\right\} \\ \varphi_y(x,y) = \Im^{-1}\left\{\dfrac{v}{u^2+v^2}\Im\left\{\dfrac{1}{I(x,y)}\Im^{-1}\left\{\dfrac{v}{u^2+v^2}\Im\left\{\dfrac{\partial I(x,y)}{\partial z}\right\}\right\}\right\}\right\} \end{cases} \tag{VI-33}$$

where $\Im\{\cdot\}$ denotes the Fourier transform, $\Im^{-1}\{\cdot\}$ the inverse Fourier transform, and (u,v) the coordinates in the Fourier plane. B is a normalization constant, needed to obtain quantitative phase results, with value:

$$B = -\frac{k}{2}NM(\Delta x)^2 = \frac{-\pi}{\lambda}NM(\Delta x)^2 \tag{VI-34}$$

Here λ is the wavelength of the light used, N and M the image size (in pixels) and Δx the pixel size.

This method is a very fast way to obtain the phase data, however a couple of restrictions apply as to what can be reconstructed:

- Equations (VI-33) become singular in the origin $(u,v) = 0$. Instead of a division by $u^2 + v^2 = 0$ a multiplication is used in this point.
- Points where $I(x,y) = 0$ also introduce singularities. The strong influence of low intensities can be avoided by not calculating the phase in those points below a certain intensity threshold.

Due to the speed of this algorithm and the absence of the need for uniform illumination, this is chosen as the preferred method for our further reconstructions.

VI.2.3 **Determination of $\partial I/\partial z$**

All of the above techniques require, besides the intensity distribution of the image, good knowledge of the derivative $\partial I(x,y)/\partial z$ near the best focus. This is usually approximated by taking the difference between two out-of-focus images, one in front of the best focus (I_- or 'Intrafocal image') and one behind best focus (I_+ or 'Extrafocal image'), and dividing by the separation $2\delta z$ between the two image planes. As in geometric optics rays are considered as straight lines these two images suffice to estimate the behavior of each individual ray near best focus.
Not much has been published about what the ideal separation $2\delta z$ should be. Keeping geometric optics in mind, it can easily be understood that smooth, slowly varying wavefronts require a large separation since the tilts of the rays will only be very small. Wavefronts that have a number of large local variations on the other hand need a shorter separation distance as their effect on the ray directionality is more pronounced.

Moreover image noise can also play a role here, but this can be easily reduced using the average of a number of defocus images at the same positions $\pm\delta z$ or the use of multiple defocus distances and combining the reconstructed phases by means of high- and low-pass filters[157].
If some prior knowledge is available about the wavefront to be determined the method described in [158] can be used. This uses the standard deviation of the noise and the mean curvature of the wavefront to estimate an upper and lower bound for $2\delta z$, as well as an optimal value. In case this optimal separation is too small to achieve by means of the available hardware it is possible in some cases to use interpolation[152] between the closest defocus images; however this procedure cannot improve the best attainable resolution.
Several papers[159, 160] also mention the use of one single defocus image for the calculation of $\partial I(x,y)/\partial z$. This will not be discussed here.

VI.2.4 **Influence of noise**

Up till now only ideal, noise free situations were discussed. Adding increasing quantities of noise can have a large influence on the final image quality, as brighter and darker areas shaped like irregular 'clouds' appear (Figure VI-2).
In an effort to model these effects we suppose the intrafocal image I_+ is superimposed with Gaussian (white) noise n_+ and analogously the extrafocal image I_- has noise n_-.Then it follows that:

$$\left(\frac{\partial I(x,y)}{\partial z}\right)_{distorted} \approx \frac{(I_+ + n_+) - (I_- + n_-)}{2\delta z} := \frac{I_+ - I_-}{2\delta z} + Noise(x,y) \qquad \text{(VI-35)}$$

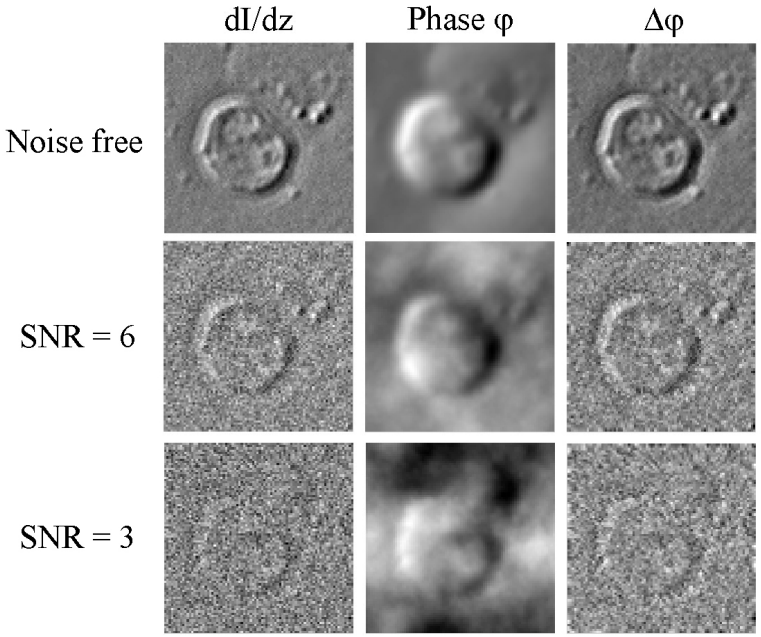

Figure VI-2: the effect of noise on the phase reconstruction (*Image: mouse blood cell, 40x, δz = 1.5μm*)

and, as formula (VI-33) is linear, we can say:

$$\varphi_{distorted}(x,y) = \varphi(x,y) + \varphi_{noise}(x,y) \qquad \text{(VI-36)}$$

In other words: the distorted phase reconstructions of Figure VI-2 are a linear superposition of an ideal phase term and a noise term. This means that if $Noise(x,y)$ or $\varphi_{noise}(x,y)$ is known the undistorted phase can be found using formulae (VI-35) and (VI-36). Unfortunately there is no direct way to determine either one of these functions. Sometimes however, in case the spatial frequencies of undistorted phase are much higher then those of the noise 'clouds', an estimation of $\varphi_{noise}(x,y)$ can be made. Here band-pass filters can be used to separate both components, as is illustrated in Figure VI-3 for two low-pass filters subtracted from a distorted phase[*]:

- Pixel-per-pixel average over nearest neighbors
- Low-pass Fourier filter

If the spatial frequencies of the image and the noise cannot be clearly separated, or when quantitative phase values are needed, the use of band-pass filters is not appropriate as it would inevitably have a large influence on the undistorted phase reconstruction as well.
In case several sets of defocus images are available, each taken at different separations δz, it is possible to use a combination of these sets using band-pass filters[157]. This method works well, but requires longer calculation times as the phase needs to be calculated multiple times.

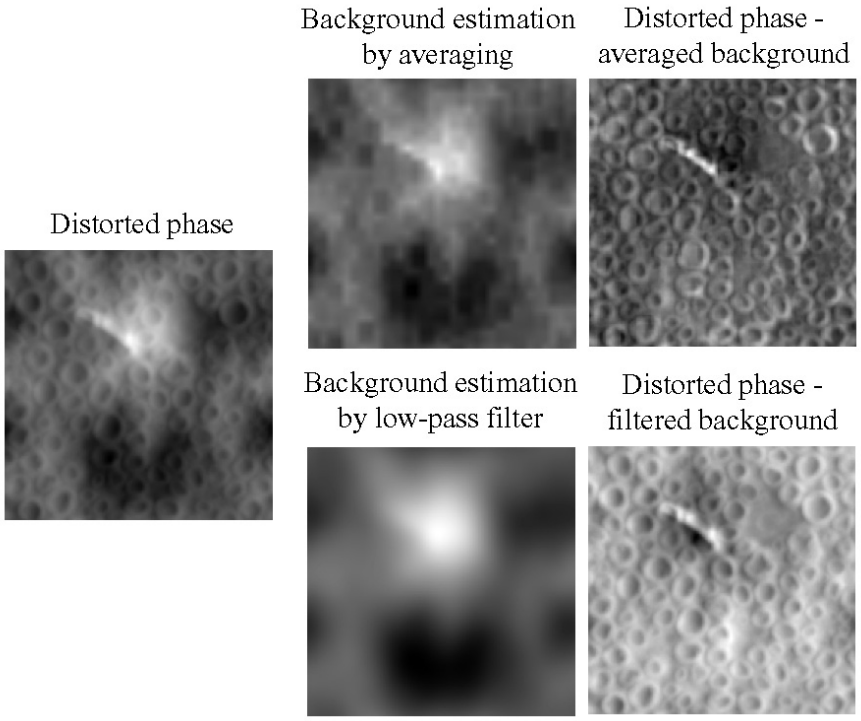

Figure VI-3: reducing the influence of noise in the reconstruction by means of low-pass filters (*Image: axons of nerve cells, 40x, δz = 1.5µm*).

[*] This method is used for illustrative purposes and is equivalent to applying a high-pass filter to the distorted phase. Using a low-pass filter on $\partial I/\partial z$ gives similar results.

VI.2.5 **Measuring defocus images**

There are several methods to obtain defocus images. The most common ones are described in the following.

a) Serial optical methods to obtain defocus images

One method sends the aberrated wavefront through a set of relay lenses (see Figure VI-4). By moving one of these lenses along the optical axis over a distance $\pm\delta z$ the defocus images I_+ and I_- are obtained.
In case of a plane wave (Figure VI-4a) the PSFs in the intra- and extrafocal planes will be exactly the same. After passing the second lens, both I_+ and I_- are therefore also exactly the same. Filled in in (VI-20) this results in $\varphi(x,y) = 0$. An aberrated wavefront however shows different PSFs in the intra- and extrafocal points (Figure VI-4b), so I_+ and I_- are no longer the same and (VI-20) can be used to calculate the phase.
This serial defocus method by means of lenses is often used in microscopic applications. Although it is easy to perform, it is not very convenient for real-time applications. A variation

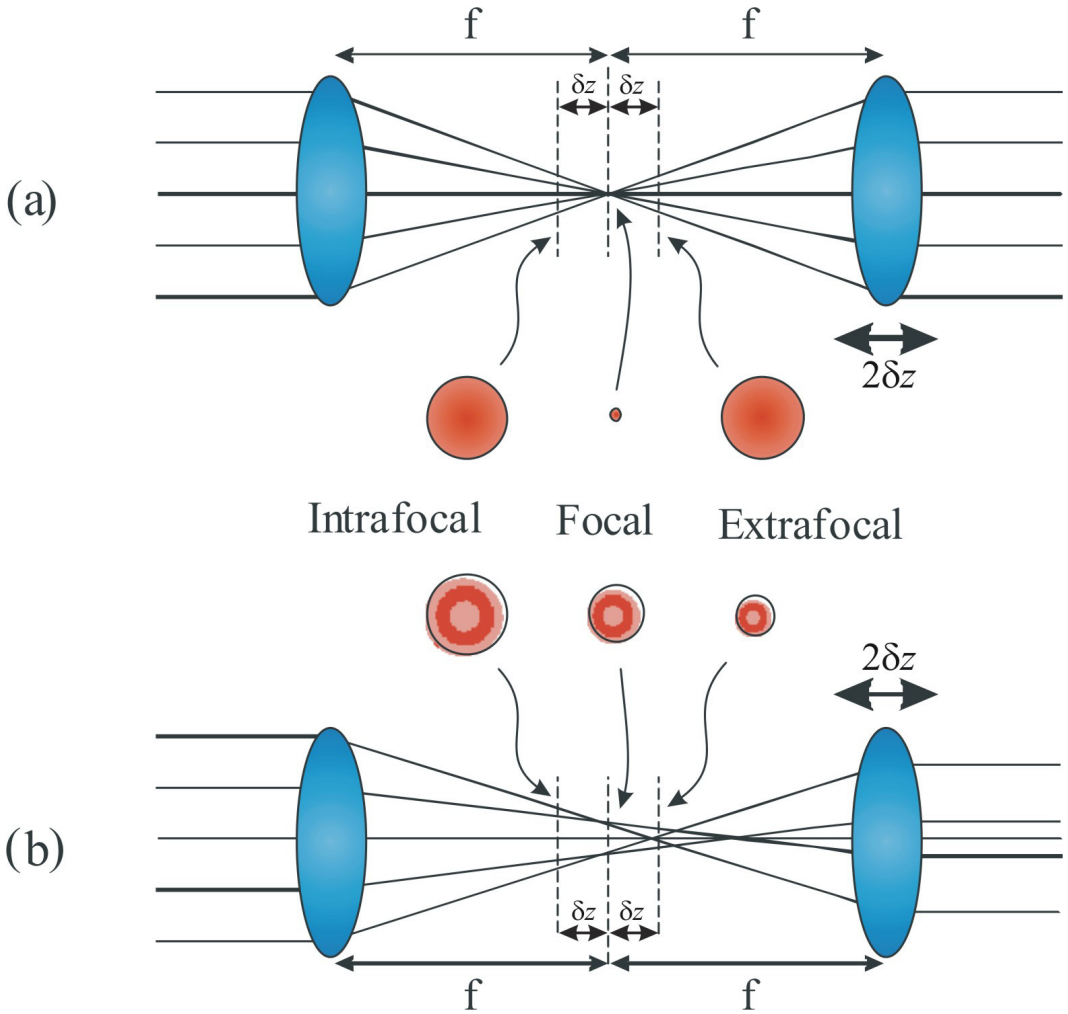

Figure VI-4: change of the PSF near the focus of a plane wavefront (*a*) *and a wavefront with defocus* Z_2^0 *and spherical aberration* Z_4^0 (*b*).

of this technique is found in astronomy[161], where it is important to monitor atmospheric turbulences in (nearly) real-time in order to compensate for the induced aberrations using adaptive optics. Here the set of relay lenses is immobile, but a membrane mirror is placed in the focal point in between.
By applying a certain vibration frequency to the mirror it is possible to monitor both defocus images with only a minimal time difference.

b) Parallel diffraction methods to obtain defocus images

A simultaneous recording of defocus images can be achieved by splitting the incident beam into three different channels, after which each of these channels is then given a different defocus state by means of a relay system as in Figure VI-4. In one channel a positive defocus is added (intrafocal), the second one remains unaltered (focal) and the third one gets a negative defocus (extrafocal).
One easy way to obtain these three channels is by means of a diffraction grating[162] (Figure VI-5a), which naturally provides a whole series of channels. Using pinholes the required diffraction spots can be selected for further use.
Combining setup Figure VI-5a with three sets of relay lenses may seem a little over-elaborate, but it provides a highly flexible system for the measurement of the defocus images.
A very elegant variation of the regular gratings are the 'quadratically distorted gratings' proposed by Blanchard and Greenaway[163, 164], that are designed in such a way that a certain amount of defocus is added to each channel (see Figure VI-5b). As a result the focal plane now contains the defocused PSF's of all three channels, which can be restored into the required defocus images by adding another lens. The disadvantage of this kind of grating is the loss of flexibility since the defocus introduced by a distorted grating is fixed.

c) Other parallel methods

These include the use of a number of beam splitters for the separation into different channels and the use of birefringent materials. Since neither one is mentioned in the literature these methods will not be discussed any further.

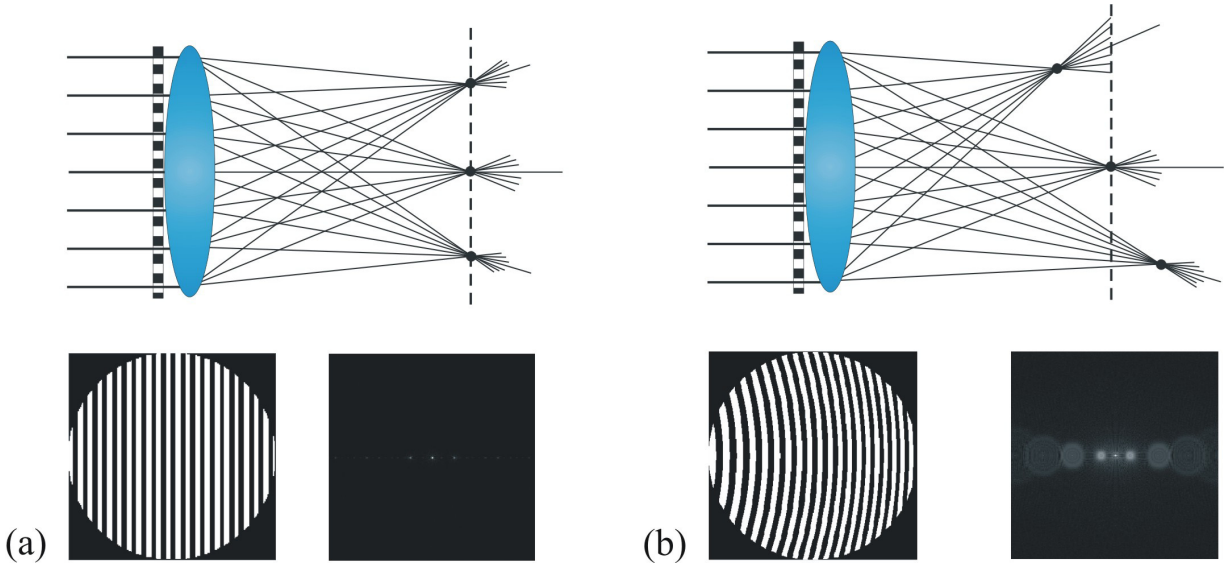

Figure VI-5: diffraction gratings and resulting diffraction patterns of (*a*) *regular grating and* (*b*) *quadratically distorted diffraction grating.*

VI.3 *Used materials*

All of the images in this chapter were recorded using a serial defocus technique by means of an Axiovert S135 inverted microscope (Zeiss, Oberkochen, Germany) with Kohler illumination (condenser NA = 0.55) equipped with a motorized (x,y)-stage (Märzhauser, Wetzlar, Germany), focus-drive and a PAL monochrome CCD-camera (Adimec MX5). The available objectives were 5x plan neofluar, 10x phase contrast, 20x LD achroplan and 40x LD achroplan.

VI.4 *Results*

VI.4.1 Comparison of reconstruction techniques

First we compare the quality of the reconstructions and the time required to obtain them for five of the above techniques: Green's function solution (VI.2.2b), Zernike polynomial fit (VI.2.2c), direct iterative solution (VI.2.2e), reweighed Fourier terms in case of uniform illumination (VI.2.2e) and the Fourier solution of the inverse Laplacian (VI.2.2g). The results are shown in Table VI-1 and Figure VI-6.
All calculations were done using Matlab 6.1 on a 1.1MHz computer with 512Mb RAM for a 60x60 image shown in the top of Figure VI-6. Since most of these techniques used a 'filter matrix' of some kind, this part of the calculations is shown separately.

It can be seen that the Green's function method needs a long time to generate the [N^2xN^2] matrix, but that once this is finished the computation is done quickly. This suggests that this method can be sped up considerably in case the filter matrix is determined on forehand (as suggested in [146]). However this is not very practical in case images of different sizes are processed. Also due to the large size of the filter matrix, only images of maximum 4000 pixels can be calculated on the computer above.
The same was found for the reconstruction by Zernike fit, which was done using polynomials of up till the 30th order (495 terms). This results in a large matrix M (VI-17) and lengthy calculations. However, as for the Greens' function solution, the filter matrix can be precalculated.
The direct iterative solution does not use a filter matrix and goes straight to the calculation itself. The entire procedure takes over 13s for 100 iterations, which is shorter then for the previous techniques. Using a faster converging iteration could improve this.
The calculation times of the last two techniques are remarkably short, both for the determination of the filter matrix as for the phase calculation itself. As in these cases the size of the matrix is [NxN], much larger images can be processed (up to 16 Mpixels).

Table VI-1: calculation times for the 60x60 image in Figure VI-6

	Filter matrix (s)	Calculation (s)	Max. # pixels
Green's functions	349	4.62	$4 \cdot 10^3$
Polynomial fit (495 Zernike terms)	27.75	0.50	$12 \cdot 10^3$
Direct iterative solution (100x)	/	13.38	Tested till $25 \cdot 10^5$
Reweighing Fourier terms	0.08	0.12	$16 \cdot 10^6$
Fourier sol. of inv. Laplacian	0.09	0.11	$16 \cdot 10^6$

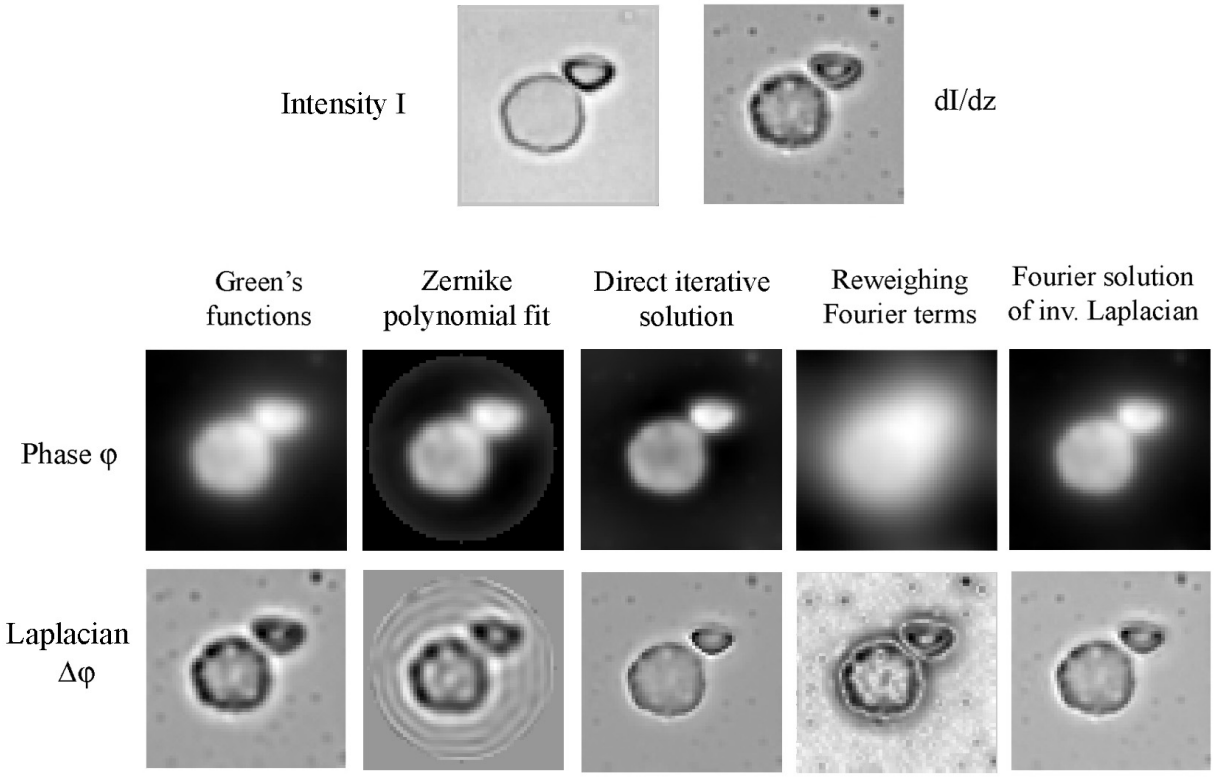

Figure VI-6: phase reconstructions using five different algorithms (Image: mouse blood cell, 40x, $\delta z = 10\ \mu m$).

Comparing the phase reconstructions by the five techniques (Figure VI-6, center row), it can be seen that all techniques give similar results. The reweighed Fourier technique however shows a very blurred reconstruction, possibly due to the fact that the requirement of uniform intensity, needed for this technique, was not met.
In order to confirm that these reconstructions show the actual phase distribution the Laplacian $\Delta\varphi$ is also calculated (bottom row), which should approximate $\partial I/\partial z$ (see formula VI-7). All techniques show a reasonable (reweighed Fourier) to good (other four) correspondence with $\partial I/\partial z$. Note the ring shaped artifacts around the object in the Zernike reconstruction Laplacian.

From the previous we can conclude that the short calculation times and accurate results of the second Fourier technique make this the most interesting method. For the following calculations only this algorithm is used unless stated otherwise.

VI.4.2 **Comparison with Zernike phase contrast**

As up till now there is no direct method to determine the phase of an object, a couple of measures need to be found that can be used as a quality check for the reconstructed phase. A first example was given in the previous paragraph, where the Laplacian of the phase was used. Another, more direct way is the use of Zernike phase contrast images, which are defined by:

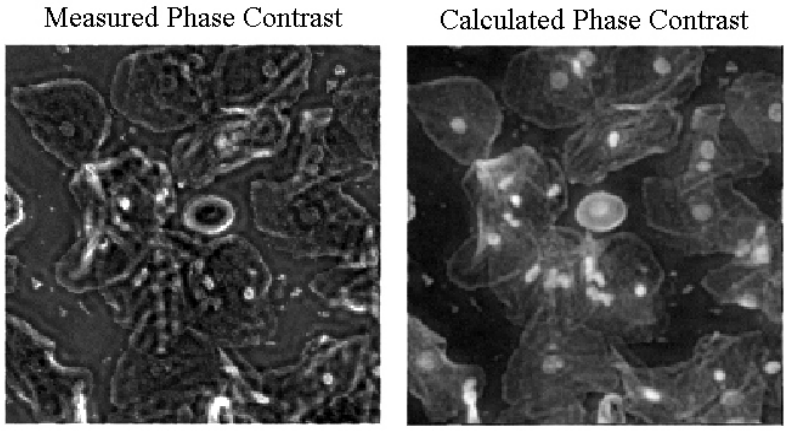

Figure VI-7: Comparison of experimentally measured and calculated bright phase contrast images (*Image: cervix cells, 10x, δz = 10 µm*).

$$I(x,y) = \left| \Im^{-1} \left\{ \left[\delta(0,0) + (1 - \delta(0,0)) a e^{\pm i\pi/2} \right] \cdot \Im\left\{ I(x,y) e^{i\varphi(x,y)} \right\} \right\} \right|^2 \qquad \text{(VI-37)}$$

where $\delta(0,0) = 1$ in the origin and $= 0$ elsewhere. Usually the transmission of the phase plate a is also defined; here the value 0.5 is used.
This is demonstrated for cervix cells in Figure VI-7, where the left image is experimentally measured and the right image is calculated using (VI-37). Comparing these images it can be seen that both images are similar, with the noteworthy difference that in the calculated image the cell nuclei have considerably more contrast.
Since brighter and darker regions in both images correspond well, this gives a second indication that the phase reconstruction is accurate.

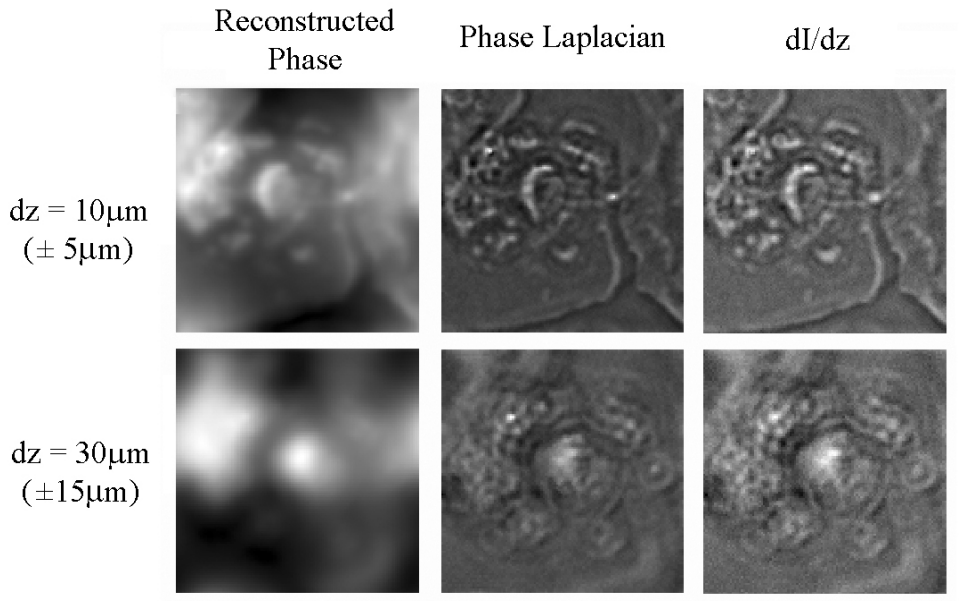

Figure VI-8: phase reconstructions of at different separations between the intrafocal and the extrafocal plane (*Image: cervix cells, 20x*).

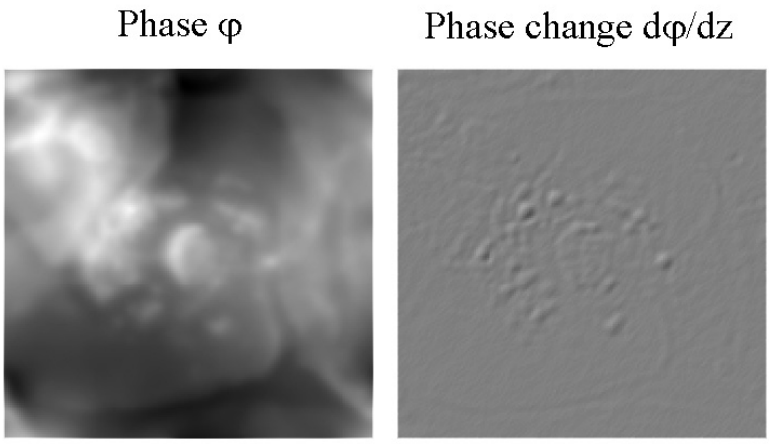

Figure VI-9: phase changes in the sample of Figure VI-8 over a distance dz = 10μm in the same grayscale as the phase (*intensity multiplied 2000x*).

VI.4.3 **Dependency of phase resolution with *dz***

This was briefly discussed in paragraph VI.2.3 and illustrated in Figure VI-8 for a sample of cervix cells. Comparing two separations (*dz = 10 μm* and *30 μm*) it can be clearly seen that smaller separations *dz* between the intrafocal and extrafocal planes lead to a higher resolution.

Further, as suggested by formula (VI-3) and reference [165], not only the intensity *I* changes along the optical axis but also the phase *φ*. Figure VI-9 shows that especially areas with rapid phase changes or with a strong curvature tend to vary along the optical axis due to both the gradient and Laplacian terms in (VI-3). However this effect only plays a minor role as the amplitude of $\partial\varphi/\partial z$ is about 2000 times lower than that of the phase.

VI.4.4 **Dependency on pupil shape**

In a first step towards the problem of ocular wavefront reconstruction the influence of a pupil is studied. Suppose now a homogeneously illuminated circular pupil. Here three basic effects can occur with the change of focus, each associated with a typical phase error:

- Change in pupil size (Figure VI-10, top row): this gives an annular $\partial I/\partial z$ which reconstructs to a defocus.
- Change in pupil shape (Figure VI-10, second row): $\partial I/\partial z$ shows four lobes, both positive and negative, which is reconstructed to an astigmatism.
- Change in pupil position (Figure VI-10, third row): $\partial I/\partial z$ has two long lobes, reconstructing to a combination of tilt and coma.

In optical systems the $\partial I/\partial z$ will be much more complex then in the above examples as a large number of local combinations between shape and shift variations will occur. These combinations are the result of higher order aberrations.
In the reconstruction of a pupil special attention is needed the choice of the image size with respect to the pupil size to avoid ‘clipping’ of the pupil. As can be seen in Figure VI-10

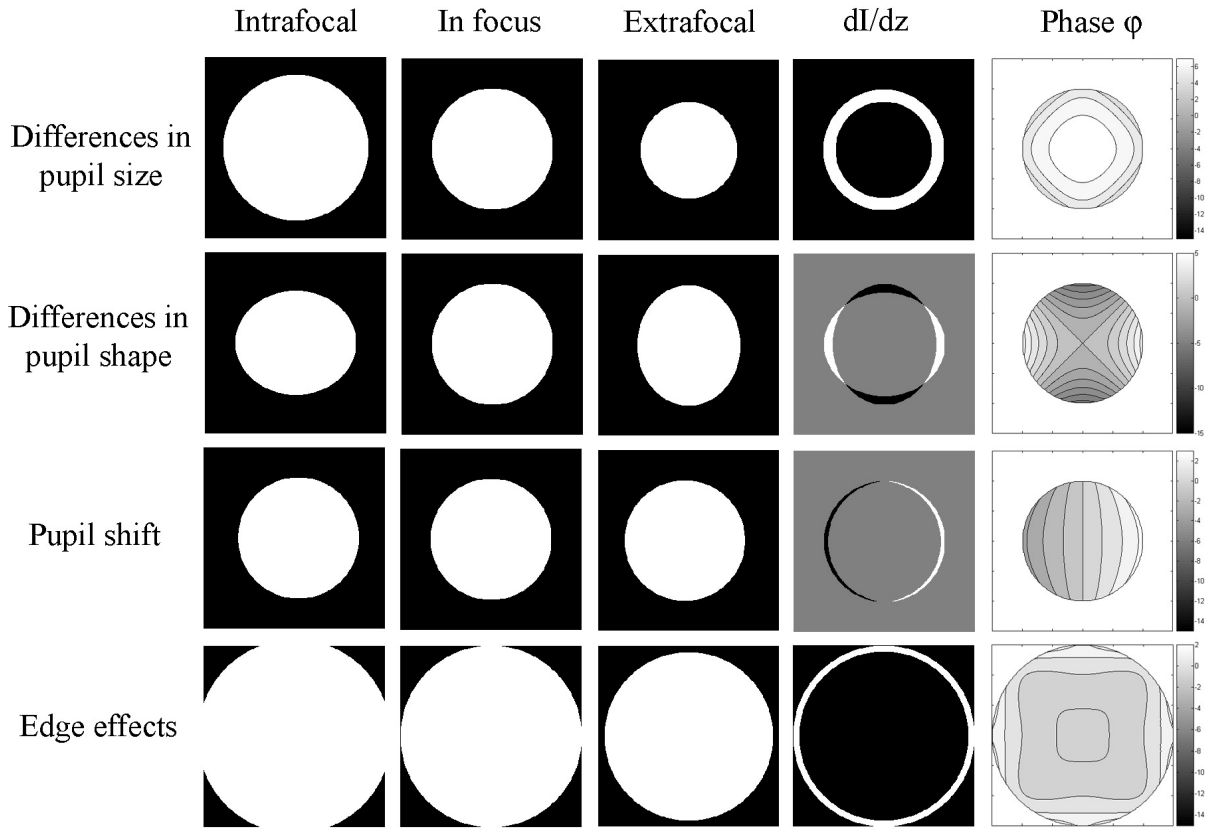

Figure VI-10: phase reconstructions of basic pupil shapes.

(bottom row) this has a strong influence on the reconstructed wavefront, which has obtained a square shape and an inverse sign compared to the top reconstruction.

VI.5 *Conclusions*

The previous examples have shown that:

- Curvature sensing is capable of achieving pixel-size resolutions, far superior to most of the non-interference based methods described in I.5.
- The different reconstruction methods give similar results and differ mainly in calculation time and maximum reconstructable image size.
- The 'Fourier solution of inverted Laplacian' method from VI.2.2g) was found to give quick and accurate results as was verified by the Laplacian of the calculated phase compared with $\partial I/\partial z$ and by phase contrast.
- Noise can seriously affect the reconstruction and can only be neutralized in very specific circumstances. Minimizing image noise prior to the calculations is a must.
- The method gets more sensitive to minute phase variances for short separation distances δz between the intrafocal and extrafocal planes. As these short distances increase the influence of noise, the use of a high quality camera with a low SNR is advised.

Chapter VII Design and first results of a curvature sensing aberrometer

With the theories described in previous chapter and the device described in [166] in mind, a curvature sensing aberrometer (CSA) can be designed. The design of the following devices and the measurements performed with them were done by Andrey Larichev from the Institute of Laser Information Technologies of the Stat University of Moscow. The phase calculations were done by our group using the methods described in the previous chapter.

VII.1 *CSA Design*

VII.1.1 **Proof of principle using the serial lens method**

A first proof of principle is given by means of a lenticular CSA (Figure VII-1). The source is an IR diode laser (λ = 850nm) the light of which is directed through a beam expander with a 60µm pinhole placed in between. The pinhole serves as an approximated point source. Next the light passes through the object (a glass plate or trial lens) that aberrates the light. A static relay system (L_1 and L_2) projects the image of the object on a CCD camera mounted on a linear translation stage. The degree of defocus in the image is controlled by the translation of the CCD camera.
The main disadvantage of this method is that it is serial, meaning that the measurement takes a certain time in which an eye can have moved. As shown in VI.4.4 even small movements can have a large influence on the wavefront reconstruction, rendering this setup less suitable for ocular wavefront sensing. However for the measurement of a static test eye the above objection is no longer valid, making it possible to do a second proof of principle. The technical parameters of the lenticular serial CSA device are given in Table VII-1.

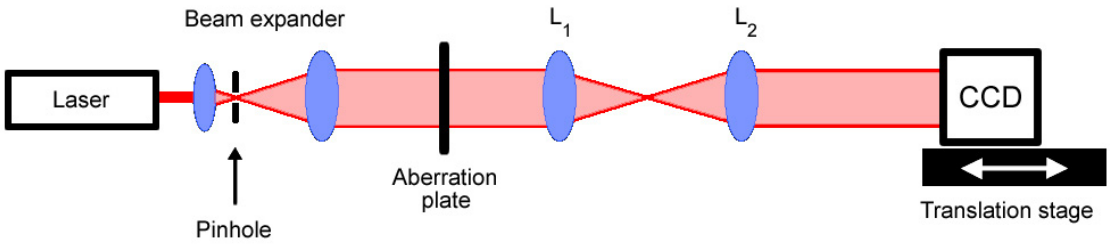

Figure VII-1: serial curvature sensor, using lenses, applied to an aberrated glass plate or trial lenses.

Table VII-1: technical parameters of the CSA components

	Lenticular CSA (PoP)
Light source	IR diode laser (850nm)
f_{L1}	50 mm
f_{L2}	50 mm
Grating period	/
CCD camera(s)	10 bits
Lens translation stage	Linear stage with µm precision

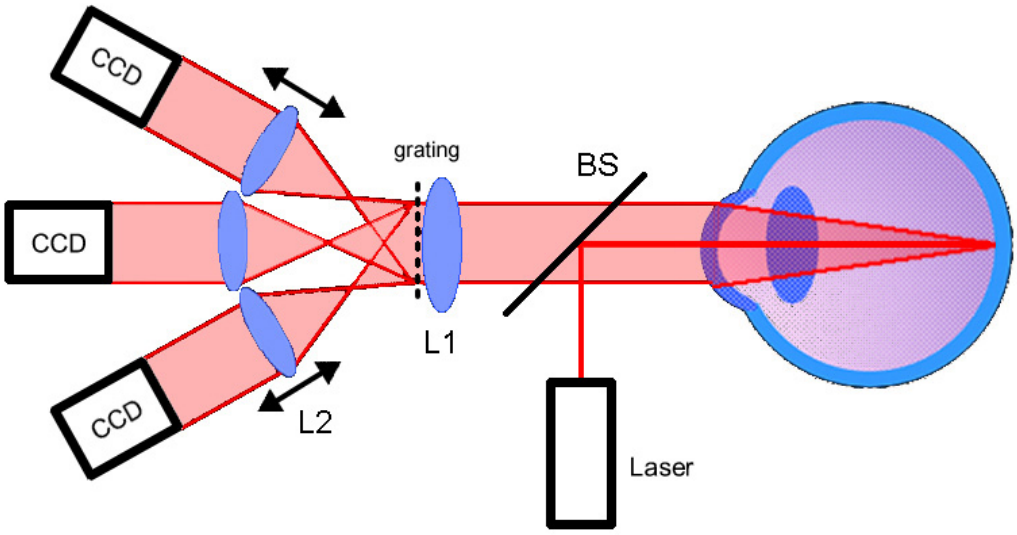

Figure VII-2: parallel curvature sensor, using grating.

VII.1.2 **Design of a parallel CSA using the grating method**

In order to avoid motion artifacts during the recording phase a parallel recording setup needs to be devised (see Figure VII-2 and VI.2.5b). Here the aberrated light beam coming from the eye is split up into three separate channels by a linear grating. Next each channel is relayed through a telescopic system and projected on a CCD camera. The second lens of each relay system can be shifted to obtain defocused images with the desired separation δz.
The largest disadvantage of this system is that it is much more elaborate and costly in nature than the lenticular CSA. However it also creates the possibility of recording short wavefront movies that enable the study of temporally changing wavefronts.
In practice this setup can easily be made by modifying a Hartmann-Shack style aberrometer, such as the MultiSpot discussed in Chapter II.

VII.2 *First results*

VII.2.1 **Verification of the method**

As a verification of the technique the setup from Figure VII-1 was used to determine the aberrations of trial lenses, the results of which are shown in Figure VII-3. Note that the alignment of the trial lenses both in the x- and the y-direction as along the optical axis is not always equally good, so the phase reconstruction might have been influenced a little.
For the non-aberrated test eye (Figure VII-3, centre) a slight defocus and spherical aberrations can be expected due to the spherical nature of the test eye's lens. Adding different amounts of defocus (Figure VII-3, top row) or astigmatism (Figure VII-3, bottom row) to the test eye also shows consistent patterns.

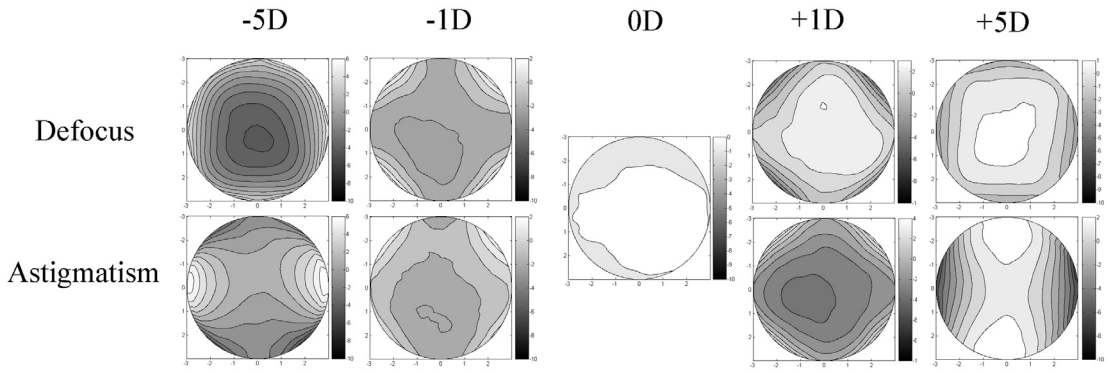

Figure VII-3: wavefront reconstructions of a model eye combined with trial lenses.

In order to estimate the quality of these reconstructions the linear Z_2^0-model defined in Chapter III is used (Figure VII-4). Again the linear fit coefficients for both the defocus and the astigmatism can be calculated (Table VII-2) and it is found to agree reasonably with the model. The deviations from the model are probably due to misalignments of the trial lenses.

However for this verification only 5 different refraction values were used. A better verification can be obtained if more measurements were included, but these were not yet available at the time of writing.

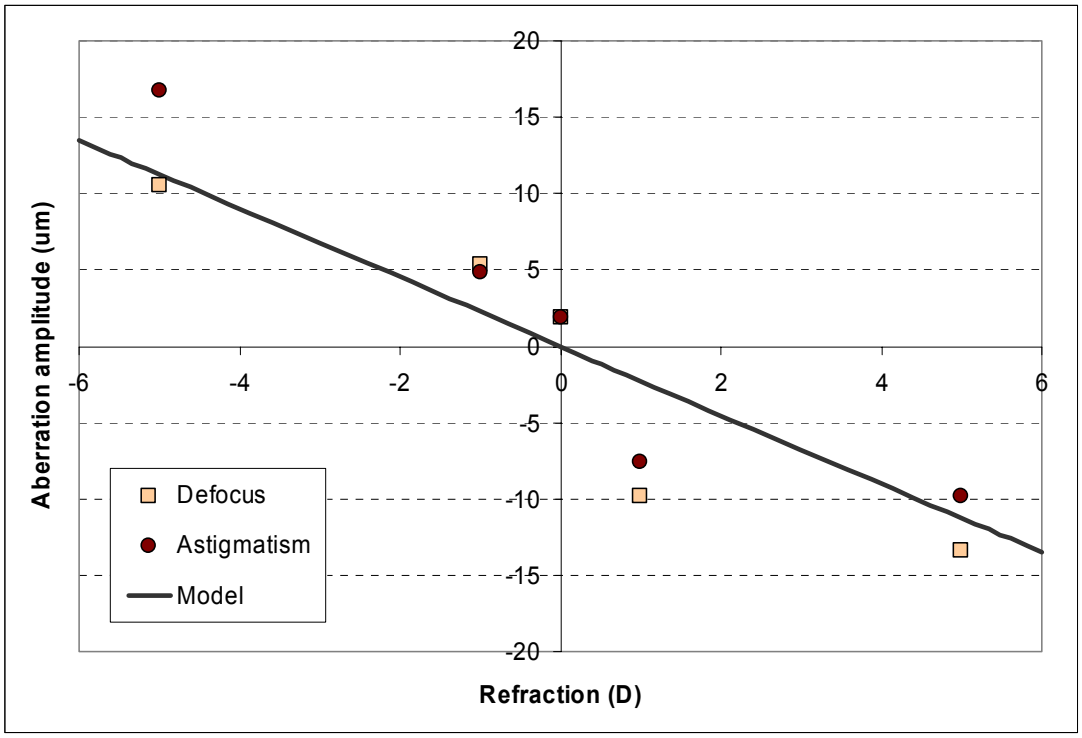

Figure VII-4: change in amplitude of Zernike terms Z_2^0 and the combined astigmatism terms Z_2^{-2} and Z_2^{+2} with refraction of the used trial lens.

Table VII-2: linear regression parameters of the datasets given in Figure VII-4

	a ($\mu m/D$)	b(μm)	R^2
Defocus (Z_2^0)	-2.5856	-1.092	0.8462
Astigmatism ($Z_2^{\pm 2}$)	-2.7863	1.204	0.8932
Model	**-2.25**	**0**	**1**

VII.2.2 **Artificial test eyes and human eyes**

Attempts to obtain measurements of artificial eyes using the setup in Figure VII-2 are currently being made. However till date this could not yet be done due to a low light return from the retina.
Later this year these experiments will be modified to include a pulsed laser instead of a continuous wave laser. This way higher intensities can be sent to the retina, which will hopefully lead to a better signal to noise ratio. Once this is achieved, the experiments could be expanded to human eyes as well.

VII.3 *Conclusions*

The curvature sensing technique promises interesting applications in ocular aberrations sensing. However many more experiments need to be done to assess the merits of this method compared to more traditional methods such as Hartmann-Shack.

Epilogue: conclusions and thoughts on the future expansion of this work

In this work we have presented different ways to assess the ocular aberrations.

Part I established that overall the 6 aberrometers under study gave similar results for the eyes in the test group, but that a number of important parameters showed considerable differences. The most notable differences were the large spread in variance, the apparent underestimation of several Zernike terms by the Nidek OPD-scan compared to the other devices and the apparent overestimation of astigmatism by the Tracey Visual Function Analyzer. As for the technical study it was seen that none of the devices fulfilled each of the minimal requirements we defined, but that the WaveLight Allegretto, the MultiSpot and the Tracey Visual Function Analyzer had implemented most of them.
In the future this part can be extended to the technical and statistical comparison of the customized excimer laser systems that use data from aberrometers to obtain the best possible personalized ablation. The questions that need to be asked are the same as for the aberrometers, and can be roughly formulated as follows: will the quality of the patient's refractive treatment depend on his ophthalmologist's choice in aberrometer/ excimer laser system, or will all systems give similar results?
The statistical comparison can be performed on a number of artificial corneas, made of hemispherical pieces in PMMA[*]. In one possible setup the wavefront of one person's is measured by an aberrometer, after which the correction is burned on several plates of PMMA. Next the profile of the PMMA plate is compared with its original profile and the ablation is known. Comparing the repeated ablation on the different plates will show the repeatability of the ablation. This can be done for eyes in a number of refractive conditions. Alternatively an artificial test eye can be used as the original aberration.
This study may also be expanded to include the function of eye trackers, which serve to compensate for movements of the patient's eye during the treatment.

In Part II the refraction corrected laminography was introduced as a method to obtain low-resolution 3D phase reconstructions of the ocular anterior segment. Overall the quality of the 3D reconstructions was not very good with both techniques proposed. Only the rough distribution of aberration sources could be seen, which mostly corresponded with the refractive index distribution in the eye.
The pupil plane reconstruction on the other hand was more informative and showed clear inhomogeneities between the nasal and the temporal sides for several subjects. This was a clue that their crystalline lenses may have tilted.
However these results only present the first steps on the path of refractive ocular phase laminography. Many different improvements can be proposed that could only partially be included in this work:

- High-resolution wavefront maps should be used, such as zonal reconstruction to obtain the highest resolution possible.

[*] Polymethyl methacrylate; a polymer often used for contact lenses and for testing the beam profiles of excimer lasers.

- The aberrometer used should be able to reconstruct non-circular pupils. Till date the WASCA (COAS) system is the only commercially available system with this ability.
- In the calculations the pupil shape needs to be taken into account in order to find tilted pupils.
- Smearing is reduced with increasing angle of incidence ψ, but at the same time the reconstructable volume decreases. For the Navarro model this is optimized at about $\psi = 48°$, although this may differ for real eyes.
- The reconstruction should use as many projections as possible.
- Better reconstruction methods need to be used, such as e.g. ART. Finding a good method might however pose a number of problems since it is not desirable to record the large number of projections that are usually needed for tomography. A number of suggestions for improvement can be found in [118], [167], [168] and [169].
- In stead of a standard eye model a number of biometrical parameters should be taken into account, as was done in Table V-1.
- The use of internal aberrations alone, obtained by subtracting the corneal aberrations from the total aberrations, will also improve the quality of the reconstructions. This is easy for anterior corneal aberrations alone, as is done by Atchison in reference [170], but rather difficult for the total corneal aberrations. One device that could potentially provide this information is the Bausch & Lomb Orbscan, but the software necessary for this kind of analysis is not available.

Part III also presented a work in progress. Till date this is limited to a successfully concluded proof of principle experiment, but, as written in Chapter VII, many different experiments needs to be done before the CSA can be used as a clinical aberrometer.

The ultimate continuation of this thesis would a Part IV that cannot be written yet: ocular phase laminography, based on curvature sensing images and using different, more reliable tomographic reconstruction techniques. With any luck, we hope to present this within a couple of years.

Samenvatting en Conclusies

De meeste ogen zijn verre van volmaakt. Ieder oog heeft een unieke set van optische aberraties die het invallende licht beïnvloeden. Deze invloeden kunnen gaan van lichtjes wazig zicht, tot vervormde of zelfs meervoudige beelden.
Tot voor kort was de enige manier om hieraan te verhelpen de toevoeging van een extra optisch element, zoals een bril of contactlenzen. Het aanpassen van deze twee types van optische correcties vereist enkel wat algemene kennis over de oogrefractie, maar de meeste patiënten behalen er goede resultaten mee. Toch er blijven nog wat kleine, niet-gecorrigeerde aberraties over die volmaakt scherp zicht in de weg staan.
Met de introductie van refractieve chirurgie kwamen er een aantal nieuwe methodes op de markt die trachtten het hoornvlies een zodanig andere vorm te geven dat de aberraties worden geminimaliseerd, hetzij door incisies in het hoornvlies, hetzij door middel van laserablaties. De eerste generaties van lasersystemen konden alleen maar gelijkaardige correcties aanbrengen als wat bereikt kon worden met een bril. Maar in enkele jaren tijd evolueerden deze lasersystemen zich tot flexibele platforms die in theorie het inverse van de oculaire aberraties kunnen 'etsen' op het hoornvlies. Om dit op een goede manier te kunnen doen is wel een zeer gedetailleerde kennis van het golffront noodzakelijk.

Eén manier om deze kennis te verkrijgen is door te zoeken naar de oorsprong van de oculaire aberraties, zoals getoond in deze thesis. Een aantal verschillende zaken die aberratiemetingen en de lokalisatie van de aberratiebronnen binnen het oog beïnvloeden worden hierin beschreven.

Eerst wordt er in **Hoofdstuk I** een inleiding gegeven tot de belangrijkste concepten die nodig zijn voor aberrometrie, zoals de meting van een golffront, een aantal afgeleide grootheden (RMS, PSF, MTF,…) en een rudimentaire beschrijving van de verschillende aberrometertypes.

Na deze introductie wordt er in **Deel I** ingegaan op de overeenkomsten en verschillen tussen 6 commerciële aberrometers en de vraag hoe betrouwbaar de metingen zijn die deze machines leveren. We vragen ons ook af of ieder toestel hetzelfde resultaat zou geven indien het werd toegepast op hetzelfde oog. Hierbij leggen we het accent niet op welk toestel 'het beste' is, maar eerder op een aantal minimale vereisten waaraan een goede aberrometer volgens ons zou moeten voldoen om betrouwbare en reproduceerbare metingen te kunnen leveren (zie **Hoofdstuk II**). Deze technische vergelijking toont dat geen enkele van de bestudeerde toestellen voldoet aan al onze minimum eisen, maar dat de WaveLight Allegretto, de MultiSpot en Tracey Visual Function Analyzer toch de meeste ervan hebben geïmplementeerd.
Vervolgens trachten we in **Hoofdstuk III** om de klinische betrouwbaarheid van de toestellen te bepalen door een reeks metingen te doen op een vaste groep ogen en een statistische analyse van het resultaat. Het blijkt dat alle 6 aberrometers gelijkaardige resultaten geven in hun golffrontmetingen, maar dat er toch belangrijke verschillen kunnen optreden als deze gegevens in verder detail worden geanalyseerd. Zo is er bijvoorbeeld een sterke spreiding in de grootte van de variantie tussen de verschillende toestellen en is er één toestel, de Nidek OPD-scan, dat bepaalde symmetrieën lijkt te onderschatten ten opzichte van de andere

toestellen. Daarnaast lijkt de Tracey Visual Function Analyzer dan weer het astigmatisme te overschatten.

Nadat de kwaliteit van de golffrontmetingen is vastgesteld, kunnen we in **Deel II** beginnen met de zoektocht naar de oorsprong van de oculaire aberraties. Dit leidt ons langs een aantal gekende tomografische technieken en hun eigenschappen (**Hoofdstuk IV**). Vervolgens worden deze methodes herwerkt om de oogrefractie in rekening te kunnen brengen. Dit laat ons toe om een 3D fasereconstructie te maken van het voorste oogsegment, gebaseerd op een aantal off-axis golffrontmetingen. De beschrijving van deze refractiegecorrigeerde faselaminografie en de manier waarop de off-axis golffrontmetingen werden verkregen wordt gegeven in **Hoofdstuk V**. Op deze manier verkrijgen we een aantal lage-resolutie fasereconstructies die globaal overeenkomen met de brekingsindexverdeling in het oog. De kwaliteit van de 3D reconstructies zijn niet zo goed, voornamelijk door 'uitsmering', een effect waarbij een sterke fasestoring in een gebied de reconstructie in een ander gebied beïnvloedt. In de epiloog worden nog een aantal suggesties gegeven over hoe deze reconstructies in de toekomst nog verbeterd zouden kunnen worden, zoals het gebruik van andere reconstructietechnieken (bijvoorbeeld: ART) en hoge-resolutie off-axis golffrontmetingen en het aftrekken van de golffrontbijdrage van het hoornvlies van de off-axis metingen.
De reconstructies van het fysiologische pupilvlak zijn daarentegen wel goed gelukt. Hier werden duidelijke inhomogeniteiten gevonden, wat kan duiden op een lichte scheefstand of verschuiving van de ooglens bij sommige mensen.

Deel III introduceert curvature sensing als een nieuwe hoge-resolutie techniek om golffronten te meten. Deze hoge resoluties kunnen worden gebruikt om golffronten in groter detail te bestuderen, maar ook om betere off-axismetingen voor laminografische reconstructies te kunnen doen. In **Hoofdstuk VI** wordt curvature sensing, een groot aantal fasereconstructietechnieken uit de literatuur en de eigenschappen van deze technieken besproken voor algemene microscopietoepassingen. Dit wordt uitgebreid in **Hoofdstuk VII**, waar een proof-of-principle-opstelling wordt voorgesteld die de aberraties van lenzen kan meten. Dit is succesvol gedemonstreerd voor een aantal ofthalmologische proeflenzen, zowel voor defocus als voor astigmatisme, maar nog niet voor menselijke ogen.

List of publications

- *Jos J. Rozema*, Dirk van Dyck, Frans J. Van de Velde, **"Phase Contrast Aberroscope"**: US patent, no. US 6002484 (1999)

- *Jos J. Rozema*, Dirk E. M. Van Dyck, Marie-José Tassignon, **"'Clinical comparison of 6 aberrometers I: technical specifications"**, JCRS (in press)

- *Jos J. Rozema*, Dirk E. M. Van Dyck, Marie-José Tassignon, **"Clinical comparison of 6 aberrometers II: statistical comparison on a test group"**, JCRS (in press)

Bibliography

[1] W. E. Leonard, verses 84-88, 'The Fragments of Empedocles', The Open Court Publishing Company, Chicago (1908); available at http://classicpersuasion.org/pw/empedocles/empalleng.htm

[2] H. Helmholtz, "Die neueren Fortschritte in der Theorie des Sehens," Preussische Jahrbücher, Jahrgang (1868). Quoted from republication in "Populäre Wissenschaftliche Vorträge", Zweites Heft, Zweite Auflage, Verlag Vieweg, Braunschweig, pp. 1–98, quotation on pp. 21–22 (1876).

[3] based on L. Pedrotti, F. Pedrotti, 'Optics and Vision', chapter 1, Prentice Hall, London, (1998)

[4] Aristotle, 'Sense and the Sensible', 350 BC (translated by J. I. Beare)

[5] F. Maurolycus, 'Photismi de Lumine', Translated by H Crew; Macmillian (1940)

[6] L. Da Vinci, 'Notebooks of Leonardo Da Vinci', Vol 1, paragraph 78, Translated by Jean Paul Richter (1888); available at http://www.knowledgerush.com

[7] Johannes Kepler, 'Ad Vitellionem paralipomena' (1604)

[8] T. Young, 'The Bakerian Lecture: On the Mechanism of the Eye', Phil. Trans. R. Soc. London, **91** , pp 23 (1801); available at http://gallica.bnf.fr

[9] C. Scheiner, 'Oculus, hoc est fundamentum opticum...', Oeniponti, Innsbruck, p 17 (1619); available at http://gallica.bnf.fr

[10] H. von Helmholtz, 'Handbuch der Physiologischen Optik', (1867); available in French at http://gallica.bnf.fr

[11] L. Seidel, Astr. Nachrichten, **43**, 1027, pp. 289 et seq.

[12] M. Born, E. Wolf, 'Principles of Optics', 6th edition, chapter 5, Cambridge University Press, Cambridge, pp.211 et seq. (1980)

[13] A. Ivanoff, 'Les aberrations de l'oeil. Leur role dans l'accommodation' , Éditions de la Revue d'Optique Théorique et Instrumentale, Paris (1953)

[14] M. Smirnov, 'Measurement of the wave aberration of the human eye', Biofizika **6**, pp.687-703 (1961)

[15] H. Howland, B. Howland, "A subjective method for the measurement of the monochromatic aberrations of the eye", J. Opt. Soc. Am. A, **67**, 1508-1518 (1977)

[16] S. Marcos et al., 'Investigating sources of variability of monochromatic and transverse chromatic aberrations across eyes', Vision Research, **41**, pp. 3861-3871 (2001)

[17] D. Malacara, 'Optical Shop Testing', appendix 1, John Wiley & Sons (1992)

[18] A. Gullstrand, Appendix II in: H. von Helmholtz 'Handbuch der Physiologischen Optik', 3rd edition, part I., p.350-358. (1909)

[19] A. Gullstrand, 'Bidrag till astigmatismens teori' (Contribution to the theory of astigmatism), PhD thesis (1890)

[20] R. Navarro, J. Santamaria, J. Bescos, 'Accommodation-dependent model of the human eye with aspherics', J. Opt. Soc. Am. A, **2**, pp. 1273-1281 (1985)

[21] I. Escudero-Sanz, R. Navarro, 'Off-axis aberrations of a wide-angle schematic eye model', J. Opt. Soc. Am. A, **16**, pp. 1881-1891 (1999)

[22] G. Smith et al. 'Designing lenses to correct peripheral refractive errors of the eye', J. Opt. Soc. Am. A, **19**, pp. 10-18 (2002)

[23] values taken from:A. Elkington, H. Frank, M. Greaney, 'Clinical Optics', 3rd edition, Blackwell Science, Oxford, pp102 et seq. (1999)

[24] L. Thibos, , M. Ye, X. Zhang, A. Bradley, 'Spherical Aberration of the Reduced Schematic Eye with Elliptical Refracting Surface', Optometry and Vision Science, **74**, pp. 548-556 (1997)

[25] L. Thibos et al., 'The Chromatic Eye: a new model of ocular chromatic aberration', Appl. Opt. 31, pp. 3594-3600 (1992)

[26] M. Born, E. Wolf, 'Principles of Optics', 6th edition, chapter 5, Cambridge University Press, Cambridge, pp.203 et seq. (1980)

[27] P.Artal et al., 'Odd aberrations and double-pass measurements of retinal image quality', J. Opt. Soc. Am. A, **12**, pp. 195-201 (1995)

[28] See e.g.: Eric W. Weisstein. "Geometric Centroid." From MathWorld--A Wolfram Web Resource. http://mathworld.wolfram.com/GeometricCentroid.html

[29] R.Cubalchini, 'Modal wave-front estimation from phase derivative measurements', J. Opt. Soc. Am., **69**, pp. 972-979 (1979)

[30] J.Wang, D.Silva, 'Wave-front Interpretation with Zernike Polynomials', Appl. Opt., **19**, pp. 1510-1518 (1980)

[31] M.Abramowitz, I.Stegun, (Eds.), 'Handbook of Mathematical Functions with Formulas, Graphs, and Mathematical Tables, 9th printing', New York: Dover, p. 880, 1972.

[32] P.Morse, H.Feshbach, 'Derivatives of Analytic Functions, Taylor and Laurent Series', §4.3 in 'Methods of Theoretical Physics', Part I, McGraw-Hill, New York, pp. 374-398 (1953)

[33] M.Abramowitz, I.Stegun, (Eds.), 'Legendre Functions' and 'Orthogonal Polynomials' Chs. 8 and 22 in 'Handbook of Mathematical Functions with Formulas, Graphs, and Mathematical Tables, 9th printing', Dover Publ., New York:, pp. 331-339 and 771-802, (1972)

[34] F.Zernike, 'Beugungstheorie des Schneidenverfahrens und seiner verbesserten Form der Phasenkontrastmethode', Physica, **1**, pp 689-704 (1934).

[35] B.Nijboer, 'The diffraction theory of Aberrations', PhD thesis, University of Groningen (1942)

[36] K.Nienhuis, 'On the Influence of Diffraction on Image Formation in the Presence of Aberrations', PhD thesis, University of Groningen, (1948)

[37] M.Didon, 'Développements sur certaines séries de polynomes a un nombre quelqonque de variables', Annales scientifiques de l'école normale supérieure, Paris, 7, pp. 247-268 (1870)

[38] G.Dai, "Modal compensation of atmospheric turbulence with the use of Zernike polynomials and Karhunen–Loève functions", J. Opt. Soc. Am. A, **12**, pp.2182 - 2193 (1995)

[39] G.Dai, "Modal wave-front reconstruction with Zernike polynomials and Karhunen–Loève functions", J. Opt. Soc. Am. A, **13**, pp.1218- 1225(1996)

[40] See e.g. the description of a similar technique: D.Malacara, 'Optical Shop Testing', 2nd ed., pp 551-553 (1992)

[41] H. Hamam, 'A direct method for calculating the profile of aberration of the eye measured by a modified Hartmann-Shack apparatus', Optics Communications, **137**, pp. 23-36 (2000)

[42] L.Thibos, R.Applegate, J.Schwiegerling, R.Webb, 'Standards for Reporting the Optical Aberrations of Eyes', in V.Lakshminarayanan, ed. 'Trends in Optics and Photonics', vol 35, pp. 232-244 (2000); available at: http://research.opt.indiana.edu/

[43] http://astron.berkeley.edu/~jrg/Aberrations/node5.html

[44] F.Zernike, 'Een nieuwe methode van microscopische waarneming', in Hand. nat. geneesk. Congres, **24**, pp. 100-101 (1933)

[45] F. Zernike, 'Diffraction theory of the knif-edge test and it's improved form, the phase-contrast method', Monthly Not. Roy. astron. Soc., **94**, pp.377-384 (1934)

[46] R.Noll, 'Zernike polynomials and atmospheric turbulence', J.Opt.Soc.Am, **66**, pp. 207-211 (1976)

[47] M. Born, E. Wolf, 'Principles of Optics', 6th edition, Appendix VII, Cambridge University Press, Cambridge, pp.767-772 (1980)

[48] D.Malacara, 'Optical Shop Testing', 2nd ed., pp 464-466 (1992)

[49] A.Janssen, 'Extended Nijboer-Zernike approach for teh computation of optical point-spread functions', J.Opt.Soc.Am. A, **19**, pp.849-857 (2002)

[50] J.Braat, P.Dirksen, A.Janssen, 'Assessment of an extended Nijboer-Zernike approach for the computation of optical point-spread functions', J.Opt.Soc.Am. A, **19**, pp.858-870 (2002)

[51] J.Braat, P.Dirksen, A.Janssen, A.van de Nes, 'Extended Nijboer-Zernike representation of the vector field in the focal region of a aberrated high-aperture optical system', J.Opt.Soc.Am. A, **20**, pp.2281-2292 (2003)

[52] J.Liang, 'A new method to precisely measure the wave aberrations of the human eye with a Hartmnann-Shack wavefront sensor', PhD thesis, University of Heidelberg (1992)

[53] W.Southwell, 'Wave-front estimation from wave-front slope measurements', J.Opt.Soc. Am., **70**, pp. 998-1006 (1980)

[54] R.Applegate, L.Thibos, D.Williams. 'Converting wavefront aberration to metrics predictive of visual performance', Invest Ophthalmol Vis Sci. (suppl), pp.44 et seq: ARVO E-Abstract 2124 (2003)

[55] X.Cheng, L.Thibos, A.Bradley, 'Estimating Visual Quality from Wavefront Aberration Measurements', J.Ref.Surg., **19**, pp.S579-584 (2003)

[56] C.Campbell, "Improving Visual Function Diagnostic Metrics," presentation at "5th International Congress on Wavefront Sensing and Optimized Refractive Correction," Feb 21-23, 2004 - Whistler Canada

[57] K.Strehl, Zeitschrift fur Instrumentenkunde, 22, pp. 213 et seq. (1902)

[58] C. Scheiner, 'Oculus, hoc est fundamentum opticum...', Oeniponti, Innsbruck (1619); available at http://gallica.bnf.fr

[59] R. Webb, C. Penney, K. Thompson, 'Measurement of ocular wavefront distortion with a spatially resolved refractometer', Appl. Opt. **31**, 3678-3686 (1992)

[60] V. Molebny, I. Pallikaris, L. Naoumidis, I. Chyzh, S. Molebny, V. Sokurenko, "Retina ray-tracing technique for eye refraction mapping," SPIE proc. 2971, pp. 175-183 (1997)

[61] R. Navarro, M. Losada, 'Aberrations and relative efficiency of light pencils in the living human eye', Optometry and Vision Science, 74, pp. 540-547 (1997)

[62] E. Moreno-Barriuso, 'Laser Ray Tracing in the human eye: measurement and correction of the aberrations by means of phase plates', PhD thesis, University of Cantabria, p 39 (2000)

[63] S.Burns, J.McLellan, S.Marcos, 'Sampling Effects on Measurements of Wavefront Aberrations of the Eye', abstract 4193 at ARVO 2003, Fort Lauderdale FL (2003)

[64] L. Naoumidis, I. Pallikaris, V. Molebny, I. Chyzh, V.Sokurenko, J. Wakil, "Device for measuring aberration refraction of the eye," worldwide patent WO0019885 (13/4/2000)

[65] M.Tscherning 'Die monochromatischen Aberrationen des menschlichen Auges' Z. zur Physiologischen Psychologie der Sinnesorgane, **6**, pp. 456-471 (1894)

[66] G.Walsh, W.Sharman, H.Howland, 'Objective technique for the determination of monochromatic aberrations of the human eye', J. Opt. Soc. Am. A, **1**, pp. 987-992 (1984)

[67] P.Mierdel et al. , M.Kaemmerer, M.Mrochen, H-E.Krinke, T.Seiler, 'Automated ocular wavefront analyser for clinical use', in Proceedings of the 10th Conference on Ophthalmic Technologies, June 29-July 4 2000, San Jose, USA, pp.86-92 (2000)

[68] M.Mrochen M.Kaemmerer, P.Mierdel, H-E.Krinke, T.Seiler, 'Principles of Tscherning aberrometry', J. Ref Surg., **16**, pp. S570-571 (2000)

[69] J. Hartmann, 'Bemerkungen über den Bau und die Justierung von Spektrgraphen', Z. Instumentenkd., 20, pp. 47-58 (1900)

[70] J. Hartmann, 'Objektivuntersuchungen', Z.Instrumentenkd, 24, 1-32 (1904)

[71] R.Shack, B. Platt, 'Production and use of a lenticular Hartmann screen', J. Opt. Soc. Am. **61**, p 656 (1971)

[72] A.Dreher, J.Bille, R.Weinreb, 'Active optical depth resolution improvement of the laser tomographic scanner', Appl. Opt. **24**, pp. 804-808 (1989)

[73] J.Liang, D.Williams, D.Miller, 'Supernormal vision and high resolution retinal imaging through adaptive optics', J. Opt. Soc. Am. A., **14**, pp. 2884-2892 (1997)

[74] A.Kudryasov, A.Larichev, L.Otten, 'High resolution, multispectral wide field view retinal imager', US patent US 6331059 B1, December 18, 2001

[75] J.Liang, B.Grimm, S.Goeltz, J.Bille, 'Objective measurement of wavefront aberrations of the human eye with the use of a Hartmann-Shack sensor', J. Opt. Soc. Am. A, **11**,pp 1949-1957 (1992)

[76] J.Santamaria, P.Artal, J.Bescós, 'Determination of the point-spread function of human eyes using a hybrid optical-digital method', J. Opt. Soc. Am. A, **4**, pp. 1109-1114 (1987)

[77] P.Artal, J.Santamaria, J.Bescós, 'Retrieval of wave aberration of human eyes from actual point-spread-function data', J. Opt. Soc. Am. A, **5**, pp. 1201-1206 (1988)

[78] R.Gerchberg, W.Saxton, 'A practical algorithm for the determination of phase from image and diffraction plane pictures', Optik **35**, pp. 237-246 (1972).

[79] I.Iglesias, N.López-Gil, P.Artal, 'Reconstruction of the point-spread function of the human eye from two double-pass retinal images by phase-retrieval algorithms', J. Opt. Soc. Am. A, **15**, pp 326-339 (1998)

[80] I.Iglesias, E.Berrio, P.Artal, 'Estimates of the ocular wave aberration from pairs of double-pass retinal images', J. Opt. Soc. Am. A, **15**, pp.2466-2476 (1998)

[81] L.Foucault, 'Sur un télescope en verre argenté', Paris observatory circular (1857) (English translation available at: http://bobmay.astronomy.net/foucault/leontop.htm)

[82] L. Foucault, 'Description des Procédés Employés pour Reconnaître la Configuration des Surfaces Optiques', Comptes Rendues Acad. Sci. (Paris), **47**, pp 958 et seq. (1858)

[83] F. Berny, S.Slansky, "Wavefront determination resulting from Foucault test as applied to the human eye and visual instruments", in: J.H Dickenson (Ed.) "Optical Instruments and Techniques", Oriel Press, Newcastle, pp.375 –386. (1969)

[84] F. Berny, 'Formation des images rétiniennes: determination de l'aberration sphérique du système optique de l'oeil. Un aspect de la théorie de la cohérence considéré du point de vue classique et quantique', PhD thesis, University of Paris, Department of Science (1968)

[85] Kato Koki (NIDEK), "Eye refractive power measurement apparatus ", US patent US6030081 (2000)

[86] S.MacRae, M.Fujieda, 'Slit skiascopic-guided ablation using the Nidek Laser', Journal of Refractive Surgery, **16**, Sept/Oct 2000, pp. S576-S580

[87] A.Plesch, U.Klingbeil, "Optical characteristics of a scanning laser ophthalmoscope", SPIE proc. 1161, pp. 390-398 (1989)

[88] F.Van de Velde, M.J.Tassignon, R.Trau "Scanning laser retinoscopy: a new technique for evaluating optical properties of the cornea after refractive surgery", SPIE proc. 3192, pp 187-194 (1997)

[89] MJ.Tassignon, F.Van de Velde, R.Trau, "Optical characteristics of the cornea after refractive surgery using scanning laser ophthalmoscopy", Invest. Ophthalmol. Vis. Sci. (Suppl.), 38, pp. 531 (1997)

[90] G.Westheimer, 'The Maxwellian view', Vision Res., 6, pp 669-682 (1969)

[91] Thibos L. Principles of Hartmann-Shack Aberrometry. J. Ref Surg Sept/Oct 2000; 16: S563-S565

[92] (Anonymous) Commercial perspective: company answers to important questions about their customized laser platform. J. Ref Surg Sept/Oct 2001; 17: S612-S613

[93] Mrochen M. Revealing Company secrets – Please tell the truth and nothing but the truth! J. Ref Surg Sept/Oct 2002; 18: S644-S651

[94] Larichev A, Ivanov P, Iroshnikov N, et al. Measurement of eye aberrations in a speckle field. Quantum Electronics 2001; 12: 1108-1112

[95] Applegate R, Thibos L, Bradley A, et al. Reference axis selection: Subcommittee report of the OSA working group to establish standards for measurement and reporting of optical aberrations of the eye. J Refract Surg 2000; 16: S656-S658.

[96] Schwiegerling J. Scaling Zernike expansion coefficients to different pupil sizes. J. Opt. Soc. Am. A. 2002; 19:1937-1945

[97] Marcos S, Burns S, Moreno-Barriuso E, et al. A new approach to the study of ocular chromatic aberrations. Vision Research 1999; 39: 4309-4324

[98] Llorente L, Diaz-Santana L, Lara-Saucedo D, et al. Aberrations of the human eye in visible and near infrared illumination. Optom. Vis Sci 2003; 80: 26-35

[99] Salmon T., Thibos L., Bradley A. Comparison of the eye's wave-front aberration measured psychophysically and with the Shack–Hartmann wave-front sensor. J. Opt. Soc. Am. A 1998; 15:2457-2465

[100] Moreno-Barriuso E., Navarro R. Laser Ray Tracing versus Hartmann-Shack Sensor for Measuring Optical Aberrations in the Human Eye. J. Opt. Soc. Am. A 2000; 17: 974-985

[101] Moreno-Barriuso E., Marcos S., Navarro R., et al. Comparing laser ray tracing, spatially resolved refractometer and Hartmann-Shack sensor to measure the ocular wavefront aberration Optom. & Vis. Sci. 2001;78: 152-156

[102] Hong X., Thibos L., Bradley A., et al. Comparison of Monochromatic Ocular Aberrations Measured with an Objective Cross-Cylinder Aberroscope and a Shack-Hartmann Aberrometer. Optom. & Vis. Sci. 2003; 80:15-25

[103] Vogel A., Rausch N., Krummenauer F., et al. Intraindividual comparison of Hartmann-Shack and Tscherning aberrometry concerning interobservation variation and overall accuracy. ESCRS Book of Abstracts, 20th congres of the ESCRS, September 2002, Nice, 213

[104] Durrie, D, Stahl E. Comparing Wavefront Devices. In: Krueger R, Applegate R, MacRae S. Wavefront customized Visual Correction: The Quest for Super Vision II. Thorofare, NJ, Slack, Inc, 2004: 161-168

[105] Wang L, Wang N, Koch D. Evaluation of refractive Error Measurements of the WaveScan Wavefront System and the Tracey wavefront aberrometer. J. Cataract Refract. Surg. 2003; 29: 970-979

[106] Thibos L, Bradley A. Variation in Ocular Aberrations Over Seconds, Minutes, Hours, Days, Months, and Years. In: Krueger R, Applegate R, MacRae S. Wavefront customized Visual Correction: The Quest for Super Vision II. Thorofare, NJ, Slack, Inc, 2004: 109-113

[107] Applegate RA, Sarver EJ, Khemsara V. Are all aberrations equal? J. Ref. Surg. 2002; 18:S556-S562

[108] Cohen J. Statistical power analysis for behavioral sciences (2nd edition). New York, NY, Academic Press, 1988

[109] W. Röntgen 'Über eine neue Art von Strahlen (Vorläufige Mitteilung)', Sitzungsber. physik.-med. Ges. Würzburg: pp.132-141 (1895)

[110] E.Pohl, 'Verfahren und Vorrichtung zur radioskopischen und radiographischen Wiedergabe eines Körperschnittes unter Ausschluβ van davor und dahinter liegenden Teilen', Swiss patent no. 155613, 30 June 1930

[111] B.Ziedses des Plantes, 'Eine neue Methode zur Differenzierung in der Röntgenographie (Planigraphie)', Acta Radio., **13**, pp.182-192 (1932)

[112] http://www.roentgen-museum.de/museum/anwendung/diagnostik/

[113] F.Natterer, "The mathematics of computerized tomography," SIAM, Philadelphia (2001)

[114] A.Kak, M.Slaney, "Principles of computerized tomography," chapter 6, "Tomographic imaging with diffracting sources," IEEE Press, New York (1987)

[115] A.Kak, M.Slaney, "Principles of computerized tomography," chapter 7, "Algebraic reconstruction algorithms," IEEE Press, New York (1987)

[116] D.Y.C. Chan, J.P.Ennis, B.K.Pierscionek, G. Smith, 'Determination and modeling of the 3-D gradient refractive indices in crystalline lenses', Applied Optics, **27**, pp 926-931 (1988)

[117] B.K.Pierscionek, 'Surface refractive index of the eye lens determined with an optic fiber sensor', J.Opt.Soc.Am A, **10**, pp 1867- (1993)

[118] S.Barbero, 'Global Optimization Strategies in ray tracing deflection tomography: Accuracy and Possibilities for evaluating the Gradient Index in Crystalline lenses', Chapter VIII in 'Optical Quality of the Cornea and the Crystalline Lens: Implementation of Objective Technique and Clinical Applications', PhD thesis, University of Valladolid (2003)

[119] E.H.Roth, G.Kluxen, In vivo measurements of the distribution of the refractive index of the human lens with a Scheimpflug's procedure on the anterior segment of the eye and a He-Ne laser beam', Fort Ophthalmol, **87**, 312-316 (1990)
[120] M.C.W.Campbell, 'Measurement of refractive index in an intact crystalline lens', Vision Res. **24**, 409 (1984)
[121] R. Navarro, E. Moreno, C. Dorronsoro, "Monochromatic aberrations and point-spread function of the human eye across the visual field", J. Opt. Soc. Am. A **15**, 2522-2529 (1998)
[122] D.A.Atchison, D.H.Scott, "Monochromatic aberrations of human eyes in the horizontal visual field", J. Opt. Soc. Am. A **19**, 2180-2184 (2002)
[123] D.A.Atchison, D.H.Scott, W.N.Charman, "Hartmann-Shack technique and refraction across the visual field", J. Opt. Soc. Am. A **20**, 965-973 (2003)
[124] C. E. Ferree, G. Rand, C. Hardy, "Refraction for the peripheral field of vision", Arch. Ophthalmol. **9**, 718-731 (1931)
[125] F.Rempt, J. Hoogerheide, W. P. H. Hoogenboom, "Peripheral retinoscopy and the skiagram", Ophthalmologica **162**, 1-10 (1971)
[126] M. Millodot, A. Lamont, "Refraction of the periphery of the eye", J. Opt. Soc. Am. **64**, pp. 110-111 (1974)
[127] R.A.Applegate, L.N.Thibos, A.A.Bradley, S.Marcos, A.Roorda, T.O.Salmon, D.A.Atchison, 'Reference Axis Selection: Subcommittee Report of the OSA Working Group to Establish Standards for Measurement and Reporting of Optical Aberrations of the Eye', J. Ref. Surg., **16**, pp. S656-658 (September/October 2000)
[128] D.A.Atchison, oral communication, February 2004.
[129] H-M. Cheng, "Magnetic Resonance Imaging of the Human Eye in Vivo", Optometry and Vision Science, **68**, 976-980 (1991)
[130] H-M. Cheng, O. S. Singh, K. K. Wong, J. Xiong, B. T. Woods, T. J. Brady, "Shape of the Myopic Eye as Seen with High-Resolution Magnetic Resonance Imaging", Optometry and Vision Science, **69**, 698-701 (1992)
[131] S. Bajt, A. Barty, K. A. Nugent, M. McCartney, M. Wall, D. Paganin, "Quantitative phase sensitive imaging in a transmission electron microscope," Ultramicroscopy, **83**, pp 67-73 (2000)
[132] Vincent R, "Phase retrieval in TEM using Fresnel images," Ultramicroscopy, **90** (2-3), pp. 135-151 (2002)
[133] B E Allman, P. J. McMahon, K. A. Nugent, D. Paganin, D. L. Jacobson, M. Arif, S. A. Werner, "Quantitative Phase Radiography with Neutrons," Nature, **408**, pp 158-159 (2000)
[134] B E Allman, P. J. McMahon, J. B. Tiller, K. A. Nugent, D. Paganin, and A. Barty, "Non-interferometric quantitative phase imaging with soft X-rays," J.Opt.Soc.Am.A, **17**, pp 1-12, (2000)
[135] J.Nelson, 'Wavefront sensing in other disciplines,' presentation at the '4th International Congress on Wavefront Sensing and Aberration Free Refractive Correction,' San Francisco, Feb 14-16, 2003
[136] R.A.Gonsalves, "Phase retrieval and diversity in adaptive optics," Opt. Eng., **21**, pp. 829-832 (1982)
[137] R.Grella, "Fresnel propagation and Diffraction and Paraxial Wave Equation," J.Optics (Paris), **13**, pp. 367-374 (1982)
[138] Derivation based on: M.R.Teague, "Deterministic phase retrieval: a Green's function solution," J.Opt.Soc.Am, **73**, pp. 1434-1441 (1983)
[139] F.Roddier, "Curvature sensing and compensation: a new concept in adaptive optics," Appl. Opt., **27**, pp.1223-1225 (1988)
[140] P.Hickson, "Wave-front curvature sensing from a single defused image," J.Opt.Soc.Am.A, **11**, pp. 1667-1673 (1994)
[141] W. S. Stiles and B. H. Crawford, ''The luminous efficiency of rays entering the eye pupil at different points,'' Proc. R. Soc.London, Ser. B **112**, 428–450 (1933).
[142] J. C. He, S. Marcos, and S. A. Burns, ''Comparison of photodirectionality determined by psychophysical and reflectometric techniques,'' J. Opt. Soc. Am. A **16**, 2363–2369 (1999).
[143] T.E.Gureyev, A.Roberts, K.A.Nugent, "Partially coherent fields, the transport of intensity equation, and phase uniqueness," J.Opt.Soc.Am.A, **12**, pp. 1942-1946 (1995)
[144] G.Gori, M.Santarsiero, G.Guattari, "Coherence and the spatial distribution of intensity", J.Opt.Soc.Am.A, **10**, pp. 673-679 (1993)
[145] F.Roddier, "Wavefront sensing and the irradiance transport equation," Appl.Opt., **29**, pp. 1402-1403 (1990)
[146] S.C.Woods, A.H.Greenaway, "Wavefront sensing by use of a Green's function solution to the intensity transport equation," J.Opt.Soc.Am.A, **20**, pp. 508-512 (2003)
[147] T.E.Gureyev, A.Roberts, K.A.Nugent, "Phase retrieval with the transport-of-intensity equation: matrix solution with the use of Zernike polynomials," **12**, pp. 1932-1941 (1995)
[148] T.E.Gureyev, K.A.Nugent, "Phase retrieval with the transport-of-intensity equation II: orthogonal series solution for non-uniform illumination," J.Opt.Soc.Am.A, **13**, "pp. 1670-1682 (1996)
[149] M.R.Teague, "Image formation in terms of the transport equation," J.Opt.Soc.Am.A, **2**, pp.2019-2026 (1985)

[150] E.Acosta, S.Rios, M.Soto, V.V.Voitsekhovich, "Role of boundary measurements in curvature sensing, "Opt.Comm. **169**, pp.59-62 (1999)

[151] S.Bara, S.Rios, E.Acosta, "Integral evaluation of the modal phase coefficients in curvature sensing: Albrecht's cubatures," J.Opt.Soc.Am.A, **13**, pp.1467-1474 (1996)

[152] D.Van Dyck, W.Coene, "A new procedure for wave function restoration in high resolution electron microscopy," Optik, **77**, pp. 125-128 (1987)

[153] H.Verheijen, 'Fasereconstructie van hoge-resolutie elektronenmicroscopische beelden,' Master thesis, Department of Physics, University of Antwerp (1988)

[154] T.E.Gureyev, K.A.Nugent, "Rapid quantitative phase imaging using the transport of intensity equation," Opt.Commun., **133**, pp.339-346 (1997)

[155] D.Paganin, K.A.Nugent, "Non-interferometric phase imaging with partially coherent light," Phys.Rev.Lett, **80**, 12, pp. 2586-2589 (1998)

[156] K.Nugent, D.Paganin, A.Barty, "Phase determination of a radiation wave field," International patent WO 00/26622 (1998)

[157] D.Paganin, A.Barty, P.J.McMahon, K.A.Nugent, "Quantitative phase-amplitude microscopy III: the effects of noise," J.Microscopy, **214**, pp 51-61 (April 2004)

[158] M.Soto, E.Acosta, S.Rios, "Performance analysis of curvature sensors: optimum positioning of the measurement planes," Optics Letters, **11**, 20, pp. 2577-2588 (2003)

[159] N.Streibl, "Phase imaging by the transport equation of intensity," Opt.Commun. **49**, 1, pp. 6-10 (1984)

[160] P.Hickson, "Wave-front curvature sensing from a single defocused image," J.Opt.Soc.Am.A, **11**, pp.1667-1673 (1994)

[161] J.W.Beletec, R.J.Dorn, T.Craven-Bartle, B.Burke, "A new CCD designed for curvature wavefront sensing," in: P.Amico, J.W.Beletic (eds.), "Optical Detectors for Astronomy II State-of-the-art at the Turn of the Millennium," Kluwer, Dordrecht (2000)

[162] M. Born, E. Wolf, 'Principles of Optics', 6th edition, Chapter VIII, Cambridge University Press, Cambridge, pp.370 et seq. (1980)

[163] P.M.Blanchard, A.H.Greenaway, "Simultaneous multiplane imaging with a distorted diffraction grating," Appl. Opt., **38**, 32, pp. 6692-6699 (1999)

[164] P.M.Blanchard, D.J.Fisher, S.C.Woods, A.H.Greenaway, "Phase diversity wavefront sensing with a distorted diffraction grating" Appl. Opt., **39**, 35, pp. 6649-6655 (2000)

[165] M.A. van Dam, R.G.Lane, "Extended analysis of curvature sensing, " J.Opt.Soc.Am.A, **19**, pp. 1390-1397 (2002)

[166] L.J.Otten, G.R.G.Erry, S.C.Woods, P.Harrison, "Wavefront characterization of cornea's," US patent 2003/0011744 (16 January 2003)

[167] M.de los Angeles Rama, S.Ríos and E.Acosta, 'New treatment for tomographic reconstruction of refractive index profiles of inhomogeneous objects from slope measurements', Jpn. J. Applied Physics, **37**, 3682-3685 (1998)

[168] E.Acosta, D.Vazquez, G.Smith, L.Garner, 'A Comparison and Analysis of Various Techniques for Determining the Gradient Index Distribution of Non-Symmetric Crystalline Lenses', *unpublished*

[169] R.J.Copland, D.R.Neal, (Wavefront Sciences), 'Tomographic Wavefront Analysis System and Method of Mapping and Optical System', Worldwide patent WO02075367 (2002)

[170] D.A.Atchison, 'Anterior corneal and internal distributions to peripheral aberrations of human eyes', J. opt. Soc. Am A, **21**, pp. 355-359 (2004)